

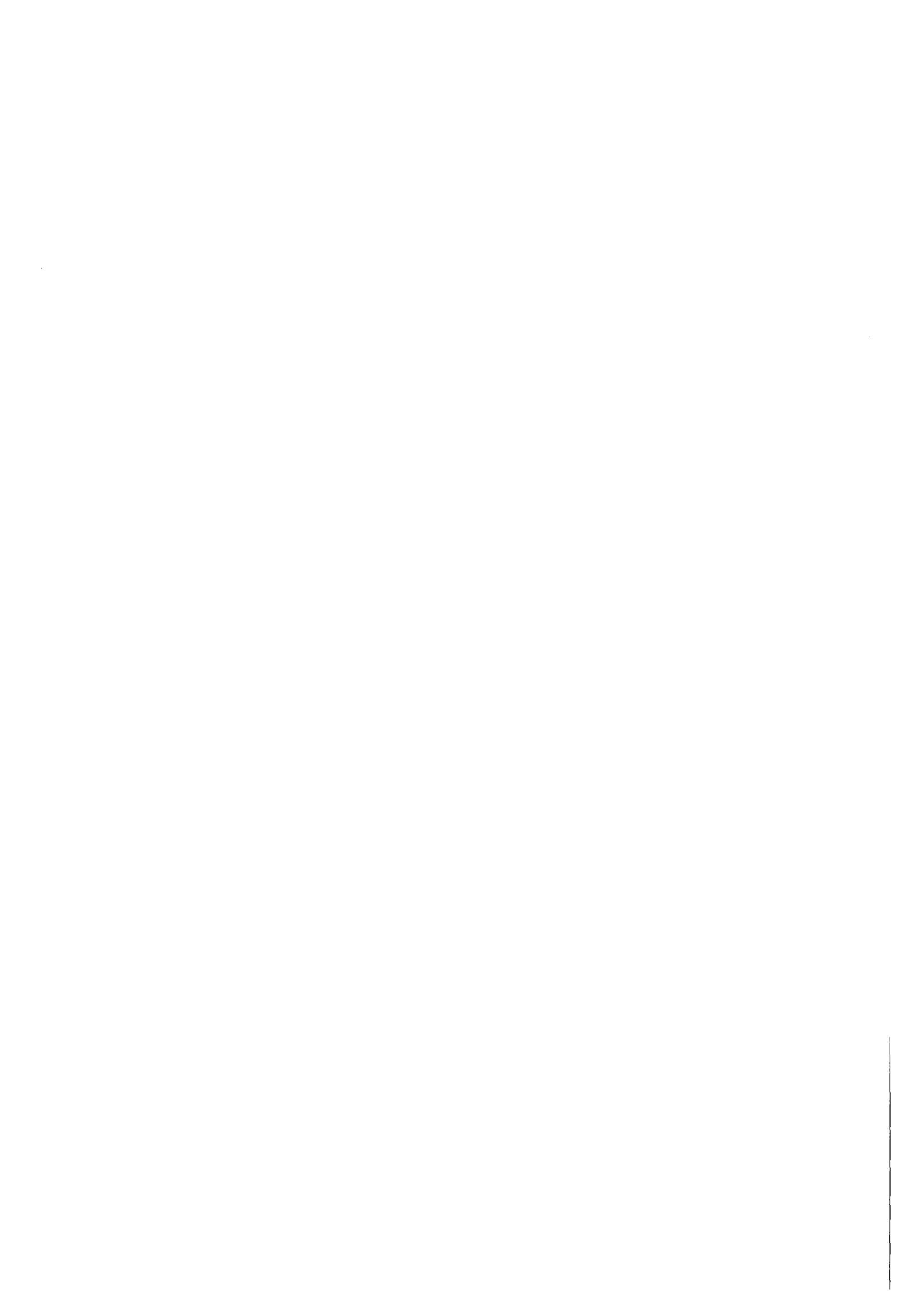
KfK 3019
November 1980

**Proceedings of
the Workshop on
RF Superconductivity**

**Karlsruhe, Federal Republic of Germany,
July 2-4, 1980**

**Editor: M. Kuntze
Institut für Kernphysik**

Kernforschungszentrum Karlsruhe



KERNFORSCHUNGSZENTRUM KARLSRUHE
Institut für Kernphysik

KfK 3019

PROCEEDINGS OF
THE WORKSHOP ON RF SUPERCONDUCTIVITY

Karlsruhe, Federal Republic of Germany
July 2-4, 1980
Editor: M. Kuntze

Als Manuskript vervielfältigt
Für diesen Bericht behalten wir uns alle Rechte vor

Kernforschungszentrum Karlsruhe GmbH
ISSN 0303-4003

Organizing Committee

- A. Citron, Kernforschungszentrum Karlsruhe
- H. Lengeler, CERN Geneva
- H. Piel, University of Wuppertal
- A. Septier, IEF Université Paris-Sud

Institutions represented

1. Brookhaven Nat. Lab., USA
2. CERN Geneva
3. Centre d'Études Nucléaires de Saclay (CEN)
4. DESY, Hamburg
5. Fermi Lab. Batavia (FNAL)
6. GSI, Darmstadt
7. High Energy Physics Lab. (HEPL), Stanford University, USA
8. Nat. Lab. for High Energy Physics (KEK), Japan
9. Siemens Erlangen
10. Stanford Linear Accelerator Center (SLAC), Stanford University, USA
11. Cornell University, USA
12. University of Geneva
13. University of Genoa
14. University of Illinois, Urbana, USA
15. University of Karlsruhe
16. University of Milano
17. University of Paris, Orsay
18. University of Wuppertal
19. Interatom, Bergisch Gladbach (manufacturer of niobium)
20. Kawecki, Lakewood, USA (supplier of niobium)

C o n t e n t

		page
1. Compilation of experimental results and operating experience	A. Citron (KfK, Karlsruhe)	3
2. Surface preparation of Niobium	P. Kneisel (KfK, Karlsruhe)	27
3. The preparation of superconducting Nb ₃ Sn-surfaces for Hf-applications	B. Hillenbrand (Siemens, Erlangen)	41
4. Surface studies and electron emissions	A. Septier (University of Paris)	53
5. Diagnostic methods of superconducting cavities and identification of phenomena	H. Piel (University of Wuppertal)	85
6. Electron loading - description and cures	C. Lyneis (HEPL, Stanford)	119
7. Heat transfer and models for breakdown	H. Padamsee(Cornell University, Ithaca)	145
8. Theoretical aspects in rf-superconductivity	J. Halbritter (KfK, Karlsruhe)	190
9. Round table discussion: "What to do next?"	G. Loew (SLAC, Stanford)	215
10. Design of superconducting accelerator cavities	H. Lengeler (CERN, Genf)	219
11. Additional design criteria for low β structures	M. Kuntze (KfK, Karlsruhe)	237
12. Joints, couplers, and tuners	R. Sundelin (Cornell University, Ithaca)	243
13. Fabrication of niobium cavities	W. Bauer (KfK, Karlsruhe)	271
14. Superconducting cavities for electron storage rings - a review	M. Tigner (Cornell University, Ithaca)	289
15. Round table discussion: conclusion	A. Citron (KfK, Karlsruhe)	317
16. List of Participants		321
17. Summary of the workshop on rf-superconductivity	A. Citron (KfK, Karlsruhe)	323



COMPILATION OF EXPERIMENTAL RESULTS AND OPERATING
EXPERIENCE

A. Citron

Kernforschungszentrum Karlsruhe,
Institut für Kernphysik
P.B. 3640
7500 Karlsruhe
Federal Republic of Germany.

I would like to start by thanking those who have sent in material for this compilation and also my collaborators who have helped me by digging out more information from their own files and from the literature.

I have restricted this compilation to those applications of rf superconductivity where high fields are needed. So I have left aside applications such as frequency standards etc. I have not included either measurements on TE-resonators. Their use as accelerator cavities has been proposed, but, to my knowledge, it has not so far been tried anywhere. I am also lacking information from the Soviet Union I know that some work in the field is going on there, but I could not obtain any information. Apart from these more or less deliberate omissions I certainly forgot many important pieces of work and I will be happy, if you can fill in the gaps I left.

I shall instantly show a table in which the laboratories upon whose work I will report are listed. Some devices are underlined. Those are the devices that either operate or have operated. I think it is important to point out that some superconducting devices have been in duty now for some time, some for several thousand hours. This, I think, is important to stress, because it can help to eliminate the original fear that superconducting devices would be very delicate to operate and would need frequent reprocessing. To my knowledge, none of the devices that have been operated under realistic conditions have deteriorated during operation. So we can say that superconducting devices can be expected to keep the performance they once had. Table 1 shows the laboratories arranged geographically.

We shall now discuss the results obtained:

The first question is what Q-values or what surface resistances can be obtained. Of course, the quantity of interest is the Q-value at the peak-field or at least at a field that is high enough to be interesting for

operation. Q-values at zero-field are often more impressive, but not very useful. It is customary to convert Q-values into a surface resistance R by means of the geometry factor $G = R/Q$. In this way, one generally finds R values which are on the range of $1 - 2 \times 10^{-7} \Omega$. But we know that this procedure is very questionable, because very often, the Q is not fixed by a general property of the surface (weighed only by the square of the magnetic field), but by the performance of some small region inside the cavity that limits the Q-value. This is borne out by the fact that, in general, degradation of peak-fields, e.g. in going from single cell to multiple cell structures is accompanied by a corresponding drop in Q-value. On the other side, low β -structures with a small G often show a low surface resistance. The reason is, of course, that the same additional source of loss affects them less, because their Q-value is lower to start with.

High R-values in the $\mu\Omega$ region (high losses) are observed in certain multiple cell cases, as I mentioned, and also in the case of the lead plated structure.

Rf losses are not considered the main problem, though, since in the range of Q-values around 10^9 or even between 10^8 and 10^9 , the rf losses are usually more or less matched by the cryogenic losses.

Most of the devices I mention are operated below the λ -point of He. Only the more recently developed low frequency devices (below 1 GHz) work at 4.2 K. The reason is, of course, that in these cases the surface resistance is dominated by the residual resistance that is independent of temperature; so it does not pay to go to the additional expense of operating at 1.8 K.

In this context I should mention the possibility of using Nb_3Sn coatings. These would look very attractive, because they would allow to use 4.2 K cooling also for higher frequency structures since the transition temperature is so much higher. Unfortunately, so far Nb_3Sn coated cavities have not been competitive with those made of pure niobium and I have

therefore not included them in my survey. But we will hear more about them in a later contribution. Unfortunately, there will be no contribution on the lead technology since John Dick from Cal Tech was not able to come.

FIELD LIMITATIONS

The field limitation we are most concerned about is the accelerating field, thus practically the voltage gain divided by the length of a structure. But we shall first discuss the quantities that are more directly related to what physically goes on in the cavity, namely peak magnetic- and peak electric field (B_p , E_p). I propose to split discussion into two parts, namely for high β -structures and for low β -structures.

HIGH β -STRUCTURES

These structures are in general simple resonators. Three types have been used, namely: cylindrical, spherical and muffin-tin structures. The range of frequency is considerable and it goes from 0.5 to 10 GHz. Due to the similarity the parameters describing the field distribution do not vary widely (table 2). We shall now look at fig. 1 which is a plot of the peak magnetic field against operating frequency. The round points are TM resonators. They show very high B_p -values, although well below the critical magnetic field which is somewhere near 200 mT. Some are definitely above the lower critical field B_c , which is not a quantity of any subsequence for high frequency application. But usually is a considerable step from them to an accelerating structure. Fig. 2, 3 and 4 show some examples of such TM resonators.

I have included in fig. 1 (triangles) actual accelerating structures, most of which have multiple cell versions. Some examples are shown in fig. 5 - 11. The Wuppertal structure shows remarkably high peak fields. It also gives an

example of the usual degradation in peak field with increasing cell number. This shows that, in particular for multiple cell structures, the field shown is not really the peak field occurring in the structure, but rather a field that is based on a field measurement somewhere in a cavity and a calculated field enhancement at another place of the cavity. Now this field enhancement can well be larger than calculated if the field does not follow the ideal shape, and the more complicated the structure becomes, the bigger the error can be. This is one reason for the decrease in peak field with cell number. That it is a valid reason is shown by the fact that Wuppertal people managed to get the peak field up to the highest value in a 65 cell structure by very careful chemical tuning which corrects the field distribution. One can thus hope that by this method one will also in other cases be able to push up the lower values for multiple cell structures. The decrease with cell number is also observed at KEK, where spherical and cylindrical cavities gave similar values and at Genoa, where however a definite spot is suspected in the three-cell cavity. So one can hope to approach the one cell value there in the near future. The bulk of the measurements clusters around the S-band, but consistently with lower values for higher numbers of cells. I was told so that the eleven-cell-version that has been operated in the CORNELL synchrotron is a rather old one and that one would expect today to be able to produce higher field values. In the region of L-band and below where because of storage ring applications a lot of interest lies, field values are unfortunately rather modest.

Also included in fig. 1 are some separator structures by BNL and the separator that has been built by Karlsruhe for CERN; it is shown in figures 12 through 14 and joins the general pattern of decreasing B_p with increasing number of cells.

If we look at fig. 1 we have the definite impression that there is an almost linear dependence of the peak field on frequency, in particular, if we admit that some of the lower values on multiple cell

structures can be lifted as was pointed out before. If one looks for a reason in terms of magnetic field, the only possible explanation is the occurrence of 'bad spots' with a certain probability per unit surface. The surface will, of course, increase with increasing wave length and therefore structure dimensions. This view seems to be supported by the fact, that multiple cell structures that obviously have more surface usually show poorer performance. But we have seen this latter fact can also be explained in a different way. The general feeling today is that this theory of field limitations is certainly not the whole story. Fig.15 shows in the similar way the electric peak field versus frequency. Because of the rather similar field geometry the general pattern is very similar to that of fig. 1. If we want to discuss these field limitations, in particular if we want to explain the decrease of the peak fields with decreasing frequency, then we are in the topic of the electron phenomena. Claude Lyneis is going to talk about that later in the day. So I limit myself here to a very simple minded consideration (fig. 16). If an electron leaves a surface perpendicular to which a periodic electric field is acting, and if the particle enters the field at such a phase that the field is directed away from the surface and is rising, then the electron will follow a trajectory that is a combination of an oscillation perpendicular to the surface and a drift away from it. If magnetic fields are present as well, the motion will be more complicated, but have in principle the same character. The distance between successive returning points of the trajectory we shall call X . One can work out that this quantity X is proportional to λ^2 , where $\lambda = c/v$. Also the kinetic energy has a maximum that is proportional to λ^2 . If we compare the quantity X to the quantity $\lambda/2$ which roughly gives the typical dimension of a cavity, then we find that in the range of frequency we consider there is a crossover (fig.16 inset): for high frequencies there are many oscillations per cell dimension whereas for low frequency the cavity dimensions were only a fraction of an oscillation loop. Now apart from the multipacting phenomenon, which Claude Lyneis is going to comment upon each extensively, two points seem to make the electrons

more dangerous in the low frequency case, a) the trajectory hits the opposite wall already after a fraction of an oscillation thereby the beam can be still quite concentrated and b) the energy contained in the beam is much higher. Both can lead to more massive deterioration of the surface. But I leave it to Claude Lyneis to give a more complete picture of these phenomena.

In fig. 17, the quantity E_{acc} is plotted against v . This is the quantity, which we are most concerned with. In this figure I omit the separator structures, because deflecting fields cannot really be compared to accelerating fields. I also include the TM resonators here only with some misgivings since the effective length of the cavity is a somewhat arbitrary quantity and one is tempted to quote a short effective length in order to obtain a high accelerating field value. In an actual accelerating structure, the effective length is more obvious. The striking feature is that the high values for Wuppertal have come down quite a bit. This I have discussed with Prof. Piel and there are two main reasons: a) because of the small dimensions, tolerance requirements are high and therefore the structure had to be operated the $\pi/2$ mode, which, of course presses the ratio E_{acc}/E_p down. Moreover, the relatively large gap - it is about 50% of the cavity diameter -, is another factor that effects this quantity adversely. A third feature, which we observe, can be avoided. As we see, the 65-cell structure that used to have a similar performance to the 3-cell structure now lies very low. The reason for this is that the 65-cell structure includes a low β section for the lowest energy electrons and that has an unfavourable peak to accelerating ratio. One could, of course, isolate this first low β section and regain the good performance for the rest of the structure. Genoa still looks very favourable. Most of the other structures are well below 10 MV/m perhaps at 3 MV/m for practical structures. Looking at fig. 17, one feels that a lot of frequency dependence has gone. It appears as if there was an optimum frequency somewhere round the C-band; but this is something we need more data on.

LOW β -STRUCTURES

Here β lies between .04 and .2. We will refer to 5 different types of structures, but their special problems will be discussed in a later talk.

The frequencies they are operated at lie between 90 and 700 MHz. The variety of structures is reflected in a larger variation and more or less favourable figures for the field parameters that are given in table 3.

Electric peak fields are generally in the region 16 to 20 MV/m and magnetic fields between 25 and 95 mT. There is no systematic frequency dependence, but we should remember that for very low β values, low frequencies are preferred.

In fig.18, I have plotted the accelerating field against the diameter of the structure. The diameter is of some economic relevance since it determines also the diameter of the cryostat and the demand of helium. The structures represented are shown in fig.19 through 27. It is seen that all structures give comparable performance. The energy gain is less favourable in the helix structures, but their advantage is a much smaller diameter.

Here is the end of my compilation. I draw no conclusions since we are only at the beginning of our work. I may mention some of the open problems on which we may have to find out an answer.

- Is there a preferred frequency ?
- Is there a preferred shape ?
- What treatments are essential, in particular is the heat treatment essential ?
- Is it possible to produce Nb_3Sn surfaces ?
- Is lead technology still competitive ?

and last not least:

- Do we find any surface treatments that do away with the electron limitations ?

Table 1:

LABORATORIES REPORTED UPON

and operating devices

	OBJECT
<u>U.S.A.</u>	
HEPL	X,S,L-band resonators, <u>recyclotron</u> <u>Urbana Microtron</u>
SLAC	X-band resonator
Cornell	Muffin-tin-structure in X,S and L-band, <u>synchrotron</u>
ANL	<u>Split-ring-structure</u>
Cal.Tech./ Stony Brook	Split-ring structure in Pb
BNL	X-band deflector, S-band-resonator
<u>Japan</u> KEK	C-band resonator (spherical and cylindrical)
<u>Israel</u> W.I.	400 MHz-re-entrant res. (from HEPL)
<u>Europe</u>	
Siemens	X-band resonators
Genoa	C-band spherical
CERN	S-band cyl. and spherical, 500 MHz sph. res.
Wuppertal	<u>X-band accelerator</u>
KfK	S-band resonators <u>S-band separator (CERN)</u> <u>90-MHz accelerator</u> <u>100-MHz helix resonators (CEA)</u> 700-MHz resonator 500-MHz resonator

Table 2:

HIGH β -STRUCTURES

Frequency range 0.5 ÷ 10 GHz

Parameters of field distribution:

$$E_p/E_{acc} = 2 \div 4.5$$

$$B_p c/E_{acc} = 1 \div 2$$

or:

$$B_p/E_{acc} = 3 \div 6 \text{ mT} \cdot \text{m/MV}$$

$$B_p c/E_p = 0.45 \div 0.77$$

or:

$$B_p/E_p = 1.5 \div 2.6 \text{ mT} \cdot \text{m/MV}$$

Table 3:

LOW β -STRUCTURES

$$0.04 \leq \beta \leq 0.2$$

Frequency range 90 - 720 MHz

Parameters of field distribution:

$$E_p/E_{acc} = 4 \div 14$$

$$B_p C/E_{acc} = 1.8 \div 14$$

or:

$$B_p C/E_{acc} = 6 \div 47 \text{ mT}\cdot\text{m/MV}$$

$$B_p C/E_p = 0.9 \div 2.2$$

or:

$$B_p/E_p = 3 \div 7 \text{ mT}\cdot\text{m/MV}$$

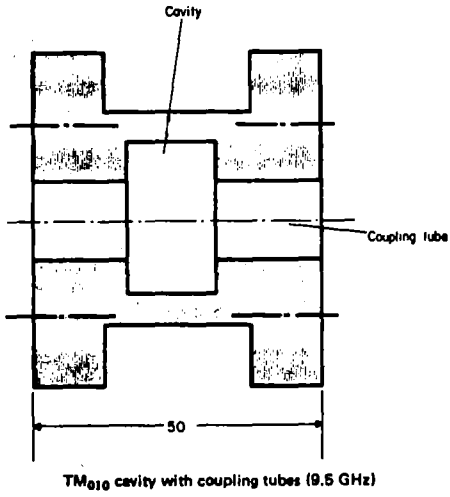


Fig. 2: X-band TM-resonator
SIEMENS

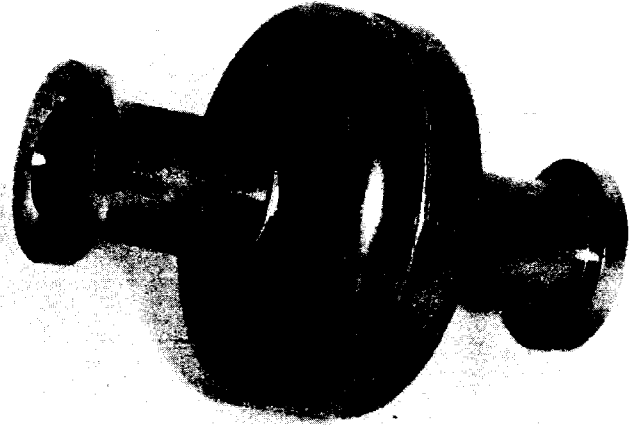


Fig. 3: TM-resonator S-band
Stanford

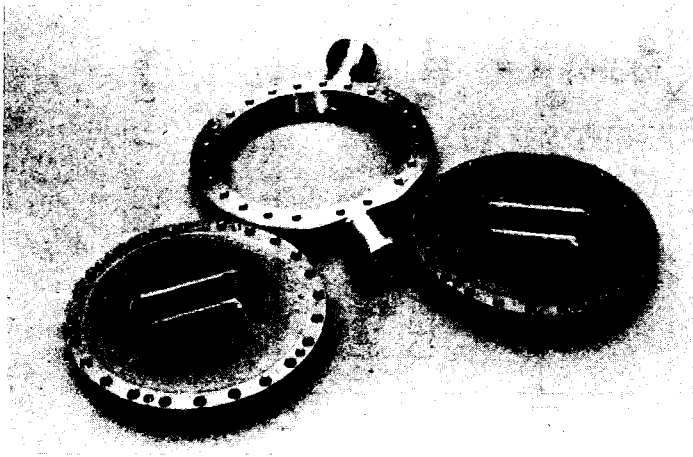


Fig. 4: S-band resonator
Cornell

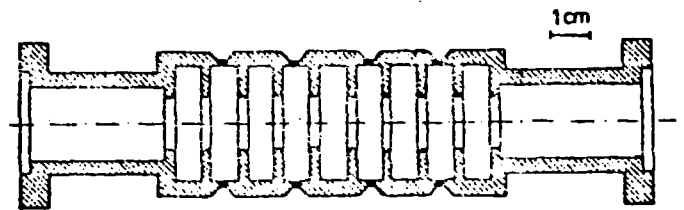


Fig. 5: 9-cell X-band accelerating
structure. Wuppertal

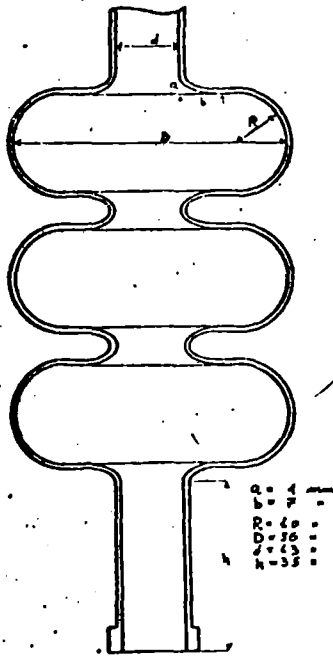


Fig. 6: 3-cell spherical structure
C-band.Genoa

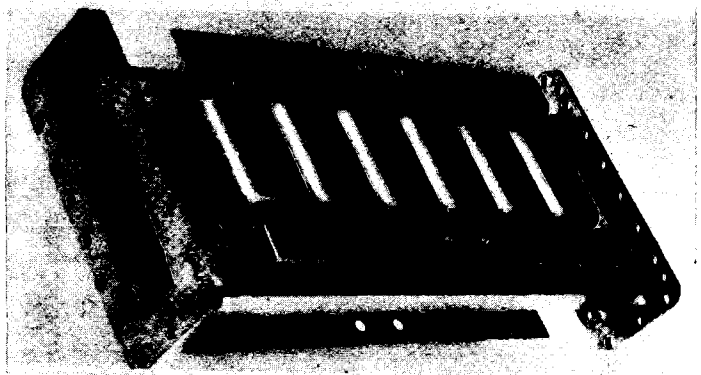


Fig. 7: 6-cell muffin tin accelerating
structure S-band.Cornell

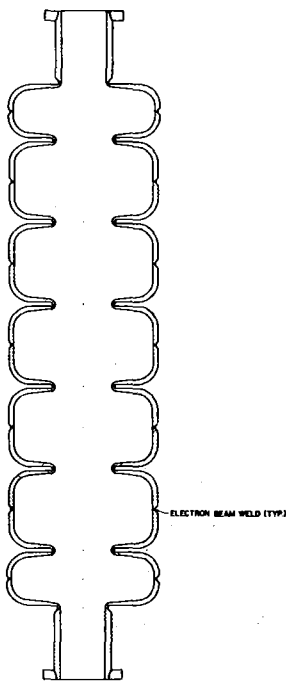


Fig. 8: 6-cell accelerating struc-
ture L-band.Stanford

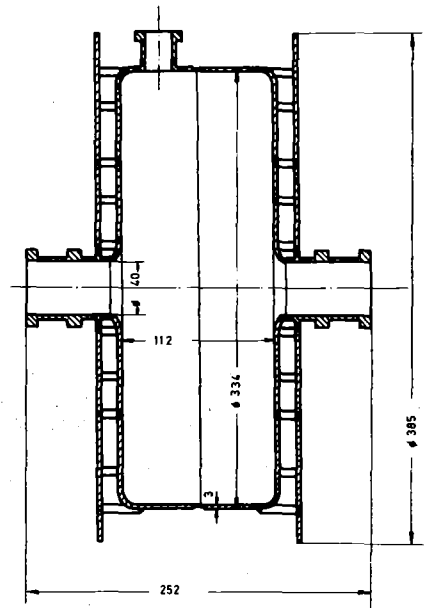


Fig. 9: 700-MHz-accelerating structure.
Karlsruhe

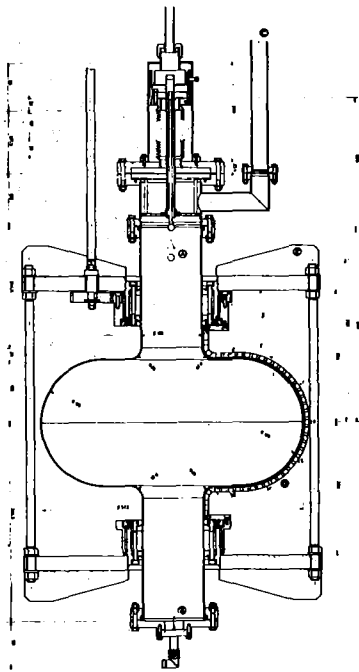


Fig. 10: 500-MHz-spherical structure, CERN

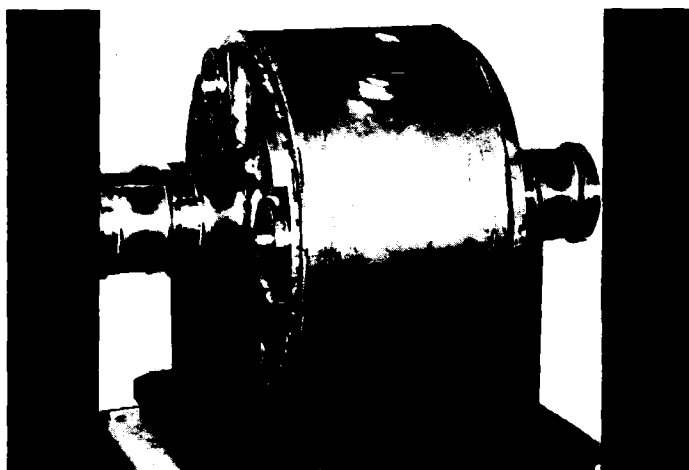


Fig. 11: 500-MHz-structure for test in DORIS, Karlsruhe

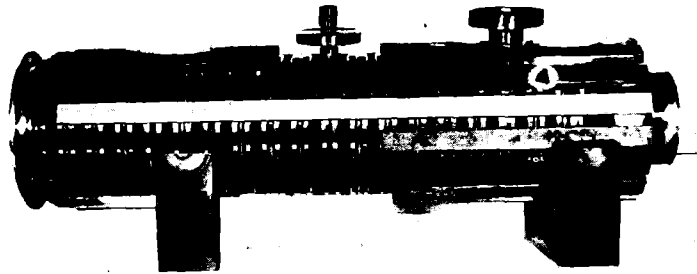
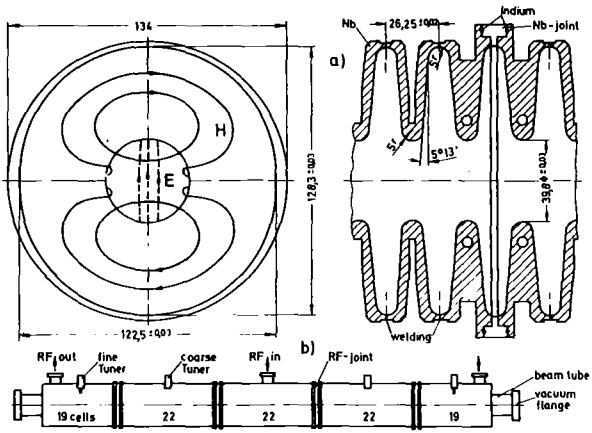


Fig. 12: S-band separator structure (schematic). Karlsruhe

Fig. 13: 22-cell separator-section Karlsruhe



Fig. 14: 104-cell deflecting structures mounted at CERN. Karlsruhe

E_p MV/m

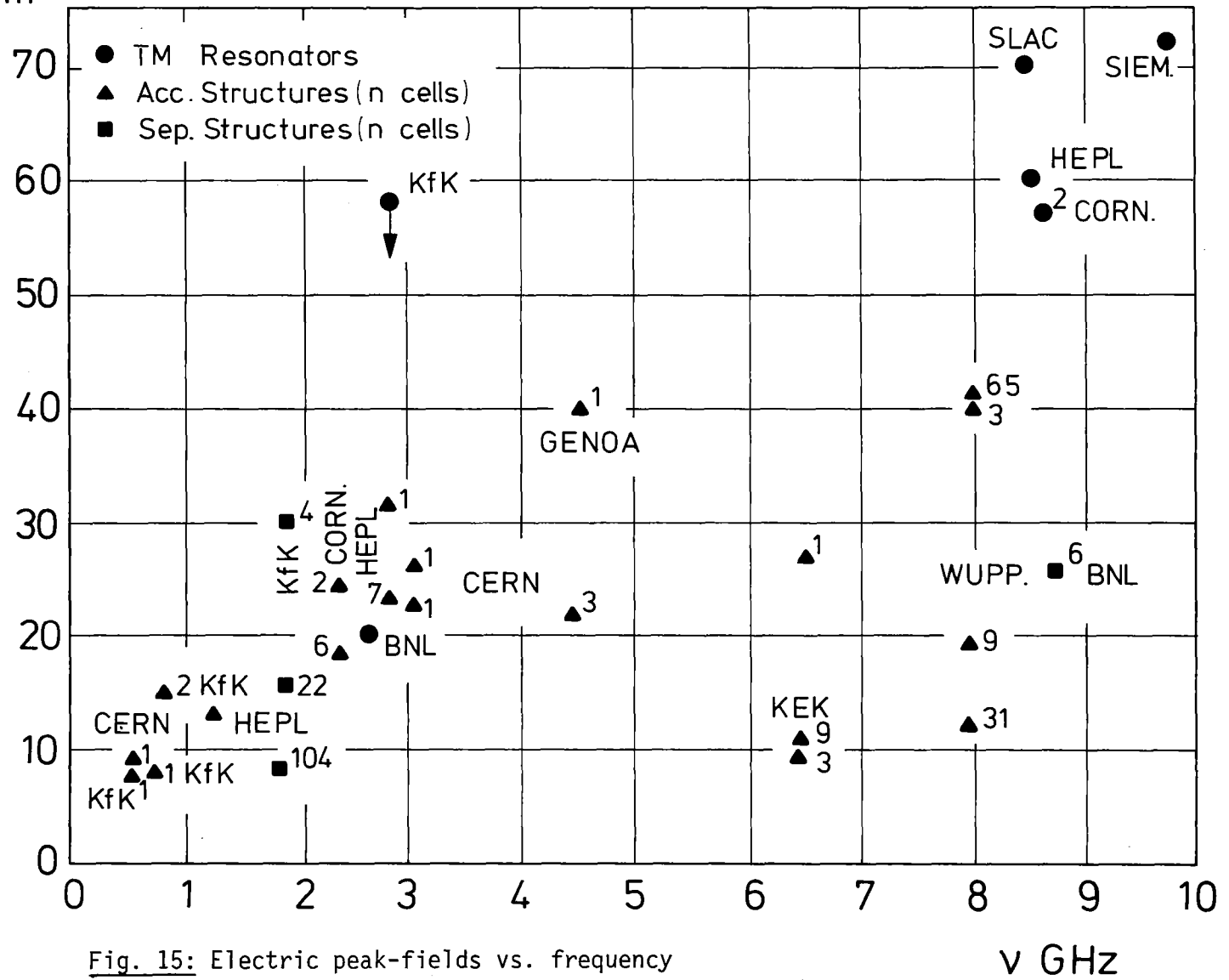
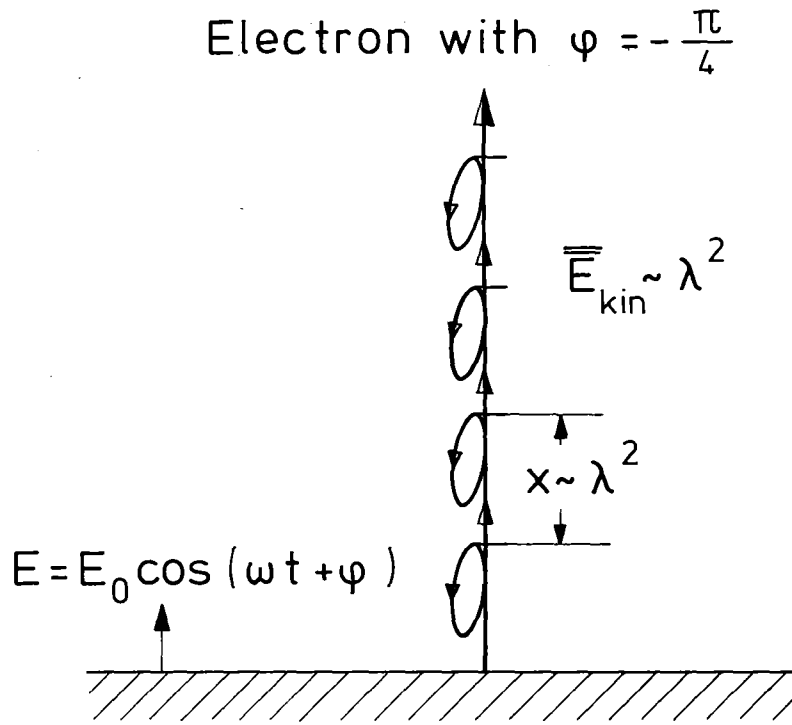


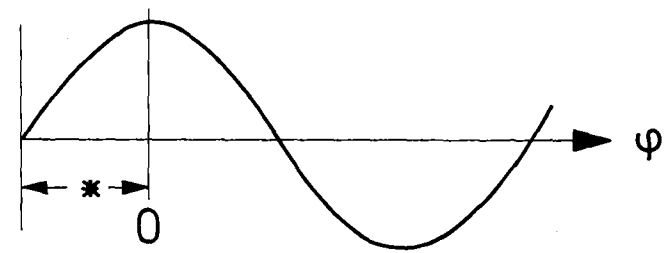
Fig. 15: Electric peak-fields vs. frequency

ν GHz



ν (GHz)	$2x/\lambda$
30	0.094
10	0.283
3	0.942
1	2.83
0.3	9.42

for $E_0 = 20 \text{ MV/m}$ $\varphi = -\frac{\pi}{4}$



* starting phases for drifting trajectories

Fig. 16: Action of rf-electrical field on electrons leaving the surface (schematic)

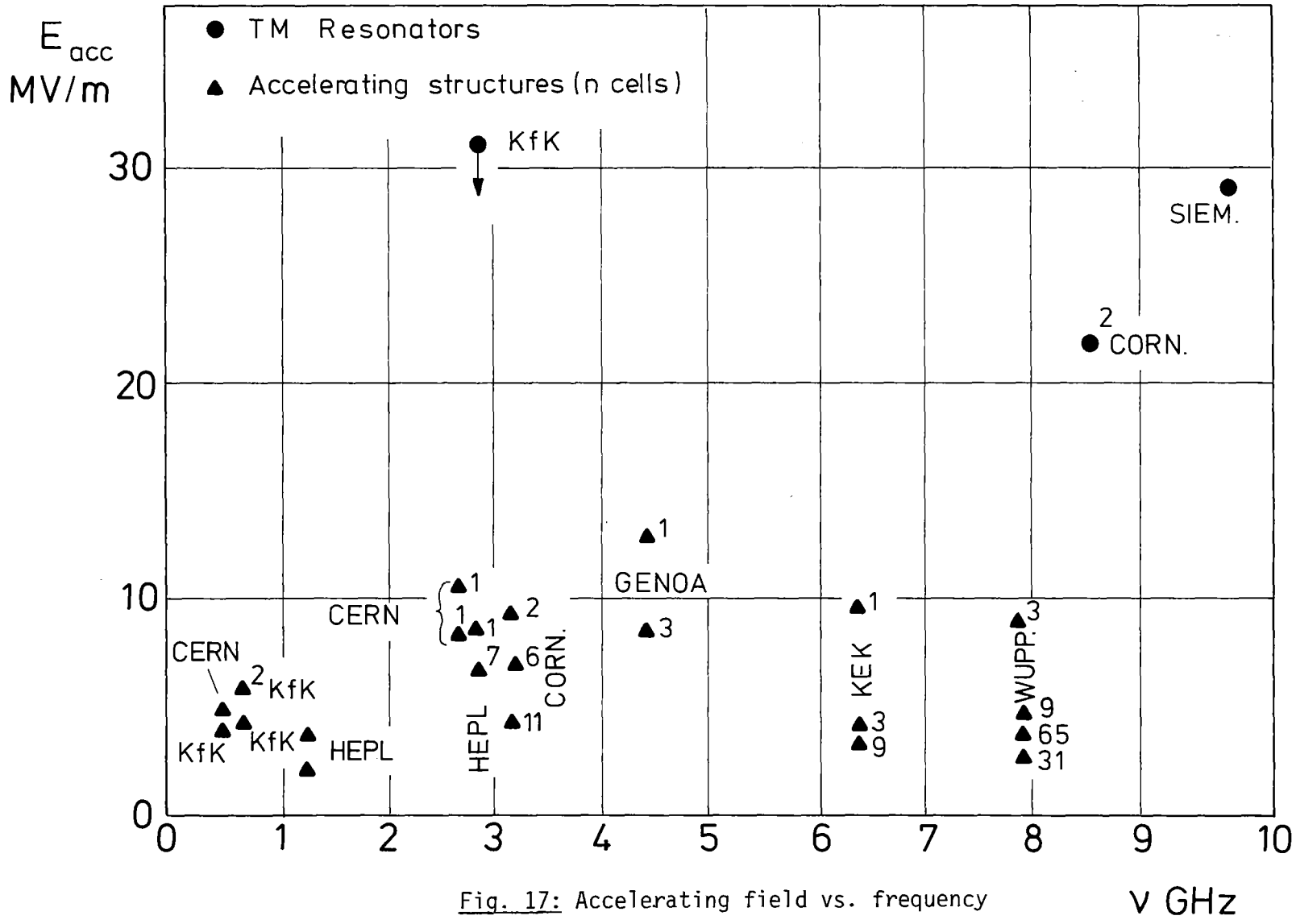


Fig. 17: Accelerating field vs. frequency

v GHz

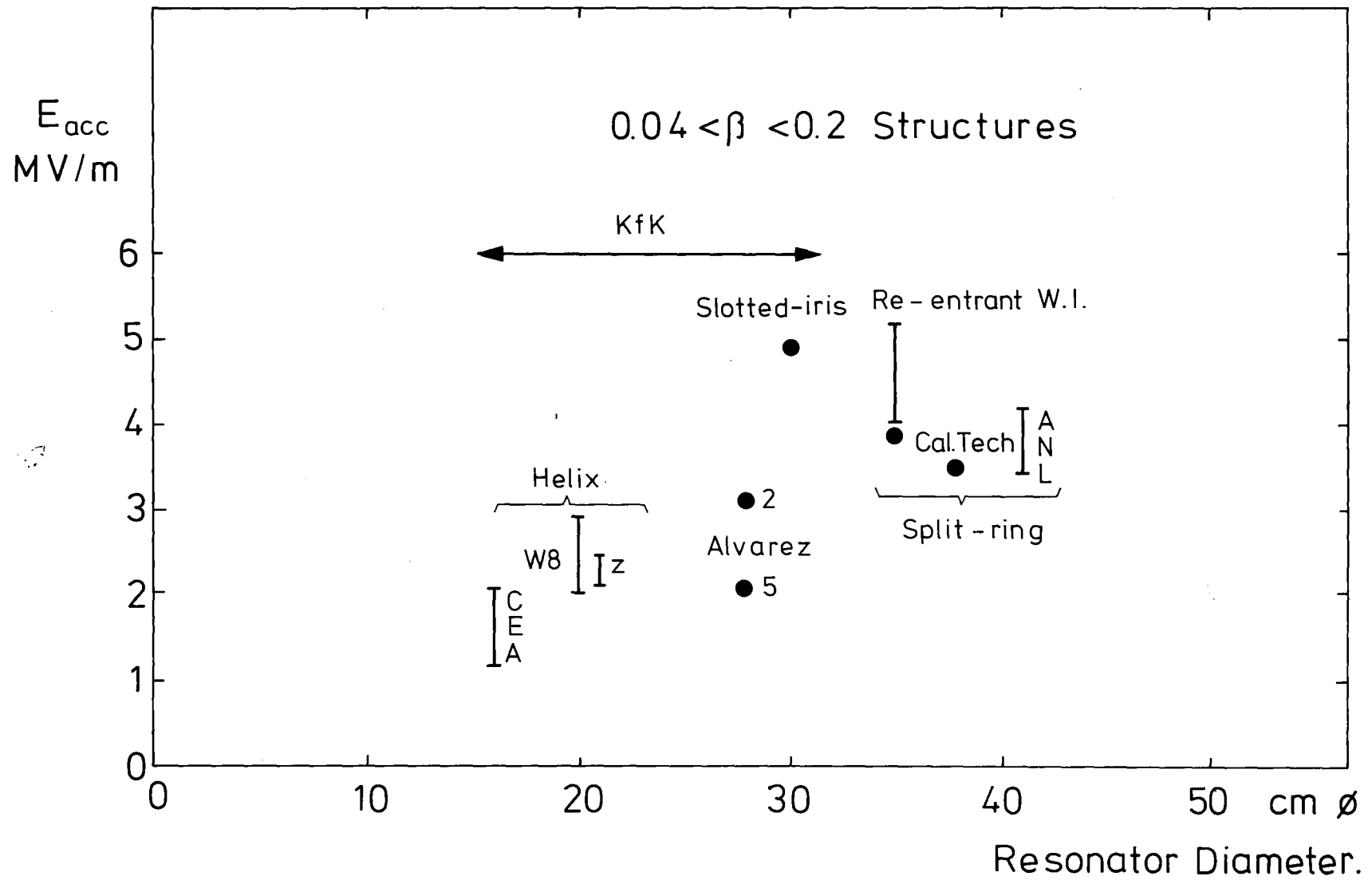


Fig. 18: Accelerating field against resonator-diameter for low β -structures

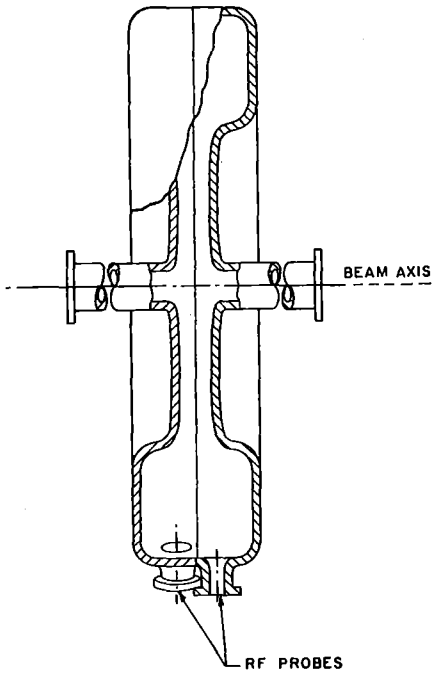


Fig. 19: 433 MHz-re-entrant cavity for heavy ion acceleration, Stanford/Weizmann Institute

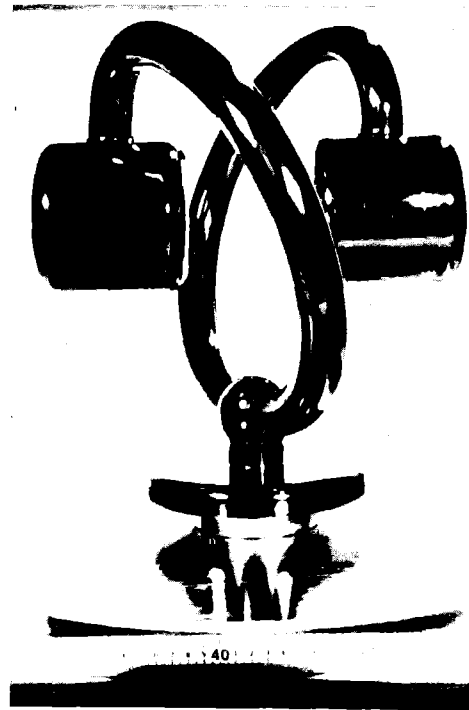


Fig. 20: 97 MHz-split-ring structure Argonne National Laboratory

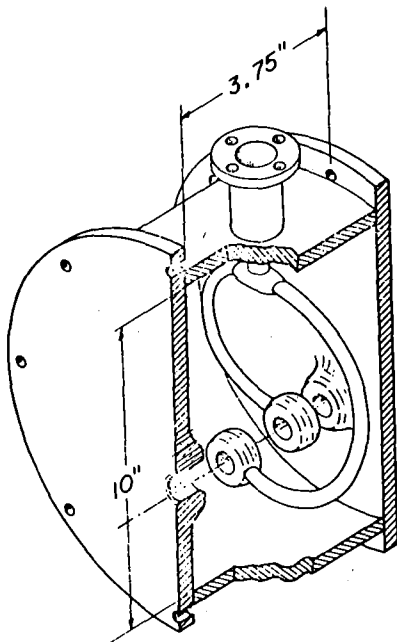


Fig. 21: 150 MHz-split-ring structure (lead-plated) Caltech/Stony Brook

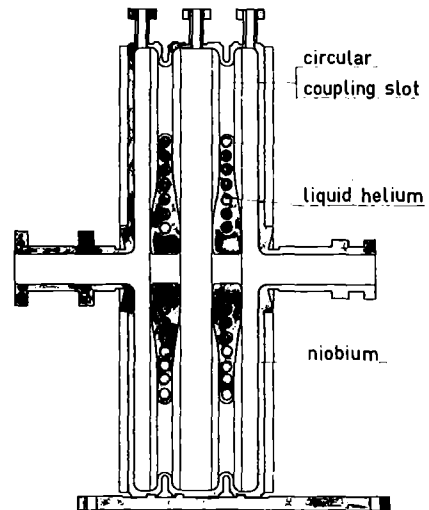


Fig. 22: 720 MHz-slotted Iris-structure, Karlsruhe

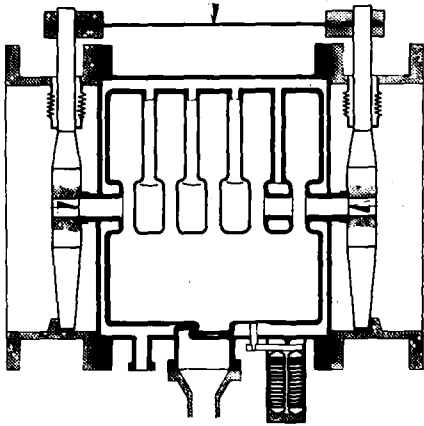


Fig. 23: 5-cell 720 MHz-Alvarez-structure, Karlsruhe

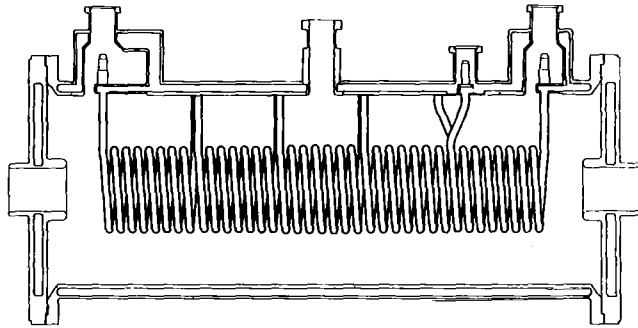


Fig. 24: 90 MHz-multiple helix-structure, Karlsruhe

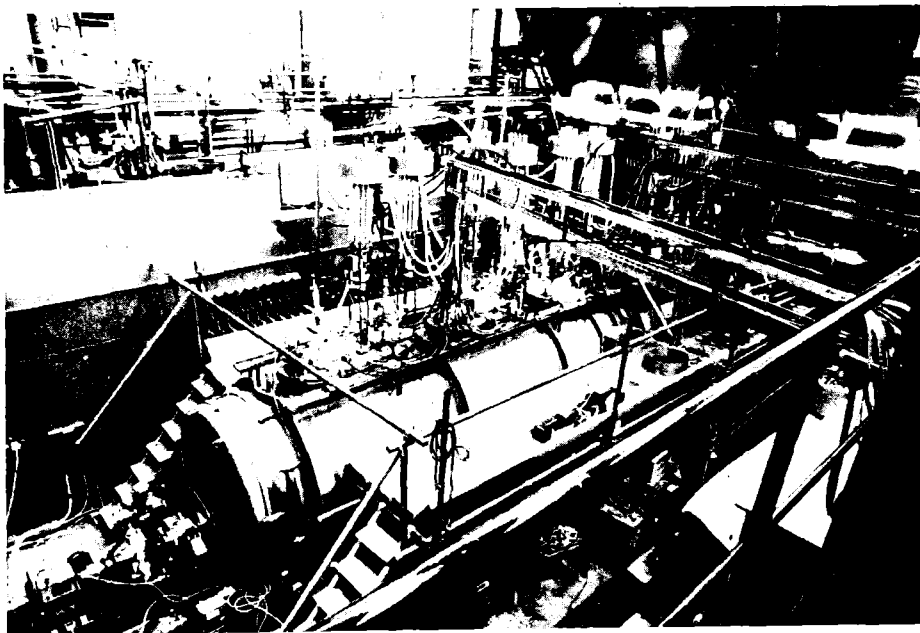


Fig. 25: Proton linear accelerator consisting of 9 helix-structures (Fig. 24) and 1 Alvarez-structure (Fig. 23)

SURFACE PREPARATION OF NIOBIUM

P. Kneisel

Kernforschungszentrum Karlsruhe
Institut für Kernphysik
P.B. 3640
7500 Karlsruhe
Federal Republic of Germany

1. Introduction

Any discussion of surface preparation for superconducting rf-surfaces is certainly connected with the question what is the best recipe for achieving high Q-values and high break-down fields. Since the break-down in a cavity is not understood so far and because several mechanisms play a role, it also is not possible to give one recipe which always works.

Nevertheless in the past certain preparation techniques for niobium surfaces have been developed and certain rules for preparation can be applied. In the following the to-days state of the art will be described. A description of the physics of the surface and the explanation of the phenomena observed in rf-cavities caused by the state of the surface will be given afterwards ^{1,2}.

It is well known that rf-superconductivity is taking place in a thin surface layer of only a couple of nm. In the case of niobium the electromagnetic field penetrates about 60 nm into the metal depending on the mean free path of the electrons in the surface sheath.

It is also known that from the point of view of rf-superconductivity best results as predicted by the BCS-theory can be achieved for a clean, defect-free metal surface. If this surface is smooth on a microscopic scale the surface resistance is smaller than for a rough surface because the current paths are shorter and therefore less dissipation takes place. A smooth surface is also desirable, if one is interested in establishing high electromagnetic fields on the superconducting surface. As is known rough surfaces lead both to electric field enhancements causing non resonant electron loading, and to magnetic field enhancements initiating rf-breakdown.

In reality of course one is not dealing with ideal surfaces. The niobium is in addition covered with oxide adsorption layers, the effects of which will be discussed in ref. ²⁾.

In the following it is attempted to give a short description of the surface in conjunction with the methods of surface treatments, which generally can be applied to niobium cavities.

2. Surface Treatments

2.1 Machining of a Surface

For the shaping of metal pieces different techniques are used as will be described in detail later during this workshop. ³⁾ Niobium, which is electron beam molten, is usually either machined on a lathe or by milling or die formed (hydroformed, spun) by sheet metal techniques. In all cases defects are introduced into the metallic surface beside the defects and impurities of the starting material.

Since niobium is already at low temperatures ($\sim 300^{\circ}\text{C}$) reacting with air ⁴⁾ - oxygen is dissolved in the niobium matrix forming clusters of suboxides which enhance the vickers hardness - great care has to be taken to avoid heating of the niobium part during machining. The choice of the lubricant not only influences the temperature of the work-piece at the tool, but also the surface finish. Generally, all lubricants containing trichlor-ethylene result in smooth surfaces; surface roughnesses of 1-2 μm are obtained. On a macroscopic scale a series of hills and valleys are present, on a microscopic scale smaller irregularities are superimposed as indicated in fig. 1.

As important as the roughness of the surface is the depth of the damage layer introduced by the mechanical deformation of the lattice during machining. The depth of this surface damage layer is depending on the machining condition as well as on the choice of the tool, influencing e.g. the pressure at the tool, or the cutting ability.

Penetration depth measurements by Hauser ⁵⁾ on niobium samples have indicated that the depth of the surface damage layer for the machining conditions used in our lab ⁶⁾ is in the order of 50 μm . If die-forming, hydro-forming or spinning techniques are used, one would expect a thinner surface damage layer. Measurements on cavities at Cornell University, where sheet metal techniques have been developed for the fabrication of resonators, ⁷⁾ indicate that after the removal of about 50 μm

reasonable results are obtained. For helix-resonators, which are build out of drawn niobium - tubes, the removal of at least 100 μm was necessary.⁸⁾ Early investigations at HEPL indicate a surface damage layer of 250 μm .⁹⁾

Prior to the removal of this surface damage layer a visual inspection of the surface is commonly done. Soaking the niobium in water for a longer period of time indicates, if there are iron-inclusions in the surface, which show up as rusty spots and can individually be treated.¹⁰⁾

2.2 Chemical Surface Treatment

For the removal of this damage layer either electropolishing or chemical polishing is commonly used. Both methods have generally two effects on a surface:

- a) "smoothing" by elimination of large scale irregularities,
- b) "brightening" by removal of superimposed smaller irregularities.

Essential for the smoothing-effect during electropolishing is the existence of a layer of high viscosity consisting out of a saturated solution of reaction products. The rate of removal of metal ions from the surface is determined by a diffusion process in the viscous layer, which depends on the concentration gradients, the temperature, the agitation of the solution.¹¹⁾

At protrusions of the surface, current densities are high establishing high concentration gradients, faster diffusion of metal ions through the layer and therefore a preferential dissolution of the peaks. At valleys the current densities are smaller, as are concentration gradients; and therefore diffusion and dissolution are smaller.

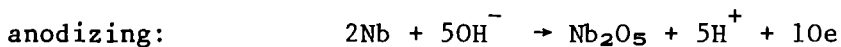
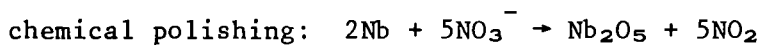
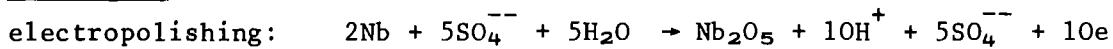
Chemical polishing of niobium is usually associated with a vigorous gas evolution; in the case of niobium the evolution of the brownish nitrogendioxide takes place; it has been suggested by several authors¹²⁾ that in this case the viscous layer forms only in the valleys and at the peaks it is swept away by the turbulent flow of the solution due to the gas evolution. Marked preferential attack then occurs at the peaks leading to a rapid smoothing.

"Brightening" occurs only if a thin surface oxide film - only a few monolayers thick - is covering the metal to be polished.¹¹⁾ It prevents the direct access

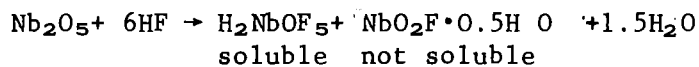
of the solution to the surface, which would cause preferential dissolution of metal from sites of high energy resulting in etching (grain-boundaries, dislocations). It has been suggested that the film undergoes a continuous process of dissolution by the acid and renewal. In order to maintain the film, the passage of metal ions across the metal/film interface occurs at the same rate at all points. Such uniform attack of the metal will remove microscopic irregularities from the surface. ¹³⁾

Although there exist several methods of chemical treatment of niobium surfaces ^{11,14,15,16}, the methods developed by Siemens company. ¹⁷⁾ for electropolishing and by ref. ^{9,18)} for chemical polishing are most often used for microwave cavities. Table I shows the summary of the applied surface treatments. Common to all processes is the oxidation of the niobium to niobium pentoxide, which is dissolved in excess hydrofluoric acid as oxifluorides. The chemistry involved is the following: ^{19,20,21)}

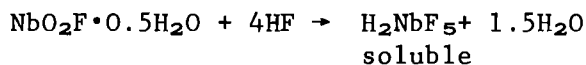
Step 1



Step 2



Step 3



The electropolished or chemically polished surfaces are contaminated with reaction products, lower oxides, sulfur and fluorine. ^{22,23)} Proper cleaning is achieved by rinsing in a diluted hydrogenperoxide solution during ultrasonic agitation and/or anodizing (oxipolishing) ^{10,24,25)}; during these steps the insoluble reaction-products are converted into soluble forms. In the case of the oxipolishing process the reactive niobium surface is in addition shifted towards "cleaner" regions of the bulk material. The amorphous Nb_2O_5 can transform into a crystalline modification, which appears as "gray oxide" during numerous subsequent oxipolishing cycles. As Grundner ²²⁾ has found, the formation of this oxide starts at certain nucleation sites as NbO , which quickly grow to form a Nb_2O_5 -layer. This gray oxide is not soluble in Hf ; in most cases chemical methods are too weak, only mechanical methods are successful. The probability of the growth of this crystalline oxide is reduced, if the niobium

was heat-treated prior to oxipolishing, which removes the spots of high energy (nucleation sites) to some extent. The state of the surface - as investigated by Grundner²²⁾ with XPS - is shown schematically in fig. 2.

In the niobium matrix, suboxide clusters are inhomogeneously distributed in a layer of about 10 nm. A 0.5 nm thick sheath of NbO and Nb₂O is sandwiched between this layer and a Nb₂O₅ layer, which is contaminated by adsorbates.

2.3 Heat Treatment

Some improvements of the surface condition can be gained by a furnace treatment for temperatures above $T \geq 1600^{\circ}\text{C}$ as indicated in table II.²²⁾ First of all the niobium surface is cleaned from residual contamination,²²⁾ if proper rinsing techniques are not available.²⁹⁾ But even in a very good vacuum ($p \leq 10^{-8}$ torr) there remain 1-2 atomic layers of surface oxides (NbO, Nb₂O) on the niobium, which are due to oxygen segregation from the bulk. For increasing residual gas pressures the oxides grow as a function of temperature and time. Typically a Nb₂O₅-layer of 1.5 nm is present on top of the niobium after cool-down. Below 700^oC the formation of suboxide clusters in the niobium matrix which are due to dissolution of oxygen from the residual gas, starts. Therefore fast cooling below 700^oC may be advantageous because of less clustering.²⁶⁾ Generally the oxide layer after a furnace treatment is thinner than after chemical treatment. There are indications for less electron loading of heat-treated surfaces, if provisions can be taken to avoid adsorption of H₂O, hydrocarbons during the handling of the cavities after the furnace treatment (e.g. glove box with inert gas, fast assembly). The main benefits of a surface treatment rather remain for the bulk than for the surface:

- a) The niobium is stress annealed and recrystallized ($900^{\circ}\text{C} \leq T \leq 1200^{\circ}\text{C}$). Investigations²⁷⁾ at Siemens company have shown that work hardened material with a high density of dislocations gave only moderate values of critical magnetic fields (X-band-TM₀₁₀-mode, $H_c^{ac} \approx 35$ mT), whereas recrystallization at 1200^oC improved the fields to $H_c^{ac} \approx 110-150$ mT.
- b) The niobium is homogenized ($1000 \leq T \leq 1300^{\circ}\text{C}$), which seems to be advantageous for welded cavities. In this temperature range the diffusion rates⁴⁹⁾ of impurities like O, C .., which have clustered in the weld during the welding process, are high enough to result in a uniform

- distribution. For heavily electropolished surfaces the dissolved hydrogen, which clusters during cool-down to cryogenic temperatures and induces stresses in the lattice, is removed during moderate firing ($T \geq 800^{\circ}\text{C}$).
- c) Above 1600°C grains are growing due to secondary recrystallization. Although investigations ²⁷⁾ comparing material of small grain size ($< 1 \text{ mm}$) and large grains ($> 10 \text{ mm}$) indicate no significant effect on the critical magnetic field of a cavity, smoother surfaces are obtained during electropolishing for large grain material because of less grain boundary etching. ⁶⁾
- d) The thermal conductivity of the material is improved to some extent, if the interstitial impurities are removed and the grains are growing ($T \geq 1800^{\circ}\text{C}$) Better thermal conductivity is desirable for the improvement of break-down fields in cavities. ²⁸⁾

3. Conclusion

There remain questions like:

- Is electropolishing to be preferred against chemical polishing?
- Is a high temperature firing ($T > 1600^{\circ}\text{C}$) necessary or can it be avoided?

Let me conclude with a few statements:

Apparently the proper surface treatment has to be developed in each laboratory and for each cavity-type. Also the material purity and homogeneity is important. Nevertheless a few steps seem to be essential:

- 1) Trivially the surface damage layer has to be removed ($50 \mu\text{m} - 250 \mu\text{m}$). Whether electropolishing or chemical polishing is the better method for this purpose is not evident. At least it seems to be apparent that electropolishing results in a more uniform removal of material, whereas chemical polishing tends to cause grain-boundary etching, if large amounts of material have to be removed.

With both methods comparable results have been achieved. In X-band-cavities peak electric field of $E_p \approx 60$ to 70 MV/m corresponding to peak magnetic fields of $H_p \approx 110 \text{ mT}$ have been obtained at HEPL ³⁰⁾ and SLAC ³¹⁾ for chemically polished surfaces. At CORNELL ³²⁾ and at SIEMENS company ^{33,34)} peak fields of $E_p \approx 55 \text{ MV/m}$ ($H_p \approx 150 \text{ mT}$) and $H_p \approx 110 - 150 \text{ mT}$, respectively, have been measured. At HEPL, ³⁵⁾ Wuppertal ³⁶⁾ and KfK ⁶⁾ both methods of chemical surface treatment have been

applied with comparable results at S-band frequencies.

At 500 MHz in the storage ring cavity of CERN³⁷⁾ accelerating gradients of $E_{acc} \approx 4.6$ MV/m have been measured after a chemical polishing of the surface. The DORIS - test cavity at KfK was only tested with electropolished surfaces and resulted in $E_{acc} \approx 4.4$ MV/m.³⁸⁾

2) Proper rinsing techniques are essential to remove surface contaminations.

3) Heat treatment at moderate temperatures ($T \lesssim 1300^{\circ}\text{C}$) serves three purposes:

a. Outgassing of dissolved hydrogen.

b. Stress annealing, which seems to be essential for heavily cold worked material and is advantageous before electropolishing in order to avoid preferential etching. For cavities made out of solid (electron beam melted) material apparently not many stresses are induced,^{27,39)} which makes a heat treatment unnecessary.

c. Homogenization, which seems in most cases to be essential for welded cavities,^{29,32,40-43)} although there exist exceptions.^{36,37)}

4) High temperature firing ($T > 1600^{\circ}\text{C}$) causes grain growth, which does not significantly influence the performance of a cavity.²⁷⁾ In addition at high temperatures and ultra high vacua the niobium is purified due to outgassing of dissolved interstitials,⁴⁴⁾ but there seems to be no effect on performance.⁴⁵⁾

Nevertheless high temperature firing is necessary to achieve very high Q-values⁴⁶⁾ (e.g. $Q > 10^{10}$ in the TM_{010} -mode at X-band).

5) Dust free assembly is essential both prior to furnace treatment and to rf-testing.

Recently the method of ion sputter cleaning has been picked up at CERN as a method for surface cleaning of niobium cavities.⁴⁷⁾ About 2 years ago investigations at CORNELL UNIVERSITY⁴⁸⁾ with ion sputter cleaning have been stopped as were tests in our laboratory 8 years ago because of discouraging results. Hopefully the CERN - group can demonstrate the feasibility of this method as a further means to improve superconducting rf-surfaces.

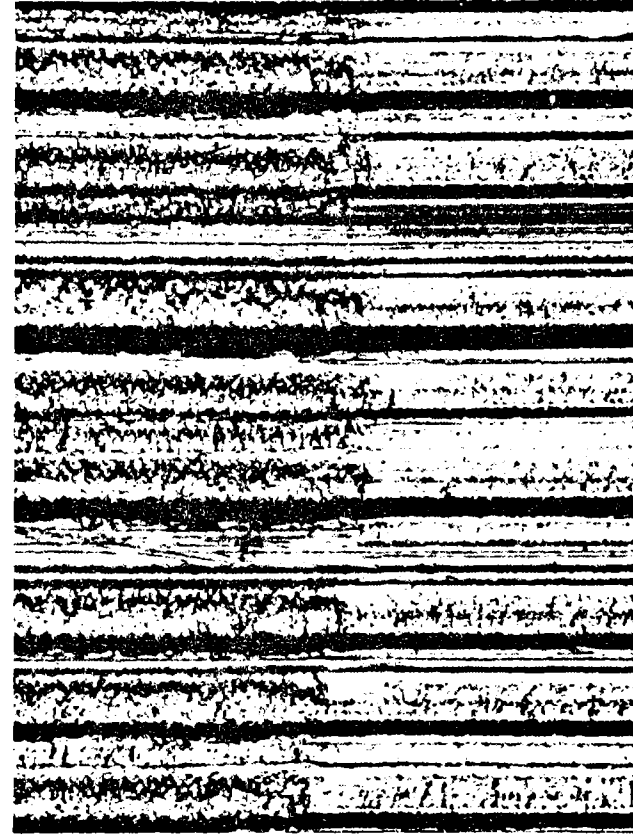


Figure 1: Topography of a niobium surface after machining on a lathe (magnification 200) from ref. 50)

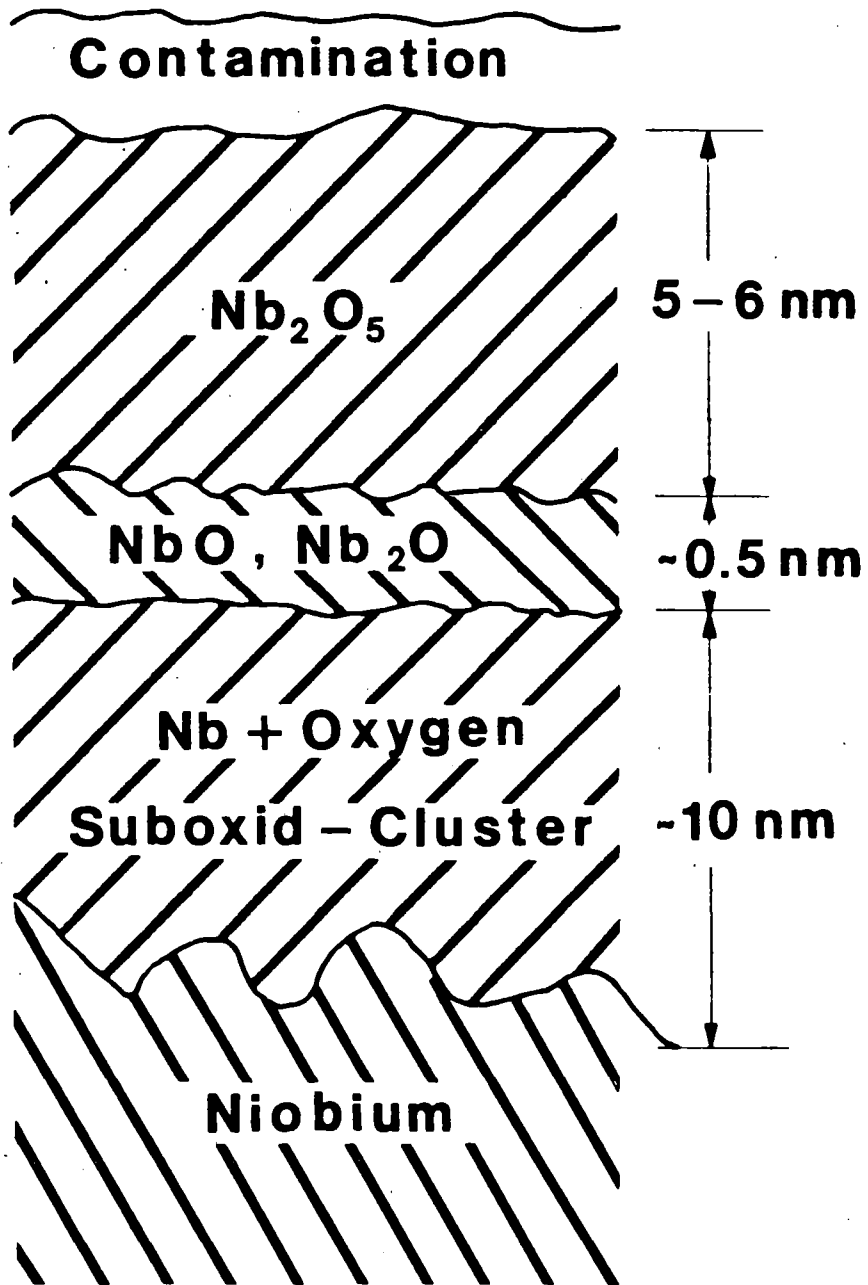


Fig. 2: Schematic diagram of a niobium surface as described by Grundner²²⁾

Table I: Chemical methods of surface preparation of niobium cavities

METHOD	SOLUTION	CONDITIONS	EFFECT	SURFACE
Electro-polishing	H ₂ SO ₄ (97%):HF (40%) = 85 : 10 by volume	10 - 15 V 25 - 35°C current oscillations	Smoothing brightening surface roughness ~.5 nm	Contaminated by reaction products S, F ...
Chemical-polishing	HNO ₃ (65%):HF (40%) = 60 : 40 by volume	Room-temp. (RT) or T<RT for smaller reac- tion rates 25 μm/min at 0°C	Smoothing (brightening) grain boundary edging	Contamination with reaction products
	HNO ₃ (65%):HF(40%): H ₃ PO ₄ (85%) = 1:1:1	room-temp. 10 μm/min		
Anodizing (oxipolishing)	20% NH ₄ OH or any diluted acid except HF	Room-temp. 0 ... 100 V voltage defines thickness ~ 2.4 nm/V	a) oxidation of residual oxides b) removal of S,F c) neutralization of acids	Sulfur removed fluorine reduced
Rinsing	H ₂ O ₂ + dist. H ₂ O + ultrasonic	Room-temp. 15 - 30 min with repeated renewal	Very efficient removal of sur- face contamination	

Table II: Effect of high temperature firing on a niobium surface

METHOD	CONDITIONS	EFFECT	SURFACE	REMARKS
Ultra high vacuum high temperature firing	1600 - 1900°C for high β -structures $\leq 1200^\circ\text{C}$ for low β -structures	Degassing of material surface cleaning: F removed S reduced C contamination due to rinsing in hydrocarbons re- duced to 1 mono- layer	State strongly depending on residual gas pressure in furnace: A) 10^{-8} Torr: 1-2 monolayers of NbO, Nb ₂ O B) P increased: formation of Nb ₂ O ₅ by further oxidation as function of T,t ~ 1.5 nm C) T < 700°C: formation of suboxide-clusters	e.g. Grundner \rightarrow due to segregation of oxygen from bulk \rightarrow responsible for A) step in $\Delta\lambda(T)$ around 7 K B) $(\Delta/kT_c)_{\text{exp}}$ $< (\Delta/kT_c)_{\text{BCS}}$ C) $R \neq R(f^2)$ Fast cool-down may reduce suboxide clustering.

R e f e r e n c e s

- 1) A. Septier,
"Surface Studies and Electron Emission", this workshop
- 2) J. Halbritter
"Theoretical Aspects in RF-Superconductivity", this workshop
- 3) W. Bauer,
"Fabrication of Niobium Cavities", this workshop
- 4) W. Schwarz, J. Halbritter,
J. Appl. Phys. 48, p. 4618 (1977)
- 5) W. Hauser,
KfK-Ext. Ber. 3/74-7, Kernforschungszentrum Karlsruhe (1974)
- 6) P. Kneisel,
KfK-Bericht 1645, Kernforschungszentrum Karlsruhe (1972)
- 7) H. Padamsee, J. Kirchgessner, M. Tigner, R. Sundelin, M. Banner, J. Stimmell,
L. Philips
IEEE Trans. Magnetics, MAG-13, p. 346 (1977)
- 8) K.W. Zieher
private communication
- 9) J.P. Turneaure, I. Weisman
J. Appl. Phys. 38, p. 4417 (1968)
- 10) H. Padamsee, private communication
- 11) e.g. W.J. McTegart,
The electrolytic and chemical polishing of metals, Pergamon Press (1959)
- 12) W.J. McTegart, R.G. Vines
Trans. Aust. Inst. Metals 5, p. 107 (1952)
- 13) J. Edwards,
J. Electrodep. Tech. Soc. 28, p. 133 (1952)
- 14) V. Sorajic,
Metalloberflächen - Angewandte Elektrochem. 27, p. 80 (1973)
- 15) J. Votruba
private communication
- 16) H. Lengeler
private communication
- 17) H. Diepers, O. Schmidt, H. Martens, F.S. Sun
Phys. Lett. 37A, p. 139 (1971)
- 18) M.L. Kinter, I. Weisman, W.W. Stein,
J. Appl. Phys. 41, p. 828 (1970)
- 19) Gmelin Handbuch der Anorganischen Chemie, Band 49 "NIOB"
- 20) D. Günzel, L. List
private communication
- 21) J. Pagetti, J. Talbot
Corrosion-Traitements-Protection-Finition 15, p. 171 (1967)
- 22) e.g. M. Grundner
KfK-Bericht 2565, Kernforschungszentrum Karlsruhe (1977)
M. Grundner, J. Halbritter
J. Appl. Phys. 51, p. 397 (1980)

- 23) G. Beranger, P. Boisot, P. Lacombe, G. Amsel, D. David
Revue de Physique Appliquée 5, p. 383 (1970)
- 24) H. Martens, H. Diepers, R.K. Sun
Phys. Lett. 34A, p. 439 (1971)
- 25) P. Kneisel, O. Stoltz, J. Halbritter, H. Diepers, H. Martens, R.K. Sun
Proc. of the 8th Intern. Conf. on High Energy Accelerators, p. 275
CERN, Geneva (1972)
- 26) P. Kneisel, O. Stoltz, J. Halbritter
J. Appl. Phys. 45, p. 2296 (1974)
- 27) H. Pfister et al.
private communication
- 28) H. Padamsee
"Heat Transfer", this workshop
- 29) A. Citron, G. Dammertz, M. Grundner, L. Husson, R. Lehm,
Nucl. Instr. and Methods 164, p. 31 (1979)
- 30) J.P. Turneaure, N.T. Viet
Appl. Phys. Lett. 16, p. 333 (1970)
- 31) P. B. Wilson, Z.D. Farkas, H.A. Hogg, E.W. Hoyt,
IEEE Trans. Nucl. Sci. NS-20, p. 104 (1973)
- 32) H. Padamsee, M. Banner, J. Kirchgessner, M. Tigner, R. Sundelin,
IEEE Trans. Magnetics. MAG-15, p. 602 (1979)
- 33) K. Schnitzke, H. Martens, B. Hillenbrand, H. Diepers
Phys. Lett. 45A, p. 241 (1973)
- 34) H. Martens, H. Diepers, R.K. Sun
Phys. Lett. 44A, p. 213 (1973)
- 35) P. Kneisel, C. Lyneis, J.P. Turneaure,
IEEE Trans. Nucl. Sci. NS-22, p. 1197 (1975)
- 36) U. Klein, D. Proch, H. Lengeler
Report WU B 80-16, Gesamthochschule Wuppertal (1980)
- 37) Ph. Bernard, G. Cavalleri, E. Chiaveri, E. Haebel, H. Heinrichs, H. Lengeler
E. Picasso, V. Picciarelli, H. Piel
Proc. of the 11th Intern. Conf. on High Energy Accelerators, CERN, Geneva (1980)
- 38) Sh. Noguchi, Y. Kojima, J. Halbritter
submitted to Nucl. Instr. and Methods (1980)
- 39) P. Kneisel, H. Padamsee
CLNS-Report 79/433, Cornell University (1979)
- 40) G. Arnolds, H. Heinrichs, W. Hoffmann, R. Mayer, N. Minatti, H. Piel,
D. Proch, W. Weingarten
J. Appl. Phys. 47, p. 1134 (1976)
- 41) V. Lagomarsino, G. Manuzio, R. Parodi
8th Intern. Cryogenic Engineering Conf., Genova, Italy (1980)
- 42) T. Furuya, K. Hosoyama, T. Kato, Y. Kojima, O. Konno
Proceedings of the 1979 Linear Acc. Conf., Brookhaven (1979)
- 43) J. P. Turneaure, H.A. Schwettman, H.D. Schwarz, M.S. McAshan
Appl. Phys. Lett. 25, p. 247 (1974)
- 44) M. Strongin, H.H. Farrell, H.J. Halama, O.F. Kammerer, C. Varmazis,
J.M. Dickey
Part. Acc. 3, p. 209 (1972)
- 45) H. Pfister
Cryogenics 16, p. 17 (1976)

- 46) C.M. Lyneis,
private communication
- 47) H. Lengeler
private communication
- 48) H. Padamsee
private communication
- 49) A. Joshi, M. Strongin
Scripta Metallurgica 8, p. 413 (1974)
A. Joshi, C. Varmazis, M. Strongin
"Role of Carbon and Oxygen Interaction on Grain Growth and Purification
of Niobium", BNL-Report, Brookhaven
- 50) H. Pfister et al.
private communication

THE PREPARATION OF SUPERCONDUCTING Nb_3Sn -
SURFACES FOR RF APPLICATIONS

B. Hillenbrand

Siemens Research Laboratories, Erlangen

1. Introduction

For HF-applications, a superconducting material with high energy gap $\Delta \sim T_c$ from general considerations offers some more or less realistic advantages compared to a superconductor with a lower Δ /1/. These potential advantages are

1. a higher working temperature (for $R_{res}(Nb) \approx R_{res}(Nb_3Sn)$)
2. a better thermal stability "
3. a higher superconducting limit ($B_c \sim T_c$)
4. a lower surface resistance R_S (if $R_{res}(Nb_3Sn)$ can be reduced)

At the moment niobium - the element with the highest T_c (9.2 K) - is nearly always used in superconducting HF-applications. Any material with a higher T_c must be an alloy or compound. The highest T_c is found for A15-compounds, and in this class of material most work has been done for Nb_3Sn with a T_c of about 18 K. Therefore it is reasonable to study the HF-properties of this well-known superconductor.

On the other hand, with Nb_3Sn , also some disadvantages must be expected. These are:

1. bad thermal conductivity
2. no possibility of shaping
3. formation of unwanted phases such as Nb_6Sn_5 and $NbSn_2$
4. increase of costs.

The first two difficulties prescribe to coat cavity-shaped substrates with a thin layer several penetration lengths thick, the other ones must be overcome by a good preparation method.

Nothing can be said in advance whether a Nb_3Sn surface will give a low residual resistance or exhibit a small electron secondary emission coefficient.

2. Choice of preparation method

Most work on Nb_3Sn concerns the development and production of a superconductor with a high current density, and this means that there are inhomogeneities acting as pinning centers. Especially for Nb_3Sn grain boundaries are thought responsible for the high current densities observed. For a HF-superconductor, however, inhomogeneities are unwanted as they may trigger thermal breakdown ^{*)}. For this reason the RCA-method - the transport of Nb and Sn via the gasphase - was ruled out, though it might allow the deposition of a Nb_3Sn -layer on a good thermal conductor like Cu.

*) As far as known little experimental or theoretical work has been done to study the efficiency of a given inhomogeneity to initiate a breakdown. Therefore it is not sure whether a high current density and good HF-properties are incompatible.

The most natural substrates for the Nb_3Sn -layer is a Nb-cavity. Then only one component - the tin - must be transported to the substrate. Plating the Nb with tin electrolytically or by evaporating on the cold substrate seems unfavourable as during the heating up there will form wrong phases (Nb_6Sn_5 , $T_c = 2.1$ K, and NbSn_2 , $T_c = 2.7$ K), which may be hard to completely remove afterwards. Therefore we decided to apply a method, where the substrate is exposed to tin vapour at a high temperature, and so did other groups (KfK Karlsruhe /2/, Wuppertal /3/, MIT /4/). From the phase diagram Nb-Sn one can see that the reaction temperature should be higher than 930° , because in this case Nb_3Sn is the only existing compound.

In the literature, it is assumed that the growth of a Nb_3Sn -layer takes place by the diffusion of tin through the grain boundary to Nb substrate (e.g. /5/), though this mechanism is not really proven. If this is true we need a fine network of grain boundaries to obtain a layer of homogeneous thickness. In our first experiments we saw that there are nucleation problems for Nb_3Sn , if Nb is simply exposed to tin vapour. But we found out that the nucleation problem may be overcome by preanodising the niobium substrates and heating in a temperature gradient or adding a small amount of SnF_2 . This is documented by Fig. 1.

Furthermore it turned out that the Nb_3Sn may be contaminated with Si from the quartz tube in which in our case the reaction takes place. Therefore we introduced a reaction room with niobium walls only.

3. The standard preparation procedure

The arrangement in which we prepare our Nb_3Sn -cavities is shown in Fig. 2. Our standard procedure is characterized by the following points.

1. A continuously pumped quartz tube (turbomolecular pump).
2. A reaction room with niobium walls only. It is evacuated through the leakage between resonator and the bottom plate.
3. Preanodisation of the niobium surfaces to be covered.
4. Heating up in a temperature gradient (Sn hotter) or adding a small amount of SnF_2 . The furnace is preheated to 750°C .
5. Annealing for three to four hours at 1050°C ,
6. Cooling within the furnace (vertical axis) by blowing cold air from below with a ventilator.
7. Cleaning of the Nb_3Sn -surface by oxipolishing (anodising in NH_3 -solution and dissolution of the oxide in HF).
8. Wet installation (as with niobium cavities).

The parameters of preparation are generally not critical. For instance one may vary the annealing temperature, duration, preanodisation voltage, start without preheating, increase the leakage of the niobium reaction room and will not find a pronounced effect.

In what way the preanodisation works is not clear. One may simply say that we produce a disturbed niobium surface which in connection with a higher tin supply by the temperature gradient or SnF_2 enables easy nucleation.

4. Results of HF-measurements

In table 1 some of our best microwave results are represented. A critical flux density B_c^{ac} of 100 mT may be obtained. Generally B_c^{ac} seems to be temperature independent. The best quality factors (low field) were $9 \cdot 10^9$ at 1,5 K and $2.7 \cdot 10^9$ at 4.2 K. Average values are 2 to $3 \cdot 10^9$ at 1.5 K and 1 to $2 \cdot 10^9$ at 4.2 K. All measurements were made at 9.7 GHz for TE_{011} - and TM_{010} -type cavities.

We have made a great number of preparations after the standard procedure but usually with some minor modification such as the temperature and duration of annealing, the time for heating up or cooling down. Therefore we can make a statistic and represent

every preparation by its best B_C^{ac} -value at 1.5 K. In Fig. 3 the relative frequency of B_C^{ac} -values in a certain interval is plotted against B_C^{ac} of the middle of this interval. The points are experimental, the curve is a calculated Gauß distribution. The good agreement demonstrated that our results are dominated by statistical defects.

5. Analysis of Nb₃Sn-layers

By our procedure we obtain a dense layer of Nb₃Sn 1 to 2 μm thick and with a grain size also of about 1 μm (Fig. 4). If such a layer prepared on a niobium sheet is bent, intercrystallin fracture in the Nb₃Sn occurs (Fig. 5). The grain boundaries are weak links as it is to be expected by their contribution to grain growth (tin enrichment). After a thermal treatment for some hours at 1050 °C without tin source the fracture becomes transcrySTALLINE (Fig. 6), indicating a "cleaning" of the grain boundaries. X-ray measurement revealed that the Nb₃Sn still is polycrystalline. Unfortunately this thermal treatment caused no improvement of the microwave properties neither in critical fields nor in quality factors. The results even were a little below the average.

The temperature independent B_C^{ac} and the rather rough polycrystalline surface can be taken as a hint that at some potrusion the superconducting critical field is surmounted. Then it would be good to smoothen the surface by polishing. Therefore the development of smoothness with oxipolishing was studied by SEM. Thereby we found out that after a total anodisation voltage of about 200 V pitting occurs as demonstrated in Fig. 7. The holes generally appear within the grains, but sometimes also in the boundaries. We could not prevent pitting neither by changing the electrolyte for anodisation nor by decreasing the dissolution velocity nor by chemical polishing nor by electropolishing. The reason for the pitting is not known, but the great number of pitting holes shows that it must be connected intimately with the structure of the Nb₃Sn-layer.

A number of AES-measurements revealed that under our conditions we obtain rather pure Nb_3Sn -layers. Also the contamination by C and O is small. Without oxipolishing there is a tin maximum on the surface and an oxygen maximum just below the surface coinciding with a tin minimum. Also with AES we could show that in an intermediate stage (e.g. in the temperature region of about 800°C) there is N-rich layer in the upper part of the niobium, probably NbN , but it seems to play no decisive role, because we obtain the same Nb_3Sn structure when we start with an oxide layer grown in pure water.

6. Conclusion

The best microwave results and even the average values we reached with Nb_3Sn could suffice for an accelerator layout as at present is usual. But the broad Gaussian curve (Fig. 3) shows that statistical defects exert still too large an influence. It will be necessary to suppress this defects to get a much smaller Gauß distribution. Another point is to use Nb sheet resonators as substrates instead of the bulk niobium cavities.

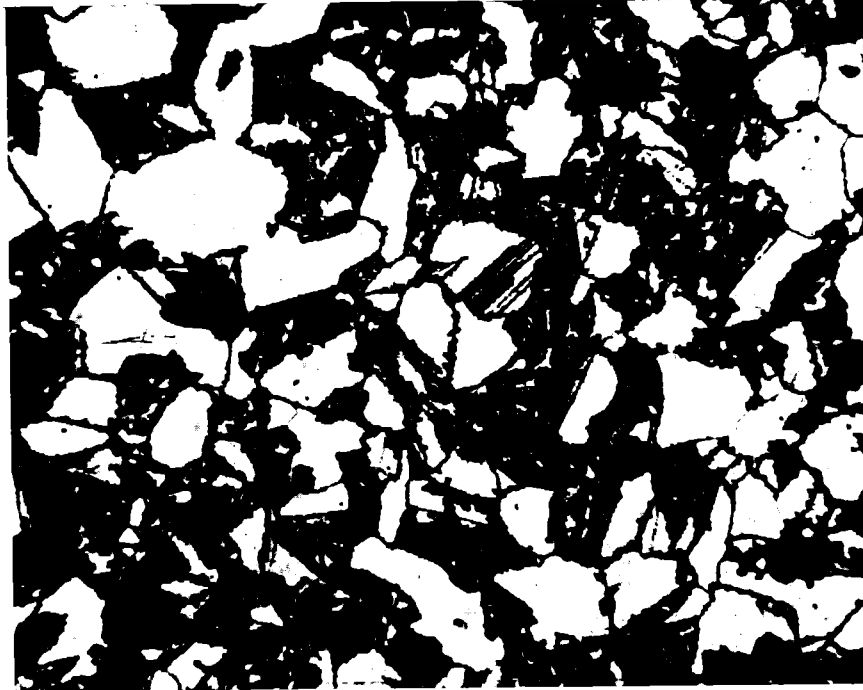
This work has been supported under the technological program of the German Federal Ministry of Research and Development.

Literature

- /1/ B. Hillenbrand u. H. Martens: J. Appl. Phys. 47 (1976) 4151.
- /2/ P. Kneisel e.al.: IEEE Transactions on Magnetism MAG-13, (1977) 496.
- /3/ G. Arnolds u. D. Proch: IEEE Transactions on Magnetism, MAG-13, (1977) 500.
- /4/ V. Diadiuk e.al.: IEEE Transactions on Magnetism, MAG-15, (1979) 610.
- /5/ H.H. Farrell e.al.: J. Appl. Phys. 45, (1974) 4024.

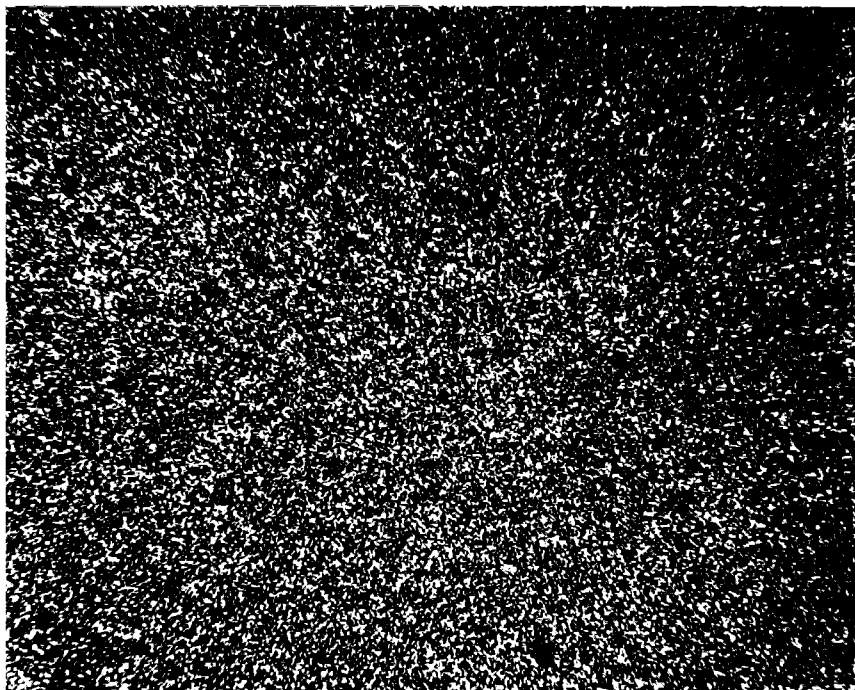
Preparation method	1.5 K			4.2 K		
	B_c^{ac} mT	$Q(B_c^{ac})$	$Q(0)$	B_c^{ac} mT	$Q(B_c^{ac})$	$Q(0)$
inner reaction room quartz HF-cleaned	100	$1.0 \cdot 10^9$	$2.4 \cdot 10^9$	-	-	$1.7 \cdot 10^9$
preanodised + temperature gradient	106	$1.0 \cdot 10^9$	$1.6 \cdot 10^9$	> 78	$4.9 \cdot 10^8$	
preanodised + temperature gradient	84	$1.8 \cdot 10^9$	$2.5 \cdot 10^9$	84	$8.6 \cdot 10^8$	$1.6 \cdot 10^9$
preanodised + SnF ₂	80	$3.7 \cdot 10^9$	$4.6 \cdot 10^9$	79	$9.0 \cdot 10^8$	$1.7 \cdot 10^9$
preanodised + SnF ₂	88	$1.5 \cdot 10^9$	$2.2 \cdot 10^9$	89	$6.9 \cdot 10^8$	$1.3 \cdot 10^9$

Table 1: Values of B_c^{ac} , $Q(B_c^{ac})$ and $Q(0)$ at 1.5 K and 4.2 K of Nb₃Sn-resonators (TE₀₁₁, 9.7 GHz).



not preanodised

0,1 mm



preanodised

Figure 1: Nb_3Sn on Nb (111) – substrate (4h, 1050° C)

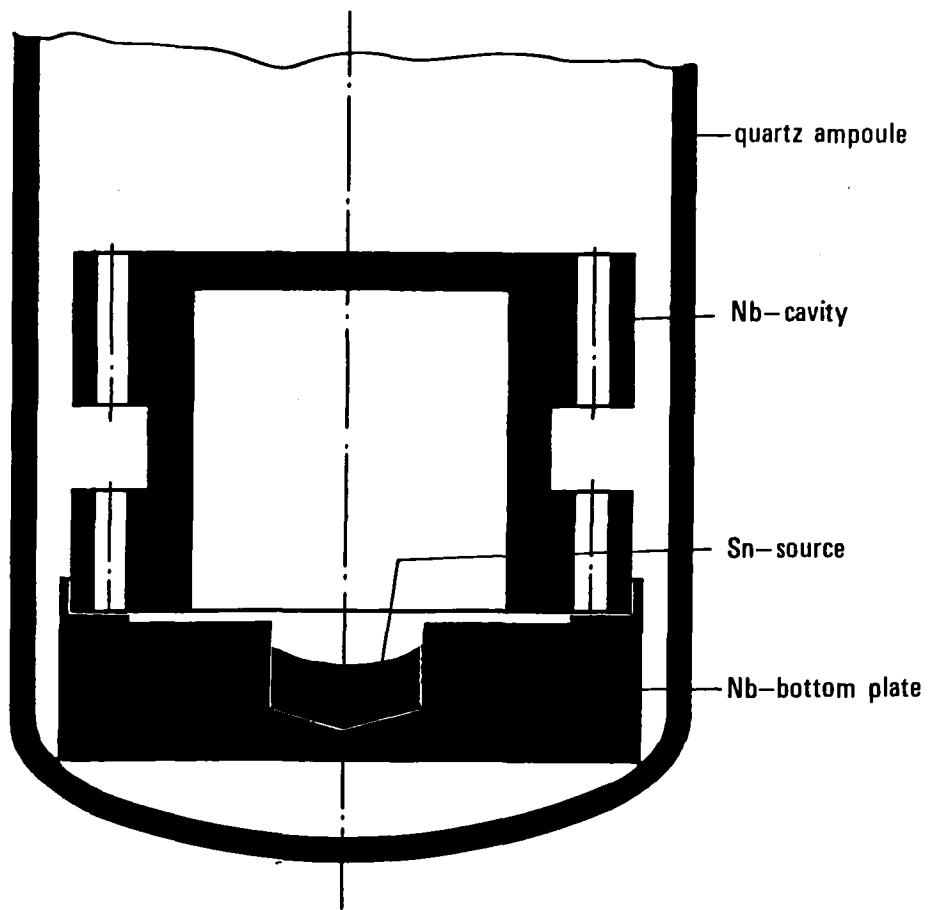


Figure 2: Arrangement for the preparation of Nb_3Sn cavities

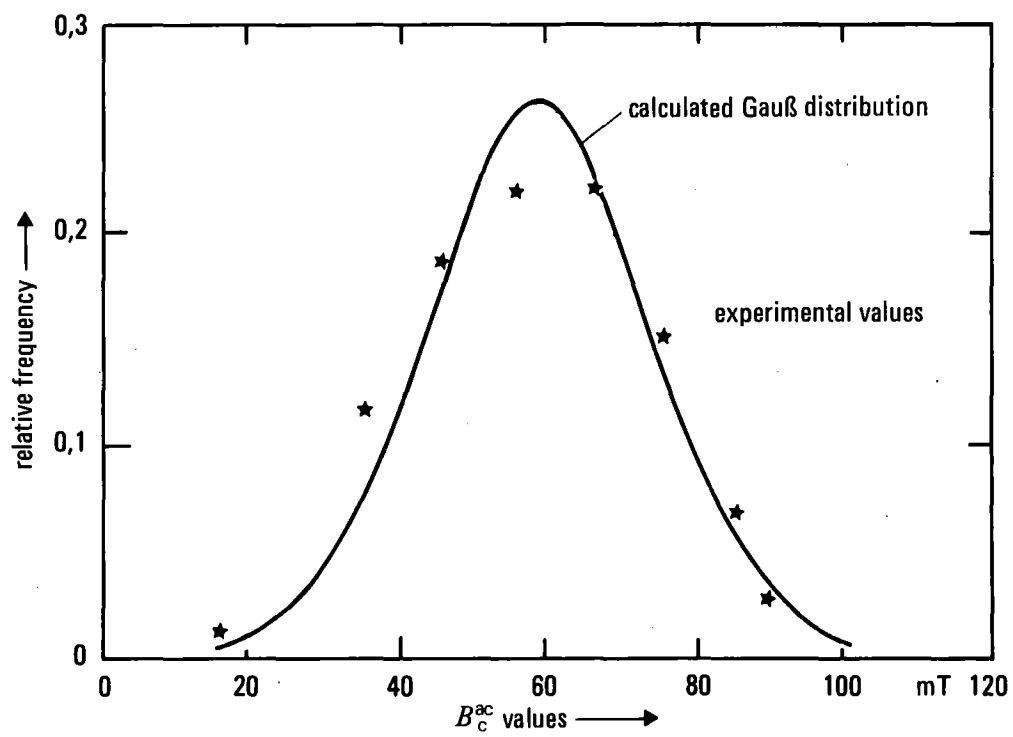


Figure 3: Distribution of measured B_c^{ac} - values (best results at 1.5 K for each preparation)



Figure 4: Nb₃Sn - layer on a Nb substrate (3h, 1050°C)

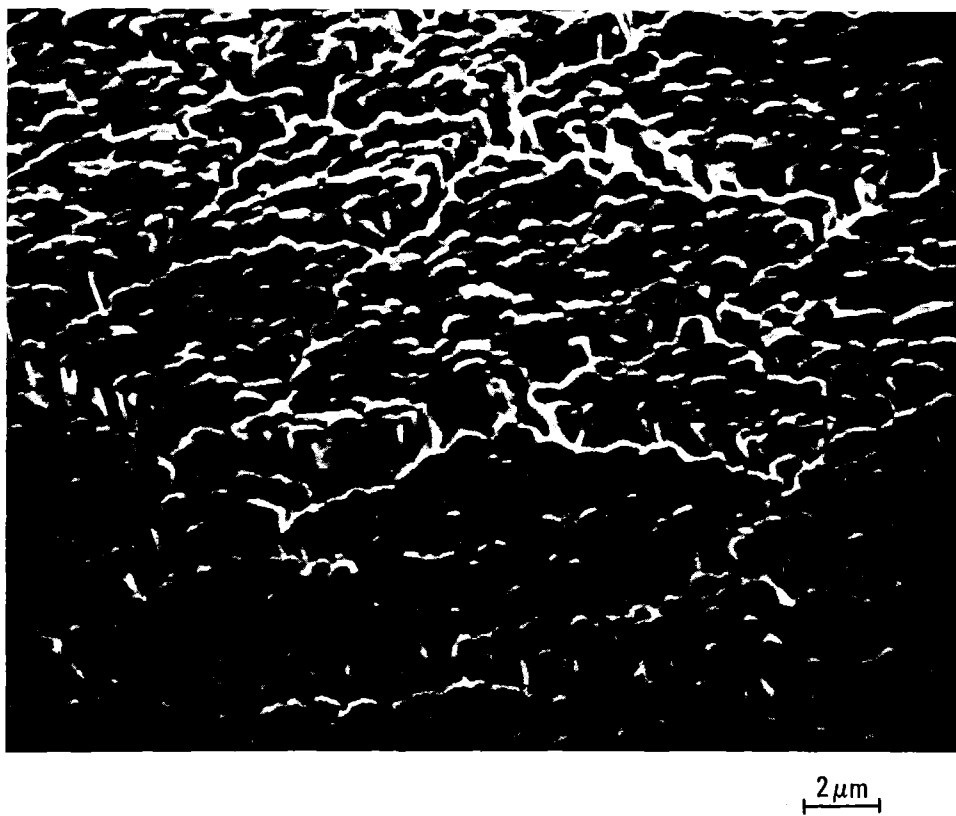


Figure 5: Intercrystalline fracture of a bent Nb₃Sn - layer on a Nb sheet

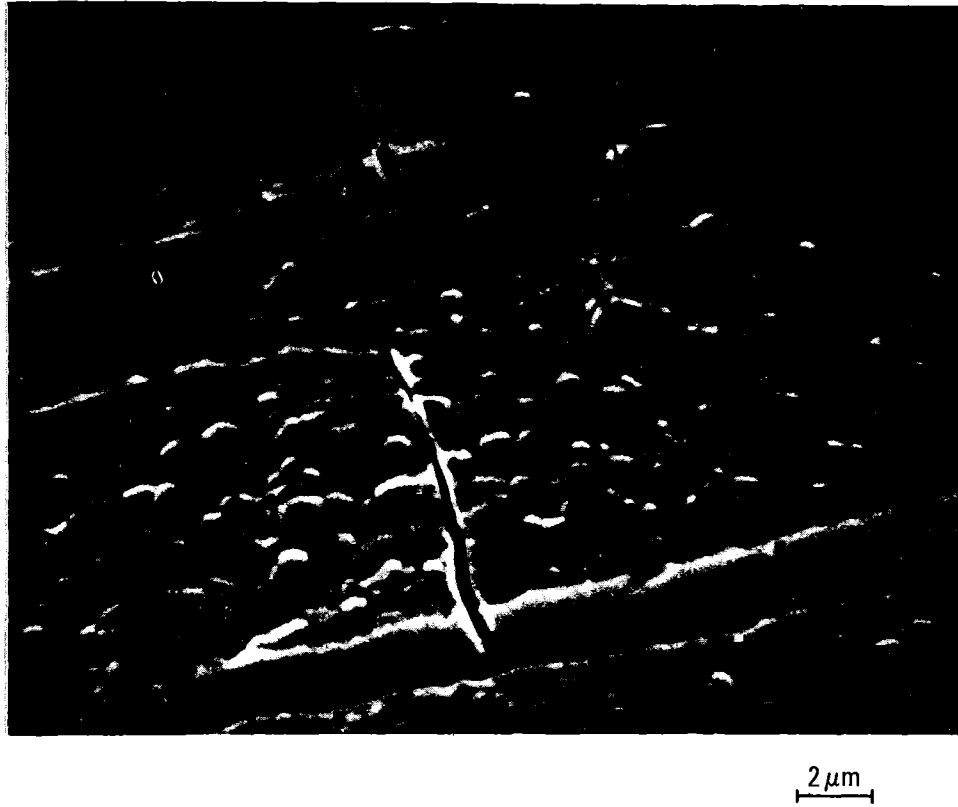


Figure 6: Transcrystalline fracture of a bent Nb₃Sn - layer on a Nb sheet

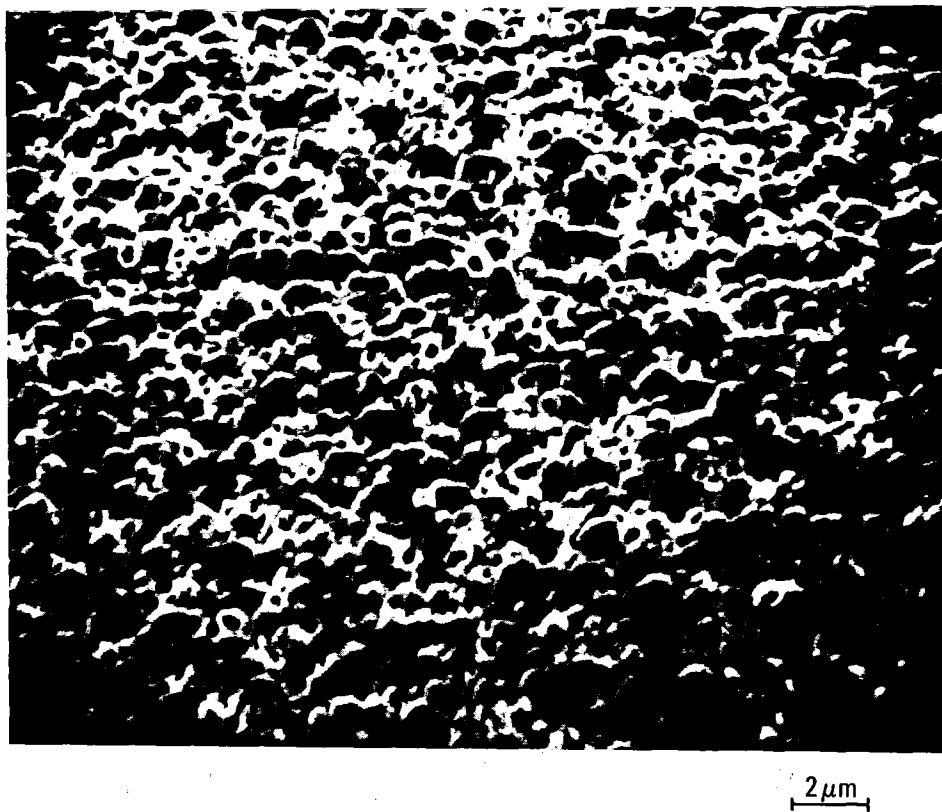


Figure 7: Pitting in a Nb₃Sn - layer after stepwise oxipolishing to 280 V total anodisation voltage

SURFACE STUDIES AND ELECTRON EMISSIONS

A. SEPTIER, CNAM, 292 rue Saint-Martin, 75141 Paris Cedex 03
and IEF, Université Paris-Sud, 91405 Orsay (France).

INTRODUCTION

One of the aims of modern surface analysis is to determine the physical and chemical structure of the surface layer of the sample. The physical structure includes topography and morphology of the surfaces on a micron and submicron scale, and the arrangement of atoms in a lattice as well as the extent, shape and type of lattice defects. The chemical structure is the distribution and concentration of elements in a surface layer on a micron or submicron scale. It can be determined with various beam techniques such as Auger spectroscopy (AES), X-ray photoelectron spectroscopy (XPS), ion scattering spectroscopy (ISS), secondary ion mass spectroscopy (SIMS), electron probe microanalysis (EPM).

Size and shape of crystals or grain boundaries, chemical composition of small inclusions, and size and type of lattice defects can be studied by electron microscopy and electron diffraction.

All methods have their advantage and disadvantage, and must be considered as complementary techniques. The optimum choice of the methods to be used depends on the problem being investigated (1).

In all analysing methods, information about the atoms or molecules contained in the surface layer, are given by particles - ions or electrons - emitted by the sample, which can be bombarded by photons, electrons or ions. But in the most commonly used methods, the information depth, which corresponds to the escape length of the outgoing particles, is often limited to a few angströms, and to perform a chemical analysis of a layer in the micron range it is therefore necessary to remove progressively the sample surface, by ion sputtering. A depth profile of one particular element can be obtained by sequential sputtering and analysis, using either AES, UPS or XPS. A continuous analysis during sputtering is also possible by a SIMS technique.

All these methods are destructive, and a scrutiny of the results is necessary, as the ion bombardment may introduce many artefacts and often has a non negligible influence on the resolution and on in-depth profiling.

Several other methods are able to provide depth profiling of one element without destroying the surface layer: Rutherford backscattering spectrometry and Nuclear microanalysis. In the first method He^+ ions are used, and for a fixed angle of observation, the energy of backscattered ions is at the same time a known function of the nature of the atom hit by the incident ion, and of the distance from the surface where the collision takes place. The energy spectrum of the backscattered ion may be directly converted into a in-depth repartition of the analyzed element.

Nuclear microanalysis is possible only with a few number of elements (2) which are able to give radioactive nuclei, when bombarded by D^+ or H^+ ions. For example, oxygen O^{16} and nitrogen N^{14} atoms bombarded by 2 MeV deuterons give O^{17} and C^{12} , after emission of a proton or an α particle, respectively.

The number of secondary protons or α particles is proportional to the oxygen- or nitrogen - content, and energy analysis of these particles give the depth profile of the impurities in the lattice.

As far as very thin surface layers are concerned, in the 50 - 200 Å range, X-ray photon spectroscopy (XPS) may be used, combined with an angular energy analysis of the emitted Auger electrons, to obtain the thickness of contaminated or oxidized layers, grown on the surface of the sample.

After this short review of the most familiar surface analysis techniques, which all have to be performed in an UHV chamber in order to avoid additional contamination of the surface, I shall briefly report on works concerning superconducting material surfaces, essentially niobium or niobium-tin.

In the first part, I will talk essentially about chemical properties of the Nb surfaces, and surface studies.

The second part will be devoted to another very important aspect of surface properties: electron emission from clean or contaminated surfaces.

PART I. SURFACE STUDIES

1. THIN FILMS

1.1 - Nb

The RF performances of sputtering thin films of Nb may be lessened by several defects: lack of uniform coverage, strains, Ar ion in the neutral lattice, gettering of contaminants by the freshly deposited material. An approach has been made (3) to evaluate the potentiality of sputtering technique by measuring RF properties of sputtered Nb coating, and using Nb as the substrate material in order to minimize the mismatch between expansion coefficients of substrate and coating. A Q_0 of 3×10^9 and a peak magnetic field of 205 Gauss were achieved, demonstrating that the sputtering technique is capable of producing Nb surfaces of good quality, at the condition that the shape of the cavity be simple enough to obtain an uniform film thickness.

In contrast, and certainly due to the strains between the substrate and the Nb films, surface resistances of Nb films sputtered on a Cu substrate, were 100 times greater than for bulk Nb.

1.2 - Nb₃Sn

Nb₃Sn is generally used in thick layers grown on Nb surfaces. A second way to use Nb₃Sn is as a covering for the Nb surface that is a few monolayers thick (4). It would be hoped that the Nb₃Sn would not be as sensitive to O₂ as pure Nb, and would form a high-T_c protective surface without introducing normal excitation. Since the layer would be much thinner than the coherence length, the losses would be determined mainly by the surface resistance of the Nb underneath.

The better quality films with a sharp transition and critical temperatures of about 16 K were produced by alternatively depositing layers of Sn and then annealing temperature ranging from 800 to 900 °C. Critical tempera-

tures are lowered by the proximity effect, varying from about 9 K for a Nb_3Sn thickness of 100 Å to about 15 K for a layer of 1000 Å thick. Nb_3Sn thin films with high T_c appear fairly uniform, with a large grain size. Other films which show a broad transition also show a rougher surface, as observed by optical and scanning electron microscopy.

After an exposure to the air, the films were measured again. Relatively small shifts in the transition curves of Nb_3Sn were observed, proving that even the thin Nb_3Sn is relatively stable in air.

1.3 - The influence of crystal orientation on the quality of Nb_3Sn layers has been studied in several laboratories and more recently by the Siemens group (5), using observation with light and scanning electron microscope, and chemical analysis by AES. The Nb_3Sn layers were grown on Nb substrates oriented along the (100) (110) (111) and (531) directions respectively. For each orientation, one substrate was chemically polished (CP), and another one CP and then oxipolished. On the CP substrates, the Nb_3Sn layer was discontinuous, and the holes may correspond to 50% of the total area for the (111) orientation. On the contrary, there is no difference in the structure of the continuous Nb_3Sn structure growing on the oxipolished substrates. It seems that oxipolishing makes easier the nucleation of Nb_3Sn on the surface and then allows an homogeneous growing of a dense Nb Sn layer, whatever may be the orientation of the Nb lattice.

Auger analysis show that the ratio between Sn and Nb signals is higher for oxipolished samples; without differences due to the orientation of the substrate, and that the Nb_3Sn layer may be considered as fairly homogeneous. On the contrary, the Nb_3Sn layer grown on substrates only chemically polished, is poor in Sn, except on the outer layers where a correct stoichiometric composition is obtained.

Oxipolishing seems a necessary procedure to obtain Nb_3Sn layers of a good quality, in addition to a clean preparation technique.

II. SURFACE IMPURITIES

2.1 - Carbon

Surface of reactor grade electron beam melted Nb have been examined (6) using a scanning electron microscope, equipped with a crystal X-ray spectrometer. The presence of carbon inclusions has been established, occurring primarily at grain boundaries. In an unfired chemically polished sample, 50 carbonaceous inclusions per cm^2 were observed, with an average diameter of 10 μm , corresponding to a volume concentration of C of approximately 16 ppm. Another sample, which was fired for 7 hours at 2100 °C, at 10^{-8} Torr, was also examined. The number of carbonaceous inclusions was lowered by a factor of 4, and the total carbon concentration by a factor of 6, compared to the chemically polished sample.

The presence of carbon on a fired Nb cavity surface has been also observed in electron microprobe studies at SLAC (7). The carbon tends to occur as inclusions with dimensions on the order of 10 microns, frequently located at crystal boundaries. They can presumably become regions of enhanced local heating leading to magnetic breakdown.

Several techniques have been successfully used to remove the carbon:

- anodization of the cavity before the final firing,
- or heating the cavity at 1900 °C during one hour in an oxygen atmosphere at pressure of 7×10^{-6} Torr .

The role of oxygen is further clarified by observations made using a residual gas analyzer during HT treatment in oxygen; an heavy evolution of CO₂ and CO is seen during the initial stage of firing.

On Auger spectra a strong carbon signal is generally observed. This carbon signal is weakest for an anodized surface, intermediate for a furnace cleaned surfaces and strongest after chemical treatments (8). Decarburization by means of a furnace treatment of an anodized surface gives a low carbon signal.

Carbon present on Nb surfaces may have different origins: (i) carbon diffusing to the surface from the volume of the sample, the C natural concentration in the best quality Nb being of the order of 15-20 ppm; (ii) carbon in adsorbed organic molecules, like hydrocarbons, which are residue from cleaning with methanol or acetone; (iii) carbon in adsorbed CO or CO₂ molecules.

2.2 - Fluorine

Fluorine has been observed by Auger electron spectroscopy on surfaces (8) chemically polished in baths containing HF, or after dissolution of Nb₂O₅ by HF (oxipolishing). F remains detectable within a depth of about 50 Å .

Nuclear analysis has been used to study the contamination by fluorine of samples subjected to various treatments in baths containing fluorhydric acid, for example oxipolishing (9). The reaction $F^{19} (p, \alpha) O^{16}$ is used, when the metal is bombarded with 2 MeV protons. Experiments were carried out with Ta, a metal having chemical properties very similar to those of Nb .

Typically, the metal surface is covered with a 20-45 Å of natural oxide and 2×10^{15} at/cm² of fluorine are found in films containing 2×10^{16} at/cm² of oxygen. Rinsing the sample in boiling water decreases the amount of fluorine by 50% and the dissolution of the surface contaminated oxide in a NH₄F - HF solution reduces the fluorine contamination to less than 1.5×10^{14} at/cm² . After anodic oxidation of the cleaned surface, it was found that after oxide growth the fluorine remains near the metal-oxide interface.

2.3 - Contamination of the oxide

The influence of the nature of the electrolyte on the film formation oxygen yield during anodic oxidation of Nb has been studied by the ENS group in Paris (10). This yield is defined as the ratio of the oxygen contained in the film to the amount of bivalent oxygen equivalent to the oxidation charge.

It has been shown that this ratio is greater than 1 for films formed in concentrated acids, implying a large incorporation of anions characteristic of the acids. The total amount of oxygen may be measured with a good precision by nuclear microanalysis. The samples were bombarded with 2 MeV D⁺ ions O¹⁷ is formed by the reaction $O^{16} (d, p) O^{17}$, and the concentration of the radioactive element O¹⁷ is then measured with semiconductor detectors placed near the sample.

From these measurements, the concentration of O^{16} is obtained, by comparison with O^{16} standards with an accuracy estimated as 2 or 3%. The nitrogen concentration may be also measured by using the reaction $N^{14}(d,\alpha)C^{12}$, and counting the emitted α particles.

The oxygen yield R may attain 1.27 when the anodization is carried out in HNO_3 , 95% and 1.49 in $HCOOH$ 98%. R increases with acid concentration and tends toward unity at low concentration. The supplementary oxygen atoms are due to anions incorporated in the oxide, NO_3^- for example. Nuclear microanalysis of N^{14} allow a direct determination of nitrogen, in Nb_2O_5 obtained by oxidation in concentrated HNO_3 . The quantitative estimation of the anion incorporation rate is deduced from the direct analysis of N . Incorporation of 1 at of N for every 100 at of oxygen has been measured. This corresponds to an incorporation of about 10×10^{14} at/cm². Concerning weak electrolytes, it seems that there is a negligible incorporation of nitrogen into the oxide.

In contradiction with these results, Nb_2O_5 grown in NH_3 aqueous solutions may be strongly contaminated by nitrogen, as shown recently (19) by an XPS study.

2.4 - Other contaminants

Sulphur, chlorine are often present on chemically polished surfaces, coming from the acid baths. This contaminants may be eliminated by heat treatment. The titanium pump in an UHV furnace is at the origin of a weak Ti signals in AES spectra (8), and Ti atoms may diffuse to a depth of about 50 Å.

III. ADSORBED GASES. OUTGASSING.

3.1 - Adsorbed gases

The influence of solute oxygen and nitrogen on the magnetic breakdown and residual losses of SC Nb cavities, was investigated experimentally by exposing the cavities to these gases at pressures up to 10^{-5} Torr during the heat treatment at 2100 K (11).

Oxygen may decrease the critical temperature (0.93 K per at %) and the electronic mean free path at the surface, causing low thermal conductivity and a lower critical field H_{c1} . Layer of NbO - or NbO_2 - are also suggested as surface contaminant. The effects of O_2 are augmented by an enhanced solute concentration at the surface during the cooldown after the normal UHV bakeout. To achieve a desired clean surface it is therefore necessary to reduce the bulk concentration of O_2 to about 1×10^{-3} at %, requiring a partial pressure of 10^{-9} Torr at 2100 K.

A direct measurement of the resistance ratio in the cavity walls by the eddy-current method was performed after a 20 h oxygen exposure. The resistance ratio R remained essentially unchanged at the value of $R=41$ implying a mean free path of about 1000 Å in the bulk of the material. No change in the critical temperature, the measured gap and the BCS part in the surface losses due to the gas exposure can be observed.

Solute nitrogen in concentrations up to about 8×10^{-2} at % (125 ppm) has no effect on the peak magnetic field. As to the influence of oxygen, bulk concentrations up to 7.5×10^{-3} at % (13 ppm) do not affect the breakdown field, whereas higher concentrations, above 1.2×10^{-1} at % (200 ppm) cause a definite

reduction in the peak field. The residual Q was in all cases lowered by the oxygen exposure, but the effect is not proportional to the O_2 concentration.

Measurements of the penetration depth $\delta(0)$ of Nb wires, before and after oxygen exposure respectively gives values of $\delta(0) \approx 400 \text{ \AA}$ and $\delta(0) \approx 720 \text{ \AA}$ respectively. To explain the large penetration depth, it is necessary to assume a mean free path of about 125 \AA in the surface sheath - which is an order of magnitude smaller than in the bulk of the material, denoting a substantial oxygen enrichment at the surface. An equally large penetration depth was measured after N_2 exposure. As large penetration depths are associated to low values of the critical field H_{c1} , we may assume that oxygen is partly responsible for the lowering of the peak field in the cavities containing solute oxygen in their walls.

The effect of various common gases on the RF properties have also been explored at SLAC (12): the cavities being filled with the gas for about 1 hour. These effects can be profound, particularly with CO_2 and CO which lower the peak magnetic field by a large factor. Dry oxygen, nitrogen, or hydrogen have only a weak influence on the values of the surface resistance and the peak magnetic field.

3.2 - Heat treatment

Four processes take place during HT firing in UHV:

- evaporation of oxides from the surface, in particular metallic NbO, and of volatiles impurities,
- lowering the overall oxygen concentration, and of the carbon concentration,
- thermal polishing,
- enhanced grain growth.

Concerning the removal of oxygen from Nb, LEED can yield the structure of the surface layers of the metal. Because the energy range of the electrons (from about 10 to 500 eV) the electrons penetrate into the sample a few monolayers, and so the diffraction patterns that are obtained are characteristic of these surface layers. The sample initially put in the chamber is heated in UHV at a given temperature T_a and then cooled down quickly in order to obtain the LEED diagram with a good resolution.

The figure 1 shows how difficult it is to remove the last traces of oxygen (4)(13). The intensity of the O_2 line in Auger spectrum is plotted as a function of the sample thermal history, and LEED patterns were taken at room temperature after cooling. In (a), the Nb single-crystal surface is covered with adsorbed oxygen. In (b), after annealing at $T_a = 1000 \text{ }^\circ\text{C}$, a faceted surface is observed, corresponding to a thin layer of a Nb oxide of unknown composition. In (c), for $T_a > 1800 \text{ }^\circ\text{C}$, the oxide layer surface - probably NbO - is again parallel to the substrate. Finally, a clean Nb surface appears for $T_a \geq 2000 \text{ }^\circ\text{C}$. (see (d)).

Other experiments show that even at 3×10^{-8} Torr of oxygen at $950 \text{ }^\circ\text{C}$ oxide structures are formed. Hence a cavity cooling from its heat treatment temperature of $1900 \text{ }^\circ\text{C}$ will pick-up oxides either from the bulk, or from residual gas in the chamber.

AES was used (14) to study the amount of gases that diffuse to the surface as the sample is cooled. In a partial oxygen pressure of 3×10^{-8} Torr,

a sample was heated to about 1400 °C during 9 minutes. While hot, the Auger pattern shows that the O concentration on the surface is less than 1/10 of a monolayer.

Upon cooling, Auger spectra are recorded and the spectrum obtained 45 sec after the beginning of the cooling process show that almost a monolayer of O is detectable, indicating a diffusion from the bulk. In effect, at the ambient pressure of 3×10^{-9} Torr, there is not enough gas hitting the sample to account for the rapid build-up of oxygen on the surface.

Since RF fields react with the metal in a very thin layer of $\sim 500 \text{ \AA}$ only, the surface preparation is extremely important to achieve high Q and high surface fields. Oxygen contaminated layers would have a lower T_c and poorer microwave performances. A layer of the semimetal NbO would also affect adversely the microwave properties.

It would be of great value to have a stable surface condition, for ease in handling the RF cavities. Several possibilities have been proposed for protecting the Nb surfaces: (i) anodic oxidation, due to the conversion of various oxide into Nb_2O_5 , that is a low-loss insulator; (ii) covering the surface with a thin layer of some high- T_c material as Nb_3Sn or NbN.

It is not yet clear what surface properties are the most important for achieving high Q and high peak RF fields. The answer to this question will be provided by a careful correlation between microwave cavity measurements and surface studies on small samples processed at the same time. It is possible than suitable surface coatings may finally provide the best solution.

IV. OXIDATION OF Nb AND Nb_3Sn

Several methods have been used to study the oxidation of clean Nb surfaces, to determine exact composition, structure and thickness of the various oxides always present on real Nb surfaces exposed to air or even to very low residual gas pressures in a UHV chamber.

4.1 - Ellipsometry

Ellipsometry, have been used to study Nb oxide growing on a Nb surface by plasma oxidation (15). It was possible to test various treatments of the surface to find the one that give the cleanest surface possible prior to growth of the plasma oxide. The best treatment was found to consist of heating the sample at HT in high vacuum. Ar and O_2 were admitted both to a partial pressure of 0.05 Torr, and a glow discharge was turned on. About 6 hours were necessary to grow 1500 \AA of oxide. From the ellipsometric data it was possible to calculate the refractive index $n = 2.30 + i 0$ for Nb oxides, and $n' = 3.0 + i 3.6$ for the Nb substrate. We shall emphasize the confirmation that - at least for optical frequencies - Nb_2O_5 is a perfect dielectric material.

To improve the properties of tunnel Josephson junctions. In situ ellipsometric measurements have been made at IBM during growth of the tunnel oxide on the base electrode in a RF plasma (16), and the results were compared with electrical measurements. Two additional processes are found to have an important influence on the junction characteristics: precleaning of the base electrode in an argon plasma before oxidation, and a further treatment of the grown

oxide in a low voltage discharge in order to remove the adsorbed residual gases. The most effective gas for this process is nitrogen. The oxides were fabricated in a controlled RF process using Ar/O₂ mixtures. The oxidation time at 0.5 vol % oxygen is long enough to permit thickness measurements of the first few monolayers. The initial slope of the growth curve is quite different from the region starting at about $t \geq 10 \text{ \AA}$, and changes again between 30 and 35 \AA . A detailed explanation of these phenomena is not available.

It is interesting to note that RF cleaning of the surface of the base electrode with Ar accelerates the oxidation process. The higher the RF voltage during Ar cleaning, the thicker the oxide film, and the lower the current density, certainly due to increased surface damage by ion bombardment.

4.2 - Ion scattering spectrometry

Ion scattering spectrometry have been successfully used with low energy ions to study the surface of anodized niobium at Argonne (17). Measurements are only sensitive to the surface monolayer and the depth profile is obtained by progressive sputtering of several hundred atomic layers. Helium ions are used for analysis and Ne ions for sputtering. The figure 2 represents the ratio of heights of the oxygen to niobium peaks for a 200 \AA anodized Nb surface. The values of the ratio corresponding to Nb₂O₅, NbO₂ and NbO are reported on the figure.

An excess of oxygen is found near the surface, which is due to adsorbed gases (H₂O, CO, O). They are two plateau-regions with a relatively sharp transition, which correspond to Nb₂O₅ and NbO respectively; they are followed by a drop off into the bulk Nb metal. If the sputtering rates for Nb₂O₅ and NbO are identical, the thickness of the NbO layer could be estimated of about 80 \AA . But it is well known that the sputtering rate depends on chemical structure, and the values of 80 \AA is only suggestive.

4.3 - Auger electron spectroscopy

A paper published by the Brookhaven group (8) reports AES measurements taken on Nb samples which were treated according to typical procedures used in the preparation of SC cavities, such as UHV degassing, chemical polishing, electropolishing and anodic oxidizing, in order to determine the oxygen depth profile of Nb surfaces.

Eigth Nb samples were machined from commercial reactor grade Nb. After surface treatment, the samples were stored in dry nitrogen and AES analysis was performed several weeks later. The UHV system in which the studies was carried out is capable of reaching 10⁻⁹ Torr. To obtain the depth profiles, surface layers are etched off by sputtering with Ar ions, with a residual Ar pressure of about 5x10⁻⁵ Torr in the system. The Auger spectrum are obtained while sputtering. Due to the large sputtering ion currents, which may create surface roughness and induce parasitic chemical reactions, the depth resolution was poor, and interpretations of the experimental data must be considered semiquantitative in character. Concentrations of O₂ below the at% level were not measurable.

Auger spectra from a clean Nb surface are obtained after removal of about 500 \AA by argon sputtering.

In furnace cleaned samples, the region of high oxygen concentration is about 75 \AA thick - in contrast with previous results (18) obtained from samples

cleaned in UHV and never exposed to air prior to the Auger analysis, which report an oxygen-rich region of only 10 Å at the Nb surface.

For chemically polished samples, oxygen penetration depth attains 100 to 150 Å, and after dissolution of oxide in acid, remains equal to about 90 Å. In addition, the various surface treatments correspond to different oxides: chemical preparations of Nb surfaces result in lower oxides than anodizing and than treatment at high temperature in UHV. In both cases, the oxide layer is made of pentoxide.

Concerning oxygen, the most significant conclusion to be drawn from this work is that the surface treatments result in surfaces covered by layers of lower oxides on the order of 100 Å thick. A typical Nb surface would have a layered structure consisting of a good dielectric pentoxide superficial layer, a two-phase ($\text{NbO}_2 + \text{NbO}$) layer, up to 50 Å thick; a two-phase layer NbO-Nb roughly 50 Å thick, followed by single phase Nb with O as interstitial.

4.4 - Auger electron spectroscopy and XPS

Very recently, at Karlsruhe (19), quantitative measurements of the oxidation of Nb surfaces have been carried out for typical procedures used in the preparation of Nb surfaces; UHV annealing, oxipolishing (OP), electropolishing (EP), handling in air, H_2O or H_2O_2 .

Measurements are performed in a X-ray photoelectron spectrometer with a base pressure in the 10^{-9} Torr region. After chemical treatment, or oxipolishing, or electropolishing, the samples are thoroughly rinsed in distilled water and dried in methanol before their transfer into the vacuum chamber. So they are in contact during about half an hour with air before starting to pump the vacuum tank.

Nb double peaks were used for the measurements. Double peaks for Nb, and Nb^{5+} ions in Nb_2O_5 are shifted by about 5.2 eV respectively, as shown on the figure 3. By a mathematical treatment of the observed peaks, it has been possible to obtain the contribution of the lower oxides. The measurement of photoelectrons at different angles of emission gives, in addition, the oxide thickness.

In all cases, the predominant oxide is Nb_2O_5 . From the XPS spectra, the contribution of lower oxides may be obtained and then separated into contributions of two different valences, with two chemical shifts, one of which corresponds to NbO, the other being attributed to Nb_2O . It is important to emphasize that within the detection limit of the spectrometer, estimated to about one half a monolayer, NbO_2 was never present in the oxide coating.

The pentoxide layer is about 22 and 15 Å for OP and high temperature treatment (HT) respectively, with local variations of about $\pm 10\%$. In contrast, EP samples are covered by a very rough pentoxide layer, whose thickness ranges from 70 to 390 Å. In all cases the mean thickness of lower oxides corresponds to about two monolayers, in contradiction to the results obtained by Hahn and Halama (50 Å).

Depth profiles measurements have been performed, with XPS and AES, by sputtering the oxides, in order to compare the results given by the two methods.

XPS results show that sputtering and electron bombardment are able to create in situ lower oxides. After one minute of Ar ion impact Nb_2O_5 has disappeared and only NbO is left on the surface.

Depth profiles obtained by AES are similar to those published by the Brookhaven group, the O content extending to a depth larger than the initial oxides thickness. A region of "dissolved" oxygen exists below the NbO layer, its extension being different for the various preparation methods. (From 20 to 40 Å for HT samples, up to 100 Å for EP and anodized samples).

XPS and AES allow the following picture of the Nb-Nb oxide interface, which is summarized on the figure 4. The formation of oxides on Nb starts with a metallic oxide, whose thickness has strong local variations, with a mean value of about 10 Å. On top of this NbO layer, an amorphous dielectric oxide Nb_2O_5 is growing. For Nb_2O_5 grown slowly, its external surface is very smooth. After cool-down in the furnace, and transfer to the XPS set up, Nb_2O_5 has a thickness of 20 Å, growing to about 60 Å further in air in some weeks. For fast grown oxides (in H_2O or in H_2O_2), after some minutes a thickness of 60 Å is reached, with strong thickness variations. In addition, underneath the NbO layer, the Nb lattice contains dissolved oxygen, which is present partly as a bulk impurity, and partly due to the oxidation of the Nb surface.

As it will be shown later, NbO_2 may appear under electron bombardment, by picking up O from the residual atmosphere in the spectrometer.

4.5 - U.V. photon spectrometry (UPS)

The electronic structure of the valence band of Nb has been studied by ultraviolet photoemission spectroscopy (20), for a better understanding of the superconducting properties of these material, which is the element with the highest critical temperature. Furthermore, the highest T_c are obtained with compounds containing Nb.

Photoyield and energy distribution curves were obtained from Nb films evaporated onto a Nb substrate in a UHV chamber with a base pressure in the 10^{-11} Torr range. There is a good agreement between theory and experiment both concerning d-band width and structures in the valence band. Nb shows interesting surface properties, and is extremely sensitive to contamination. As an example, there is noticeable change in the EDC three hours after an evaporation despite the fact that the ambient pressure is better than 1×10^{-10} Torr.

The initial stages in the oxidation of Nb have been studied by the same UV photoemission technique, for photon energies below 12 eV.

Changes of structure in the electron distribution curves obtained in UPS are correlated with formation of different types of Nb oxides. At least three different oxides, or mixtures of oxides have been observed. NbO_2 and NbO oxides seem to form first a protective layer. The pentoxide Nb_2O_5 is obtained after heavier oxidation.

The first experiments were carried out at room temperature.

Except for the appearance of a peak corresponding to initial energies located 4 eV below the Fermi level with increasing exposure to oxygen, the initial increase in work function from 4.3 to 5.5 eV is the most remarkable

change. The fact that the work function then remains stable from 20 L to at least up to 10^4 L exposure indicates that the Nb surface is passivated very quickly due to the formation of a thin protective oxide layer. From the evolution of the shape of the energy spectrum it is clear that this layer is metallic in character.

When the oxidation is performed at elevated temperature, the protective layer may be broken up and a new oxide is formed, probably NbO_2 . If the samples are oxidized at high temperature, and atmospheric pressure, the energy distribution curves become progressively characteristic of an insulator, probably Nb_2O_5 .

The figure 5 represents the different oxidation stages for Nb.

Other experiments on oxidation of Nb and Nb_3Sn were performed using thin foils of Nb and photons with higher energies ($h\nu \geq 100$ eV), in a UPS equipped with an AES (21).

A successful method for obtaining atomically clean Nb surfaces is described:

- an heating to temperatures greater than 2000 °C in UHV with $p \approx 10^{-9}$ Torr for 15 minutes evaporates off Nb oxides,
- temperature is then lowered to 1400 °C for 15 minutes, to allow carbon to diffuse from the surface to the bulk,
- finally, the surface must remain at about 800 °C, prior to measurement, to prevent a chemisorption of O_2 or CO.

With this procedure, contamination free AES and UPS spectra are obtained.

In these experiments, chemical shifts of the peaks have been measured, and their observation confirms the existence of three stages in the oxidation processes, corresponding to the formation of the distinct Nb oxides: NbO , NbO_2 and Nb_2O_5 . The oxygen would initially diffuse into the bulk, forming a NbO layer. The NbO layer continues to grow deeper into the bulk and a new NbO_2 oxide nucleates at the surface. These new layer also propagates into the bulk material as the Nb_2O_5 nucleates at the surface. Finally, a Nb_2O_5 layer grows into the bulk and perhaps a mixed phase of NbO_2 remains included in the Nb_2O_5 as it grows. At room temperature, and with 10^3 LO_2 exposure the oxide grows deeper than the escape depth at 21.2 eV in the Nb_2O_5 (which is about 20 Å).

In a second serie of experiments, clean and oxidized Nb_3Sn surfaces were studied using photoemission spectroscopy, to determine valence and core levels. For clean Nb_3Sn , the valence band bears a strong resemblance to Nb.

The first stages of the oxidation of Nb_3Sn were also studied. Compared to Nb, the oxides of Nb_3Sn form a protective layer, but the oxygen penetration is not as deep - as shown by the energy spectra corresponding to a metallic emission, even for near the saturation. In the higher energy data, chemical shifts of the peaks can be associated with SnO_2 and Nb_2O_5 , in addition to Nb_3Sn or Nb metal and other Nb oxides. After annealing the sample to 1000 °C, the outer layer of the oxide is composed essentially of SnO_2 and Nb_2O_5 , with a thickness of about 10 - 15 Å, that is less than for pure Nb.

V. IRRADIATION EFFECTS

Electron irradiation effects on oxidized Nb foils and Nb₂O₅ was studied by AES (22). From observed shift of the energy peaks, one is able to examine the beam effect on the specimen. The figure 6 represents two series of Auger spectra recorded from an oxidized Nb foil, bombarded by electrons of energy $E_p = 2$ keV and with a current $I_p = 15$ μ A and from a pure Nb₂O₅ powder as a reference. In a spectrum corresponding to oxidized Nb, the transition peaks involving valence electrons appear to be doublet, the separation of each doublet being about 5 eV. The low energy peak in each doublet exists only in the oxide state, and corresponds to Nb atoms bound to oxygen. The other peak is the "metal" peak. By irradiation, the metal peak grows at the expense of its oxide counterpart and in the meantime the oxygen peak height reduces correspondingly. The surface of the oxidized sample becomes enriched with Nb due irradiation-induced dissociation of the oxide, and loss of oxygen. At the same time, the carbon peak shape remains graphite-like in form, indicating that no carbide builds up under electron bombardment.

The beam irradiated region, on both type of specimens, can be easily recognized by a colour change: the white colour of the Nb₂O₅ powder decreases and the dark colour of metallic and lower oxide (NbO) mixture increases by bombardment.

The observation of dissociation and reduction of surface oxide was supported by ESD measurements, by measuring the H⁺, OH⁺ and O⁺ signals with a quadrupole mass analyzer. A sharp increase of the O⁺ signal is observed in the earlier stages of electron bombardment. After 5 h of bombardment, O⁺ dominates the final ESD spectrum. (ESD = Electron Stimulated Desorption).

A careful analysis of the observed Auger peaks leads to the conclusion that the superficial layer of an oxidized Nb foil was enriched with about 50 % of Nb, due to beam irradiation, the altered layer being more than 100 Å thick.

These observations clearly show that the electron beam can greatly alter the composition of the Nb oxide, under particular conditions and some precaution must be taken when using a combination of AES and simultaneous ion sputtering, since the sputter-etch rate can increase within the illuminated beam area.

The action of electron irradiation on thin Nb oxides have been studied independently by XPS (19), after impact of 1 keV electrons with a density of 100 μ A/cm². With irradiation, the oxide NbO₂ appears and grows till about 3 monolayers in 70 minutes; at the same time, the Nb₂O₅ intensity decreases and the oxygen concentration in the metal slightly increases. No change can be observed in the region of lower oxides.

If higher current densities are used in the electron beam, the NbO₂ signal shrinks and the Nb₂O₅ signal grows, because O is picked up from vacuum, in agreement with our observations (23).

Thus, the electron beam action may be very different, depending on the experimental conditions, and most particularly on current density and residual atmosphere composition.

The action of low energy ions have been observed in the same experiments: after Ar sputtering with 1 kV ions (2.5 μ A/cm²) Nb₂O₅ disappears and a lower oxide (NbO) is created by the ion bombardment, which extends to a depth larger than the initial oxide thickness.

In addition, Ar ion bombardment change the line shape of the carbon signal from graphite (hydrocarbons) to carbide.

The bombardment of Nb₂O₅ with Kr⁺ or O₂⁺ ions also leads to the development of a surface layer of NbO (24). The layer begins to form at 3.4×10¹⁵ ions/cm² as random nuclei of diameter 10 to 15 Å which can be resolved by transmission electron microscopy. The final thickness of the surface layer is roughly 300 Å. In these experiments, Nb₂O₅ films were peeled off from oxidized Nb plates, then supported on grids and bombarded by 35 keV ions. The bombarding current was kept to about 5 μA/cm² to avoid thermal heating. High energy electron diffraction gives patterns which are characteristic of NbO.

This phenomenon can be understood from a model which combines preferential oxygen sputtering at the surface, diffusion of the relevant point-defects and random nucleation of the suboxide NbO. A gradual colour change from white to black was observed during bombardment with darkening complete at a dose of about 1-3×10¹⁷ ions/cm².

Irradiation of Nb and oxidized Nb surfaces by high energy ions in superconducting cavities has led to contradictory results. At Brookhaven (25) irradiation by high energy protons lead to an heavy degradation of Q and RF peak field values, the anodized cavities showing a considerably greater degradation than those not anodized. On the contrary, experiments carried out in the Siemens laboratory on anodized cavities after irradiation by 1 or 3 MeV protons, were unable to show any influence of the irradiation upon the Q and the peak magnetic field (26).

In the Siemens experiments, the whole cavity was homogeneously irradiated, and the calculated density of defects produced in Nb were 10 - 100 times greater than that obtained at Brookhaven. At Brookhaven, only an area of 1 cm² was bombarded with protons.

It is suggested that the observed degradation is not due in any way to the formation of lattice defects in Nb.

Considering now the action of ions on the oxide, lower oxides are certainly formed by reduction of Nb₂O₅. But again, the total energy dose in the oxide is 10 to 100 times greater in the second serie of experiments. In conclusion, Nb₂O₅ seems to have a high resistance to radiation.

From various experiments performed with ion bombardment, we may conclude that ion bombardment creates lower oxide (NbO, NbO₂) by reduction of Nb₂O₅, and progressively transforms a smooth surface into a rough surface. Surface damages certainly accelerates the oxidation of Nb surfaces, O being taken from the residual atmosphere, and an equilibrium between sputtering and readsorption of oxygen may be observed. All these phenomena explain that in the depth profiles obtained by AES, the O content extends to a depth larger than the true oxide thickness.

Thus by combining AES (or ISS) and ion sputtering it is difficult to obtain the real composition and distribution of oxides in the surface layer. Only relative comparisons between profiles of differently prepared samples can be made by this destructive methods. Only XPS, UPS, without ion sputtering will be able to give quantitative results - but only for very thin surface layers -.

PART II. ELECTRON EMISSION

I. INTRODUCTION

One of the principal limitation in achieving high accelerating fields in microwave cavities is the phenomenon of multipactor. In Nb cavities operating in S-band, studies at Stanford, Cornell, Karlsruhe and Wuppertal, have shown that one surface multipactor is the dominant limiting mechanism.

Resonant multiplication may take place provided that the secondary emission coefficient of the surface is larger than unity. According trajectories calculations, in cylindrical or in rectangular muffin-tin cavities, the electrons return to the surface with kinetic energies in the 50 - 1000 eV range, and it is clear that the secondary emission coefficient in this primary energy range plays a crucial role in determining the strength of the multipactor barriers.

Several laboratories have measured the secondary emission coefficient for materials of interest to superconducting accelerators cavities, the surfaces of the samples being prepared by the methods commonly employed for superconducting cavities.

At Cornell University, the material tested were Nb, anodized Nb, Nb₃Sn, NbN, Ti and TiN. These two last materials have been deposited in the past as coating for surfaces of conventional microwave copper cavities in an attempt to suppress multipactor, and more recently on Nb cavities.

At Paris, we have measured Nb, oxidized Nb, Cu, and thin layers of Ti and C deposited on Nb.

At CERN, a systematic study of the influence on secondary emission from Nb of various surface treatments have been recently carried out.

The influence of thin oxide layers on the secondary emission has been studied at Karlsruhe.

2. SECONDARY EMISSION FROM Nb SURFACES

In the Cornell experiments [27], the sample were placed in a UHV system pumped out to 10⁻⁹ Torr, and the area under test was cleaned by ion sputtering. An Auger spectrum was registered immediately after.

Values of δ are given as a function of primary electron energies E_p , that are varied from 200 to 2000 eV, for surfaces in typical situations: before cleaning, after cleaning (i.e. after removal of a 200 Å thick layer by ion sputtering) and finally after exposition to air (Fig. 7).

For a clean Nb surface, δ_{\max} attains about 1.2 and the energy domain $E_1 < E < E_2$ in which δ is greater than unity extends from about 100 to 1300 eV. After cleaning, the secondary emission from Nb covered with a 2000 Å thick layer of Nb₂O₅, is lower than the one from clean Nb. Before cleaning, the emission is comparable in both cases. But Nb₂O₅ reduces the width of the energy domain $E_1 - E_2$ to about 150 - 800 eV. In all cases, an exposure to air increases the secondary emission yields.

Auger spectra show that in pure Nb, a carbon peak is always present, even after cleaning. In Nb₂O₅ the carbon peak is present before cleaning, disappears after ion sputtering, and slightly reappears after an exposure to air. Nb₂O₅ is always contaminated by nitrogen, due to the NH₃ bath.

These results for Nb and anodized Nb suggest that cavities surfaces prepared by wet chemical methods are likely to show strong multipactoring, but that the situation may be improved by an argon discharge, cleaning the contaminated surfaces in situ.

Secondary emission from clean Nb₃Sn may be compared to the emission from clean Nb, with a δ_{\max} of about $\delta_m = 1.3$

The new material NbN ($T_c \approx 16\text{ K}$) has a secondary emission coefficient larger than unity, and the curve $\delta(E_p)$ is quite close to the curve corresponding to Nb₂O₅.

Clean Ti would be a very interesting material, as its δ coefficient remains lower than unity ($\delta_m \approx 0.95$), but unfortunately, an exposure to air markedly increases δ_{\max} to about 1.35. In comparison the emission of a thin layer of TiN, 1000 Å thick, obtained by reactive sputtering of Ti in a N atmosphere, is larger than the emission from Ti before cleaning, with $\delta_m \approx 1.5$, similar after cleaning ($\delta \approx 0.95$) but is less severely affected by an exposure to air (Fig. 8).

This suggests that TiN may prove a more favourable coating than Ti for the suppression of multipactor, at the condition to prepare the material in situ and then avoid subsequent contamination.

Having in mind these results the Cornell group attempted to determine how the RF performances of SC cavities can be affected by applying thin coatings of similar materials, as well to try to overcome the multipactor barriers (28).

Single cell X-band and S-band muffin-tin cavities have been coated. Before coating the Q_0 factor of S-band cavities lie between 5×10^9 and 1.5×10^{10} . At high RF power, multipactor barriers were encountered between 4 - 5 MeV/m and 7 - 10 MeV/m. Very thin coatings films (150 - 300 Å) of Ti, TiN and Rh, have been deposited on the walls of the cavities. Of these three materials, Ti has the most pronounced effect on Q_0 while TiN has the least. The presence of a normal metal film increases the surface resistance but does not create hot spots at high power, so that fields up to 8 MeV/m can still be realized. Unfortunately the multipactoring behaviour remains unaltered by Ti, and adversely affected by TiN. Only the rhodium coatings appear to have beneficial effects, and this may perhaps be related to the absence of any significant oxide layer. In addition, it is not sure that the very thin films used in these experiments were continuous, and that Nb islands with high values of δ were not present.

At CERN (29), various aspects of secondary electron emission have been recently studied, in order to explain the influence on the secondary emission coefficient δ of (i) the surface treatment, (ii) the electron dose, (iii) the angle of incidence of the primary electrons, and (iv) the temperature.

Concerning the surface treatment, the conclusions are the following:

- baking the vacuum chamber containing the sample at 300 °C during 24 hours decreases δ . After this treatment, a short exposure to the air increases slightly δ without recovering the initial values of the emission.

- electropolishing seems to have a weak influence on δ , which decreases only at high primary energies.

- a gaseous discharge in Argon at a pressure of 10^{-2} Torr, with an ion dose of about $10^{18}/\text{cm}^2$, the ion energy being 1 keV, decreases δ by a large factor. The figure 9 shows the curves corresponding to an unbaked surface, and to a baked surface after cleaning by gas discharge.

If the gas discharge cleaning is performed in an unbaked system, the secondary emission of the cleaned surface is instable, and δ increases slowly with time. On the contrary, if the discharge cleaning takes place in a baked system, the emission coefficient has low and stable values.

- the influence on δ of the electron dose is in good agreement with our results (30).

- if a baked surface is cooled to 4.2 K, the values of δ are the same that the values obtained at ambient temperature before cooling (see Fig. 10).

Auger spectra show that after a gaseous discharge, the carbon and oxygen peaks disappear. The ion bombardment seems to sputter the oxide layer, and also the Nb layer containing adsorbed oxygen. The total absence of carbon is surprising, as carbon is present in the original sample, but we may assume that carbon is eliminated by the discharge, after a chemical reaction with oxygen, like in an outgassing process at high temperature. After an electron bombardment with a dose of about $1.2 \times 10^3 \text{ C}/\text{cm}^2$, carbon and oxygen peaks are again present in the Auger spectra. Electron bombardment is at the origin of a chemical transformation of a surface, after induced adsorption of molecules from the residual atmosphere.

Very important results have been obtained concerning the evolution of the parameter E_1 and E_2 which characterize the two electron primary energies for which $\delta = 1$, for various conditions: (i) for an unbaked surface, E_1 is less than 30 eV; (ii) after baking and gas discharge, E_1 is raised to 140 eV, and δ_m lowered from 2.5 to 1.23; (iii) an exposure to air during 8 hours lowers E_1 to 34 eV, and a new bakeout increases E_1 till 100 eV; (iv) a new discharge will be necessary to recover the preceding value of $E_1 = 140 \text{ eV}$.

A gas discharge in Argon seems a good method to clean the surface and to suppress high order barriers of multipactor, by rising the values of E_1 .

III. ACTION OF THE ELECTRON BEAM ON SECONDARY EMISSION

The first experiments made in our laboratory to study the secondary emission of various metal surfaces in 1977-1978 have pointed out the strong influence of the electron bombardment on the evolution of δ . For these experiments, a vacuum chamber with a residual pressure of about 10^{-8} Torr was used.

For all specimens (Nb, oxidized Nb, Cu, Au) cleaned in methyl alcohol before their introduction into the chamber, it was observed a rapid decrease of δ during the first 10 or 20 minutes of bombardment (Fig. 11 (a)), the de-

creasing-rate being approximately proportional to the electron dose. For Nb, or Cu, which are always covered by a native oxide layer, the initial decrease of δ is followed by a slow increase, and after several hours, a stable value of δ is attained. This value increases if the sample is exposed to air, in agreement with Cornell and CERN experiments.

If the sample is coated by a Nb_2O_5 layer 400 to 1000 Å thick, δ decreases continuously towards its final value, with $\delta_m \approx 1.05$ (Fig. 11 (b)).

Some experiments have been carried out in an Auger electron spectrometer with imaging possibilities. The bombardment regions of the Nb samples were visible on the screen, and analysis of bombarded and unbombarded regions gave different results: the oxygen peak is higher in the irradiated zones, and the carbon peak lower, than in the surrounding regions.

The chemical action of the electron beam is particularly strong on a clean copper surface, covered by its natural oxide layer. A few seconds of bombardment with a current density of about 1 mA/cm² is sufficient to change the colour of the bombarded area from red to purple corresponding to the growing of a dielectric layer, probably made of Cu-oxide. At very low electron dose, the irradiated region is not visible in high vacuum, but if the sample is exposed to air, the purple colour appears slowly, and the superficial oxide layer grows continuously during days.

Such a visible phenomenon was not observed with Nb or Nb_2O_5 surfaces, contrasting with other experiments (22). The composition of the residual atmosphere in the vacuum chamber that differs in the respective experimental devices, certainly plays an important role.

More recently, experiments were performed in a better vacuum (3×10^{-10} Torr) after outgassing the vacuum chamber at 300 °C during 24 hours (31). The evolution in time of δ was shown to be more rapid than in previous experiments, made at a pressure about 10^{-8} Torr. In the new system, the primary electron energy has been varied from 50 to 2500 eV. The limit value of δ under bombardment is the same in both cases for Nb surfaces.

Several thin film coatings were studied: Ti and C. Very thin films of both materials have an important action on the emission, and δ_m decreases to values lower than unity for a Ti film thickness of about 100 Å. (Fig. 12).

Carbon film, obtained by evaporation from high purity carbon electrodes, have a curve $\delta(E_p)$ which strongly differs from the metal curves. The region with $\delta > 1$ is reduced more and more by the electron bombardment, but without rotation of the initial linearly growing part of the curve. The energy corresponding to $\delta = 1$ is only 200 eV, and the peak in $\delta(E_p)$ becomes sharper and sharper by increasing the layer thickness (Fig. 13). Values of $\delta_m < 1$ are obtained with a thickness of about 100 - 150 Å.

IV. INFLUENCE OF A THIN OXIDE LAYER ON SECONDARY EMISSION

In order to explain the influence on the secondary emission yield of the oxide layer, and of the adsorbates, that always cover Nb - or Nb_3Sn - surfaces, and also the variation of the emission induced by electron or ion impact, experiments have been carried out at Karlsruhe, by X-ray photoelectron spectroscopy (19)(32). The "secondary electrons" that are measured, are slowed-down photoelectrons.

It can be shown that the true secondary electrons produced by electron impact are proportional to the "secondary electrons" created by X-rays, and because the shape of the curve giving δ as a function of the primary electron energy E_p is universal for homogeneous materials, it may be assumed that the electron current measured in X-ray experiments is directly related to the maximum value δ_m of δ . Thus only variations of δ_m are reported, for various surface treatments, and in relation with the chemical composition of the oxide layer. XPS shows that homogeneous layers of Nb_2O_5 are found for dry oxides (obtained by H.T. treatment of Nb) about 20 Å thick, whereas wet oxides (obtained by oxipolishing, electropolishing, or washing in water) are thicker (about 60 Å) and inhomogeneous. Wet oxides contain adsorbed H_2O molecules and all oxides may contain adsorbed hydrocarbons or CO_2 on their surface.

Wet oxides are positively charged by irradiation with X-rays, and this positive d.c. charging enhances electron emission by lowering the work function. On the contrary hydrocarbons become negatively charged, enhance the work function and then lessen the secondary emission.

Large variations of secondary emission observed during electron - or ion - bombardment may be explained at least qualitatively by taking into account both types of adsorbates, and the charge variations at the oxide surface. In addition, electron bombardment has a strong chemical action on the oxide itself and on the adsorbates. With electron impact the main change for the O-adsorbates (H_2O , O) is the transformation of Nb_2O_5 into NbO_2 , the growth of the oxide at the expense of the adsorbate and of the residual atmosphere. For the C adsorbates (CO , CO_2 , CH_3OH , oil molecules), polymerization may be induced by the electron beam.

Namely, δ_{max} is enhanced over δ_{max} relative to clean Nb by 30 % for dry Nb_2O_5 , by 50 % for Nb_2O_5 containing chemisorbed water molecules, and strongly reduced if hydrocarbons present on the surface are polymerized by the electron beam.

Water adsorption and O-adsorbates may be eliminated by heat treatment or by helium or ion processing, thus reducing δ .

With oxide containing hydrocarbons, δ decreases of about 40 % for an electron dose around $1 C/cm^2$. At Paris or at CERN, variations of 30 and 40 % respectively were found for an electron dose of $10 C/cm^2$ with oxides having a different composition, and also the residual atmosphere was different.

From this work, it is suggested to reduce the secondary emission by covering the surface with very thin films of polymerized hydrocarbons, which would give lower emission than Nb_2O_5 oxide layers, but it will be a difficult task to elaborate stable layers in situ, and avoid the contamination of their surface. It seems more realistic to cover the surface with a thin carbon film.

V. FIELD EMISSION

At very high field levels, loading and X-ray emission which result from field emitted electrons also limit the field level that can be achieved in practice in SC cavities.

Field emission experiments at helium temperature have been performed at Stanford (HEPL) both for d-c and RF fields in order to study field emission enhanced by resonant tunneling of electrons through surface-states associated with adsorbed atoms (33).

Field emission from clean surfaces occurs at values of the field greater than 3×10^7 V cm⁻¹, as shown by experiments with a point cathode facing a plane anode.

Field emission between broad area electrodes occurs for field values 10 to 100 times smaller than this and currents are observed which are many orders of magnitude greater than those predicted by the Fowler-Nordheim law. These apparent discrepancies between systems utilizing point-to-plane geometry and systems using broad area electrodes are easily explained by the existence of microscopic projections on the surface of large electrodes, even after polishing. On the tip of these micropoints, the local field may be enhanced by a factor β greater than 10^2 , compared to the mean field existing between the electrodes. In addition, the anomalous behavior of the emitted current may be due to the presence of adsorbed atoms on the surface, which introduce a potential well in the potential barrier. If bound states of the adsorbate are slightly under the Fermi level, resonant tunneling of electrons from the metal to the vacuum increases dramatically the current, as the transition probability of electrons of energy equal to the adsorbate level is greatly enhanced. Experimental measurements of the energy distribution of emitted electrons demonstrate the existence of this resonant tunneling process.

Using the point-to-plane geometry, enhancement factors of 10^3 to 10^4 for the emitted current are easily observed between a very clean tip surface and a tip covered with adsorbates (Fig. 14).

Processing techniques can be applied in cavities to reduce field emission. As an example, a low current glow discharge in helium at a pressure of 10^{-4} Torr, has two specific actions on the surface: destruction of the emitting micropoints having the maximum field enhancement factor, and desorption of the atoms bound to the metal - or to the oxide surface.

In cavities, at high field levels, field emitted electron can be accelerated to high energies, and X-rays are produced. The variation of the intensity of X-radiation as a function of the peak electric field in the cavity are in good agreement with theory, assuming field electron emission from the wall. Helium processing at relatively low power level during hours, is able to reduce X-ray emission by large factors and consequently to increase the power injected in the cavity. A careful study of the influence of the processing on the emitted X-ray radiation led to the conclusion that sputtering of adsorbed atoms takes place in the earlier stages of processing, corresponding to a lowering of the apparent field enhancement factor β , and an increase of the work function. From these experiments, the factor β cannot be considered only as a geometrical factor, but like a fitting factor, as pointed out by Halbritter (34).

In Nb cavities, the local RF field is enhanced at geometrical protrusions by a factor β of about 200, for cleaned surfaces. After adsorption, the values of β calculated from FN plots may be as high as 500 - 600. This apparent increase of β may be explained in terms of resonant tunneling.

Finally the reduction of field emitted electrons currents, that was observed in microwave cavities by rising the frequency from S-band to X-band may be also explained by a reduction of the apparent β factor, due to the finite transit time of the electrons through the oxides and a reduced positive charging of the surface (34).

Large area Nb electrodes were also used in experiments carried out at He temperature at Orsay (35), in order to study the influence on the field emitted

electron current of the thickness of a Nb_2O_5 coating. No ion processing was made in the d.c. experimental diode, but a measure of the temperature increase of the cathode on the order of a few K, show that this electrode is permanently bombarded by ions created by the electrons hitting the anode and stimulating the desorption of gaseous species. After a few hours, the I.V. characteristics of the diode are stable enough to obtain reproducible results.

It was shown that an increase of the Nb_2O_5 thickness from zero (Nb + natural oxide) to 1600 Å decreases the current by several orders of magnitude (Fig. 15). At the same time the apparent enhancement factor remains nearly constant, between 150 and 200 for oxide thicknesses ranging from 50 to 400 Å. For thicker oxides, β decreases and reaches 60-90 for a layer thickness of 1600 Å.

VI. DISCUSSION

A survey on electron emission phenomena from oxidized metal surfaces by Halbritter was, at the same time, an attempt to explain the great number of observations made in various laboratories, which often were in contradiction and not- or misinterpreted. (35).

The basis for a satisfying explanation was found later (32) in the presence or the absence of electric charges in the outer atomic layers of the oxides - or in superficial adsorbates. These charges can be induced naturally be the adsorption of atoms - as mentioned earlier - but also by electron or ion bombardment, and by electron secondary emission under X-ray or electron bombardment. The sign of this charges depends on the chemical composition of the adsorbates and on the energy of the bombarding particles. As an example, for very low or high electrons energies, the secondary electron emission coefficient is less than unity and the surface becomes negatively charged. On the contrary, for δ greater than unity, the oxide surface becomes positively charged.

The conduction of electrons through the Nb oxide layer results from two phenomena: field emission from the metal to the conduction band of the oxide, which is for Nb_2O_5 very close to the Fermi level, and also hopping conduction through impurities levels located in the forbidden band, and from this levels to the conduction band.

The electric field applied to the metal surface has two origins: the external field, shielded by the high dielectric constant of the Nb_2O_5 oxide ($\epsilon \approx 30$), and essentially the short range action of the charges existing on the oxide surface.

For these reason, positive charges distributed on the surface may be considered as "holes" in the potential barrier, when an high external field is applied normal to the surface (Fig. 16), and the field emission is dramatically enhanced. This phenomenological model is equivalent to the quantum mechanical resonant tunneling model.

If now an electron bombardment is able to create superficial positive charges - as an example by ionizing oxygen vacancies which originally contains two electrons - the energy diagram is locally distorted, and even without an external field, electrons are emitted, leading to a local value of δ which may attain values as high as 100 or 1000 ; as a consequence, the mean value

of δ over the whole surface increases. This phenomenon was in the past called "Malter effect". Only the electrons injected from the metal into the conduction band of the oxide are able to pass over the potential barrier.

Conversely, negative charges on the surface locally reduce the secondary emission. It was the case for carbon or hydrocarbons adsorbates, and graphite layers deposited on the surface.

For thicker and thicker oxide layers, the distance between the Fermi level and the conduction band of the oxide increases rapidly, thus reducing the tunnel current flowing from the metal to the conduction band and consequently, decreases the field emitted current.

Another consequence of the presence of positive charges in the oxide layer on Nb surface is the lowering of the apparent work function of the surface, and the enhancement of the apparent field factor β , which increases the field emission.

As far as secondary emission is concerned, evolution of the secondary emission coefficient under electron bombardment towards lower values may explain the observed possibility to overcome multipactor barriers of high order, the multipacting discharge decreasing in intensity with time and finally die out.

Experiments on the lowering of δ_m towards values less than unity by deposition of thin films have to be continued. From the Cornell work, one might be tempted to try thicker coating of Rh, or perhaps Au, about 500 Å thick, in order to obtain a continuous layer and a complete coverage of the underlying Nb. It is conceivable that the RF losses in such a thick normal metal coating might be lessened by the superconducting proximity effect.

Our experiments with carbon films are encouraging, as carbon may lower δ_m to $\delta_m < 1$, and considerably decreases the $E_1 - E_2$ domain for which $\delta > 1$, before bombardment. The influence of C under a graphite form is in agreement with the suggestion by Halbritter to cover the surface with hydrocarbons films. It will be now necessary to measure the surface resistance of carbon covered Nb surfaces, and to attempt to suppress multipacting barriers in real cavities by using thin carbon coatings.

The CERN work demonstrates the important effects on δ and on the $E_1 - E_2$ domain of (i) a thorough outgassing before cooling the surface, (ii) a very low residual pressure ($\approx 10^{-10}$ Torr) and (iii) ion cleaning by an argon discharge. Such a ion processing is well known to decrease dramatically the field emission currents. Adsorbed nitrogen is known to lessen field emission, and could certainly be used for ion processing. From the experiments at IBM (16), nitrogen gives better results for cleaning a Nb surface. A careful study of the influence of ion processing by a discharge in nitrogen on secondary and field emission would be necessary.

Finally, we may emphasize that a decrease of the maximum secondary emission yield to values less than unity is not a necessary condition to avoid multipactor: it would be sufficient to obtain a yield less than unity for electrons energies corresponding to the energy spectrum of the electrons active in the multipacting process. For these reason, an evolution of δ in which the initial linear part of the curve giving $\delta(E_p)$ rotates clockwise under electron or ion bombardment will be highly favourable.

We suggest to coat the surface with thin layers of materials having their curve $\delta(E_p)$ displaced to higher energies than the homogeneous materials used till now. It is well-known that metals with high δ coefficients have at higher energies than metals with weaker values of δ_m . Surprisingly, following this reasoning, metals with a high value of δ_m , like Au or Pt, could be superior to others, as far as high order multipactor is concerned.

Another possibility would be to study emission coefficients of porous layers, that have emission properties very different from those of homogeneous layers.

REFERENCES

- 1 WERNER, H.W. - Modern methods for thin film and surface analysis. Mat. Sci. and Engng 42, 1980, p.1
- 2 BERANGER, G., D. DAVID, E.A. GARCIA, X. LUCAS - Etude de la contamination superficielle des métaux au moyen de la microanalyse nucléaire. Rev. Phys. Appliquée 10, 1975, p.87
- 3 PADAMSEE, H., J. KIRCHGESSNER, M. TIGNER, R. SURDELIN, M. BANNER, J. STIMMEL, L. PHILLIPS - Fabrication and performances of muffin-tin microwave cavities for accelerator use. Cornell University CLNS-340 and IEEE Trans. MAG 13, 1977, p.346
- 4 DICKEY, J.M., M. STRONGIN, O.F. KAMMERER - Studies of thin films of Nb₃Sn or Nb. J. Appl. Phys. 42, 1971, p.5808
- 5 UZEL, Y., B. HILLENBRAND, K. SCHNITZKE - Zur Preparation von Nb₃Sn Schichten auf einkristalliner Nb-unterlage. DPG, Fachausschuß Tiefe Temperaturen, Freudenstadt 1980
- 6 SUNDELIN, R., E. von BORSTEL, J. KIRCHGESSNER, D. RICE, M. TIGNER - 3 GHz SC accelerator cavity for use in an electron synchrotron. IEEE Trans. NS 20, 1973, p.98
- 7 HOYT, E.W. - Nb surfaces for RF superconductors. SLAC PUB 977, oct. 1971
- 8 HAHN, H., H.J. HALAMA - AES depth profile measurements of Nb for SC cavities. J. Appl. Phys. 47, 1976, p.4629
- 9 MAUREL, B., D. DIEUMEGARD, G. AMSEL - Nuclear study of the fluorine contamination of Ta by various polishing procedures and its behavior during subsequent anodic oxidation. J. Electrochem. Soc. 119, 1972, p. 1715
- 10 CHERKI, C. - Film-formation oxygen yield in the anodic oxidation of Nb. Electrochimica Acta, 16, 1971, p.1727
- 11 GIORDANO, S., H. HAHN, H.J. HALAMA, C. VARMAZIS, L. RINDERER - Influence of solute oxygen and nitrogen on SC Nb cavities. J. Appl. Phys. 44, 1973, p.4185

- 12 WILSON, P.B., Z.D. FARKAS, H.A. HOGG, E.W. HOYT - Recent measurements at SLAC on SC Nb X-band cavities.
SLAC PUB 1228, March 1973 and IEEE Trans., NS 20, 1973, p.104
- 13 DICKEY, J.M., H.H. FARRELL, O.F. KAMMERER, M. STRONGIN -
Surface studies on Nb and some implications for superconductivity.
Phys. Lett. 32 A, 1970, p.483
- 14 STRONGIN, M., H.H. FARRELL, H.J. HALAMA, O.F. KAMMERER, C. VARMAZIS,
J.M. DICKEY - Surface condition of Nb for SC RF cavities.
Particle Accelerators 3, 1972, p.209
- 15 KNORR, K., J.D. LESLIE - Ellipsometric measurements of the plasma
oxidation of Nb and Ta and their interpretation.
J. Electrochem. Soc. 121, 1974, p.805
- 16 BROOM, R.F., R.B. LAIBOVITZ, Th. O. MOHR, W. WALTER - Fabrication and
properties of Nb Josephson tunnel junctions.
IBM Journal, 24, 1980, p.213
- 17 GRAY, K.E. - ISS depth profile of anodized Nb.
Appl. Phys. Lett. 27, 1975, p.462
- 18 JOSHI, A., M. STRONGIN -
Scripta Metallurgica 8, 1974 p. 413
- 19 GRUNDNER, M., J. HALBRITTER - XPS and AES studies on oxide growth and
oxide coatings on Nb.
J. Appl. Phys. 51, 1980, p.397
- 20 LINDAU, I., and W.E. SPICER - Oxidation of Nb as studied by the UV
photoemission technique.
J. Appl. Phys. 45, 1974, p.3720
- 21 MILLER, J.N. - Photoemission studies of clean and oxidized Nb
and Nb₃Sn surfaces.
Ph.D. Thesis, Stanford 1980 (to be published in J. Appl. Phys.)
- 22 LIN, T.T., D. LICHTMAN - Electron irradiation effects on oxidized
Nb foil and Nb₂O₅.
J. of Mat. Sci. 14, 1979, p.455
- 23 LAVAREC, M., P. BOCQUET, A. SEPTIER - Variation du coefficient
d'émission électronique secondaire de surfaces réelles sous l'effet
du bombardement électronique primaire.
C.R.Acad. Sci. Paris, 288 B, 1979, p.77
- 24 MURTI, D.K., R. KELLY -
Preferential oxygen sputtering from Nb₂O₅.
Thin Solid Films, 33, 1976, p.149
- 25 HALAMA, H.J. - Effects of radiation on surface resistance of SC Nb cavity.
Appl. Phys. Lett. 19, 1971, p.90

- 26 MARTENS, H., K. WHOLLEBEN -
Irradiation of SC cavities with protons.
Phys. Lett. 42 A, 1973, p.393
- 27 PADAMSEE, H., A. JOSHI - Secondary electron emission measurements
on materials used for SC microwave cavities.
J. Appl. Phys. 50, 1979, p.1112.
- 28 PADAMSEE, H., M. BANNER, M. TIGNER -
Suppression of multipactoring in SC cavities.
IEEE Trans., NS 24, 1977, p.1101
- 29 HILLERET, N. - Influence of surface treatment, electron dose, and
temperature on secondary emission from Nb surfaces.
1980 - Private communication.
- 30 LAVAREC, M., P. BOCQUET, A. SEPTIER -
Lowering of the secondary electron emission coefficient of real
surfaces due to the primary electron bombardment.
Proc. 8th Int. Symp. on Discharges and Electr. Insul. Vac.,
Albuquerque, 1978, p. C 3-1.
- 31 NGUYEN TUONG Viet, G. SAYAG, A. SEPTIER -
Secondary emission from Ti and C thin films on Nb.
(unpublished).
- 32 GRUNDNER, M., J. HALBRITTER -
On surface coatings and secondary yield of Nb₃Sn and Nb.
J. Appl. Phys. 51, 1980 (to be published)
- 33 SCHWETTMANN, H.A., J.P. TURNEAURE, R.F. WAITES -
Evidence for surface-state enhanced field emission in RF SC cavities.
J. Appl. Phys. 54, 1974, p.914
- 34 HALBRITTER, J. - On electron emission phenomena from oxidized metal
surfaces. Their application to electron loading in Nb high
frequency cavities.
KfK Ext. 3/781, 1978
- 35 SAYAG, G., NGUYEN TUONG Viet, H. BERGERET, A. SEPTIER.
Field emission from oxidized niobium electrodes at 295 and 4.2 K .
J. Phys. E 10, 1977, p.176.

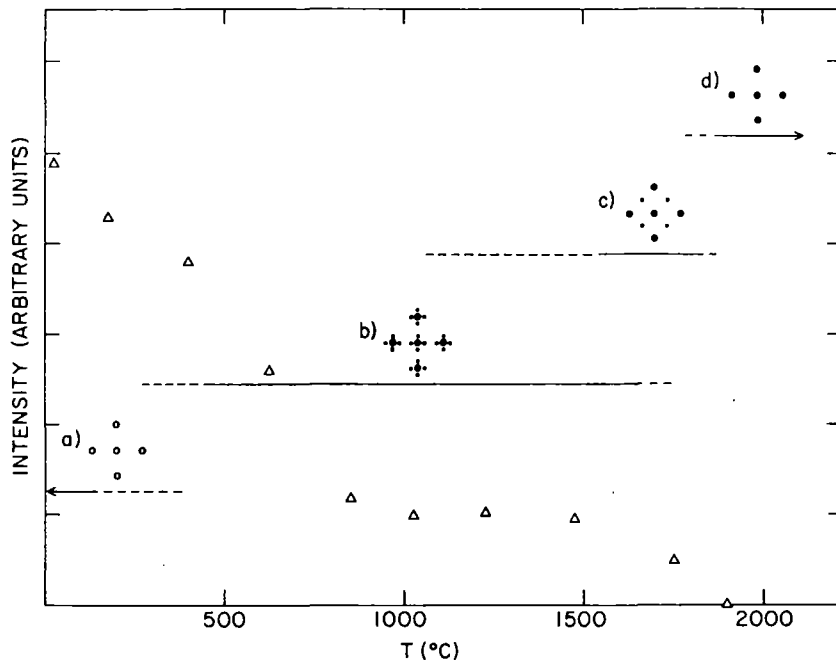


Fig. 1 - Intensity of the oxygen peak in Auger spectrum as a function of the sample thermal history. The different diffraction patterns observed at corresponding regions are indicated. (a) uncleaned Nb, covered with adsorbed oxygen; (b) faceted structure (Nb oxide); (c) monolayer (NbO) parallel to the substrate; (d) clean Nb surface. (from (4) and (13))

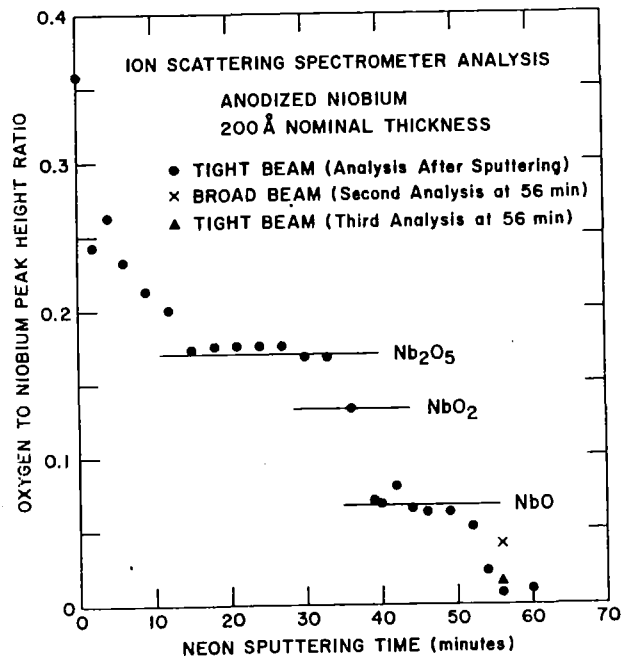


Fig. 2 - Ratio of heights of the O to Nb peaks in the ISS spectrum for a 200 Å anodized Nb surface plotted against sputtering time. (from (17)).

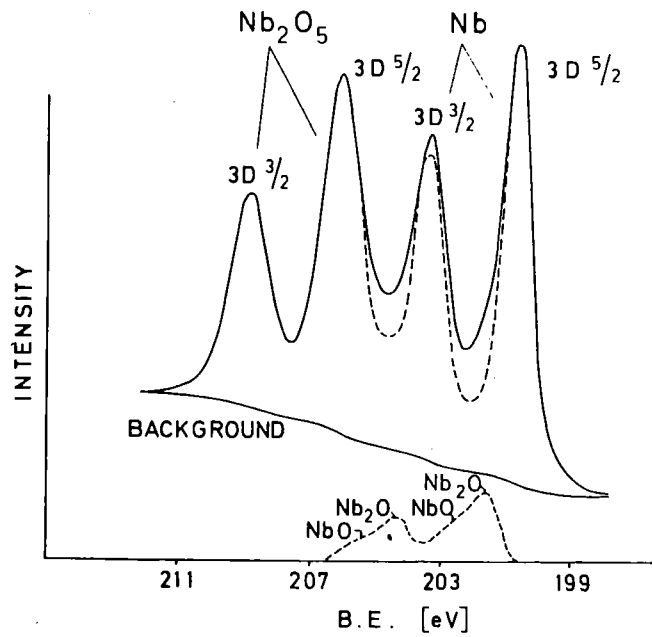


Fig. 3 - Typical XPS spectrum from a Nb surface around 200 eV. The double peaks correspond respectively to Nb and Nb⁵⁺. After subtracting the background, the dashed curves are obtained, which describe the lower oxides (from (19)).

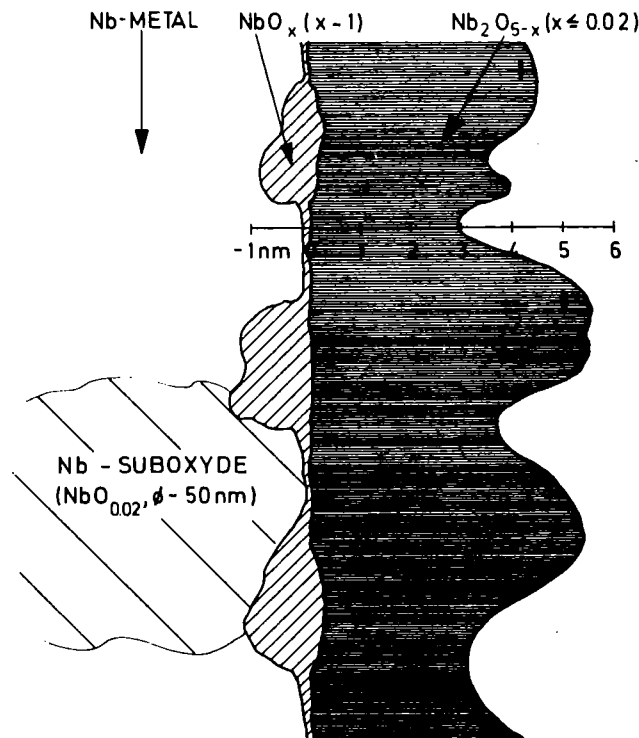


Fig. 4 - Results of an XPS study of Nb. Sketch of a wet oxidized Nb surface. (from (19)).

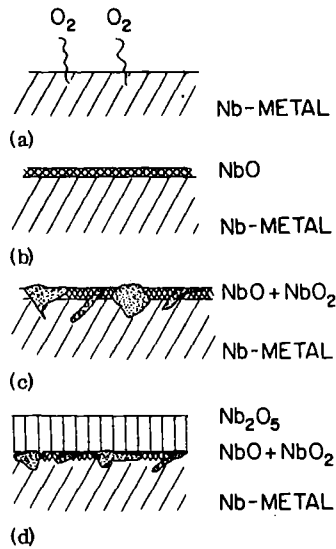


Fig. 5 - Results of an UPS study of Nb : schematic representation of the different stages for Nb (from (20)).

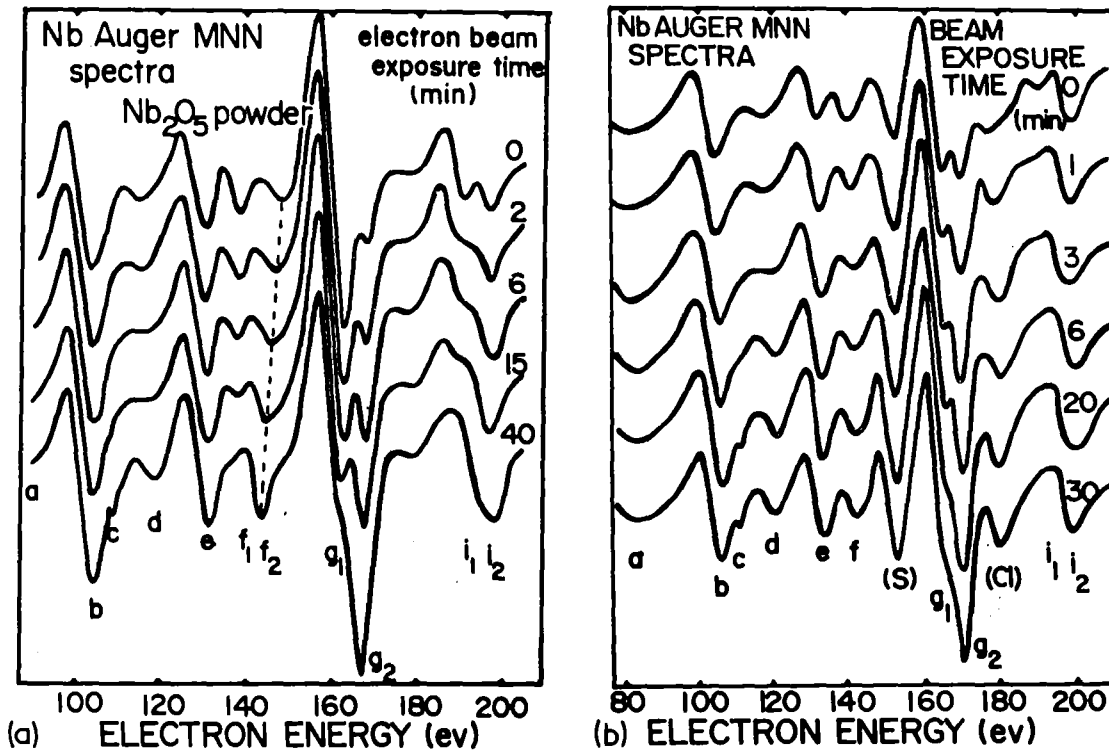


Fig. 6 - Variations of Auger spectra with beam exposure time.

(a) Nb₂O₅ powder ; beam voltage, 2 keV ; beam current, 15 μ A.

(b) oxidized Nb foil. f₁, g₁, i₁ : "oxide" peaks (Nb⁵⁺) ; f₂, g₂, i₂ : "metal" peaks (Nb).
The "metal" peak grows at the expense of its "oxide" counterpart (from (22)).

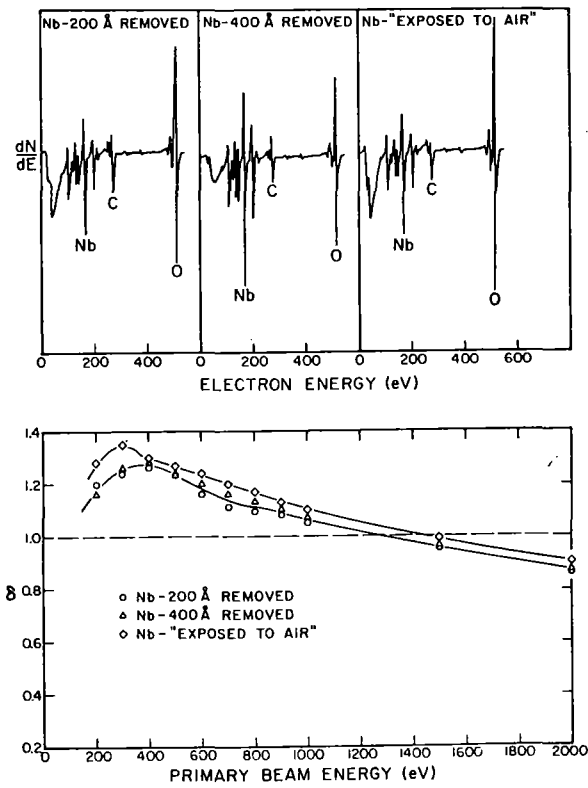
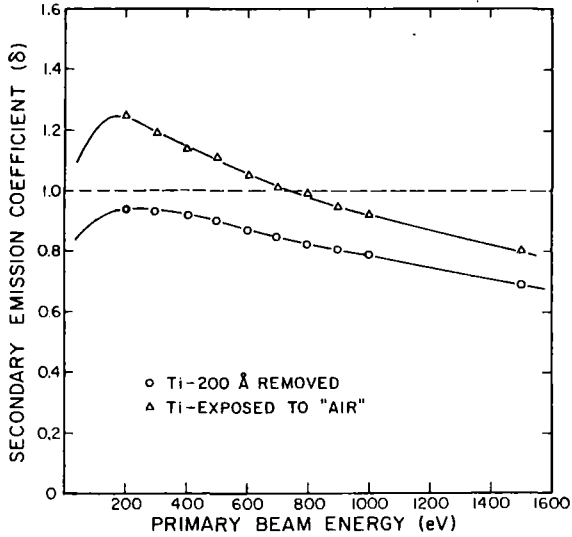
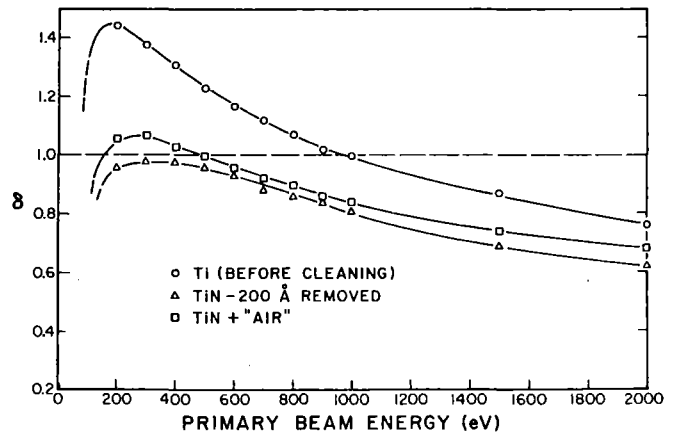


Fig. 7 - Secondary emission (SE) and Auger spectra for clean Nb and Nb exposed to air (from (27)).



(a)



(b)

Fig. 8 - SE from Ti and TiN. (a) clean Ti and Ti exposed to air. (b) as-prepared, clean, and exposed to air TiN (from (27)).

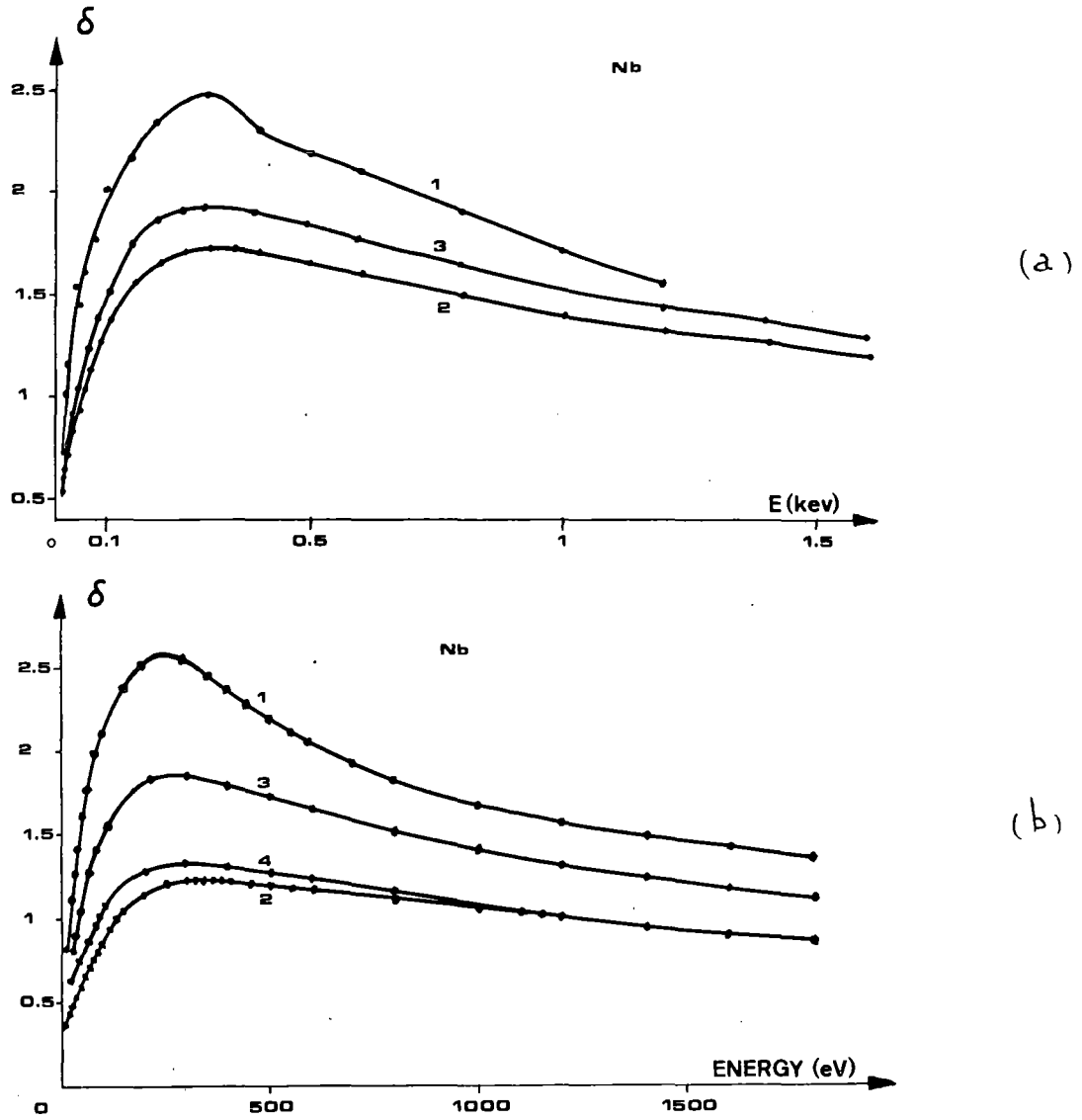


Fig. 9 - SE from Nb. (a) 1, unbaked; 2, baked; 3, baked+exposure to air. (b) 1, unbaked; 2, baked+gas discharge; 3, baked+g.d.+exp. to air; 4, 3+g.d. (from (29)).

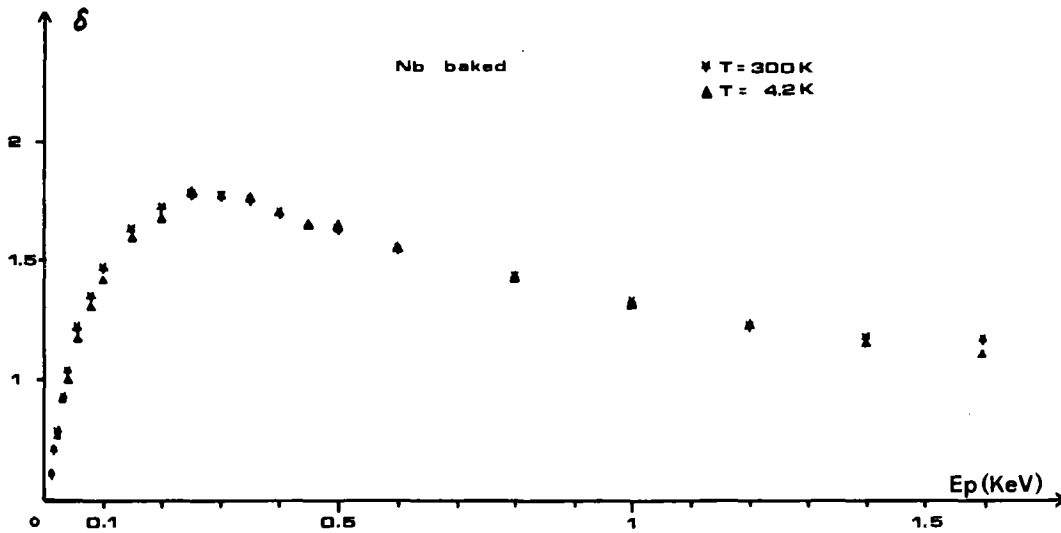


Fig. 10 - SE from a baked Nb surface. \ast , before cooling, Δ , after cooling to 4.2 K. (from (29)).

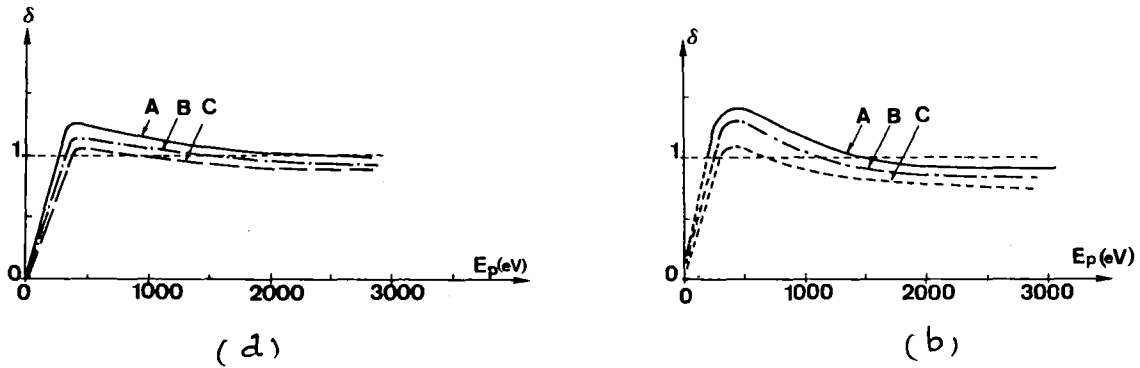


Fig. 11 - SE from Nb and Nb₂O₅. Influence of the electron bombardment ($E_p = 1000$ eV; $j_p = 10 \mu\text{A}/\text{mm}^2$). A, $t = 0$; B, $t = 5$ min; C, $t = 15$ min. (a) Nb; (b) Nb + 400 Å Nb₂O₅ (from (23))

$p = 5 \cdot 10^{-10}$ Torr

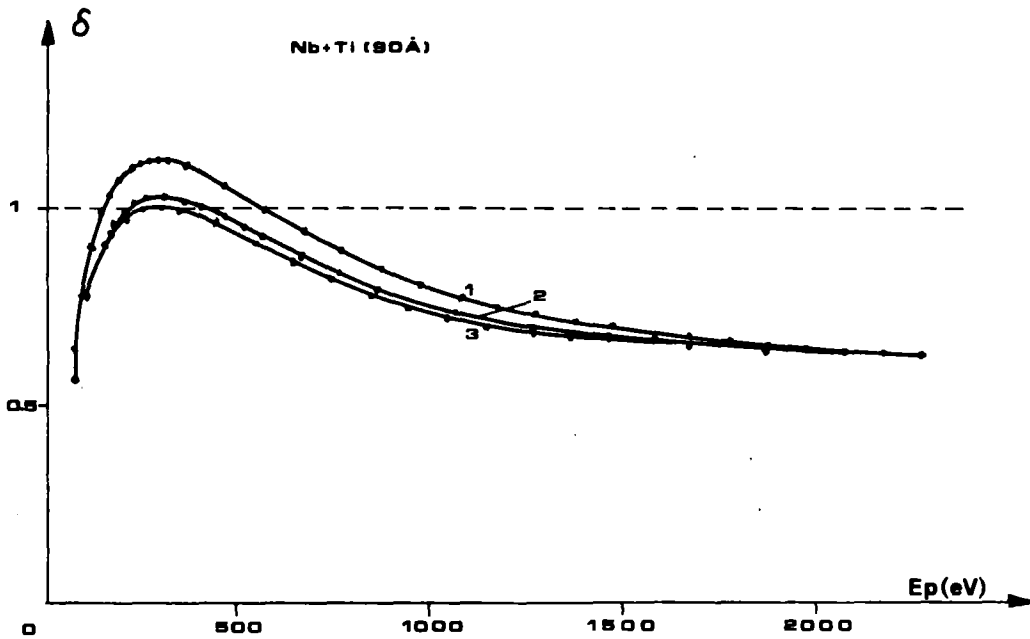


Fig. 12 - Influence of the electron bombardment on SE from thin Ti film on Nb, after baking. 1, $t = 0$; 2, $t = 1$ hour; 3, $t = 15$ hours (from (31))

$p = 3 \cdot 10^{-10}$ Torr

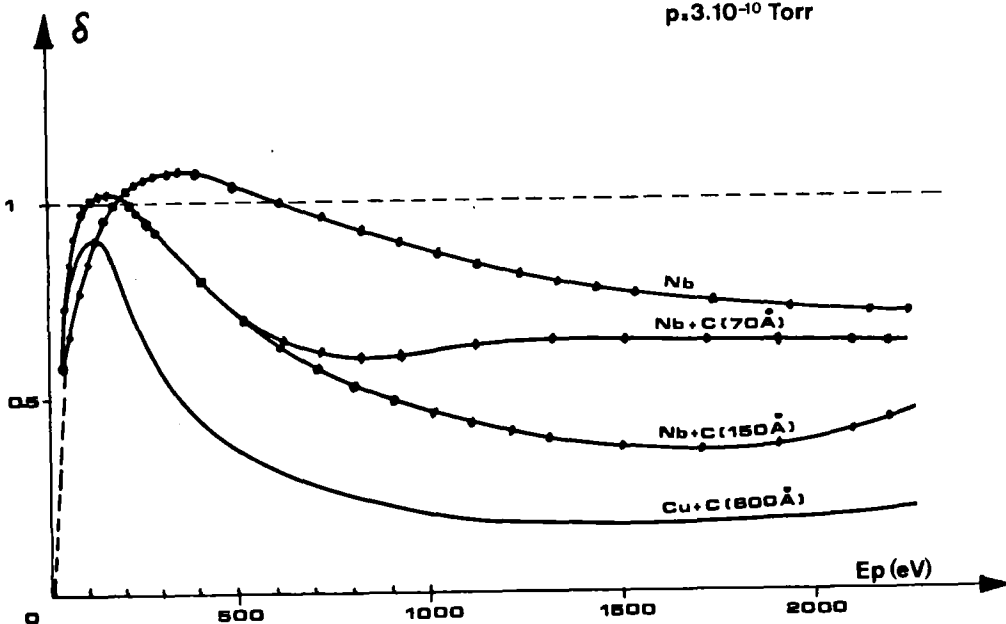


Fig. 13 - SE from thin C films, after baking and bombardment during about 1 hour. (from (31)).

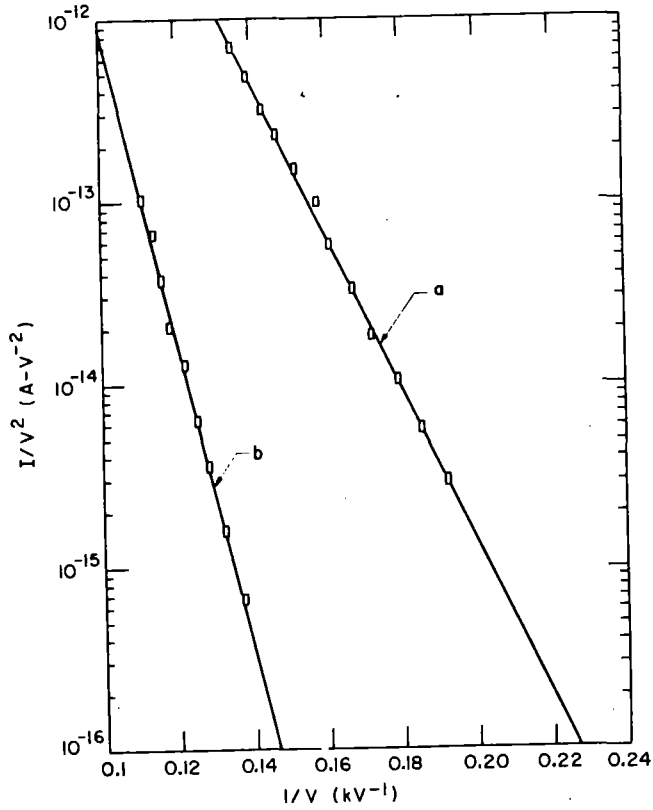


Fig. 14 - Fowler-Nordheim plots of d.c. field emission data.
 (a) adsorbed atoms present on the emitting point surface.
 (b) emission after cleaning of the tip by reverse field desorption. (from (33))

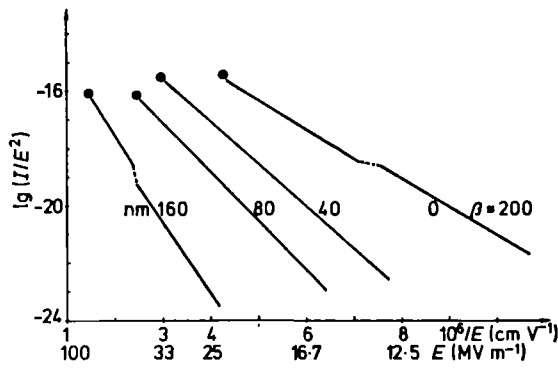


Fig. 15 - F.N. plots of current emitted by plane Nb electrodes covered with various oxide layer thickness (from (35)).

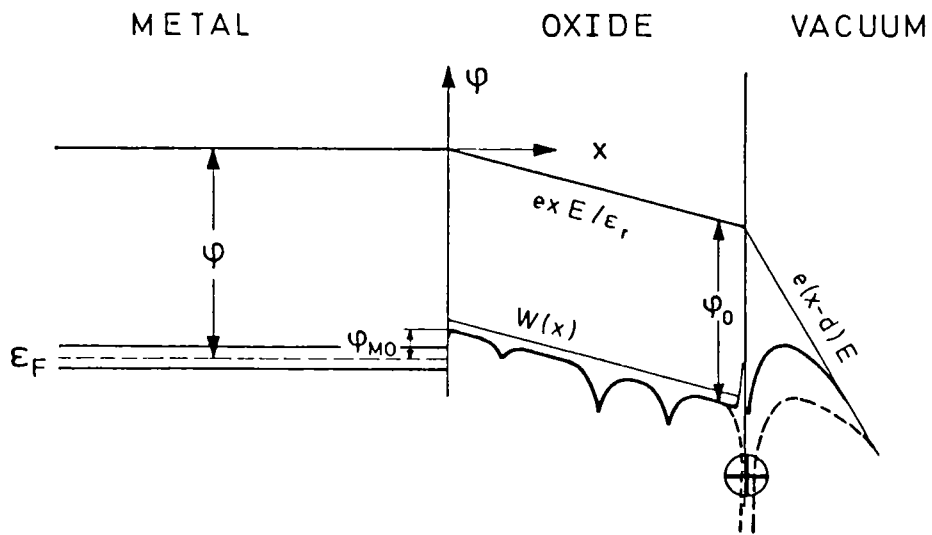


Fig. 16 - Electrochemical potential ϕ for electrons in an oxide coated ($\epsilon_r > 1$) metal subject to the electric field E . The total emission current depends on the field emission into the oxide, the field assisted - hopping conduction through the oxide, and the field emission into vacuum, where the electrons tunnel through the indicated potential barriers (from (34)).

DIAGNOSTIC METHODS OF SUPERCONDUCTING CAVITIES AND IDENTIFICATION
OF PHENOMENA

H. Piel

University of Wuppertal
Federal Republic of Germany

1. INTRODUCTION

During the 1970s a great number of diagnostic techniques applicable to superconducting rf cavities have been developed and refined in several laboratories. A variety of methods has been used to gain more insight into energy loss mechanisms additional to those which are always present when an rf field interacts with a superconducting surface. In order to review different diagnostic techniques it is useful to sketch a picture of the "inner life" of a cavity operated at high fields. Numerous experiments and theoretical analysis performed in the past have lead to the following ideas of the main energy loss processes [for a recent review see refs. 1,2]. Practically every superconducting cavity contains on its rf surface very small regions which are either normal conducting or become normal conducting at fields well below the bulk critical field of the superconductor. These weak spots can be present from the very beginning or they can be produced by impacting high intensity and high energy electrons during the operation of the cavity [3,4]. During the increase of the rf field these spots will produce an increasing heat flux which finally leads to a temperature increase of its surrounding above T_c [5] or to the onset of film boiling on the cavities outside [4].

Both phenomena will give rise to a breakdown of the rf field (quenching). Multipacting, especially onside multipacting has been identified as one of the most annoying field limiting effects in superconducting cavities [6]. This effect manifests itself by changes in the rf signal emitted by the cavity and by small areas of increased temperature on the cavity wall. Light emitting microparticles on the cavity surface have been observed in many instances [7,8]. They can emit electrons which heat up the cavity wall. The observation of rf field emitted electrons and their production of Bremsstrahlung when hitting the cavity wall has been with us since the first tests of low frequency (< 3 GHz) cavities.

In my talk I want to review the diagnostic techniques which have been developed to identify and understand these phenomena and I also will try to correlate specific experimental observation with the particular energy loss process. I will however, restrict myself to those measurements which are performed on cavities under operating conditions at low temperatures.

In all experiments the rf signal emitted by the cavity, its amplitude and frequency as a function of the field level, bath temperature and time can be analysed. The second class of diagnostic techniques uses the intensity and the energy of the X-rays emitted from the cavity at high field levels. To this group of techniques I also want to add the observation of light emitted from the cavity interior and the measurement of free electron currents inside the resonator. The third and very important diagnostic method is the measurement of the temperature of the cavity wall. The importance of this method is evident from the fact that almost each energy loss mechanism will lead to an increase of the heat flux from the cavity to the surrounding helium bath. My talk will therefore be divided into three paragraphs.

2. THE "TELL TALE FEATURES OF THE RF-SIGNAL"

A test of a s.c. cavity is performed by applying a pulsed rf-signal ($U_i(t)$) to the cavity and observing the reflected signal ($U_r(t)$) and the signal transmitted by the cavity ($U_t(t)$). Frequency and amplitude of this signal contain the basic informations about the cavities response to the external rf-signal. Fig. 1 shows a schematic experimental set-up to analyse these signals.

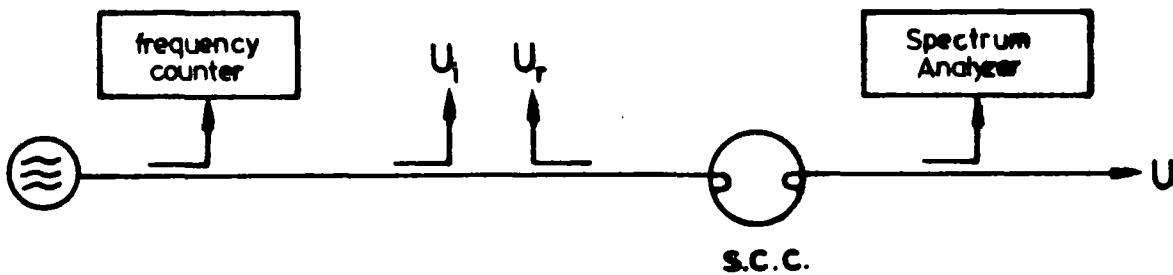


Fig. 1:

Fig. 2 shows $U_i(t)$, $U_r(t)$ and $U_t(t)$ from an ideal s.c. cavity - generally measured at low field levels.

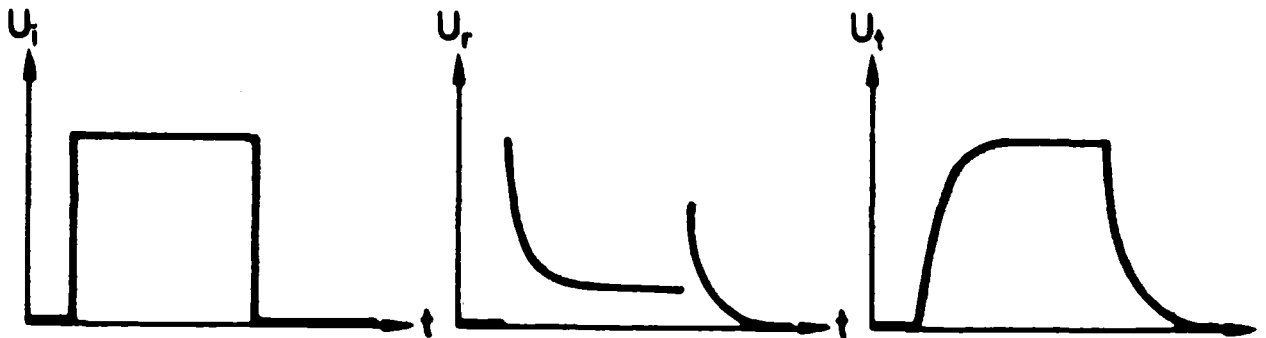


Fig. 2: $U_i(t)$, $U_r(t)$ from an ideal cavity

The amplitude and the decay times of these signals are used to determine the loaded Q of the cavity (Q_L) the coupling factor (β) to the rf driving network and the field level excited in the cavity i.e. the peak electric field E_p , the peak magnetic field H_p or the effective accelerating field E_a . The unloaded cavity Q (Q_0) as a function of E_p measured at different bath temperatures gives an integral measurement of loss mechanisms and their field dependence. As I want to concentrate on diagnostic techniques I will not discuss the different ways of analysing $Q_0(E)$ data. The observation of the time dependence of U_t at different field levels will give additional informations and I will try to compile a catalogue of signals and their correspondence to specific energy loss phenomena.

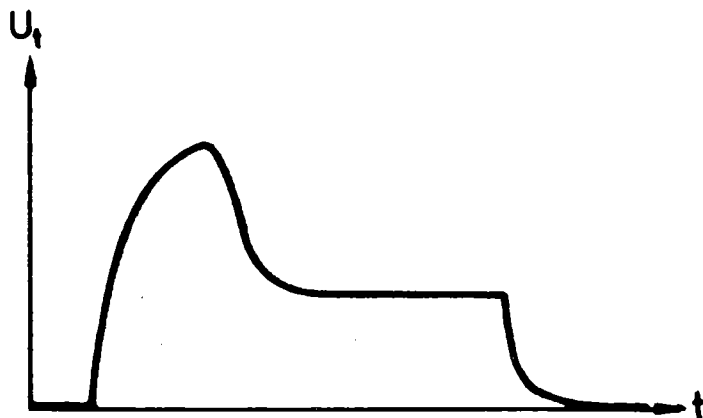


Fig. 3:

$U_t(t)$ from a cavity with high residual losses.

Fig. 3 shows U_t from a cavity with a rf surface [see e.g. ref.9] of high residual resistance ($R_{res} > 1 \mu\Omega$ typically). Already during the build up time of the field the temperature of the surface increases, Q deteriorates, β reduces and the cavity stabilizes at a low field level. Another well known loss mechanism which can show up already at low field levels is electron multipacting.

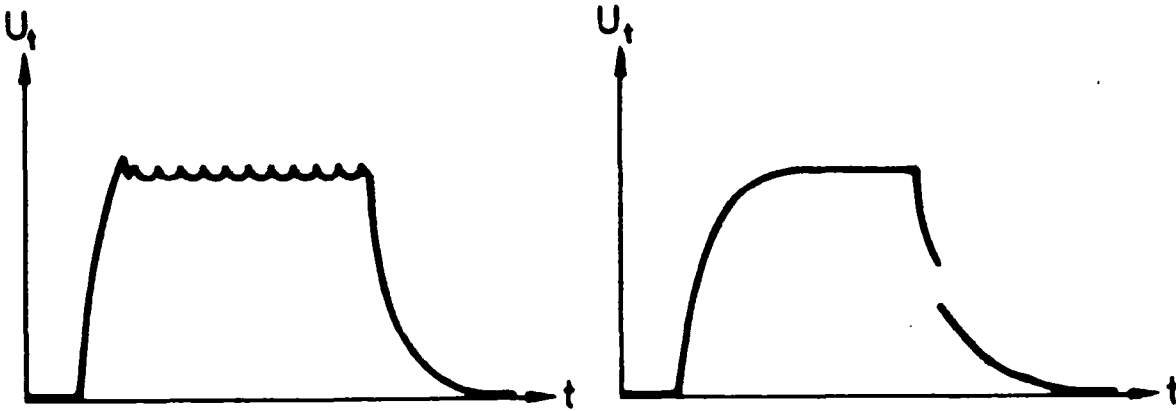


Fig. 4a:

Fig. 4b:

Typical rf signals from a "multipacting cavity"

Fig. 4 shows characteristic U_t signals at multipacting barriers [10,11]. Multipacting will appear at very definite field levels (very high order multipacting can result in softer limitations). As the field rises one will fall (sometimes after a slight overshoot) into a multipacting threshold like shown in fig. 4a. A further increase of the rf power will not increase the field. At this level often processing is done to surmount the barrier by electron bombarding the small surface area responsible and thereby reducing the secondary emission δ coefficient below 1 [12]. By applying high power signals to the cavity a soft multipacting barrier (δ close to 1) can be overcome due to the lack of time needed for its build up. Then frequently a signal like in fig. 4b is observed. The excessive energy loss by multipacting indicates itself during the slow decay of the rf field and very low Q jumps are observed in the decay slope. To identify multipacting the observation of the frequency of U_t is valuable. Frequency changes of as much as 10 kHz have been observed in GHz-cavities [11]. The multipacting electrons can also give rise to the excitation of higher order modes in the cavities frequency spectrum [13].

If one succeeds to circumvent multipacting by an appropriate cavity geometry [14,15,16] or by electron processing one may come to higher electric fields where field emission becomes the next obstacle. Field emission loading is particularly observed in low frequency (large volume!) cavities and the U_t signal looks like in fig. 5.

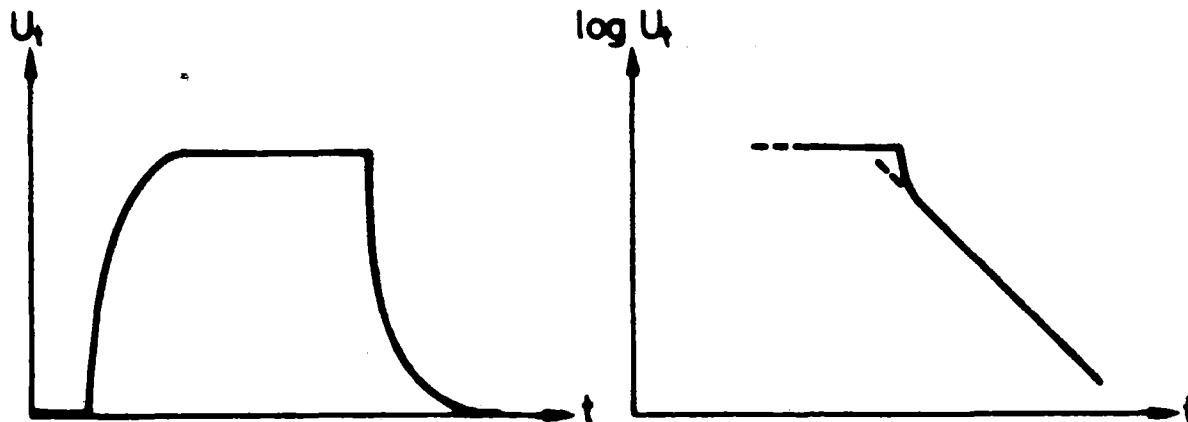


Fig. 5a

Fig 5b

$U_t(t)$ and $\log U_t(t)$ from a cavity with field emission loading

The presence of field emitted electrons can be seen from U_t by the non-exponential decay. The use of a logarithmic amplifier makes this observation more evident. It is important to use such an amplifier to analyse \dot{U}_t because a non-exponential decay can be overseen quite easily and may lead to significant errors in the determination of the achieved Q- and field levels.

In the presence of strong electron currents in the cavity either caused by multipacting or by field emission higher eigenfrequencies of the cavity, the so called higher order modes, can be excited. $U_t(t)$ then shows a time dependence like in fig. 6.

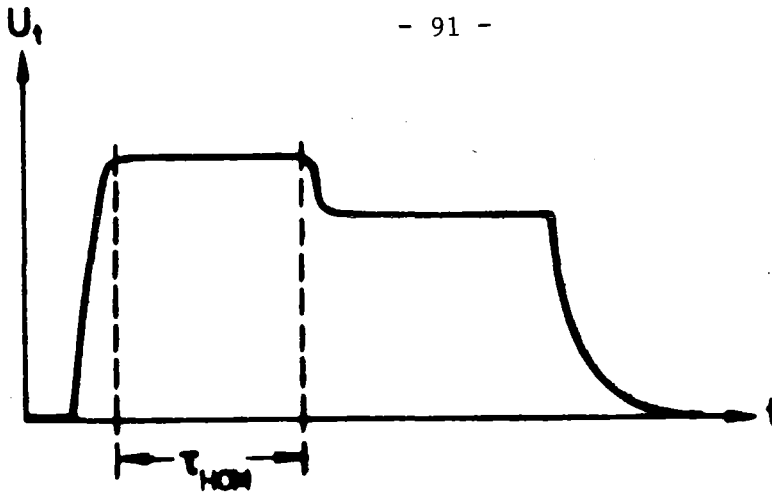


Fig. 6: Higher order mode excitation

Some time after the excitation of the fundamental mode a higher cavity mode is excited by the free electrons which act as coupling currents. This delay time τ_{HOM} is generally one or two orders of magnitude longer than the unloaded decay time of the fundamental mode and decreases with increasing internal currents. This HOM excitation has been observed at Stanford [13] and at CERN [4]. Most higher order modes don't couple as well to the rf probe as the fundamental mode. Therefore, once the higher mode is excited U_t decreases. If HOM's of high frequencies are excited this picture however can change and U_t may show an increase after τ_{HOM} . If there is a suspicion of HOM excitation a spectrum analyser is a very useful tool and U_t should only be used as a first indication.

In practice all superconducting cavities, also those which are apparently free of electron loading phenomena ($f > 10$ GHz), will have some surface imperfections which are often classified as weak spots and which are assumed to be of microscopic size [5]. Such weak spots may be normal conducting or superconducting but with a low critical field and (or) a low critical temperature compared to the parameters of the bulk material. Superconducting weak spots have been observed in recent CERN experiments and can show up in the U_t signal at the field level

of their phase transition. At this field a new loss mechanism is switched on and a sudden change in the cavity Q results which leads to a U_t -signal like shown in fig. 7.

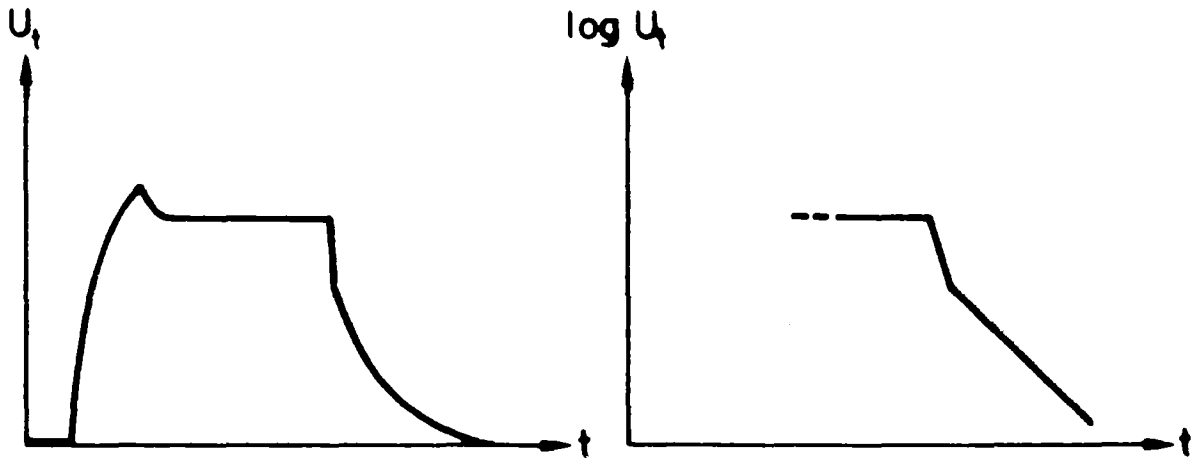


Fig. 7a

Fig. 7b

Phase transition of a weak spot

This signal can be mistaken for a multipacting signal (fig. 4a) however, one can increase U_t easily by applying more rf-power to the cavity. If one then observes the decay of U_t with a logarithmic amplifier, one will observe a kink in the decay slope, corresponding to two Q -values. We know that weak spots of this nature can be attributed to a surface damage caused by impacting high energy and high intensity field emitted electrons.

If not limited by electron loading the cavity field will be finally limited by a quenching phenomena induced by the described weak spots. The high heat flux density produced by these areas will either drive their environment on the rf surface normal and lead to an unstable state or the film boiling limit on the outside of the cavity wall will be exceeded. Both phenomena will lead to a sudden dissipation of the energy stored in the cavity at a fixed field level - the "quench field". This limitation often described as "magneto thermal" breakdown will lead to a U_t signal

like shown in fig. 8.

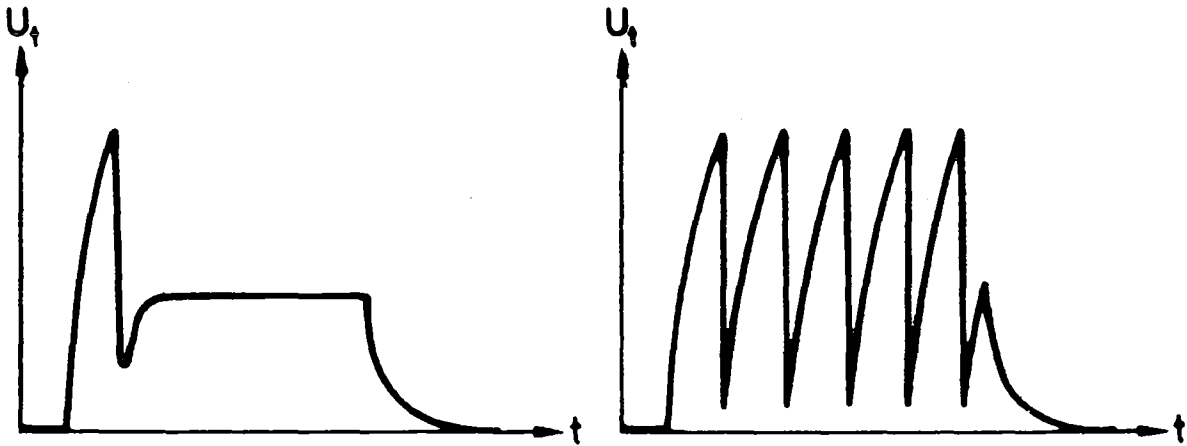


Fig. 8a

Rf-breakdown - quenching

Fig. 8b

If a single quench like in fig. 8a or a self-pulsing quench like in fig. 8b will result depends on the cooling conditions, the coupling factor β and the cavities Q . The quench time τ_q is in general one or two orders of magnitude below the characteristic decay time τ of the undisturbed cavity. In cavities with poor vacuum an rf breakdown by gas discharge is possible. U_t will then be very similar to fig. 8b, however, in general at much lower field levels.

Impacting electrons from field emission or multipacting or a changed surface heating by an excited higher order mode can also lead to an excessive heat flux into a small surface area. Therefore, the U_t signals of fig. 8 can show up combined with those of fig. 4,5 or 6.

In conclusion of this chapter one can say that all known Q and field limiting phenomena can be observed by a careful analysis of the rf signal emitted by the cavity. To do this the "diode signal" should not only be observed directly but also via a logarithmic amplifier. Aside of the frequency counter, generally used in a cavity experiment, a spectrum analyser can reveal valuable informations about higher order mode excitations.

3. DETECTION OF X-RAYS, ELECTRONS AND LIGHT

The observation of the cavities rf signal is an excellent diagnostic tool in order to see if one is in trouble. It will also tell what kind of limiting mechanism is present. A more detailed analysis of the problems cause however needs additional experimental information. Right from the beginning of the work with low frequency (large volume) cavities X-radiation was detected. X-ray intensities are monitored using essentially four different instrumentations: Ionisation chambers, NaJ-crystal detectors - with [17] and without collimation, pin hole X-ray cameras [18] and scanning surface barrier detectors close to the cavity wall [4]. The first three detectors are used outside the cavity cryostat and the latter inside the helium bath. Ionisation chambers and NaJ detectors are used to measure the intensity of the Röntgen radiation and their dependence on the peak electric surface field. The X-ray intensity increases exponentially with increasing field and is analysed using the Fowler-Nordheim relation [19]. The methods involved will be discussed in the report of C. Lyneis. With NaJ detectors not only intensity but also the energy of the emitted X-rays can be measured. The determination of the maximum energy of the observed Bremsstrahlenspectrum gives information about the internal electron trajectories. The measurement of the spatial distribution of the X-radiation also is used for this purpose. The measurements may be used to determine location and distribution of electron emitting sources if used in combination with trajectory calculations. Recently at Karlsruhe an experiment was performed with a 700 MHz TM-like cavity, where X-ray spectra have been taken together with the X-ray intensity distribution along the cavity wall [17]. A NaJ-detector together with a collimator was used and the experimental set-up is shown in fig. 9. Figs. 10 shows some typical results of the measured spatial and energy distribution. The emission of high

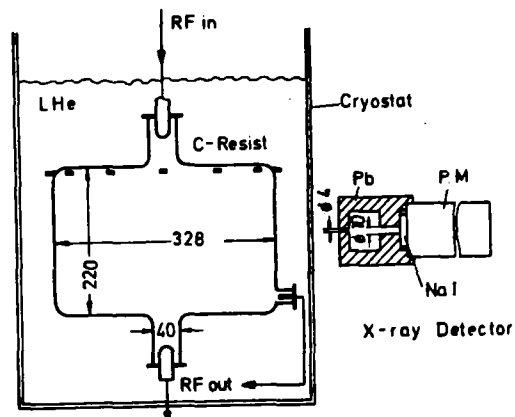


Fig. 9: Sketch of the experimental set-up of the Karlsruhe 700 MHz cavity [17]

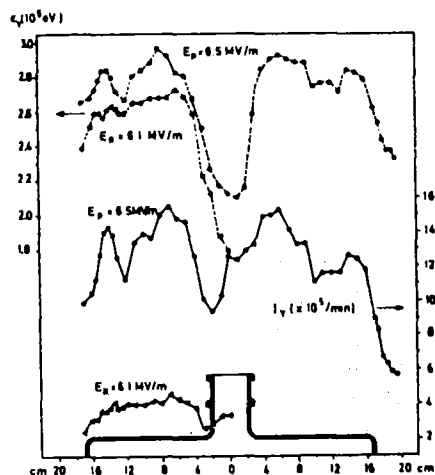


Fig. 10: X-ray distribution in intensity I_γ and energy ϵ_γ at the endplate of the Karlsruhe 700 MHz cavity at a field level $E_p = 6.1$ and 6.5 MV/m [17]

energy X-rays is concentrated on the top and bottom plate of the cavity. Those data point to field emitted electrons and the importance of secondary processes which smear out the effect of several point like sources expected to be responsible for electron field emission. An information of the same nature has been obtained already in 1973 by X-ray photography of a L-band cavity operated at high fields at Stanford, where a pin hole camera together with an image amplifier was used [18]. The experimental set-up used is given in fig. 11 and one of the beautiful pictures is shown in fig. 12.

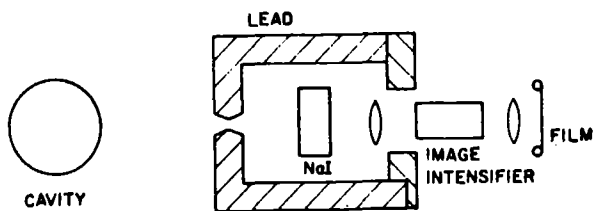


Fig. 11: Components of the Stanford X-ray camera

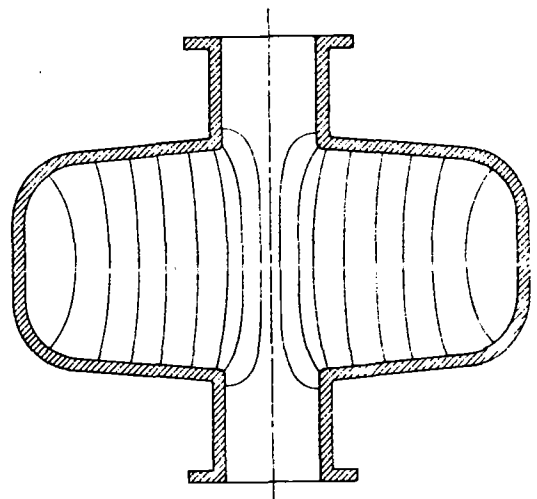
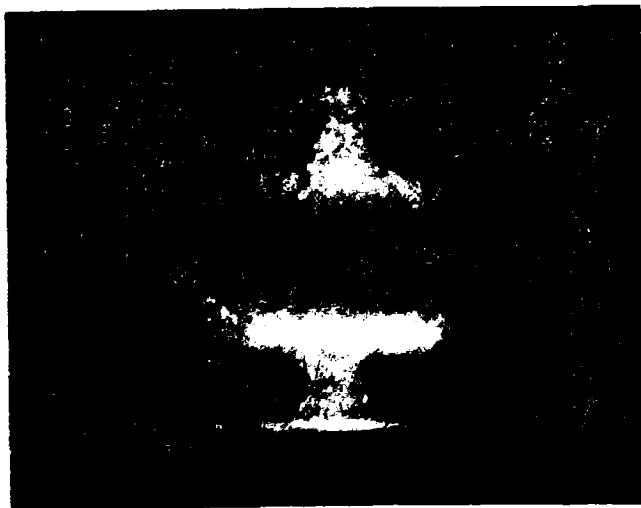


Fig. 12: X-ray-photography and crosssectional view of the Stanford L-band cavity

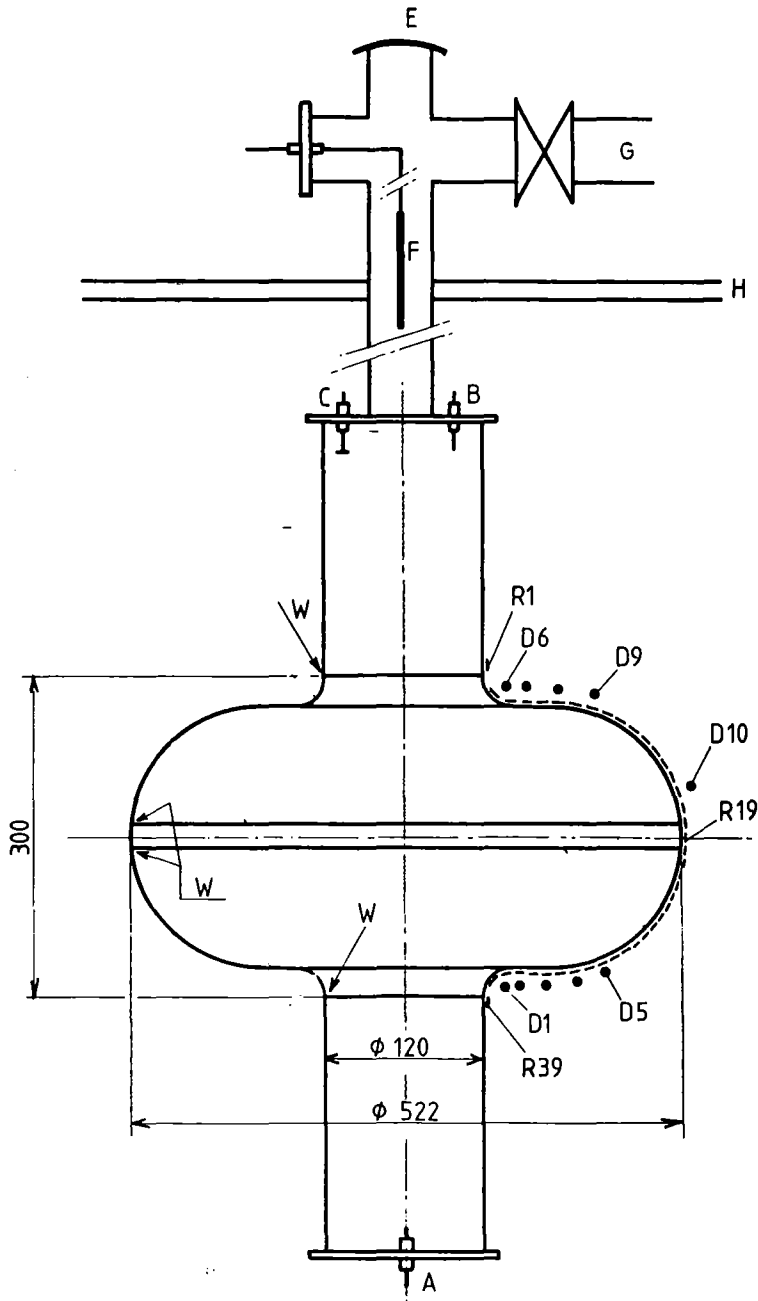


Fig. 13: Sketch of the CERN 500 MHz cavity [4]
A,B,C = rf probes; E = viewing part;
F = retractable electrode for glow discharge
cleaning; R1-R39 = scanning carbon thermometers;
D1-D10 scanning X-ray detectors; W = weld

A simple minded picture of field emission would start from a single (or a few) field emitting sources. The electrons from this source would move in one place and hitting the cavity wall would produce a line like X-ray source. One would therefore expect a strong azimuthal peaking of the X-radiation. This is not observed with both described techniques and one has to conclude that secondary multiplication processes play an important role. This is confirmed by the observed X-ray energies which only can be explained by a twostep process [18]. Some light on this problem is also shed by an experiment done a few weeks ago at CERN which uses ten scanning X-ray detectors on a 500 MHz single cell cavity like shown in fig. 13. The solid state silicon detectors used (RT 1 Radiation Transducer, Quantrad Corporation, 2261 South Carmelina Avenue, Los Angeles) have a sensitive surface of 6 mm diameter and a sensitive thickness of 100μ . They are used in a charge sensitive mode as "solid state ionisation chambers". Fig. 14 shows plots of X-ray intensities measured with these detectors in different locations as a function of the azimuthal angle. X-ray emission peaked along one meridian of the cavity is clearly observed. At the bottom part of the cavity the X-ray sources are distributed along a very narrow line on top of broad almost uniform distribution. At the equator the intensity is low and uniform in distribution. At the top part of the cavity a very broad distribution is observed. This X-ray distribution has yet to be analysed by trajectory calculation including multiplication processes like in ref. 18. It appears to be likely however that the narrow part of the distribution is caused by the impact of primary electrons field emitted by a point source, whereas the broad distribution at the top of the cavity may be explained by secondary electrons which can gain higher energies in the

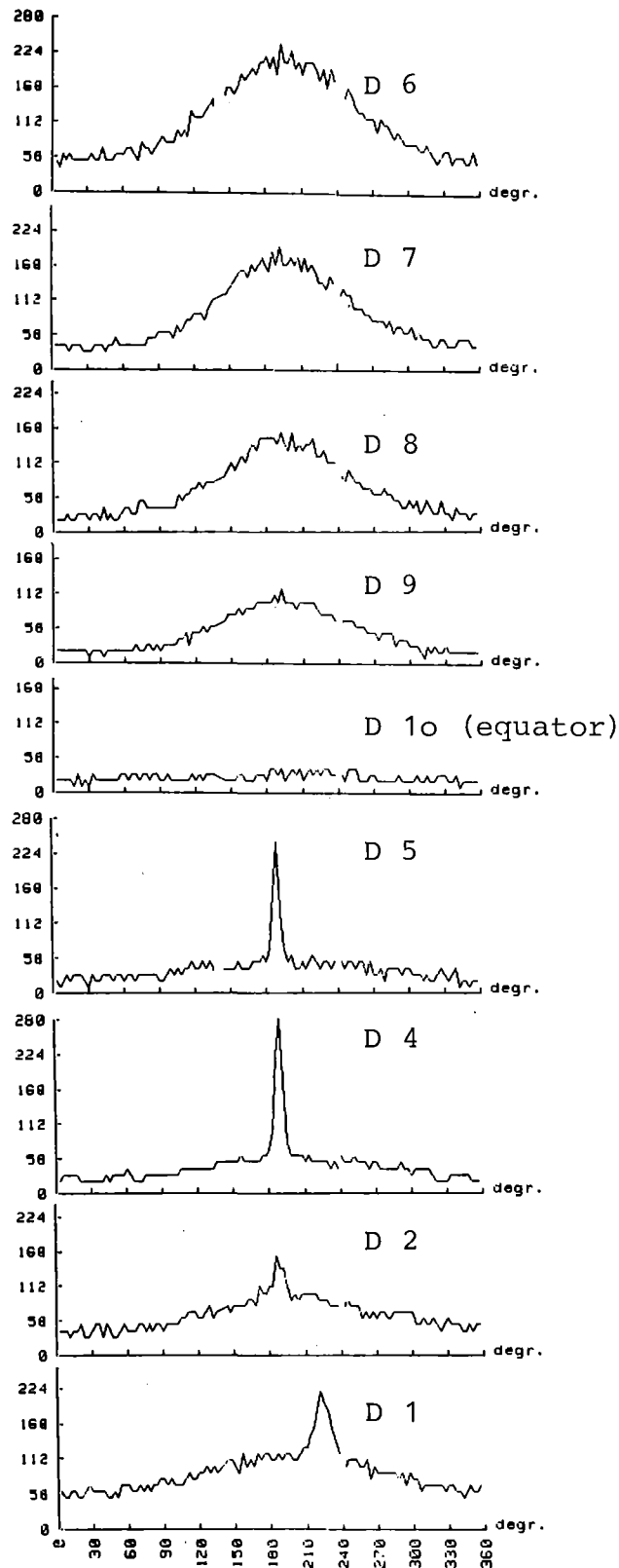


Fig. 14: Spatial distribution of X-ray intensity measured with the CERN 500 MHz cavity at $E_a = 3.4$ MV/m
Vertical axis: X-ray intensity in relative units
Horizontal axis: azimuthal position in degrees.

cavity field than the primary ones. The integrated X-ray intensity from the upper part of the cavity is considerably higher than the one from the peak dominated lower part. According to first trajectory calculations [20] the photon energy in the peak region is considerably lower than the one of the X-rays coming from the top of the cavity. The shielding by the cryostat may therefore eliminate the sharp spikes in the X-ray distribution. Taking this into account and also assuming several field emitting sources at high fields, the Karlsruhe and Stanford X-ray intensity distributions do not contradict the ones of CERN.

In high frequency cavities or in cavities where the mean free path of an electron is too short, X-ray emission cannot be expected even under the presence of strong field emitting sources. In such cases internal electron probes, like shown in fig. 9 are very useful diagnostic tools (see also ref. 7). They will indicate the relative strength of the internal electron currents by picking up low energy secondary electrons. Bias voltages will depend on the special geometry of the probe and the cavity and range between +50 V and + 100 V [17,21]. Also one is at present not able to determine the collection efficiency of such a probe it is observed that the measured electron currents follow quite accurately a Fowler-Nordheim relation and result in very similar local field enhancement factors compared to those from X-ray intensity measurements which in low frequency cavities are done simultaneously [see e.g. ref. 17]. In most experiments the rf couplers are used simultaneously as electron probes.

Glowing micro particles (dust) have been seen in some instances [7,8] and have been considered to be

responsible for glow emission of electrons. It is therefore useful to have an optical window to inspect at least parts of the cavities' surface during high field operation. Mounting of a cavity in a "dust-free" environment can eliminate such glow emitters [8]. Also processing at high field levels can destroy these sources [7]. The current emitted glow emission unfortunately follows an exponential relation quite similar to the Fowler-Nordheim law and one may have to consider rf field emission from a hot microscopic particle [28]. Optical inspection can help to distinguish field and glow emission. Optical devices to view a large portion of the cavities' rf-surface during high field operation are therefore in preparation [22].

4. TEMPERATURE MEASUREMENTS

As each energy loss mechanism will finally lead to an increase of the temperature of the cavity wall, temperature measurements are of prime importance to identify causes for field and Q-limitations. C. Lyneis at Stanford was in 1972 the first to use a chain of rotating carbon resistors mounted in a few millimeter distance from a cavity wall to detect the location of a quench area [23]. Fig. 15 shows the first published oscilloscope trace of a heat puls detected by a carbon resistor close to quench area.

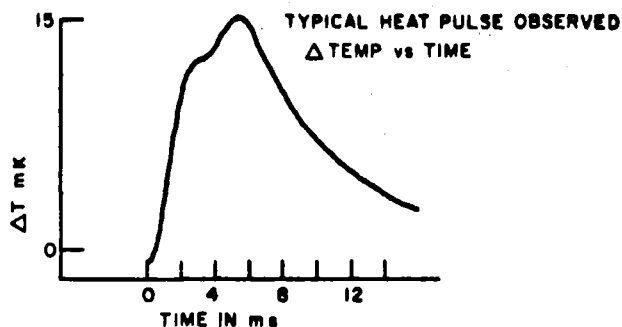


Fig. 15: "Typical heat pulse observed by a carbon resistor located a few millimeters from point of thermal magnetic breakdown"[5].

This method has been used thereafter by many groups working in this field (see e.g. ref. 24). The carbon thermometers used are 56 or 100 Ω (1/8 W or 1/4 W) Allen Bradley resistors, the bakelite insulation of which is often grinded off to increase their sensitivity. Different electronic schemes have been used to readout the resistance value of the many thermometers generally used on one cavity [24,25] either using an oscilloscope display or an automatic data acquisition system. During a quench all the energy stored in a cavity is set free and a substantial heatflux develops which leads to film boiling and a marked increase of the temperature of the helium film close to the quench area. This can be detected easily even in superfluid helium and also if the resistor is not in contact to the cavity wall.

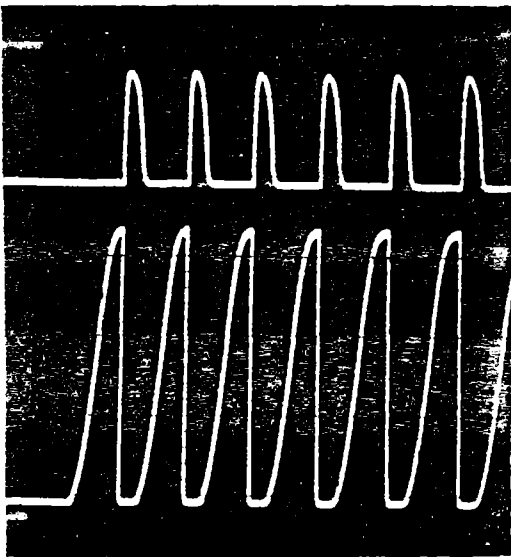


Fig. 16: Heat pulses (upper trace) associated with a self pulsing breakdown (lower trace) observed in the CERN 500 MHz cavity [4] for $T < T_{\lambda}$.

Fig. 16 shows heat pulses associated with a self pulsing breakdown. The time duration of these heat pulses is typical in the millisecond region and their amplitude varies between 15 mK and 1.4 K depending on the helium bath

condition, the energy stored in the cavity and the distance of the resistor from the breakdown location. Using this technique quenches induced by multipacting electrons, which can change their location from rf puls to rf puls, have been discriminated from breakdown triggered by permanent surface damages and thereby preferred areas for electron multipacting have been identified [33]. Several experiments [e.g. 4,23] have shown a preference for quench areas in the bottom part of a cavity. This part of the cavity in general is not cooled as well, it is also the part which collects "falling dust" it will be cooled first and therefore residual gas in the cavity will be condensed first in this region. Whatever else may be the reason for the quenching preference is not yet clear.

Quenches especially in multicell structures deposit so much energy into the helium bath that second-sound waves can be detected. At Stanford several resistor rings are placed around the accelerating structure to pick up second-sound in order to localize the specific cell in which the breakdown occurs [13]. In Argonne second-sound waves from quenches in a split ring resonator are detected by single crystal germanium resistance thermometers [26]. The oscilloscope trace of fig.17 shows a second-sound signal initiated by a breakdown in a split ring resonator [27]. Using an array of typical 15 germanium thermometers one can reconstruct the location of the surface damage within 1 or 2 cm (speed of second-sound at $T < 2.1$ K: ≈ 20 m/s).

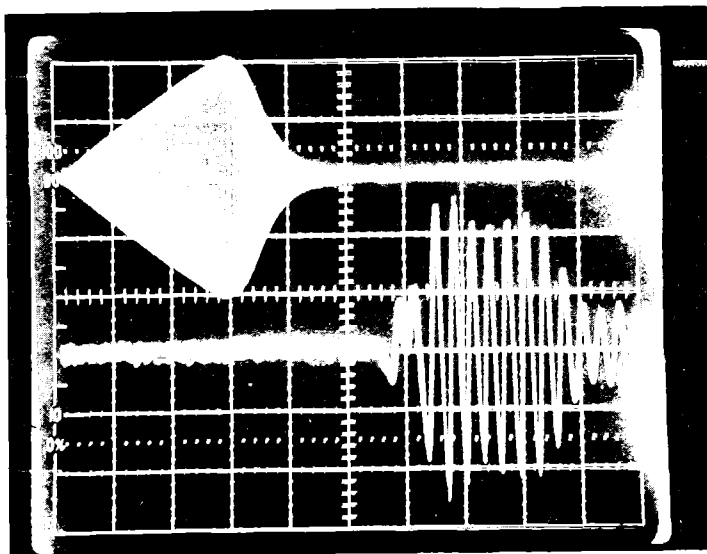


Fig. 17: " Oscilloscope display of the second-sound pulse associated with thermal breakdown of a resonator. The upper trace displays the rf field in the resonator, which is driven to $E_a = 3$ mV/m at which point the resonator becomes thermally unstable and the field collapses. The lower trace displays the temperature of a sensor which shows a second-sound pulse arriving 13 msec after breakdown." [27]

At this point although not connected to thermometry another method to localize a "bad cell" in a multicell structure shall be mentioned. In the Karlsruhe - CERN - Separator [28] a poor cell was localized by measuring the resonators' Q as a function of the mode excitation. The knowledge of the field distribution of all resonator modes is necessary for the application of this diagnostic technique. In the separator tests also carbon thermometers were used to detect bubbles rising from the quench area. (With a speed of approximately 16 cm/s). Quench areas can be detected by their "bubble production" also by visual inspection, therefore, a cryostat window and an internal illumination can be quite useful[28]. The detection of quench areas is certainly a most useful diagnostic procedure. A temperature map of the surface of a cavity well below the

breakdown field however, will reveal even more information about the nature of high loss areas. Experiments on S-band muffin tin structures done at Cornell [24] and measurements of surface temperatures with germanium thermometers in Argonne [26] point into that direction. Temperature mapping can only be done for bath temperatures above the λ temperature. The main obstacle for a temperature mapping experiment is the fact that only the temperature of the outside of the cavity wall can be measured which is very effectively cooled by the surrounding liquid helium. In a recent experiment at CERN [25] it was shown that temperature mapping can be carried out quite well in a subcooled helium bath (favourable subcooled condition: bath temperature slightly above T_λ and bath pressure ≈ 1000 mb). In a subcooled bath bubbles are absent and therefore the micro convection produced by bubbles rising from the heated surface is switched off. This reduces the cooling capability of liquid helium substantially and increases the heat transfer resistance between the niobium surface and the helium. Also the carbon thermometer which has to be in thermal contact to the cavity (fig. 18) is decoupled stronger from the cooling liquid. In a test experiment a weak spot on a 2 mm thick niobium wall was simulated by a heating resistor (fig. 19).

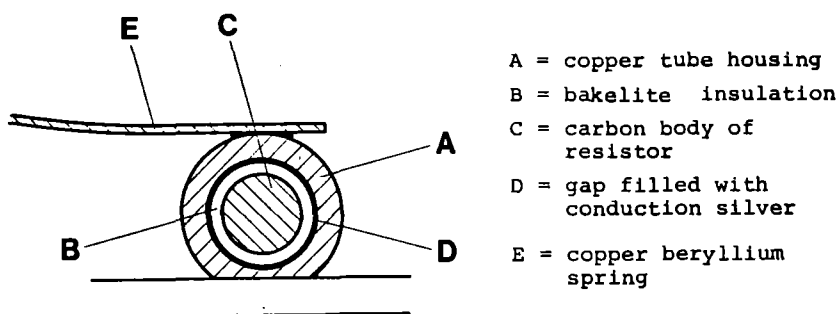
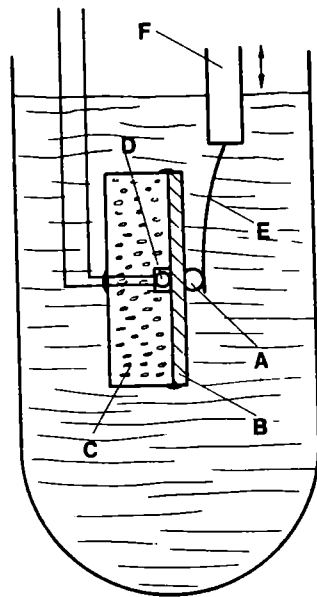


Fig. 18: Cross section through the carbon thermometer

Fig. 19:

Set-up for testing a carbon thermometer



- A = carbon thermometer
- B = niobium sheet metal
- C = styrofoam insulation
- D = heating resistor
- E = copper beryllium spring
- F = movable rod

In fig. 20 the temperature distribution around this "simulated weak spot" is shown. It can be localized within ± 3 mm. The temperature increase ΔT on the outside wall was also measured as a function of the power P_H applied to the heating resistor. The resulting data are shown in fig. 21. The observable heatflux and the corresponding temperature increases range over almost four decades. The set-up used for the temperature mapping of a 500 MHz spherical cavity is shown schematically in fig. 13 and in the photographs of fig. 22.

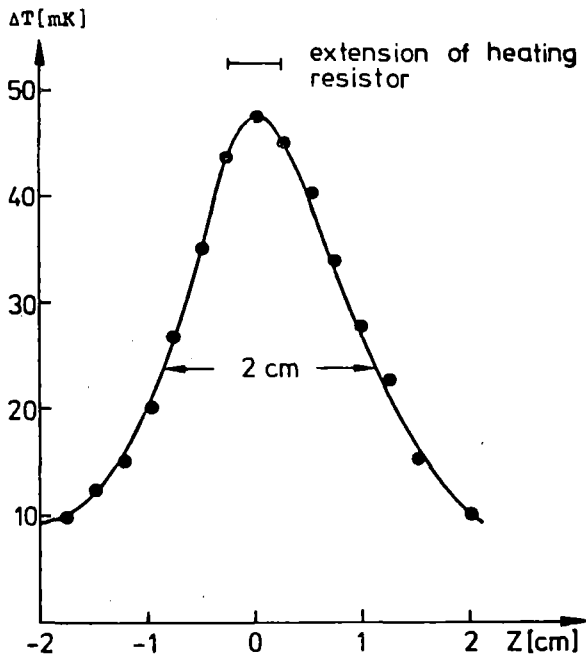


Fig. 20:

Temperature distribution around the location of the heating resistor placed at $z=0$

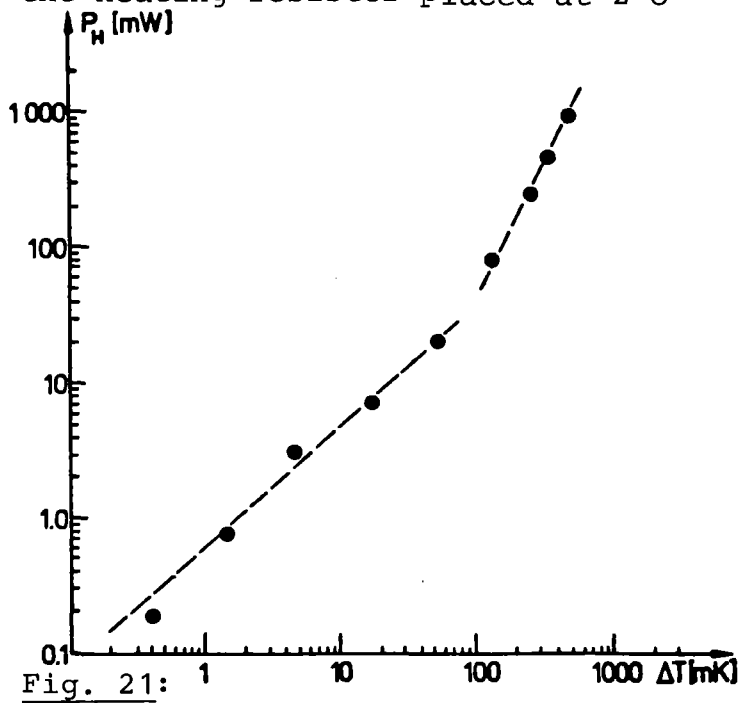


Fig. 21:

Temperature increase ΔT of the niobium wall (fig.19) and related heating power P_H of the resistor.

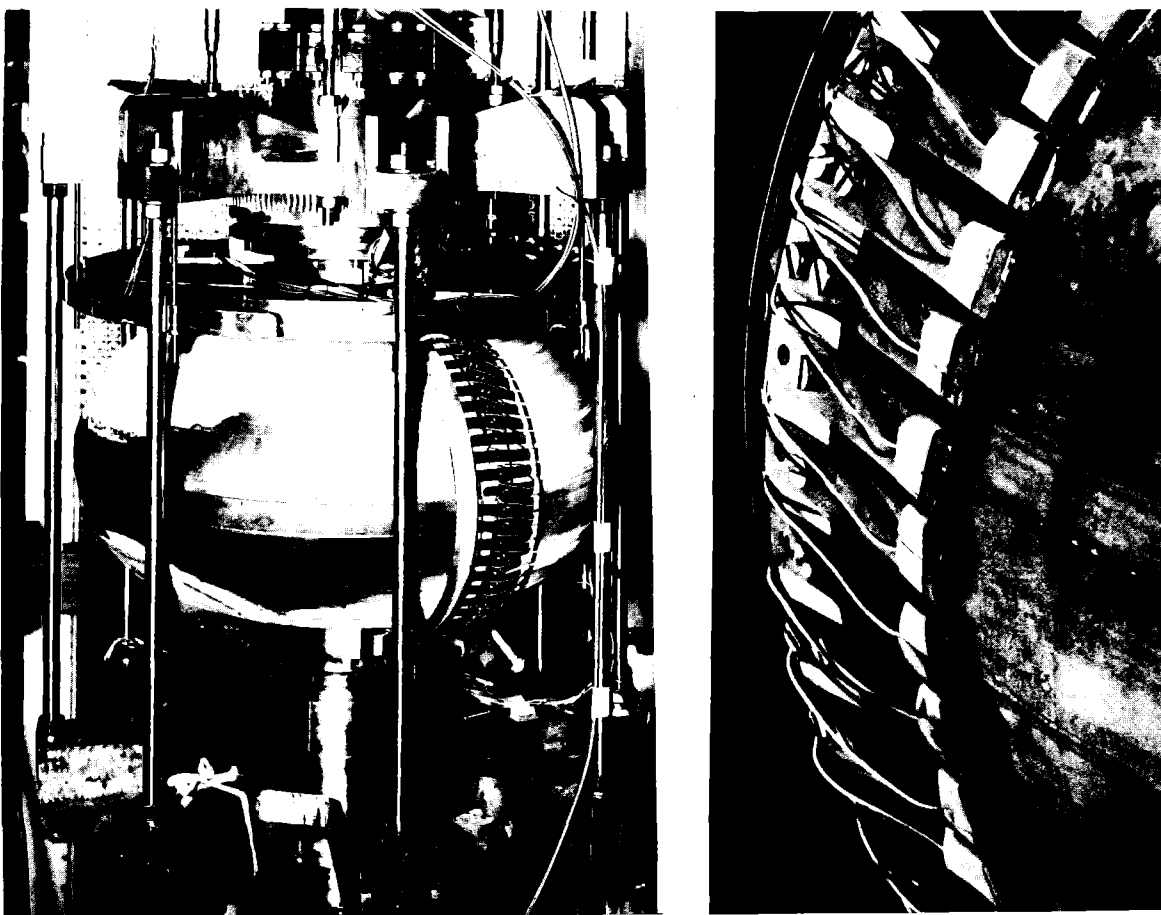


Fig. 22: General configuration and close up view of the carbon thermometer scanning system.

39 carbon thermometers (100Ω , $1/4$ W Allen Bradley) are gliding under spring tension on the cavity wall and can be turned all around the cavity. The resistor voltages and their angular position are read by a computer controlled data acquisition system. [30] Fig. 23 shows a 3 dimensional temperature map of the superconducting 500 MHz niobium cavity operated at an effective accelerating field of 3.2 MV/m. This measurement was done in a subcooled helium bath at a temperature of 2.3 K. On the x-axis the distance along one circle of constant latitude around the spherical cavity is plotted. The y-axis shows the number of carbon thermometer (with resistor 1 corresponding to the top of the cavity and resistor 39 to the bottom of the resonator). The vertical axis displays the temperature increase ΔT detected by the carbon resistor. The residual resistance of this cavity was rather poor ($R_{res} \approx 330 \text{ n}\Omega$). It can be attributed to the very non-uniform high loss area at the

cavity top. The observed top to bottom assymetry compared with other tests showed up problems in the procedure of the chemical treatment of the cavity.

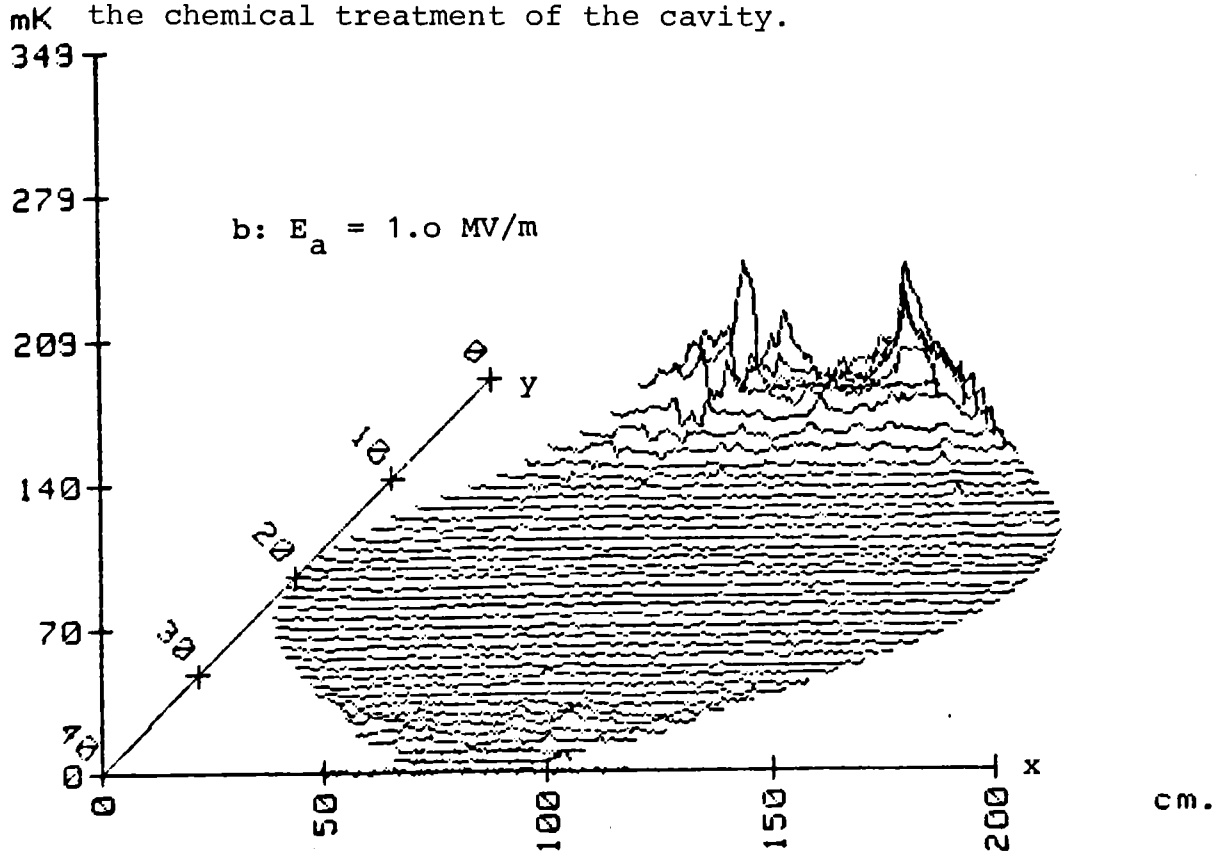


Fig. 23: Temperature map of the CERN 500 MHz cavity at an accelerating field of 1.0 MV/m

In fig. 24 typical temperature profile of the upper part of the cavity is plotted, measured by thermometer 4 along its path around the resonator for three different field excitations. By measuring such a profile in two successive scans but with otherwise identical conditions one can test the reproducibility of the temperature measurement. It is within stepping accuracy (3° in the shown data) for finding the location of the observed temperature peaks and the absolute value of the temperature is remeasured with deviations of less than 2%.

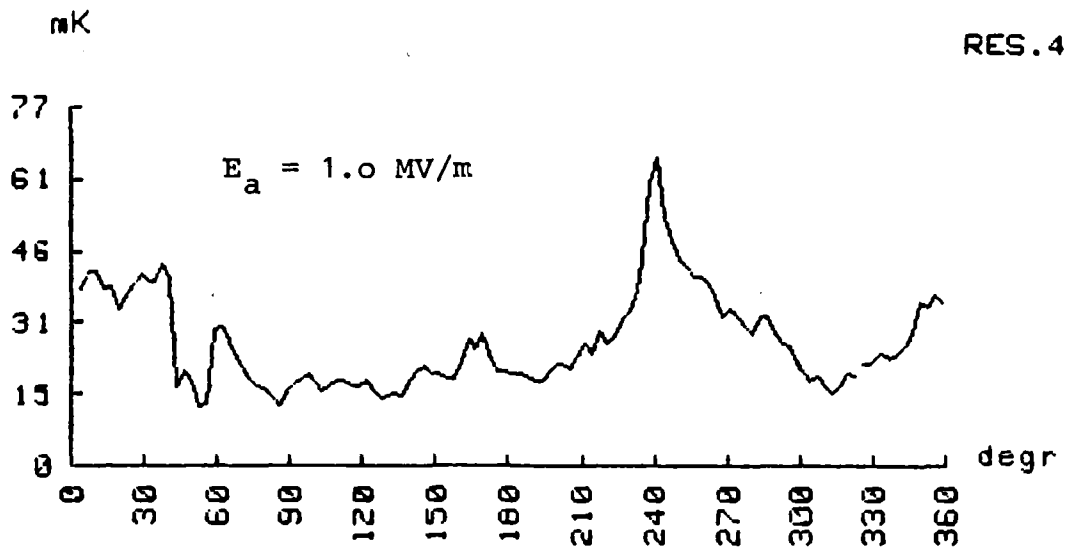
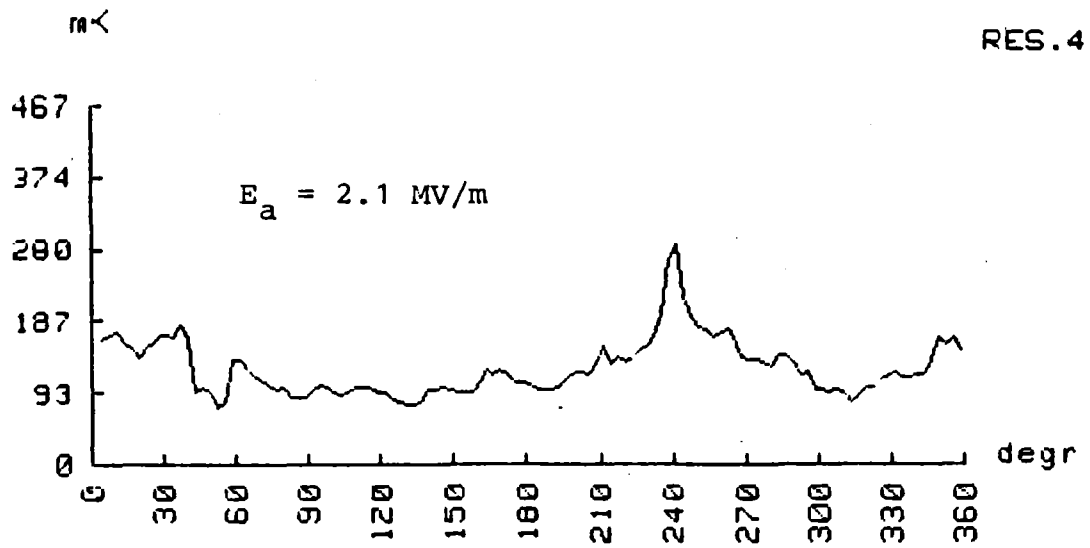
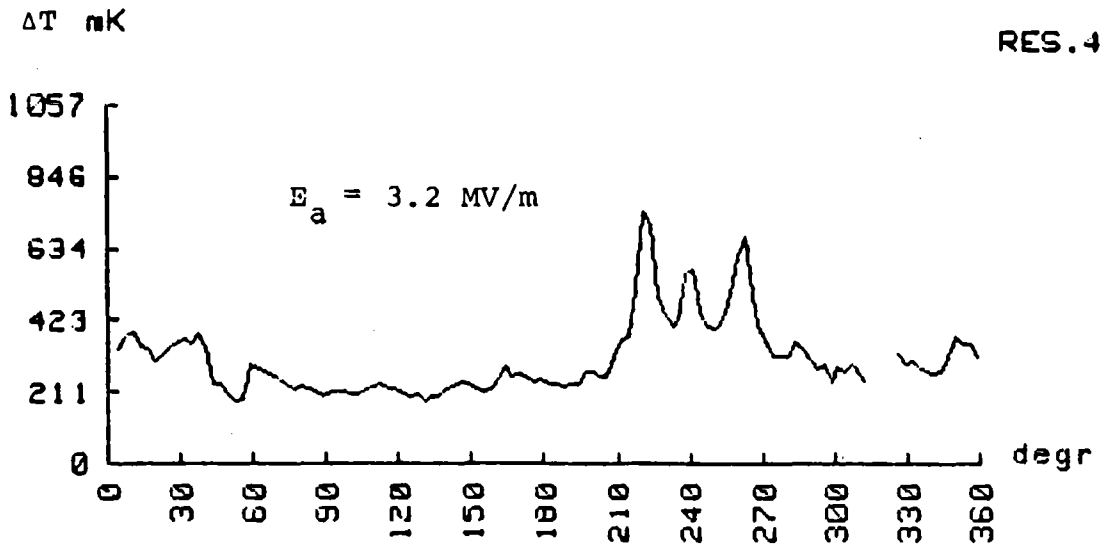


Fig. 24: Temperature profile measured by resistor 4 along its path around the cavity for three different accelerator fields E_a .

Fig. 25 shows a temperature map at a field level ($E_a = 3.2$ MV/m) where electron loading already is a significant energy loss mechanism. One recognizes the line like loss regions produced by impacting electrons field emitted by point sources which since long have been assumed to exist.

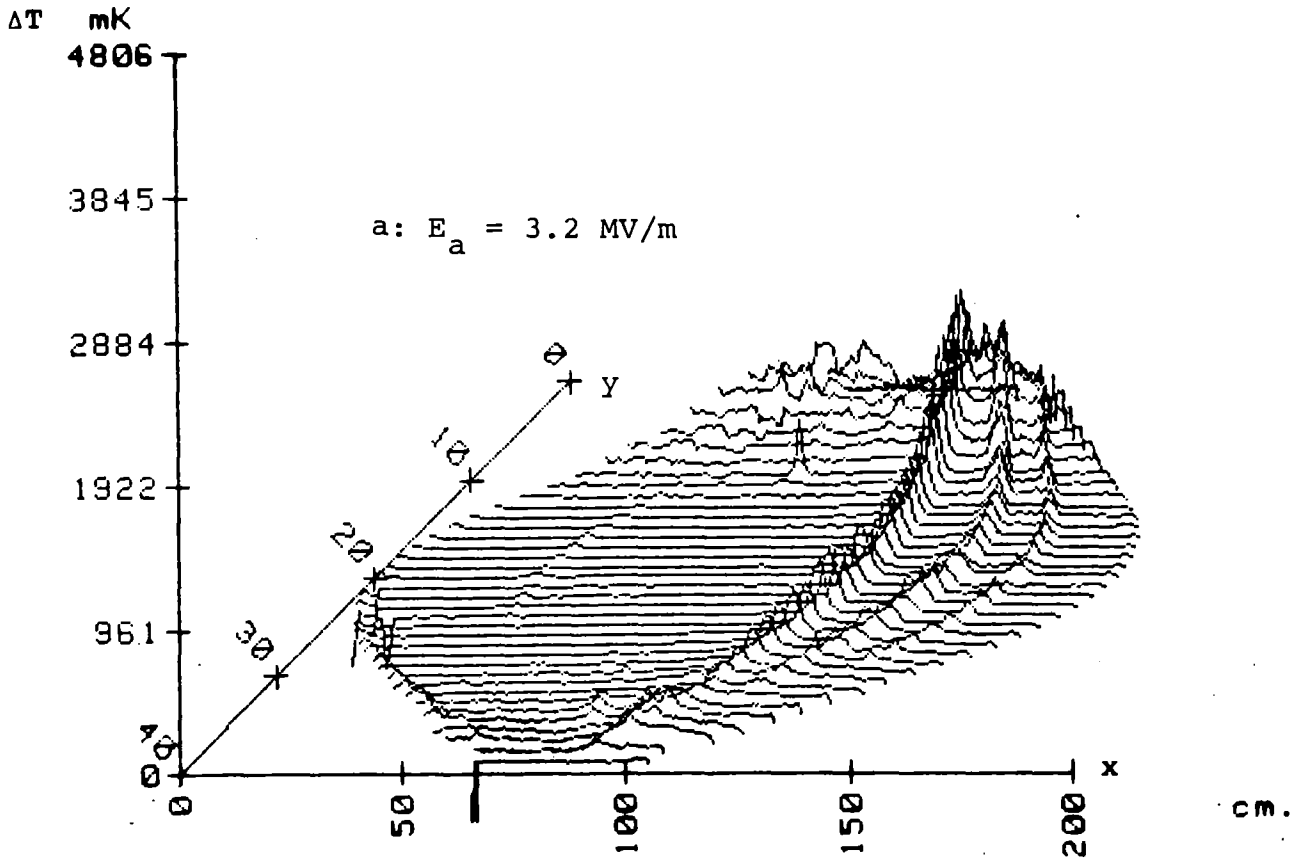


Fig. 25: Temperature map of the CERN 500 MHz cavity at $E_a = 3.2$ MV/m with line like regions of increased temperature due to the impact of electrons field emitted by point sources.

During the same experiment but after some intense electron processing at high fields ($E_a \approx 5.2$ MV/m) a quench was observed which manifests itself in the map of fig. 26.

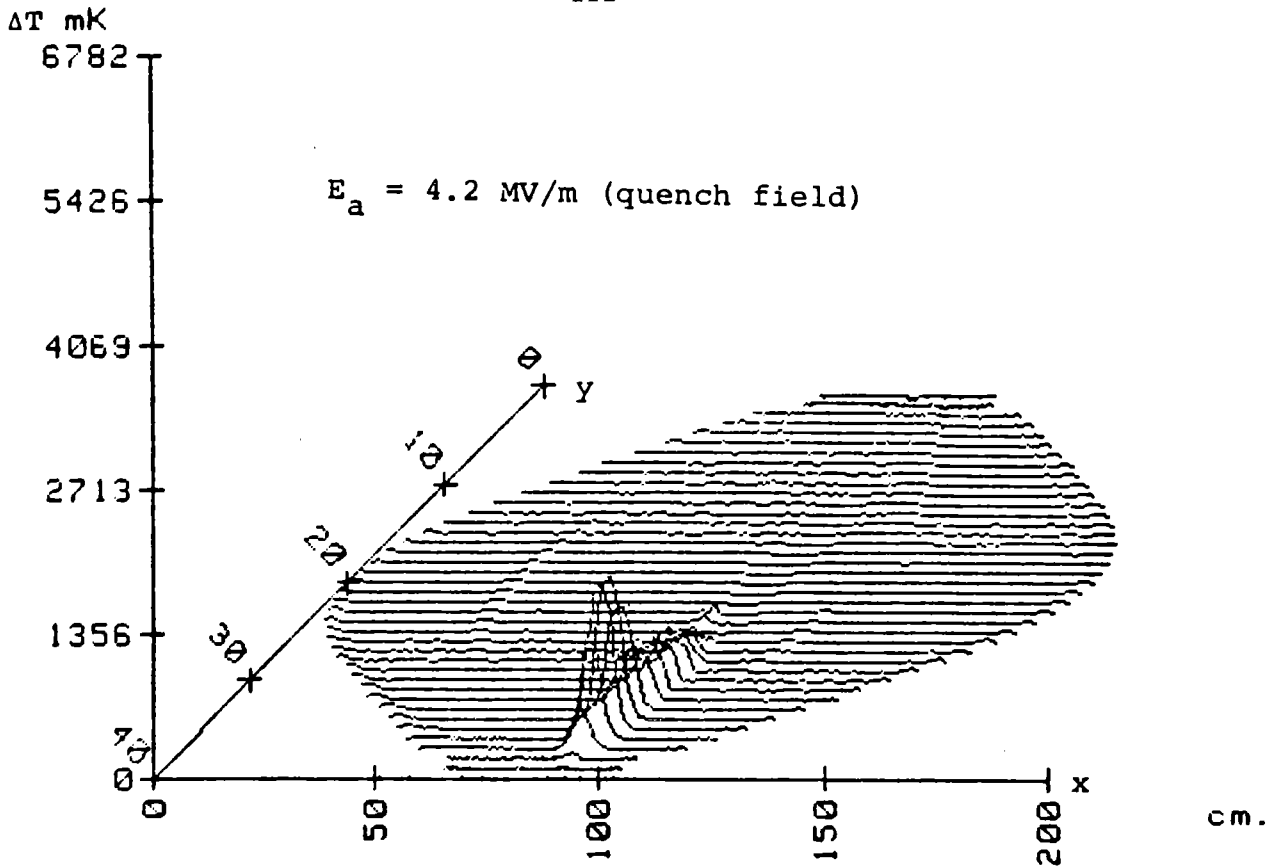


Fig. 26: Temperature map taken during quenching (U_t signal like in fig. 8a)

(Because of a single fast quench (see fig. 8a) only the quench area is heated.) This quench was produced by overheating an area of permanent surface damage, which was produced during the electron processing. This can be seen from the map in fig. 27 which shows this damage well below the quench field (compare also fig. 22 where this damage is not yet present). The electron beam however which produced this damage is not present in fig. 25. The electron processing however which produced the quench was done at a much higher field. The damage causing beam did return after a glow discharge cleaning of the cavity (2).

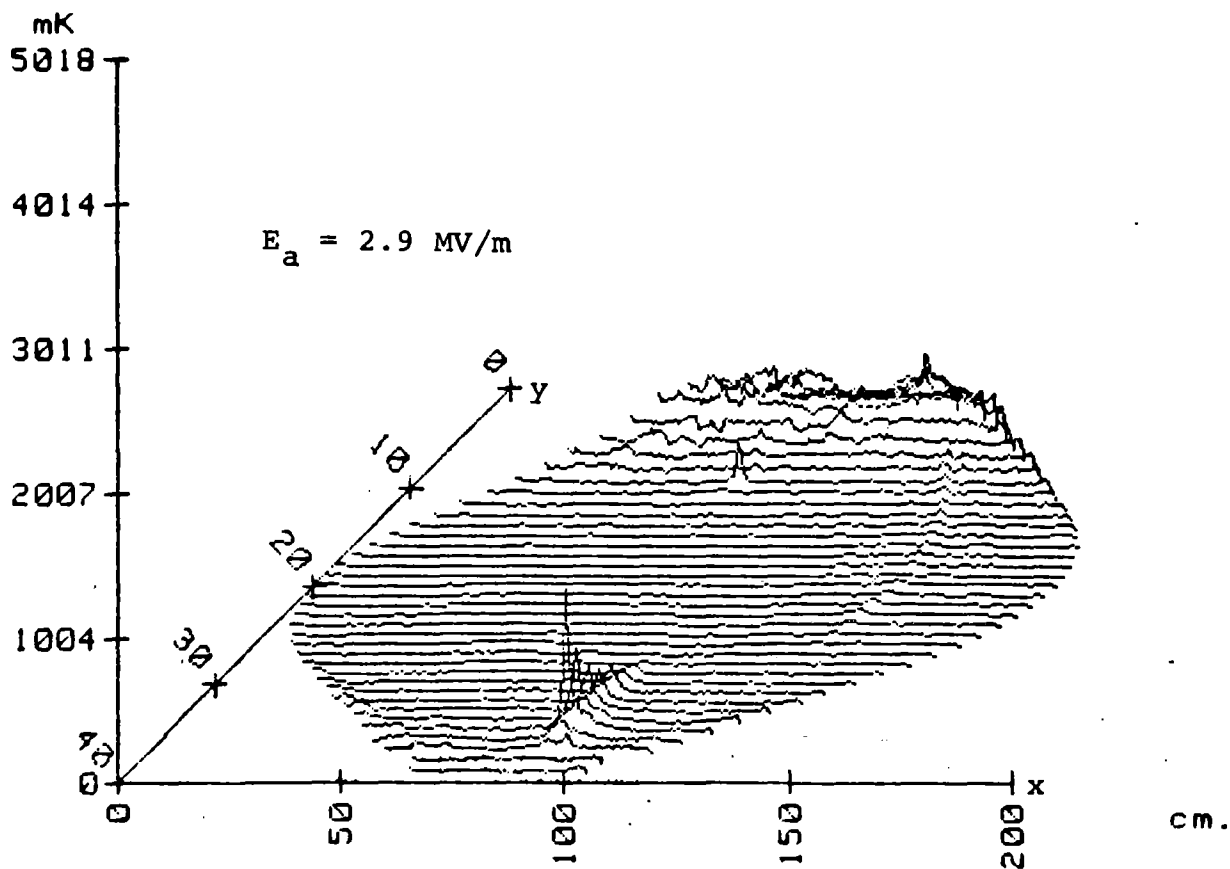


Fig. 27: Temperature map of the 500 MHz cavity below the quench field.

The discharge cleaning which effects only a very thin surface layer ($\ll 100 \text{ \AA}$ thick) did reduce the residual resistance down to $80 \text{ n}\Omega$ mainly by cleaning the upper part of the cavity. This can be seen from the map of fig. 27 taken after the glow discharge (please note the change of the temperature scale).

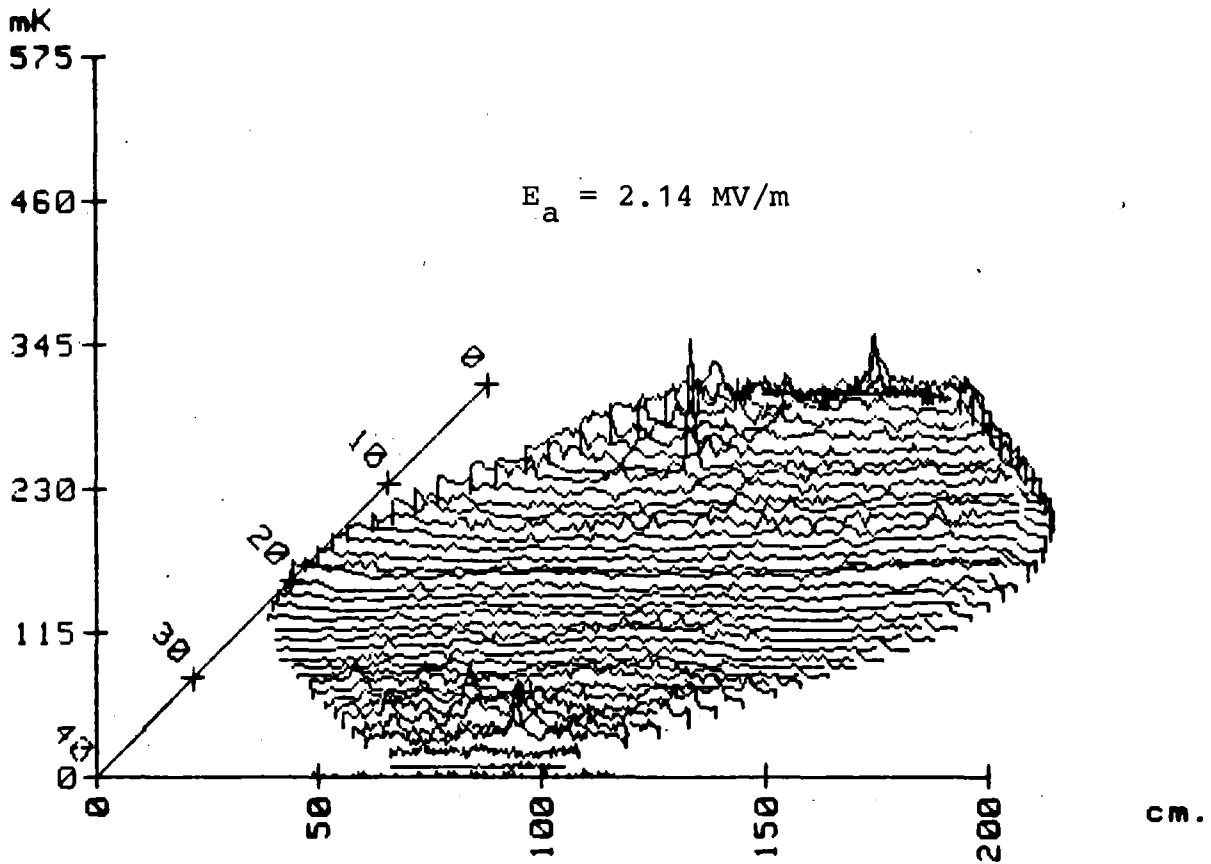


Fig. 28: Temperature map after a glow discharge cleaning at $E_a = 2.14$ MV/m

The spike resistor 10 (arrow in figs. 27 and 28) which was not reduced by the argon discharge is a nice example of a normal conducting spot which is thermally stable up to high fields.

Another important observation is that the surface damage by electron bombardment is removed. From this one concludes that this type of damage effects only a very shallow surface layer (less than 100 \AA thick). This narrows in the thickness of the damage, compared to earlier experiments at Cornell. After the glow discharge cleaning the cavity also was found highly sensibilized in respect to electron field emission.

In a temperature map taken at $E_a = 3.4$ MV/m (fig. 29) one can now clearly see the electron impact line which produced

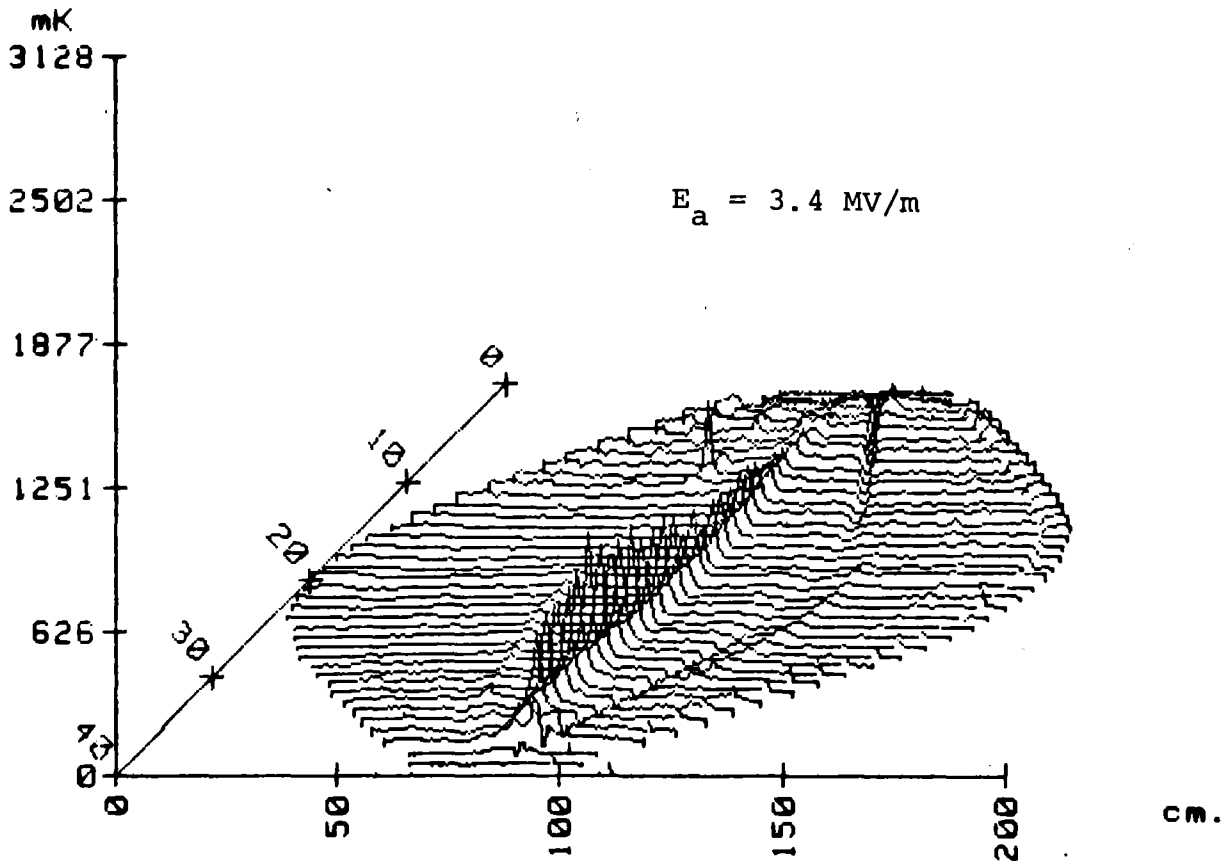


Fig. 29: Strong surface heating by an impacting electron beam considered to be responsible for the surface damage shown in fig. 27.

the damage shown in fig. 27. The production of an invisible surface damage by electron impact has been observed earlier [10]. The temperature maps shown here confirm these findings in a truly visible form.

Temperature mapping of a superconducting cavity in subcooled helium is just in its infancy. The data analysis at CERN has just started and many more experimental observations are to be expected.

5. CONCLUDING REMARKS

A large number of diagnostic techniques has been developed in the past ten years by which we have gained considerable insight into the energy loss mechanism present in a superconducting cavity. Some of the techniques are applicable to practically all cavity shapes. This is true in particular for the observation of the rf signal emitted from the cavity, the detection of breakdown locations with carbon resistors, the measurement of intensity, energy and spatial distribution of X-radiation by NaJ detectors and the detection of internal electron currents by probes in almost field free regions of the cavity. Other more powerful methods can be applied only to cavities of simple shape, like the scanning X-ray detectors and temperature mapping carbon thermometers. These latter techniques however, may teach us how to interpret on save grounds the informations collected by the more easy and more general to use diagnostic procedures.

ACKNOWLEDGEMENTS

I am very thankful to U. Klein and H. Lengeler for their help and corrections in the course of preparing this review. Indispensible were also the extensive informations and written comments of many representatives of institutions working in this field: K.W. Sheppard of Argonne, H. Padamsee of Cornell, A. Schwettman of Stanford HEPL, P. Kneisel of the Kernforschungszentrum Karlsruhe, Nguyen Tuong Viet of Orsay, H. Pfister of Siemens AG. and G.A.Loew of SLAC.

REFERENCES

1. J. Halbritter, private communication
2. M. Tigner, IEEE Trans.Mag-15, (1978)
3. C.M. Lyneis, P. Kneisel, O. Stolz, J. Halbritter
IEEE Trans. Mag-11, No.2, p.417 (1975)
4. Ph.Bernard, G.Cavallari, E.Chiaveri, E.Haebel, H.Heinrichs,
H.Lengeler, E.Picasso, V.Picciarelli and H.Piel, contribution
to the 1980 Conference on High Energy Particle Accelerators,
Geneva (1980)
5. A. Denitz and H. Padamsee, CLNS-434, Cornell University
(1979)
6. C.M. Lyneis, "Electron loading" review talk given at
this workshop
7. J. Kirchgessner, H. Padamsee, H.L. Phillips, D.Rice,
R. Sundelin, M. Tigner and E. Borstel, IEEE Trans. NS-22,
No.3, p.1141 (1975)
8. W. Bauer, A. Citron, G. Dammertz, M. Grundner, L. Husson,
H. Lengeler, E. Rathgeber, IEEE Trans. NS-22, No. 3,
p. 1144 (1975)
9. J. Halbritter,
private communication
10. J.N. Weaver, H. Schwarz, T.I. Smith and P.B. Wilson,
HEPL-PC-1 (1968) Stanford University
11. J. Halbritter, Part.Acc. Vol. 3, p.163 (1972)
12. A. Septier, "Surface Studies", review talk given at
this workshop.
13. H.A.Schwettman, Stanford University, private communication
14. C.M. Lyneis, H.A. Schwettman and J.P.Turneure,
Appl. Phys. Lett. 31, p. 541 (1977)
15. U. Klein and D. Proch, Proc. of the "Conference on
Future Possibilities of Electron Accelerators" Charlottes-
ville 1979

16. H. Padamsee, D. Proch, P. Kneisel and J. Mioduszewski, contribution to the conference on Applied Superconductivity 1980, Santa Fé, Oct. 1980
17. K. Yoshida, M. Yoshioka, J. Halbritter
IEEE Trans NS-26, No. 3 (1979)
18. I. Ben Zvi, J.E. Crawford and J. P. Turneaure
IEEE Trans. NS-20, No. 3, p.54 (1975)
19. K.A. Schwettman, J.P. Turneaure and R.F. Waites,
Journ. of Appl. Phys. Vol.45, No. 2, p. 914 (1974)
20. H. Heinrichs, CERN, private communication (1980)
21. U. Klein, University of Wuppertal and H. Padamsee,
Cornell University - private communications
22. Nguyen Tuong Viet, Orsay, private communication
23. C.M. Lyneis , M. McAshan and Nguyen Tuong Viet,
Proc. of 1972 Proton Linear Acc. Conf. (Los Alamos, 1972)
p. 98.
24. H. Padamsee, J. Kirchgessner, M. Tigner, R. Sundelin,
M. Banner, J. Stimmel and H.L. Phillips, CLNS-340,
Cornell University (1976)
25. H. Piel, R. Romijn, CERN, private communication
26. K.W. Shepard, C.H. Scheibelhut, R. Benaroya and L.H. Bollinger
IEEE Trans. NS-24, No. 3, p.1147 (1977)
27. K.W. Shepard, Argonne National Lab., private communication
28. G. Dammertz, L. Husson, H. Lengeler and F. Rathgeber,
Nucl. Inst. and Meth. 118, p. 141 (1974)
29. U. Klein, D. Proch and H. Lengeler, WU B 80 -16 (1980)
University of Wuppertal
30. Ph. Bernard, G. Cavallari and E. Chiaveri, private communication

ELECTRON LOADING - DESCRIPTION AND CURES*

C. M. Lyneis

High Energy Physics Laboratory
Stanford University
Stanford, California 94305

*Work supported by NSF Grant No. PHY-79-05286.

ELECTRON LOADING - DESCRIPTION AND CURES

Introduction

The phenomena of electron loading plays a particularly important role in the performance of superconducting cavities designed for use in accelerators. The high Q_0 of superconducting cavities makes them extremely sensitive to both the resistive and reactive components of electron currents in the rf fields. The deleterious effects of electron loading include shifts in the resonant frequency making the synchronization of multiple structure accelerators more complex, absorption of rf power requiring more rf drive and more refrigeration, and limitations of gradients which can be attained. In the past several years progress has been made on understanding and reducing electron loading in superconducting cavities. However, further work must be done before accelerator builders can consistently attain high gradients in superconducting accelerators. Although this paper will review the field of electron loading it will by necessity emphasize the more recent work in the field and be devoted mainly to aspects of the problem for niobium cavities designed for velocity of light structures.

Electron loading can be divided into two main categories, multipacting and non-resonant electron loading (NREL). While most electron loading falls into one or the other category, it may be that in certain cases the two phenomena will be linked, i.e., NREL electrons feeding into a multipacting region. Electron multipacting is presently better understood than NREL and as a result more techniques exist for dealing with it. In the past few years a great deal of work has focussed on electron multipacting, but there now exists a great need to direct that effort toward understanding and reducing NREL.

Multipacting

Electron multipacting is a high vacuum resonant avalanche process which occurs in microwave cavities. Characteristically a secondary electron is emitted at low energy, typically 10 eV or less, as the result of the impact of an electron. The secondary electron is accelerated by the rf field and then impacts the surface generating further secondaries. The two types of multipacting which have been identified in superconducting cavities are one-point and two-point multipacting. In one-point multipacting the electrons generated by secondary emission are accelerated away from the wall and then back to the same region of the wall by the rf field. In two-point multipacting the electrons are emitted from one surface and accelerated across the cavity where they collide producing secondaries which then reverse the process.

Four conditions must be satisfied for multipacting to occur. First, the electrons must receive a net increase in kinetic energy during the trajectory. Second, the secondary emission coefficient δ must be greater than one for the typical energy and angle of the impacting electrons. Third, for one-point multipacting the initial and final points of the trajectory must be approximately the same. For two-point multipacting in cavities with a symmetry plane in the cavity center the initial and final points of the trajectory must be at points corresponding to reflection across the symmetry plane. In cavities lacking such symmetry the situation is more complex. Fourth, the resonance condition requires that the initial and final phases must differ by an integral number of rf periods for one-point multipacting. In two-point multipacting between symmetry points in the cavity, the phases must differ by a half integer number of rf periods.

One-point multipacting in disk loaded cylindrical cavities provides a clear example of electron loading both in terms of experimental evidence and in terms of fitting the multipactor simulation models.⁽¹⁾ Multipacting of this type also occurs in the muffin-tin cavity as has been demonstrated experimentally and through calculations.⁽²⁾ A typical trajectory is shown in Fig. 1 for 3rd order one-point multipacting. This trajectory was calculated in one of the cells of the Stanford Superconducting Accelerator at an accelerator gradient E_{acc} of 2.15 MV/m. The phase of the electron is measured relative to the peak of the rf electric field. The electron begins its trajectory at -90° in phase, that is, just as the electric field changes direction so as to accelerate the electron away from the wall. In Fig. 1 the relative strength and direction of the electric field as a function of distance from the wall is illustrated, and qualitatively one can see that the electron tends to move along the electric field lines. This shows that both E_r which is approximately constant in the r direction and E_z which increases linearly with distance away from the wall contribute to the electron's motion. The magnetic field B_ϕ , which is 90° out of phase with respect to the electric field, acts through the Lorentz force tending to bend the electron back towards the wall. Multipactor simulation calculations indicate that the electron impact energy is given approximately by

$$\epsilon = a \frac{E_r^2}{f^2} \quad (1)$$

where a is $(9.0 \pm 2.0) \times 10^3$ eV, E_r is the radial electric field at the surface in MV/m and f is the frequency in GHz. The above equation is

for electrons emitted with zero energy whereas in reality the secondary electrons are emitted with range of energies mainly between 0 and 10 eV. The calculations indicate that the final impact momentum is approximately the sum of that given by calculating the momentum from Eq. (1) and the initial momentum of the secondary electron. So if the initial momentum is ignored Eq. (1) slightly underestimates the impact energies. The resonance condition for this type of multipacting is

$$B_n = \frac{bf}{n} \quad (2)$$

where b is 23 ± 3 mT, B_n is the local magnetic field, n is the order of multipacting and f is the frequency in GHz. Although Eqns. 1 and 2 are useful for estimating the fields and impact energies for one-point multipacting in disk loaded cavities, if the geometry is significantly altered from the simple shape in Fig. 1 the equations no longer hold. Accurate values for the fields at which multipacting occurs and typical impact energies can only be found by direct calculation of the trajectories using the actual fields in the cavity.

Although two-point multipacting has often been discussed^(3,4,5) its relevance and actual contribution to electron loading in superconducting cavities has only been demonstrated in a few special cases.⁽⁶⁾ In disk loaded velocity of light structures electron dynamics calculations indicate the existence of trajectories which satisfy the resonant condition and the symmetrical landing point conditions for two-point multipacting.⁽⁵⁾ Satisfying these two conditions however is not sufficient to produce multipacting and there are two reasons to expect that two-point multipacting does not occur across the gap in velocity of light structures.

First the impact energies are much too high, typically ϵ is greater than 100 keV whereas the secondary emission coefficient for Nb drops below 1.0 at about 1 keV and decreases at high impact energy approximately as $\epsilon^{-.35}$ ^(2,7,8). Second, slight changes in either the initial position or phase of the electrons result in grossly different landing points and phases. This indicates a very small phase space available for this type of multipacting. As will be discussed in the section on NREL such back and forth trajectories may occur as a result of backscattered electrons, but this process does not lead to two-point multipacting.

In narrow gap cavities and low-beta structures two-point multipacting can occur. For example in a highly re-entrant cavity 500 MHz cavity two-point multipacting was observed across a 10 mm gap in agreement with trajectory calculations.⁽⁶⁾ However, the two-point multipacting in this cavity was easily overcome. Two-point multipacting may occur in low-beta structures such as helices⁽⁹⁾ or split rings,⁽¹⁰⁾ but at present the trajectories involved in multipacting in these structures remains unknown.

The secondary emission coefficient depends on the type of metal, the conditions of the metal vacuum interface, the electron impact energy and angle. For secondary emission from Nb there is an extensive literature^(8,11) with more recent work focussing on the "real" surfaces. That is, surfaces prepared under conditions comparable to those used in preparation of rf cavities.^(2,12,13) For niobium surfaces which are prepared by heating to high temperature in UHV and measured without exposure to air, the secondary emission coefficient δ increases rapidly with increasing impact energy rising above 1.0 at 170 eV and reaching a maximum of 1.22 at an impact energy of about 350 eV.⁽⁸⁾ Above this energy δ slowly decreases dropping below 1.0 at about 850 eV. The effects of various surface treatments, exposures to gases, and contamination can cause the secondary

emission coefficients to increase or decrease but the curve retains the same general shape. These effects will be discussed in more detail in the section on methods for suppressing multipacting.

Multipacting can be suppressed by breaking any one of the four necessary conditions discussed above. The first approach was to alter cell geometry so as to reduce E_r at the outer wall.⁽¹⁾ This was done by reducing the corner radii at the outer wall and by decreasing the taper of the side wall. As E_r is reduced the impact energy decreases according to Eq. (1). In single-cell cavities it is possible to reduce the value of E_r as low as desired by adjusting the geometry and thereby eliminate one-point multipacting. This approach was also successful in two-cell muffin-tin structures which were reshaped so as to reduce the ratio of E_{\perp}/E_{axial} from 10% to 1.8%⁽¹⁴⁾ and thereby eliminate multipacting up to E_{acc} of 7.5 MV/m at S-band. In many-cell structures, the problem is more complex since the fields may not be symmetric due to differences in the boundary conditions on the two sides of end cells. These effects are evident in the performance of the modified 6m-structure in the Stanford SCR where the 3rd order multipacting is stronger in cells adjacent to the unexcited cell than in the main cells.

The second geometrical approach to suppressing one-point multipacting is paradoxically to round out the outer wall rather than to make the corners sharper. In the spherical cavity the outer wall of the cavity is made completely round which increases the gradient of E_r along the outer surface and this alters the electron trajectories causing the end points to be far from the starting points.⁽¹⁵⁾ Although the electrons can gain sufficient energy and field levels exist where most electrons return in a integer number of rf periods, the electrons rapidly move to the center plane where E_r changes sign. For the electrons which

cross the symmetry plane the sign change in E_r disrupts their phasing. Secondaries generated very close to the center line do not gain sufficient energy due to the low value of E_r .⁽¹⁵⁾ Multipacting has not been detected on single-cell cavities tested at 4.5 GHz,⁽¹⁶⁾ 3.0 GHz⁽¹⁷⁾ and 0.500 GHz.^(18,19) On the other hand, none of the tests on spherical cavities to date have been done on anodized cavities, which provides the most stringent test for multipacting. An important question is whether structures constructed out of many spherical cells will be multipactor free. A 3-cell structure with spherical cavities which operates at 4.5 GHz has been tested.⁽²⁰⁾ In the π -mode no multipacting was detected up to the maximum accelerator gradient of 10 MV/m. Both the $2\pi/3$ mode and $\pi/3$ mode did show multipacting. So it remains an open question whether structures constructed from spherical cells will be multipactor free particularly at lower frequencies.

Another successful approach to multipactor suppression involves placing grooves in the surface of the cavity where multipacting normally occurs. This technique has been used to eliminate multipacting in the muffin-tin cavities.⁽²¹⁾ The rectangular grooves are located in the cup bottoms where multipacting is known to occur through direct thermal detection and multipactor simulation calculations.⁽²²⁾ The groove geometry which is specified by the depth and width of the grooves and the spacing between the grooves was typically 2:2:1. In a series of tests at Cornell on grooved two-cell S-band muffin-tin cavities no evidence of either second or third order multipacting was found in contrast to measurements performed on similar cavities without grooves.⁽²¹⁾ More recently at Karlsruhe both rectangular and triangular grooves have been put in S-band cylindrical cavities.⁽²³⁾ These cavities were then tested after a variety of surface preparation techniques and multipacting was only briefly observed in one

test where the cavity had been anodized. The geometry of these cavities except for the grooves is the same as that used in earlier multipacting tests at Stanford.⁽¹⁾ So it appears that both rectangular and triangular grooves are useful in suppressing multipacting.

Trajectory calculations done at Cornell for rectangular grooves in the surface indicate that, because the perpendicular electric field is strongly attenuated at the bottom of the groove, secondary electrons generated in the groove bottoms remain trapped and gain insufficient energy to create further secondaries. For other trajectories the grooves cause path length changes altering the returning phase of the electrons. DC secondary emission measurements also show that grooves in the surface reduce δ but not to a value less than 1.0 .

Reduction of the secondary emission coefficient by surface coatings or cleaning represents another possibility for suppression of multipacting. In conventional room temperature cavities coating of Ti or TiN in conjunction with rf processing have been successful in suppressing multipacting.⁽²⁴⁾ Coatings of Ti and TiN on Nb have demonstrated reduction of the secondary emission coefficients in dc measurements,⁽²⁾ but surfaces which are exposed to air after coating the secondary emission coefficient increases to levels similar to that before coating and to date the results on superconducting cavities using this technique have not indicated successful suppression of multipacting.⁽²⁵⁾ Another technique carried over from room temperature cavities is ion cleaning. So far this technique has resulted in an increase in electron loading for the 500 MHz CERN cavity.⁽¹⁴⁾ High power room temperature processing on Nb cavities has been suggested and preliminary experiments are underway at SLAC, but it is too early for definitive results.⁽²⁶⁾

Another possible method for suppression of multipacting is to disrupt the phase relationship of the electron trajectories by injecting a second rf field into the cavity. At Cornell this approach has been used for the muffin-tin cavities.⁽²¹⁾ In an L-band cavity the field was initially limited to E_{acc} of 4.2 MV/m by multipacting in the cup bottom. By exciting the TM_{111} mode (rectangular geometry) it was possible to raise the field to 5.5 MV/m. Unfortunately, somewhat contrary to expectations the high field could only be maintained in the presence of the higher order mode. That is, when the TM_{111} mode was switched off, the multipacting reappeared causing the field to drop back to the lower level. While it is probable that this technique would also be successful in cylindrically symmetric single-cell cavities, it seems unlikely that it would be successful in multi-cell structures where the field profile for the higher order mode would be very complex.

Non-Resonant Electron Loading

The second general class of electron loading phenomena which occurs in microwave cavities can be labelled non-resonant electron loading (NREL) to distinguish it from multipacting phenomena. It is often referred to as field emission loading in the literature, but the details of how the electrons are produced is not well understood. This type of behavior can generally be distinguished operationally from multipacting because of several differences between the manifestation of the loading in the cases of multipacting and

non-resonant phenomena. Multipacting generally occurs at definite levels or in bands so that the loading does not monotonically increase with increasing field. In NREL above a certain threshold the loading generally increases exponentially with increasing field. Whereas in multipacting the typical impact energies range from 50 eV up to a few keV, the typical impact energies of electrons involved in NREL are much greater, often producing x-rays of sufficient energy to penetrate the cavity walls and be detected. Because the theories put forth so far are only partially successful in explaining NREL a description of experimental facts concerning NREL follows.

A very important characteristic of NREL is the exponential growth of loading and x-radiation with field amplitude. A convenient way to parameterize this growth is to fit the radiation to an exponential function and this is usually done using a modified Fowler-Nordheim expression which takes into account the time dependence of the fields, the generation of x-radiation, and the absorption of x-radiation by the cavity walls.^(27,28) The growth of the radiation with increasing field can then be given in terms of a field enhancement factor β . In Table 1 data for NREL in velocity of light disk loaded cavities over a wide range of frequencies is summarized. Although these data represent only a small portion of all cavity measurements, they were chosen because they demonstrate the basic frequency dependence of NREL. Although there is some scatter in values between 0.5 and 1.3 GHz, the highest values for E_p/f are approximately $17 \text{ MV(m-GHz)}^{-1}$. Above 1.3 GHz the values of E_p/f decrease slowly reaching about 7 MV(m-GHz)^{-1} at 8.6 GHz. The fact that electron loading and maximum gradients in these cavities scale approximately as $1/f$ is a serious problem for the application of superconducting cavities in low frequency velocity of light structures. A striking feature

of this data is that although E_p and β vary considerably with frequency, the product βE_p is approximately a constant over the entire range of frequency. In the Fowler-Nordheim theory β is interpreted as the enhancement factor of the electric field at the emission point. So the fact that βE_p is approximately constant may imply that the maximum field is determined when the primary emission current reaches a certain level. However, this leaves open the question of why β scales approximately as $1/f$.

Table 2 illustrates that cavity geometry is also an important factor in the peak electric fields which can be attained in superconducting cavities. The data in Table 2 are from accelerator cavities designed for non-relativistic particles in contrast to the velocity of light cavities summarized in Table 1. For low-beta cavities a wide range of values exist for E_p/f and they are considerably higher than those in Table 1. So it seems clear that geometry has a very strong effect on NREL and any general theory of NREL will have to include a model for the electron trajectories involved. Electron dynamics in similarly shaped cavities with different resonant frequencies scale exactly if the field amplitudes are scaled with frequency and this may partially explain the frequency dependence in Table 1.

Various types of experiments have been done which give some clues as to the nature and sources of NREL. Measurements on the x-radiation energy spectrum have shown^(32,38) that some x-rays produced have energy in excess of that which can be achieved by an electron in one transversal of the cavity. However, the relative number of these high energy x-rays has been explained by back-scattering with low energy loss. Extracting detailed information from the x-radiation energy spectrum is difficult since the x-ray absorption characteristics of the wall dominate its shape particularly at lower energies. The spatial distribution

of x-rays coming out of cavities has been investigated using an x-ray pin hole camera,⁽³⁸⁾ a collimated NaI detector,⁽³¹⁾ and silicon barrier detectors.⁽³⁹⁾ Basically these experiments indicate that the x-radiation is emitted most strongly from the cavity disks near the axis of the cavity. The x-ray pin hole camera data showed that the radiation was approximately axially symmetric. The recent improvements in thermal detection methods coupled with rotatable silicon barrier detectors at CERN promise to give more detailed information about NREL.⁽³⁹⁾

At present the only active technique for reducing NREL is helium-ion sputtering or helium processing, which is frequently successful in reducing NREL in superconducting Nb cavities. In an L-band single-cell cavity⁽²⁸⁾ helium-ion processing was done over a period of 51 hours and the x-radiation from the cavity was reduced by a factor of more than 10^4 . The most rapid progress in reducing x-radiation due to NREL occurred during the first 5 hours of processing and this was interpreted as being due to the removal of adsorbed gases on the cavity walls. Although in velocity of light structures helium-ion sputtering can greatly decrease NREL it generally does not yield an increase in field amplitude once the breakdown field has been reached. In low-beta Nb cavities such as the split rings and helices helium-ion sputtering is frequently used yielding significant improvements in cavity performance.⁽¹⁰⁾ This may be due to the higher ratios of E_p/f in these structures which make helium-ion sputtering more favorable. A drawback to using helium ion sputtering in multi-cell structures is that helium left behind can cause large shifts in the resonant frequency of the structures.⁽⁴⁰⁾

The recent results from CERN using thermal diagnostics^(18,39) suggest that progress in understanding NREL may be made by combining the information gained

from the thermal measurements with a study of possible electron trajectories. Since some of the thermal maps appear to be the result of impacting electrons, it is interesting to ask what types of trajectories and emission processes are taking place. As a first step in such a program, we have begun trajectory calculations using the 500 MHz CERN cavity as a model. In order to keep the calculations manageable three assumptions are made. First, only the trajectories of the primary electrons are included. Second, the initial phases of the electrons are distributed in phase consistent with Fowler-Nordheim emission where βE_p is assumed to be 5000 MV/m. The consequence of this assumption is that the greatest number of electrons are emitted at the peak of the electric field and the number emitted for phases advanced or retarded more than 25° diminishes rapidly. The third assumption is that the energy density deposited by such a distribution of electrons is proportional to the temperature rises detected.

At this time, the results of these trajectory calculations are still qualitative, but they give several insights into the problem of NREL. First, over a small region of the iris, there is the possibility for electrons emitted with different phases to all land in approximately the same location. In Fig. 2a the trajectories for electrons with initial phases of $0, 5^\circ, \dots, 25^\circ$ at an accelerator gradient of 2.9 MV/m are shown. All electrons emitted from this point with phases between $+5$ and $+25^\circ$ land a very narrow strip of the cavity wall. In Fig. 2b the trajectories of electrons emitted from the same point but with advanced phases of -5° to -25° are shown. For electrons emitted early the landing points are widely distributed indicating no pileup of impacting electrons. In Fig. 3 trajectories for retarded electrons again at a gradient of 2.9 MV/m

are shown for two starting locations differing by 8.7 mm. This illustrates how strongly the electron trajectories depend on the starting point in this part of the cavity. A second implication is that if the sort of electron pile-up illustrated in Fig. 2a is important, then a very limited portion of the cavity can contribute to this process. Figures 4a and 4b show retarded electron trajectories for the same emission point but at gradients of 2.3 MV/m and 4.6 MV/m. This demonstrates that as the fields are increased the impact points of the electrons move progressively farther into the cavity away from the iris.

The results of sample calculations of the integrated impact energy for the primary electrons from an emitter located at the point of peak electric field is shown in Fig. 5. The trajectories are calculated at a gradient of 4.1 MV/m. The electrons' initial phases are distributed according to a Fowler-Nordheim emission model with βE_p equal to 5000 MV/m. The distribution of impact energy is quite similar to some of the thermal maps measured on the 500 MHz LEP cavity^(18,19,39) indicating that this model gives results consistent with the CERN measurements. It also indicates that the area of the cavity most strongly bombarded by electrons is in the region where the breakdown has been observed in the 500 MHz LEP cavity. To expand this model and make it more quantitative a Monte-Carlo calculation including secondary electrons must be done.

Conclusion

Further progress in understanding and effectively dealing with electron loading could greatly enhance the development of superconducting structures. Multipacting can be controlled through careful cavity design or grooving

of the surface, at least in simply shaped cavities. NREL still presents many problems for superconducting accelerated structures, although vigorous programs to study the problems are underway in a number of laboratories.

Acknowledgement

The author wishes to express his gratitude to individuals from CERN, Wuppertal, Cornell, SLAC, Orsay, KEK, INDFN-Genoa, KFZ-Karlsruhe, who sent him information on current work going on in their laboratories, much of which is as yet unpublished.

References

1. C. Lyneis, H. A. Schwettman and J. P. Turneaure, Appl. Phys. Lett. Vol. 31, No. 8, October 1977, p. 541.
2. H. Padamsee, A. Joshi, J. Appl. Phys. 50, 2, February 1979, p. 1112.
3. P. Kneisel, O. Stoltz and J. Halbritter, J. Appl. Phys. 44, 4, April 1973, p. 1785.
4. A. J. Hatch, Nucl. Instr. and Meth. 41, 1966, p. 261.
5. J. Halbritter, KfK-Ext 3/78-1 (KfK, Karlsruhe, 1978).
6. U. Klein (private communication).
7. R. E. Simon and B. F. Williams, IEEE Trans. Nucl. Sci., NS-15, 3, 1968, p. 167.
8. R. Kollath, Physik Z. 38, 202, 1937.
9. A. Citron, J. L. Fricke, C. M. Jones, H. Klein, M. Kuntze, B. Piosczyk, D. Schulze, H. Strube, and J. E. Vetter, Proc. 8th Int. Conf. on High Energy Accelerators, CERN, 1971, p. 278.
10. R. Benaroya, L. M. Bollinger, A. H. Jaffrey, T. K. Khoe, M. C. Oleson, C. H. Scheibelhut, K. W. Shepard, W. A. Wesolowski, IEEE Trans. Nucl. Sci. Vol. MAG-13, 1, January 1977, p. 516.
11. R. Warnecke, J. Phys. Radium 7, 270, 1936.
12. M. Lavarec, G. Boguet, A. Septier, C. R. Hebd, Seances Acad. Sci. Ser. B(France), Vol. 288, 4, June 1979.
13. N. Hilleret (to be published in Nucl. Inst. and Meth.).
14. P. Kneisel and H. Padamsee, CLNS-79/433 (Cornell, August 1979).
15. U. Klein and D. Proch, Proc. Conf. on Future Possibilities for Electron Accelerators, Charlottesville, Va. 1979.
16. V. Lagomarsino, G. Manuzio, R. Parodi and R. Vaccarone, IEEE Trans. on Magnetics, Vol. MAG-15, 1, June 1977, p. 25.
17. U. Klein, D. Proch and H. Lengeler, University of Wuppertal, WU B 80-16, May 1980.

18. P. Bernard, H. Heinrichs, H. Lengeler, E. Picasso and H. Piel, (CERN) LEP Note 209, February 1980.
19. H. Lengeler (private communication).
20. R. Parodi (private communication).
21. H. Padamsee (private communication).
22. H. Padamsee, J. Kirchgessner, M. Tigner, R. Sundelin, M. Banner, J. Stimmel, and L. Phillips, IEEE Trans. Magnetics, MAG-13, 1, June 1977, p. 346.
23. P. Kneisel (private communication).
24. M. Tigner, Rev. Sci. Inst. 38, 1967, p. 444.
25. H. Padamsee, M. Banner and M. Tigner, IEEE Trans. Nucl. Sci. NS-24, 3, June 1977, p. 1101.
26. G. Loew (private communication).
27. H. Schopper, H. Strube and L. Szecsi, Externer Bericht 3/68-6 Kernforschungszentrum Karlsruhe, 1968.
28. H. A. Schwettman, J. P. Turneure and R. F. Waites, J. Appl. Phys. 45, 2 February 1974, p. 914.
29. J. Halbritter (private communication).
30. H. Lengeler (private communication).
31. K. Yoshida, M. Yoshioka, J. Halbritter, IEEE Trans Nucl. Sci. NS-26, 3, June 1979, p. 4114.
32. C. Lyneis, Y. Kojima, J. P. Turneure, Nguyen Tuong Viet, IEEE Trans. Nucl. Sci. NS-20, 3, June 1973, p. 101.
33. P. Wilson, Z. D. Farkas, H. A. Hogg and E. W. Hoyt, IEEE Trans. Nucl. Sci. NS-20, 3, June 1973, p. 104.
34. J. E. Vetter, B. Piosczyk, J. L. Fricke, 1972 Proton Linear Accelerator Conference, Los Alamos, New Mexico, October 1972, p. 145
35. K. W. Shepard, C. H. Scheibelhut, P. Markovich, R. Benaroya and L. M. Bollinger, IEEE Trans. Magnetics, MAG-15, 1, January 1979, p. 666.

36. P. H. Ceperley, I. Ben-Zvi, H. Glavish, S. S. Hanna, IEEE Trans. Nucl. Sci., NS-22, 3, 1975, p. 1153.
37. K. Mittag, IEEE Trans. Nucl. Sci. NS-24, 3, 1977, p. 1156.
38. I. Ben-Zvi, J. F. Crawford and J. P. Turneure, IEEE Trans. on Nucl. Sci. NS-20, 3, June 1973, p. 54.
39. P. Bernard, G. Cavallari and E. Chiaver, private communication
40. C. Lyneis, J. Sayag, H. A. Schwettman and J. P. Turneure, IEEE Trans. Nucl. Sci. NS-26, 3, June 1979, p. 3755.

Table 1

Frequency GHz	E_p MV/m	E_p/f MV/(m-GHz)	β	$\beta_f E_p$ MV/m	Cavity-Lab
.5	8.3	16.6	660	5500	DORIS-1
.5	5.0	10.0	1200	6000	DORIS-2 ²⁹
.5	9	18.0	500-800	4500-7200	LEP-spherical CERN ³⁰
.7	6-7	8.5-10.0	660-1100	3960-7700	700 MHz ³¹ Karlsruhe
1.3	10.9	8.4	314	3422	L-band HEPL
	21.5	16.5	377	8105	L-band ³² HEPL
2.85	30.0	10.5	115	3450	S-band HEPL
	35.3	12.4	210	7410	S-band ³² HEPL
8.60	58.2	6.8	80	4660	X-band ³³ SLAC

Table 2

Frequency GHz	E_p MV/m	E_p/f MV/(m-GHz)	Cavity Type
.080	24	300	Helix ³⁴
.097	16.8	173	Split Ring ³⁵
.430	17.3	40.0	Re-entrant ³⁶
.720	22	30.6	Alvarez ³⁷

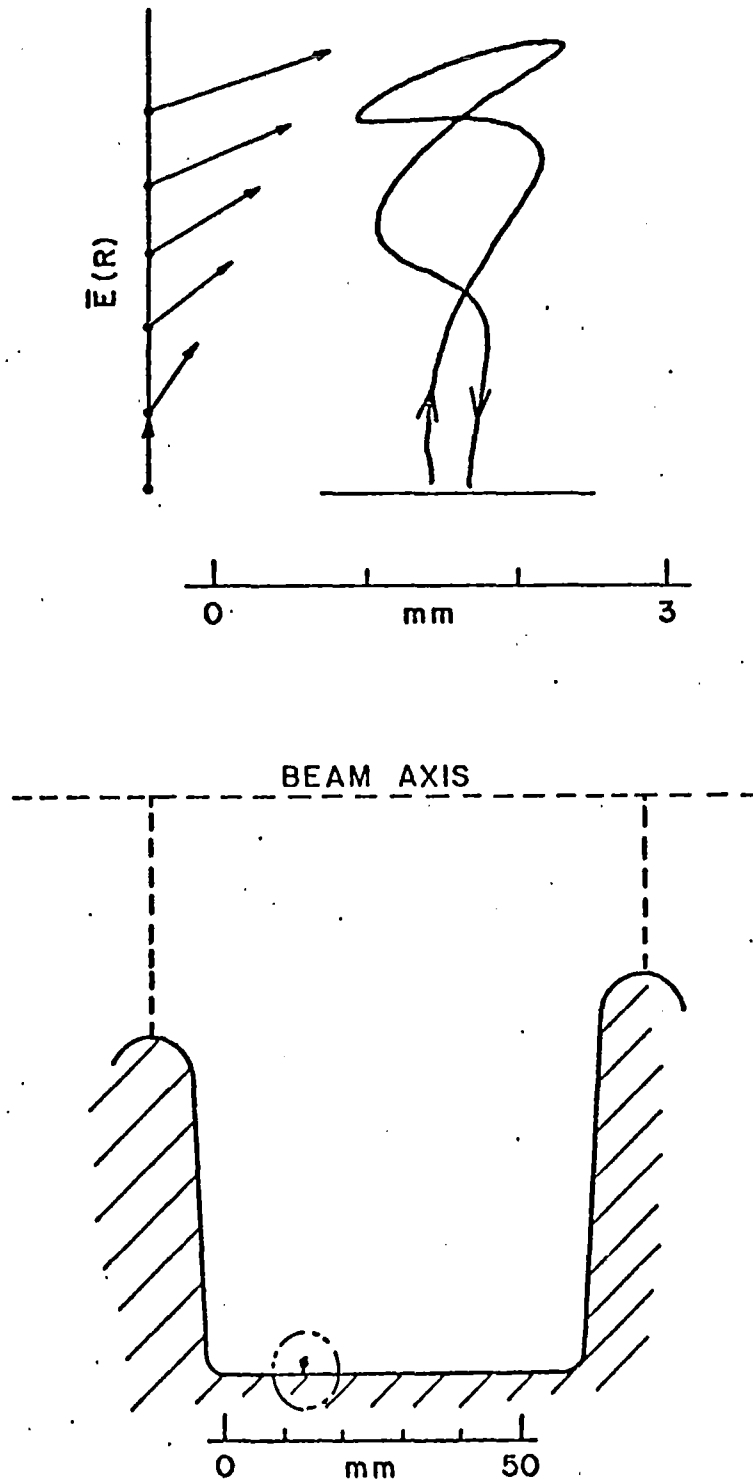


Figure 1. An example of a 3rd order multipacting trajectory in the Stanford SCA structure at an accelerator gradient of 2.15 MV/m. The relative strength and direction of the electric field as a function of distance away from the wall is shown on the left of the trajectory.

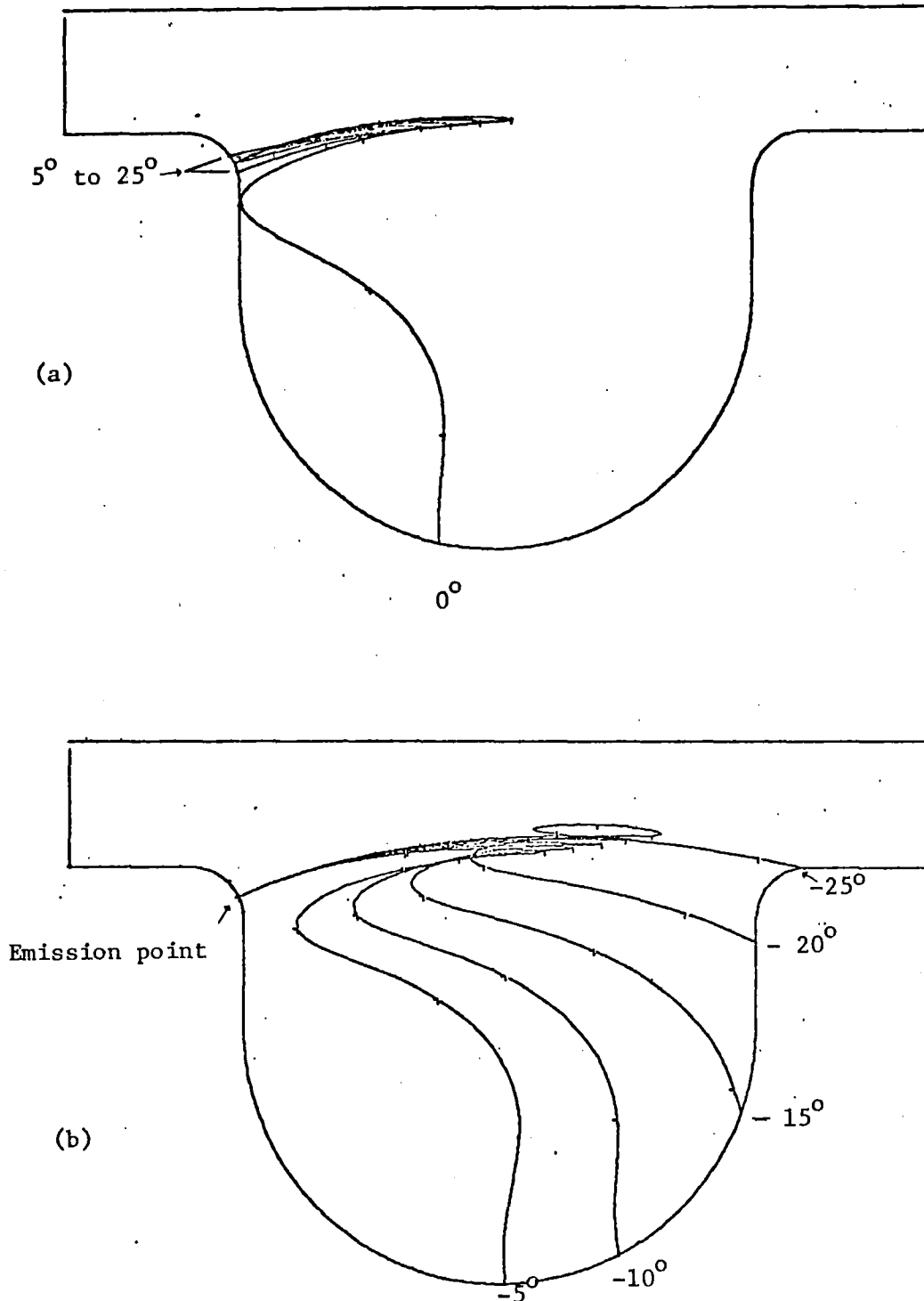


Figure 2. Comparison of the trajectories emitted with retarded phases and those with advanced phase. In (a) the starting phases vary from 0 to 25° . In (b) the starting phases vary from -5 to -25° . The gradient for both (a) and (b) is 2.9 MV/m .

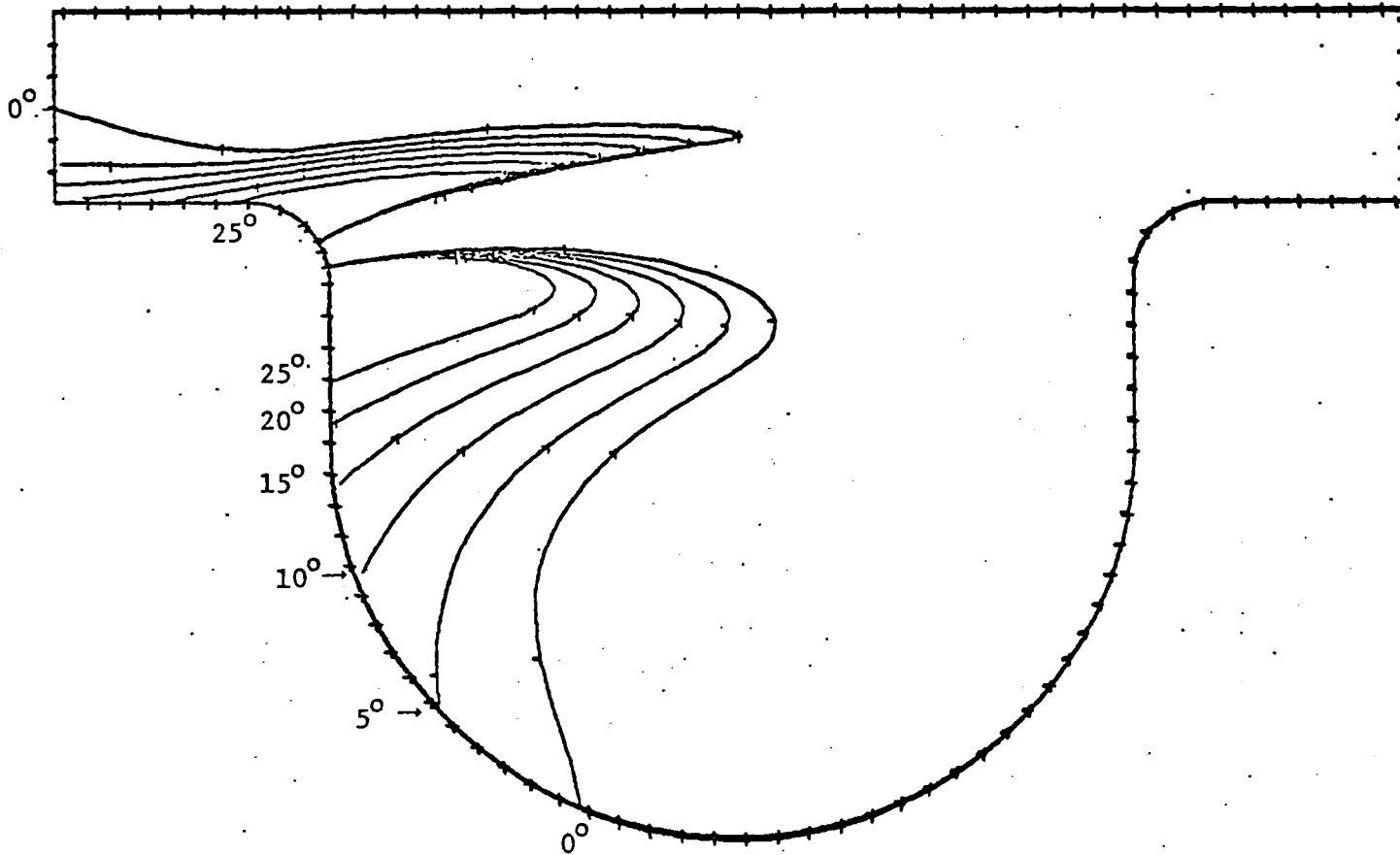


Figure 3. The trajectories for retarded electrons from two emission points differing in position by 8.7 mm. The calculations are done for a gradient of 2.9 MV/m and 500 MHz, with starting phases from 0° to 25° .

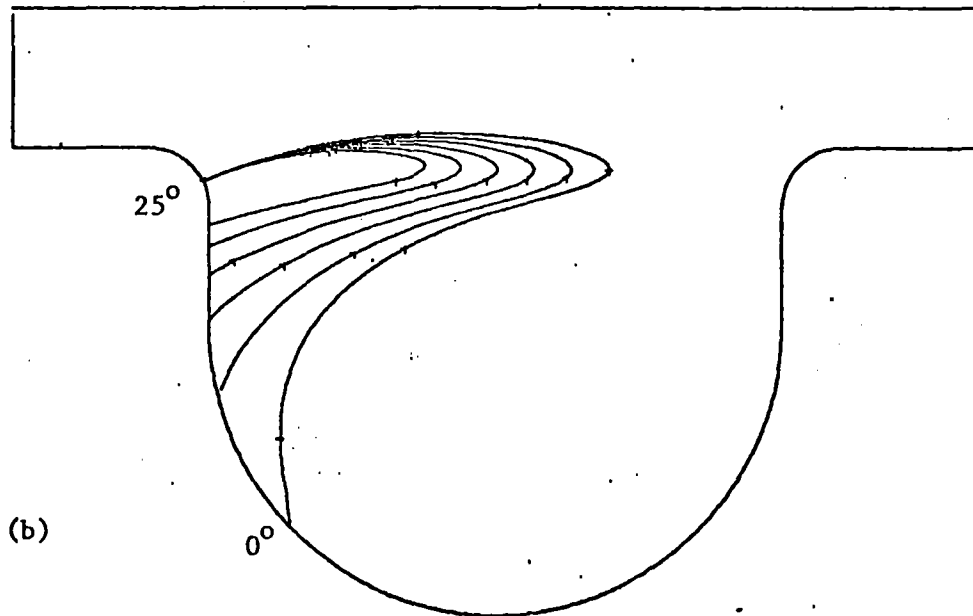
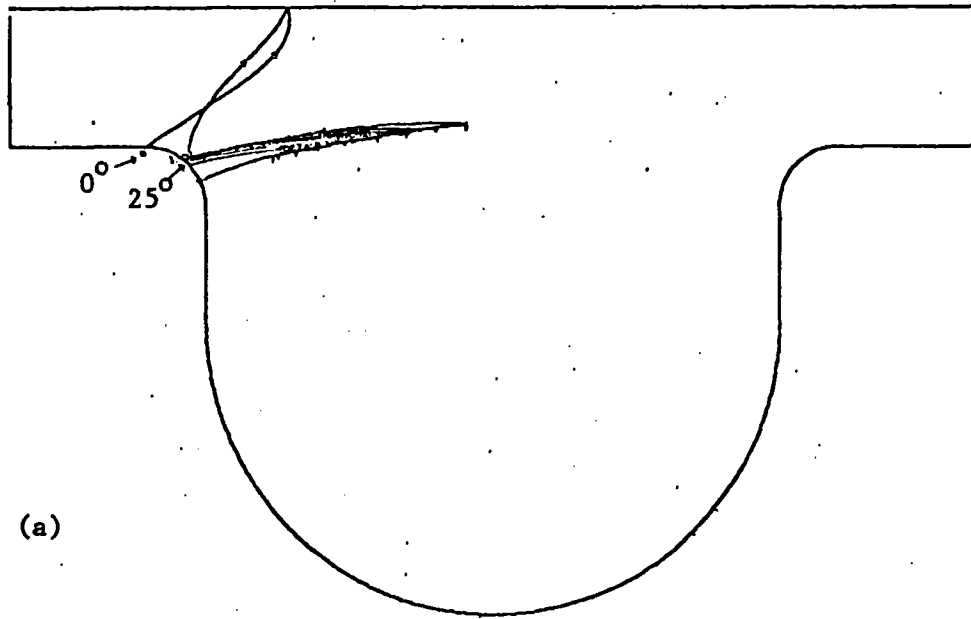


Figure 4. Trajectories for electrons with retarded phases from the same emission point but at differing fields. The gradient is 2.3 MV/m in (a) and 4.6 MV/m in (b).

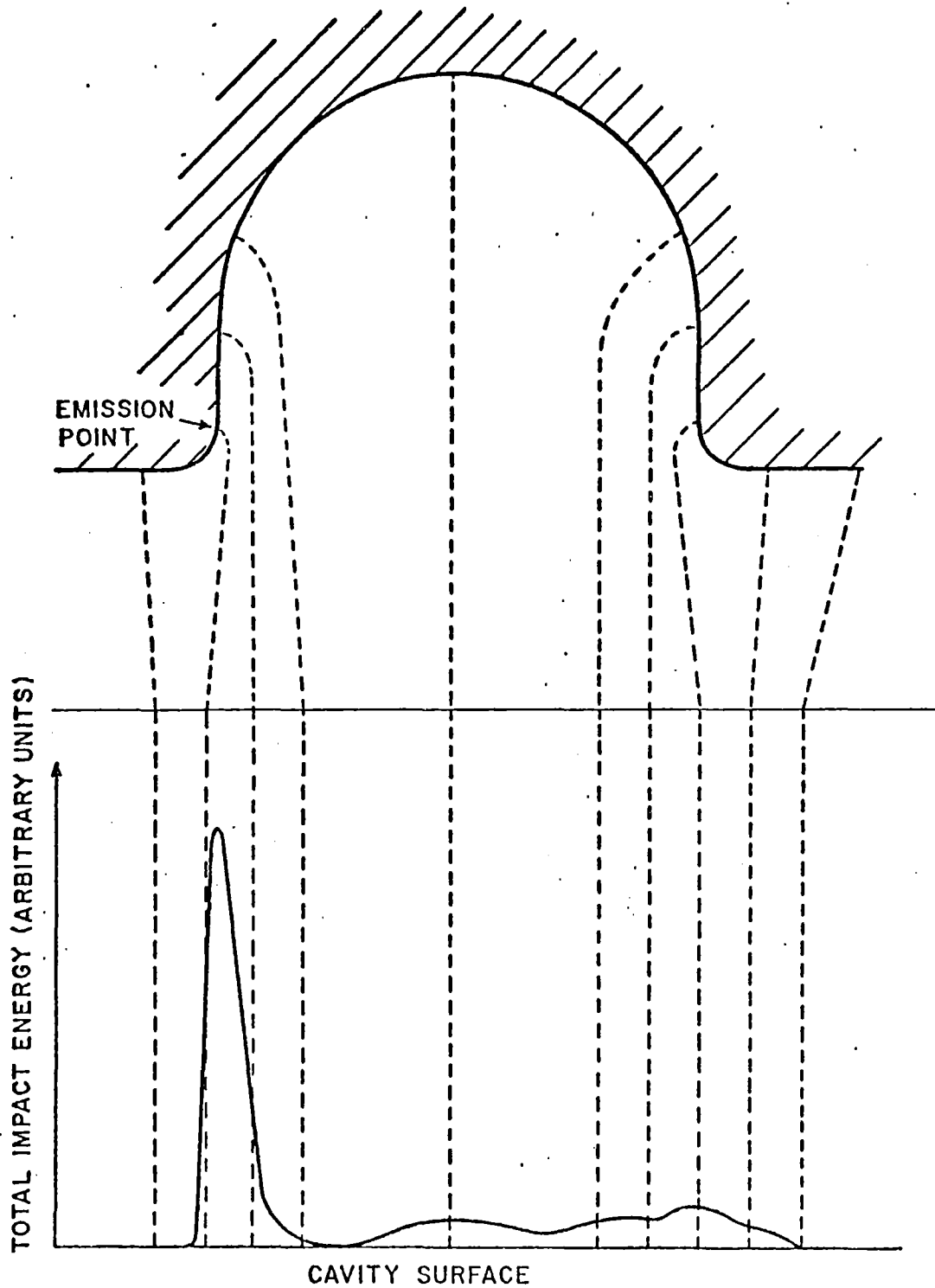


Figure 5. The distribution of total impact energy along the cavity wall for electrons emitted from a single point located in the region of maximum electric field. The emission phases are calculated using the Fowler-Nordheim expression with βE_p of 5000 MV/m. The gradient is 4.1 MV/m.

HEAT TRANSFER AND MODELS FOR BREAKDOWN

H. Padamsee
Laboratory of Nuclear Studies
Cornell University
Ithaca, NY 14853

I. Introduction

The focus of this talk will be the phenomenon of breakdown and how much is understood or not understood about it. I shall delineate and discuss the nature of various factors that play a role in determining the maximum or breakdown field strength in superconducting cavities. Electron related effects will be separated out since these have been covered in previous talks. The remaining factors may very broadly be divided into two categories: heat transport processes and heat production processes. I shall concentrate on heat transport processes and then briefly mention production processes. Finally I shall attempt to bring the two categories together in a discussion of models for breakdown developed by various people including myself and applied to Niobium. Accordingly, the talk is divided along the following lines:

I. Heat Transport

1. Thermal conductivity
2. Conductance across the solid-He boundary (Kapitza Resistance)
3. Limits for heat transfer in He-II and He-I

II. Heat Production

1. Microwave surface resistance including residual resistance
2. Defects
3. "Critical Fields"

- ### III. Models for thermal, thermal-magnetic breakdown incorporating all of the above.

I. Thermal Conductivity

Fig. 1 shows the thermal conductivity for annealed Nb¹⁾ and for annealed Pb²⁾ in the temperature range 1.5°K to the transition temperature, and for comparison, the thermal conductivity of two coppers³⁾. For normal metals the electrons contribute significantly to heat transport. In pure metals their contribution is the dominant term. Electrons are scattered by lattice vibrations (phonons) and imperfections (defects and impurities). To a first approximation the scattering probabilities of the two mechanisms can be considered independent. By analogy with the kinetic theory of gases, it is easy to show that the temperature dependence of the thermal resistivity should depend on temperature as: $1/K = B/T + AT^2$ where the first term reflects the contribution of imperfections (defects and impurities) and the second term of the phonons.

In the superconducting state the contribution of electrons to the thermal conductivity decreases as electrons condense into Cooper pairs and the transport of heat by lattice vibrations becomes more important. The temperature dependence of the electronic thermal conductivity is more complicated to derive than the simple arguments possible in the normal state. However it has been calculated from the theory of superconductivity and is shown in Fig. 2.⁴⁾ There is not too much difference whether impurities or phonons are the dominant scattering mechanisms.

The phonon conductivity is limited by scattering from electrons, point defects, dislocations (line defects) grain boundaries and sample boundaries. The phonon-electron scattering decreases strongly with temperature, as electrons condense into Cooper pairs, as shown in Fig. 3,⁵⁾ and the conductivity therefore increases.

We are now prepared to explain the shape of the curves for superconductors, Nb and Pb. Below T_c the conductivity decreases as the number of electron carriers decreases. However the phonon-electron scattering also decreases so that eventually the phonon conductivity starts to increase until it reaches the maximum imposed by scattering due to defects, grain boundaries, etc.

One of our graduate students at Cornell has recently compiled a review of the various measurements of the thermal conductivity of Nb.⁶⁾ From the various measurements it is apparent that scattering of phonons by point defects is insignificant for samples with r.r.r. \approx 10-20 which would include reactor grade Nb. The dominant scattering mechanism for phonons is by dislocations and grain boundaries (which may also be treated as dislocations) so the height of the maximum will depend on strength of these mechanisms.

There have been various measurements of the thermal conductivity of reactor grade Nb before and after annealing and the prominent features are the appearance of the phonon peak after annealing due to the growth of large crystals, i.e. reduction in grain boundaries and dislocations. These measurements have been made by Mittag,⁷⁾ at Stanford⁸⁾ and at Cornell¹⁾.

In comparison with Nb, the thermal conductivity of Pb shows a much higher value in the phonon region. Since the Debye temperature of Pb (94.5°K) is much lower than that of Nb (275°K) there are many more phonon carriers. However these figures on Pb are only partially relevant since most labs use composite systems, i.e. thin Pb layers on copper substrates. Both the thermal resistance of the transition layer and the Kapitza resistance at He interface play an important role in the effective thermal conductivity, and these will be discussed later.

Returning to Nb, let us discuss the possibility to raise the thermal conductivity still further. Even in the superconducting state when electron carriers are rapidly freezing out, the remaining electrons can be made to play a larger role by reducing the impurity scattering. Fig. 4 shows the thermal conductivity of Nb samples of increasing purity characterized by increasing r.r.r.'s¹⁾⁹⁾¹⁰⁾¹¹⁾. For samples with a high value of r.r.r., the electron conductivity remains comparable to the phonon even at 2°K.

The impurity variable has been ignored up to now, and for good reason. Commercially available Nb has Ta impurity contents of the order of 500-1000 ppm. Besides Ta, C, N, O and H are also a problem. Non Ta impurities, though present in smaller amounts, are interstitial so that they can be very effective scattering centers. For example, the electrical resistivity of Nb¹²⁾ is of the order of $5\mu\Omega\text{-cm}$ per at % of C, O, N as compared to $0.2\mu\Omega\text{-cm}$ per at % Ta.¹³⁾ For purification, multiple pass zone refining in a high vacuum helps and r.r.r. up to 2000 have been obtained¹⁴⁾. Carbon can be effectively removed by heat treating at 1800°C and 10^{-5} Torr O_2 followed by annealing very close to the melting point to remove other interstitial impurities. By this technique r.r.r. of several thousand have been obtained¹⁵⁾.

An alternative approach, and one that may lend itself more readily to cavity production is to purify the Nb by electro-deposition¹⁶⁾. This is a well-known process and can yield Ta and C concentration <5 ppm. Then, only a high temperature anneal (~2200°C) in a high vacuum ($<10^{-10}$ Torr) should remove the interstitials. At Cornell, K. Krafft has measured the Ta content of an electrodeposited sample using neutron activation analysis and indeed has found this to be less than <5 ppm. After outgassing the sample at 2200°C at 5×10^{-9} Torr she obtained the result shown in Fig. 5. The absence of a significant phonon peak is due to excess strains caused by the resistive

annealing technique. Further annealing in a better vacuum is contemplated as the next step. At HEPL, an X-band cavity has been fabricated out of electrodeposited Nb. A-peak field value of 1100 Gauss has been achieved¹⁷⁾.

Finally Fig. 6 shows the thermal conductivity of Nb_3Sn ¹⁸⁾ which is very low due to the small grain size (1-10 μ m) and possibly large number of dislocations and strains due to the diffusion growth process.

2) Kapitza Conductance

Unlike the subject of thermal conductivity, the heat transport across a solid-He interface is much less understood, in spite of the substantial amount of research, both experimental and theoretical¹⁹⁾.

When heat (Q) flows from a solid body into liquid He there is a small temperature difference (ΔT) across the interface. The ratio $\Delta T/Q$ is effectively the thermal resistance for the boundary. This temperature discontinuity was first observed for solid-He II interface by Kapitza and is since called the Kapitza Resistance (R_k) or its inverse the Kapitza Conductance (H_k). H_k depends on temperature, pressure, the elastic properties of the solid, the structure of the surface, as well as the properties of liquid He. I will concentrate on the solid-He II interface for which most of the experimental work has been done, and make just a few remarks regarding solid-He I.

To a good approximation heat transport across the solid-He interface takes place predominantly via the phonons. Since He-II is an insulator, the electrons must give up their energy to the phonons before it is transmitted across the interface. This is even more so for superconductors for which phonons are the dominant heat carriers. By analogy with black body photon radiation, phonons can be treated as bosons whereby it is possible to derive an upper bound to phonon transmission across the interface.

$$H_k^{PRL} = \frac{2\pi^4 K_B^2}{5\hbar\theta_D^2} \left(\frac{3N}{4\pi}\right)^{2/3} T^3.$$

For solids of interest to us the numbers are

Pb:	$2.8T^3$ watts/cm ² K	$\theta_D = 100^\circ\text{K}$
Nb:	$0.69T^3$	275
Cu:	$0.44T^3$	343

Fig. 7 shows measured values the Kapitza conductance of Nb⁷⁾, Pb²⁰⁾ and Cu²⁰⁾ together with the phonon radiation limit.

The measured values show a T^3 to T^4 power law and are typically an order of magnitude or more below the PRL limit, the highest values ever measured being about a factor 5 below.

The theoretical understanding of the lower phonon transmission is that there is a large impedance mismatch across the interface. As a result, a large fraction of the phonons impinging on the interface cannot get through. The acoustic impedance is given by the product of the density (ρ) and sound velocity (V_s). For solids, ρ is typically 5 gm/cc and $V_s \sim 5 \times 10^5$ cm/sec and for liquid He, ~ 0.14 gm/cc and first sound velocity $\sim 2.4 \times 10^4$ cm/sec so that the acoustic impedance of a solid may be 10^2 to 10^3 times greater than the impedance in He. This is the basic idea underlying Khalatnikov's²¹⁾ acoustic

mismatch (AM) theory, from which H_k values can be calculated. Results are shown in Fig. 7 also. The problem, however, is that the AM theory predicts H_k values that are more than an order of magnitude lower than the measured values.

As can be seen from Fig. 7, on the experimental side there are considerable variations in the data due largely to variations in surface preparation, and to some extent also to measurement difficulties. These difficulties are related to measurement of the actual area over which the phonon transmission takes place and the measurement of the temperature of the boundary on the solid side. The latter problem is especially acute in materials of low conductivity such as superconductors, and is a serious problem if there is an additional boundary layer of low K , such as a surface damage layer or a thick oxide layer.

Judging from the many studies of the variations in H_k with surface preparation, several important trends emerge: 1) surface strains, damage layers, oxide layers and chemical impurity layers all lower H_k . Sometimes surface strains are introduced inadvertently during sample mounting (e.g., In joints, solder joints, etc.) and this is probably responsible for some of the large variation in the data. ²⁰⁾ The data ⁷⁾ on annealed vs. as received Nb are in agreement with this trend. 2) Monolayers of surface contaminants on very clean samples, e.g. pump oil, physio-chemisorbed surface impurities raise H_k .

In spite of the large variation of the data, it is clear that the AM theory is unsatisfactory. The theory however works much better at temperatures less than 1°K, and for various solid-solid interfaces such as In-sapphire, which suggests that additional phonon transmission mechanisms peculiar to He become operative above 1°K. It is unlikely that the superfluid properties of He-II are involved in additional transport mechanisms since the

problems are present in solid-He³ interfaces as well.

Various theoretical modifications²²⁾ of the AM theory have been proposed to explain the enhanced transmission. I will briefly mention a few to give a flavor for the subject.

1) A very dense layer, $\sim 15 \text{ \AA}$ thick, of helium atoms nears the solid surface serves as an acoustic matching unit. The dense layer is formed due to VanderWaals attraction between the solid and He. The problems are that the increased conductance is not enough, the temperature dependence is stronger (T^4) than usually observed (T^3). However the agreement between predicted and observed pressure dependence is improved over the AM theory.

2) Impinging phonons from the liquid cause a surface disturbance of the charge density which modifies the potential in which the electrons move. Therefore there is an additional transmission of energy through this coupling mechanism between phonons in the liquid and conduction electrons. The problems are once again that the predicted increase in conductance is small. Recent measurements for Pb in the normal and superconducting states, which carefully exclude strain effects, show that this effect is of relatively minor importance²⁰⁾.

3) Phonons impinging on the surface of the solid at angles larger than the initial angle are not totally internally reflected as expected but due to some loss mechanism, related to the detail nature of the surface, set up evanescent waves and transfer of energy. The source of this dissipation could be surface roughness, the first few monolayers of adsorbed helium, or monolayer contaminants.

To summarize, no single simple explanation is likely to be found. It is probably important to consider details of the energy density of the phonons as a function of frequency. The transmission probability for phonons is also a function of frequency, the high frequency (higher temperature) phonons having a higher probability.

Solid-solid interfaces such as Pb-Cu²³⁾ have been in use for quite some time and the use of Nb-Cu²⁴⁾ is increasing. For Pb-Cu interfaces two sets of measurements have been reported. In the first²⁵⁾, thin Pb layers were "tinned" on to copper samples and then "sweat" together. The thickness of the resulting Pb layer was 40 μ m. The conductance measured was $0.64T^{2.8}$ in the first test and $0.13T^{4.1}$ in a second test 2 months later. Thicker samples (200 μ m) gave lower H_k throughout the temperature range of interest and a higher power law. In the second²⁶⁾ set of measurements, the interface was made by vacuum casting Pb and Cu cylinders together. $H_k = 0.11T^{3.7}$ was obtained. Taking the highest values for Pb-Cu together with the highest value for Cu a net conductance of 0.34 watts/cm²K is expected at 1.5°K compared to 0.13 for Nb.

Schmidt²⁷⁾ prepared Nb-Cu interfaces by diffusion welding at 850°C and 10^{-6} Torr. He obtained $H_k = 0.11T^3$ watts/cm²K. Taking the highest value for Cu-He II surfaces, the net conductance expected at 1.5°K is 0.20 compared to 0.13 for Nb-He, a 50% improvement.

To summarize the composite materials case, at 1.5°K the conductance for Cu-Pb is almost a factor of 3 higher than Nb and that of Nb-Cu is at best only 50% better than Nb.

Finally some remarks about two topics: Kapitza conductance at large heat currents and conductance for solid-He I interface. Usually H_k is defined as: $\lim(Q/\Delta T)$ as $\Delta T \rightarrow 0$. At large values of ΔT , H can be derived from phonon radiation laws:

$$H\Delta T = \sigma(T+\Delta T)^4 - \sigma T^4$$

so that

$$H(T, T_b) = H_k \left[1 + \frac{3}{2} \frac{\Delta T}{T} + \frac{1}{4} \left(\frac{\Delta T}{T} \right)^3 \right] \text{ where } \Delta T = (T - T_{\text{Bath}})$$

This relationship has been found to be experimentally valid²⁸⁾ in the range $0 < \Delta T < \Delta T^*$ where ΔT^* is the temperature difference at the onset of film boiling, discussed in the next section.

If the radiated phonon energy is the only important contribution to H_k then we would expect H_k will not change through T_λ . Experimentally there are considerable difficulties in measuring H_k above T_λ . Values of H_k are much larger due to more phonons available at higher temperatures so that ΔT is much smaller and difficult to measure. Accurate temperature measurements on the He-I side pose great difficulties compared to the superfluid since convection effects begin play a role at small heat fluxes.

3. Heat Transfer in He-II

High frequency cavities use He-II for cooling because the improvement factor due to the lower surface resistance far outweighs the cost of providing additional refrigeration. The thermal conductivity of He-II is enormous. In small channels for example it can approach values about 10^4 times higher than in Cu²⁹⁾.

The transport of heat in He-II is analyzed using superfluid hydrodynamics. In terms of the two fluid model, the mechanism of heat transfer in superfluid He is based on a counterflow of two components; the normal component, that carries the heat, moves away from the source, and the superfluid towards the source. This phenomenon is referred to as zero net mass flow or internal convection. For small velocities the only dissipative process arises from the normal fluid viscosity. Above a certain critical velocity turbulent motion occurs in one or both components and additional loss mechanisms occur.

At the critical heat flux density a phase transition from He-II to vapor takes place. Several investigations have been made regarding the value of the critical flux vs. temperature; a typical curve³⁰⁾ is shown in Fig. 8. The shape of the curve can be well understood in terms of superfluid hydrodynamics. The height of the maximum depends on the length of the cooling channel, approaching an asymptotic value of 1 watt/cm² for long channels. G. Krafft³⁰⁾ was able to identify the phase transition from He-II to gas as the cause of the breakdown of heat transport in He-II. Using the peak flux equation from superfluid hydrodynamics (i.e. the graph in Fig. 8) and the Kapitza conductance $H = H_k f T^3$, the maximum surface temperature ΔT^* prior to superfluid breakdown may be estimated for solid-He II interfaces. This procedure was found to give agreement with measured values of ΔT (~1K) for a Ag-He II surface²⁸⁾.

4. Heat Transfer in He-I

The thermal conductivity of He-I is $\sim 0.8 \times 10^{-4}$ watts/cm K. At lower temperatures it decreases almost linearly to 0.4×10^{-4} .³¹⁾ For vanishingly small heat currents heat transfer is by conduction alone since the tendency towards microscopic convective motion is prevented by viscous resistance. As the heat flux increases above critical value streamline convection begins, which changes over to the turbulent state. Around 5 mW/cm² bubbles³²⁾ start to form on the heated object and help carry away the heat more effectively. This condition is known as nucleate pool boiling. In the nucleate boiling range bubbles of helium vapor are formed at nucleation sites on the heated surface and depart from the surface. The bubbles transport the latent heat of the phase change and the heated surface is cooled. Nucleate boiling (NB) continues until the heat flux reaches the peak nucleate boiling flux (PNBF). For heat flow above the PNBF (or the burn out heat flux), the activated nucleation sites are so numerous that the bubbles at the surface coalesce and the

heated surface is covered with a film of vapor. This is the film boiling range. Fig. 9 shows the heat transfer coefficient for He-I vs. the temperature difference between the heated surface and the helium bath³³⁾.

The PNBF as well as the shape of the NB curve depend on a large number of variables: nature of the heating surface, roughness, pressure, temperature of helium, surface orientation and geometry³³⁾.

- 1) The nature of the heating surface does not affect the NB curve to a great extent but the value of the PNBF could be different for each surface.
- 2) The heat transfer coefficient increases with increasing pressure but the PNBF are lowered. Lowering the pressure also lowers the PNBF by a factor 2 up to λ -point. Fig. 10 shows the behavior of the maximum flux before film boiling for the same sample through the λ -point. This means that if the heat flux on the He side is approaching 1 watt/cm^2 and is just below the film boiling limit below the λ -point, it may exceed the PNBF above the λ -point. This phenomenon has been observed in thin wall (0.5 mm) cavities operating near the breakdown threshold.³⁴⁾ Above the λ -point, there is a large drop in Q and breakdown threshold. Similar discontinuities across the λ -point have been observed at CERN³⁵⁾, suggesting that film boiling can play an important role for maximum achievable gradients.
- 3) A rough surface increases the heat transfer coefficient but has very little effect on the PNBF.
- 4) The major effect of surface orientation is on the PNBF. The lowest PNBF value is obtained with the heating surface facing downward. Vertical surfaces exhibit PNBF values 3 times higher and horizontal surfaces facing upward about 4 times higher at 4.2°K .

5) PNB decreases with the height of the boiling surface. Bubbles leaving the surface set up a thermosyphon action. The bubbles leaving the lower portion of the heated surface are transported to the upper portion by the fluid motion decreasing the quality in this region. High heating surfaces are therefore more unstable than short-heating surfaces.

II. Heat Production

I shall now turn to the other part of the picture--heat production.

1) Surface Resistance:

The microwave surface resistance has been amply discussed in the other review talks. The various possible sources of residual resistance heating have also been thoroughly covered.

2) Defects:

Localized heat sources with large losses have been loosely referred to as defects. So far there are only a few types of defects that have been definitely correlated with observed breakdown. These are: small balls of Nb left behind as weld spatter, non-superconducting inclusions identified by their different color appearance upon anodization²⁴⁾, certain kinds of "dust" particles, probably metallic shavings, or oxide from welds, deliberately introduced into cavities from the vacuum system.³⁶⁾ It is not known whether all dust particles that light up in the rf are potential breakdown sources. In addition it is known that beam welds can be sources of defects but the exact nature of the source has not been determined.³⁶⁾

In a large fraction of cases, however, optical examination of the breakdown region in open cavities have not revealed any prominent irregularities in the vicinity. Much work remains to be done in this area.

3) Critical Fields:

The upper limit to H_{rf} is determined by the appropriate critical field. For type I superconductors In, Sn and Pb, the superheating critical field has been shown experimentally to be the limit.³⁷⁾ Near T_c , $H_{rf}/H_c = 3.5$, 3.1 and 1.5 have been obtained for these materials and these values agree with H_{sh}/H_c . At lower temperature both experiment and theory show H_{sh}/H_c decreases, e.g. for Sn at $t = 0.8$, the ratio is reduced to 2. For Pb a value of 1.4 has been obtained at $t = 0.3$.

For Type II superconductors both theory and experiment predict a lower H_{sh}/H_c and a weaker temperature dependence. For Type II alloy samples of SnIn and InBi values of H_{rf} between H_{sh} and H_{c1} were found²⁷⁾. Therefore it is not yet clear what the situation for Nb ($K \sim 0.8$) should be. Theory predicts $H_{sh} = 1.3 H_c$ so that a value between $H_{c1} = 1780$ to $H_{sh} = 2600$ gauss is expected. In any case, except in isolated cases, experimentally observed values for Nb are far below H_{c1} --a reflection of the fact that other limitations play a role.

III. Models for Breakdown

One school of thought³⁸⁾ is that there are local regions of low H_c (or H_{c1} or H_{sh}) which are suddenly driven normal at H_{rf} . Without any further increase in H , this region grows to a macroscopic size by driving the neighboring superconductor to a high temperature due to the excess power dissipation. The other school of thought is that there are always local lossy (or defect) areas that cause a highly non-uniform surface temperature distribution. Above a certain power level a temperature instability may result near one of these defects due to the exponential nature of the surface resistance and the limitations in heat transport processes--driving a macroscopic region normal. In one case the driving force is a magnetic instability and in the other a thermal instability. There is a third possibility, inter-

mediate between thermal and magnetic. The temperature in the neighborhood of a defect does not increase unstably but exceeds the local critical temperature which depends on the value of H at the surface through $H_{\text{surf}} = H_c(0) [1 - (T/9.2)^2]$.

Two distinct types of experimental observations lend support to the thermal instability, at least below 500 gauss. In the first, heating is observed at or near a breakdown spot below H_{rf} . At Cornell we observed³⁶⁾ heating at weld defects well below H_c , and recent experiments at CERN³⁹⁾ also show similar results. Secondly, in a recent series of experiments done at Cornell by Proch, the breakdown fields obtained in the two pass band modes (π and $\pi/2$) of a 2-cell cavity were determined by individually exciting the modes. A common breakdown spot for both modes was observed by thermometry. Then both modes were excited simultaneously and different ratios of field amplitudes were selected to obtain breakdown at the same spot. If the magnetic instability model were applicable one would expect $(H_{\pi/2}) + (H_{\pi}) = \text{constant}$ whereas in the case of the temperature instability one would expect: $H_{\pi}^2 + H_{\pi/2}^2 = \text{constant}$ (Fig. 11.) In several test cavities for which H_{rf} ranged from 150 to 500 gauss the 2nd result was quite unambiguously obtained. Furthermore when equal power is applied in both modes, the peak value of H at the breakdown location is $\sqrt{2}$ higher than H in either mode alone, quite strongly ruling out a magnetic instability.

If, as the above experiments suggest, the temperature distribution near defective areas is the determining factor, then all the heat transfer considerations discussed earlier indeed play an important role in ultimate breakdown field levels.

Several authors have developed quantitative models incorporating some of the various aspects of heat transfer and production discussed here under various simplifying assumptions, Hillenbrand, et al.⁴⁰⁾ made the first

model calculations for the instability threshold for Nb without defects. Isagawa⁴¹⁾ extended these calculations to include lateral heat flow and wall curvature effects. Lyneis et al.⁴²⁾ calculated instability thresholds for line defects and also for the defect free case. At Cornell we have developed a computer code based on an iterative solution of heat flow equations to solve for the equilibrium temperature distribution in the vicinity of a small circular defect.⁴³⁾

The common feature of all the thermal models is the calculation of the equilibrium surface temperature for a fixed rf power. As the rf power is increased new equilibrium temperatures are calculated. Above a certain power level, the temperature of the surface increases unstably--basically due to the exponential nature of the rf surface resistance. The lowest field (power level) for which an equilibrium temperature distribution can be determined is defined as H_{rf} .

Using the Cornell code it is possible to study the dependence of a thermal or thermal-magnetic instability threshold on several variables such as: defect size, defect resistance, bath temperature, rf frequency, $K(T)$, $H_k(T)$, wall thickness, residual resistance and heat transfer limits to the He bath. A slight modification of the model allows the proper calculation of the defect free case. As one can imagine, the phase space of variables for this kind of calculation is enormous. I shall attempt to give just a few typical, but interesting, results in detail and then summarize the general trends.

Results for Defect Free Nb (Frequency and temperature dependence)

For zero residual resistance (Fig. 12) the low frequency (<3 GHz) H_{rf} 's are higher than H_c at 1.5°K, so that thermal instability should not be a problem at frequencies less than ~6 GHz. At 6 GHz the limit is 1700 Gauss

and decreases to 1100 Gauss at 8.6 GHz. These values are in good agreement with results of defect free model calculations of Isagawa and Lyneis. The inclusion of a R.R. of $1 \times 10^{-7} \Omega$, corresponding to a Q_0 of 2×10^9 lowers H_{rf} and also weakens somewhat the frequency dependence. At X-band, for example, H_{rf} is limited to 850 Gauss at 1.5°K. This is less than experimentally measured values for best cavities at Siemens⁴⁰⁾, HEPL⁴⁴⁾, Cornell³⁴⁾ and SLAC⁴⁵⁾. I offer two possible interpretations for this discrepancy. In the first case, it is not clear that the concept of a uniform residual resistance is valid, i.e. in the exceptional cavities, it is possible that the high field regions are both defect free and have very low residual losses. Secondly, note that for the defect free case, most of the temperature drop between the rf surface and the helium bath takes place at the Nb-He II interface (at 8.6 GHz, for example, the temperature of the rf surface just below the instability threshold is only 0.14°K above the bath temperature and the power input to the rf surface is 20 mw/cm²). This indicates the important role played by H_k . From my earlier discussion on H_k , it is conceivable that the H_k for these cavities was a factor 2-3 higher than the values measured by Mittag, depending on the details at the surface. This effect would be sufficient to increase H_{rf} to the observed values or higher.

The temperature dependence of H_{rf} from 1.3 to the λ -point is shown in Fig. 13 and compared with the experimental results of Hillenbrand et al. There is good agreement in the shape of the curves, and the difference in the absolute value could be attributed once again to H_k . A final noteworthy case for the defect free calculation is at 500 MHz and 4.2°K, where $H_{rf} = 1500$ Gauss was calculated.

To summarize, the defect free results, thermal instability will not be a problem except at very high frequencies. In this case the value of H_{rf} will be quite sensitive to H_k .

Defects

I shall discuss the typical results for a defect case using S-band frequency, annealed Nb at 1.5°K bath temperature. The defect chosen is 0.15 mm in radius (150 μ m) with a surface resistance of $8 \times 10^{-4} \Omega$ (1/3 the resistance of Nb in the normal state). Typically one such defect per 10 cm² would contribute a residual loss of 56n Ω or a Q_0 of 3.5×10^9 .

Calculated temperature profiles for 4 values of the magnetic field are shown in Fig. 14. As the field is increased the temperature in the vicinity of the defect increases. At the highest field for which a stable temperature exists the temperature of the superconductor in the immediate vicinity of the defect is 1.2° below the critical temperature ($T_c \sim 7.35^\circ$). At the threshold, the power input to the surface through the defect alone is ~ 94 m Watts which corresponds to a power density of 132 watt/cm². The decrease in Q expected from the heated neighborhood is 20%, just below breakdown.

Fig. 15 shows the temperature profiles along an axial line through the center of the disk from the defect to the helium bath. The Kapitza drop is 0.42°K. The temperature on the He side of the Nb is shown in Fig. 16. These curves predict that the temperature increase should be observable well below breakdown. The highest value of the heat flux at the helium side just below the defect is 1/4 watt/cm², significantly lower than the film boiling limit. The effect of lateral heat flow forced by the Kapitza resistance helps distribute the heat more uniformly on the He side to the safe value. As shown in Fig. 17 the bath temperature dependence of the breakdown field is much weaker in the presence of defects than in the defect free case, as shown earlier in Fig. 13. Finally,

The inclusion of a uniform R.R. on top of the defect lowers H_{rf} to 690 Gauss. Once again it is not clear whether R.R. ought to be included in the defect model, since the defect themselves contribute to R.R.

Special cases:

- 1) One interesting question is: what information does the calculation provide regarding the nature of the instability? Is it thermal or thermal-magnetic? The lower curve in Fig. 18 shows the temperature in the immediate neighborhood of the defect as the rf field level is increased. The instability threshold is indicated by the arrow.

Values of T_c calculated from

$$H_{rf} = 2000 \text{ (Gauss)} [1 - (T_c/9.2)^2]$$

are also shown in the uppermost curve to indicate how far the surface temperature is from the critical temperature. The instability threshold (indicated by the arrow) is almost 2°K less than T_c at 700 Gauss showing that the driving force is definitely thermal. It is interesting to note that if T_c' as calculated from

$$\sqrt{2} H_{rf} = 2000 \text{ (Gauss)} [1 - (T_c'/9.2)^2]$$

is compared (middle curve) the surface temperature is below even this lower value of T_c' . This feature is consistent with Proch's observations on mode mixing discussed earlier.

- 2) At 500 MHz and 4.2K, using a R.R. of 1×10^{-7} the same size defect used at S-band showed a breakdown field of 314 Gauss. A film boiling limit of 0.3 watt/cm^2 was used and was exceeded around 225 Gauss. Above 225 Gauss, the conductance to the helium bath was automatically adjusted down so that at no mesh element did the heat flow exceed 0.3 watt/cm^2 .

Using this procedure a thermal instability was finally encountered at 314 Gauss.

To summarize the results of the defect model, the breakdown field level depends on a variety of factors related to heat transport and production. Primarily the exponential nature of the surface resistance plays the predominant role. At 4°K it is conceivable that film boiling can play an important role. Following the thermometry results of CERN and Cornell and the mode mixing experiments, it seems that thermal instability is the major driving force. The complete phase space of variables is still being explored but some general conclusions and problems are summarized here.

- 1) The breakdown field increases with decreasing frequency. The general trend shown by experimental data at lower frequencies is the opposite. However, lower frequency cavities also suffer from e^- loading effects and these may be a major factor in the discrepancy. Furthermore, low frequency rf structures are larger and more difficult to process so that the probability of having poorly processed areas and therefore bigger defects is higher.
- 2) The breakdown field is essentially independent of wall thickness in the defect free case up to very small thicknesses, in which case the field increases slightly. In the presence of defects H_{rf} is essential independent of thickness up to 1 mm. For smaller thicknesses, H_{rf} decreases, because the lateral heat flow is impeded.

Finally a last bit of titillating information obtained from toying with the idea of improved thermal conductivity. Referring to some of the thermal conductivity curves displayed for purified Nb in Fig. 4, Table I shows the result for H_{rf} of plugging in these curves for the S-band test case discussed earlier.

Table I

<u>R.R.R.</u>	$\frac{K(4^\circ K)}{\text{watts/cm}^\circ K}$	<u>H_{rf} (model)</u>
10	0.1	730
300	0.7	1000
1900	3	1260
17000	20	1400

These calculations show that improved cooling of the superconductor in the vicinity of a defect should allow more power to be dissipated at the defect before thermal instability sets in--and thereby higher ultimate breakdown field levels.

Acknowledgements

Many thanks are due to Dieter Proch, Claude Lyneis and Kathy Krafft for valuable discussions during the course of preparing this talk. I am especially grateful to Kathy Krafft for allowing me to use results from her thesis research. Special thanks are due to Prof. Piel for sending me information on current activities at CERN and Wuppertal.

References

- 1) L. Phillips, Cornell University, private communication (data from 1,3 to 4.2°K) and G. K. White and S. B. Woods, Can. J. Phys. 35, 892 (1957), (data from 4-9°K).
- 2) Y.S. Touloukian, R.W. Powell, C.Y. Ho and P.G. Klemens, TPRC vol. 1, "Thermal Conductivity", JFI/Plenum N.Y. 1970, Pb pp. 175, curve #55.
- 3) V.J. Johnson, Wadd Technical Report 66-56, pt. II, "A Compendium of the Properties of Materials at Low Temperature (Phase 1), Part 1 Properties of Solids", NBS (1960).
- 4) L.P. Kadanoff and P.L. Martin, Phys. Rev. 124, 670 (1961).
- 5) J. Bardeen, G. Rickayzen and L. Tewordt, Phys. Rev. 113, 982 (1959).
- 6) K. R. Krafft, Cornell University, Laboratory of Nuclear Studies, Report no. CLNS 80/468.
- 7) K. Mittag, Cryogenics 13, 94 (1973).
- 8) H. Brechna, SLAC, private communication.
- 9) A. Gladun, C. Gladun, M. Knorn and H. Vinzelberg, J. Low Temp. Phys. 27, 873, (1977).
- 10) Y. Muto, K. Noto and T. Fukuroi, Proc. 11th Int'l. Conf. Low Temp. Phys., Vol. 2, p. 930 (St. Andrews, 1968).
- 11) W. Wasserbach, Phys. Stat. Sol. B84, 205 (1977).

- 12) J. Berthel, K.H. Berthel et al., Phys. Metals and Metallography vol. 35, no. 5, p. 23 (1973); K. Schulze, J. Fub, H. Schultz and S. Hofman, Z. Metallkunde 67, 737 (1976).
- 13) R. W. Meyerhoff, J. Electrochem Soc. 118, 997 (1971).
- 14) R.E. Reed, J. Vac. Sci. Technol. 9, 1413 (1972).
- 15) See 14
- 16) See 13 and Berthel et al., Ref. 12
- 17) C. M. Lyneis, HEPL, private communication.
- 18) G.E. Childs, L.J. Ericks, and R.L. Powell, "Thermal Conductivity of Solids at Room Temperature and Below. A Review and Compilation of the Literature", NBS Monograph 131 (1973).
- 19) The following reviews, and work cited therein are intended as general references: T.H.K. Frederking, Adv. in Cryogenic Heat Transfer, Chem. Engr. Progr. Symp. Series 64, no. 87, p. 21 (1968); G.L. Pollack, Rev. Mod. Phys. 41, 48 (1969), N.S. Snyder, Cryogenics 10, 89 (1970); L.J. Challis, J. Phys. C7, 481 (1974); D. Cheeke and H. Ettinger, J. Low Temp. Phys. 36, p. 121 (1979).
- 20) F. Wagner, F.J. Kollaritis K.E. Wilkes and M. Yaqub, J. Low Temp Phys. 20, p. 181 (1975).
- 21) J.M. Khalatnikov, Zh. Eksperim.i.Teor, Fiz. 22, 687 (1952).
- 22) A.C. Anderson, Proc. Phonon Scattering in Solids, ed. L.I. Challis, V.W. Rampton and A.F.G. Wyatt (Plenum, N.Y., 1976), p.1.
- 23) Y. Bryunseraede, D. Gorle, D. Leroy and P. Morignot, Physica 54, 137 (1971); K.W. Shepard, J.E. Mercereau, and G.J. Dick, IEEE Trans. NS-22, 1179 (1975).

- 24) K.W. Shepard, C.H. Scheibelhut, P. Markovich, R. Benaroya, and L.M. Bollinger, IEEE Trans. Mag-15, p. 666 (1979); T. Yogi, Caltech, private communication
- 25) L.J. Challis and J.D.N. Cheeke, Phys. Lett. 5, 305 (1963).
- 26) L.J. Barnes and J.R. Dillinger, Phys. Rev. 141, 615 (1966).
- 27) C. Schmidt, J. App. Phys. 46, 1372 (1975).
- 28) T.H.K. Frederking, Chem. Engr. Progr. Symp. 64, no. 87, p. 21 (1968).
- 29) D.S. Betts, Cryogenics 16, 3 (1976).
- 30) G. Krafft, Thesis, Kernforschungszentrum, Karlsruhe Report no. KFK-1786 (1973), English Translation from Argonne National Lab, Report ANL-Trans-1032.
- 31) R.V. Smith, Cryogenics 9, 11, (1969).
- 32) H. Tsuruga and K. Endoh, Proc. of the 5th Int'l. Cryogenic Engineering Conf., ICEC5, Kyoto, p. 262 (1974).
- 33) C. Johannes, Proc. of the 3rd. Int'l. Cryogenic Engr. Conf., ICEC3, p. 97 (1970).
- 34) H. Padamsee, M. Banner, J. Kirchgessner, M. Tigner and R. Sundelin, IEEE Trans. Mag-15, p. 602 (1978).
- 35) H. Piel, Univ. of Wuppertal, private communication.
- 36) H. Padamsee, J. Kirchgessner, M. Tigner, R. Sundelin, M. Banner, J. Stimmel and H. L. Phillips, IEEE Mag-13, p. 346 (1977); See also Cornell University, Lab. of Nuclear Studies report CLNS-340 (1976).
- 37) T. Yogi, G. J. Dick and J.E. Mercereau, Phys. Rev. Lett. 39, 826 (1977).
- 38) J. Halbritter Proc. 1972 Appl. Sup. Conf., Annapolis (IEEE, N.Y. 1972) p. 662.
- 39) P. Bernard, H. Heinrichs, H. Lengeler, E. Picasso and H. Piel, LEP note 209 (1980).

- 40) B. Hillenbrand, H. Martens, K. Schnitzke, H. Diepers, Proc. 9th Int'l. Conf. on High Energy Accelerators, Stanford 1974, p. 143.
- 41) S. Isagawa and K. Isagawa, KEK, private communication.
- 42) C.M. Lyneis and J.P. Turneaure, IEEE Trans. Mag-13, p. 339 (1976).
- 43) A. Deniz and H. Padamsee, Cornell University, Laboratory of Nuclear Studies Report CLNS-79/434 (1979)--see also revised version to be published.
- 44) J.P. Turneaure and Nguyen Tuong Viet, Appl. Phys. Lett. 16, 333, 1970).
- 45) P.B. Wilson, Z.D. Farkas, H.A. Hogg, and E.W. Hoyt, SLAC PUB-1228 (1973).

Fig. 1: Thermal conductivity of Nb, Pb and Cu.

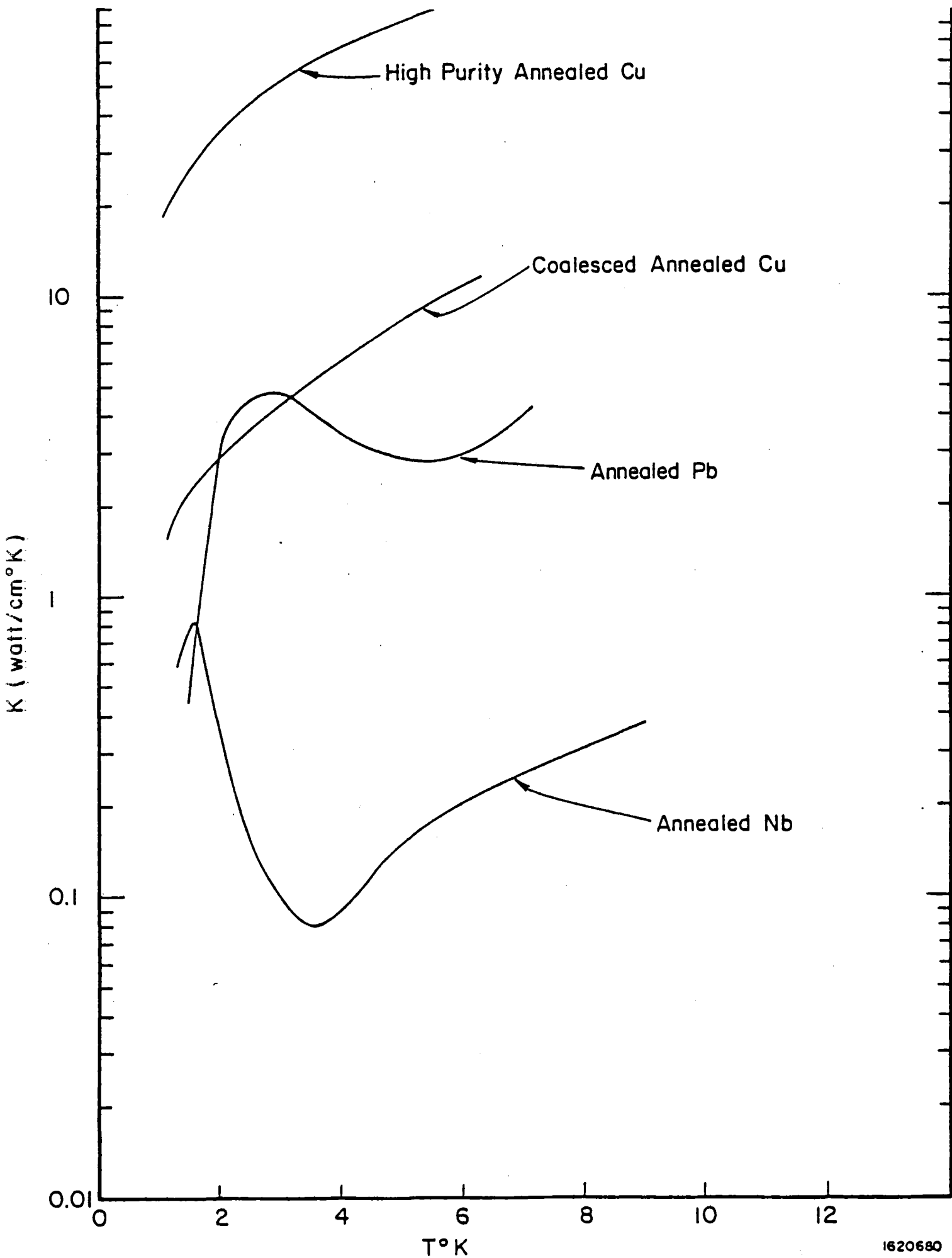


Fig. 2: Ratio of the electronic thermal conductivity in the superconducting state (K_s) to the electronic thermal conductivity in the normal state (K_n) as calculated in Ref. 4.

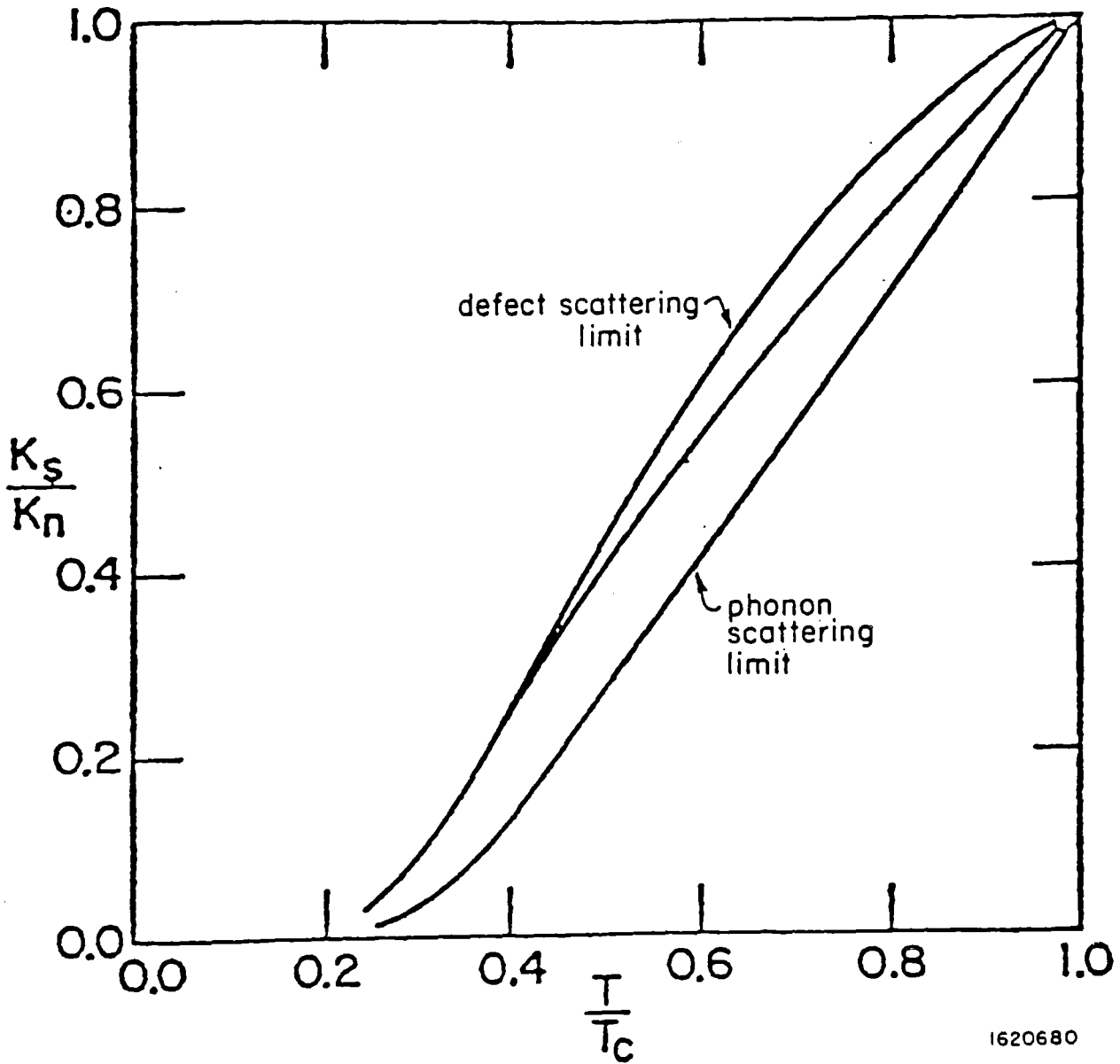


Fig. 3: Ratio of the phonon conductivity in the superconducting state (κ_{gs}) to the phonon conductivity in the normal (κ_{gn}) when electron scattering is predominant as calculated in Ref. 5.

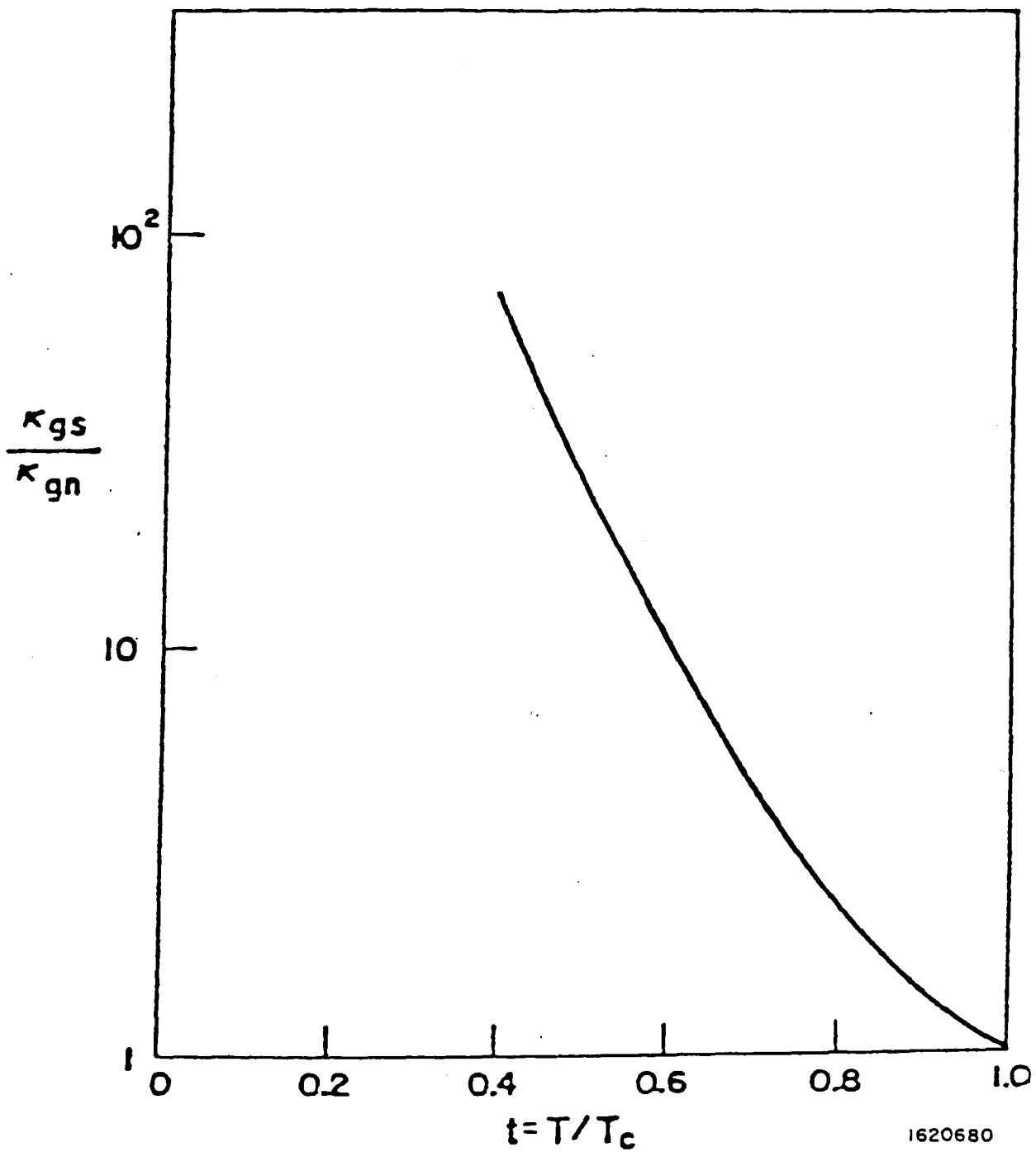


Fig. 4: Thermal conductivities of four Nb samples with different residual resistivity ratios (R.R.R.), showing the effect of impurities on the thermal conductivity of Nb.

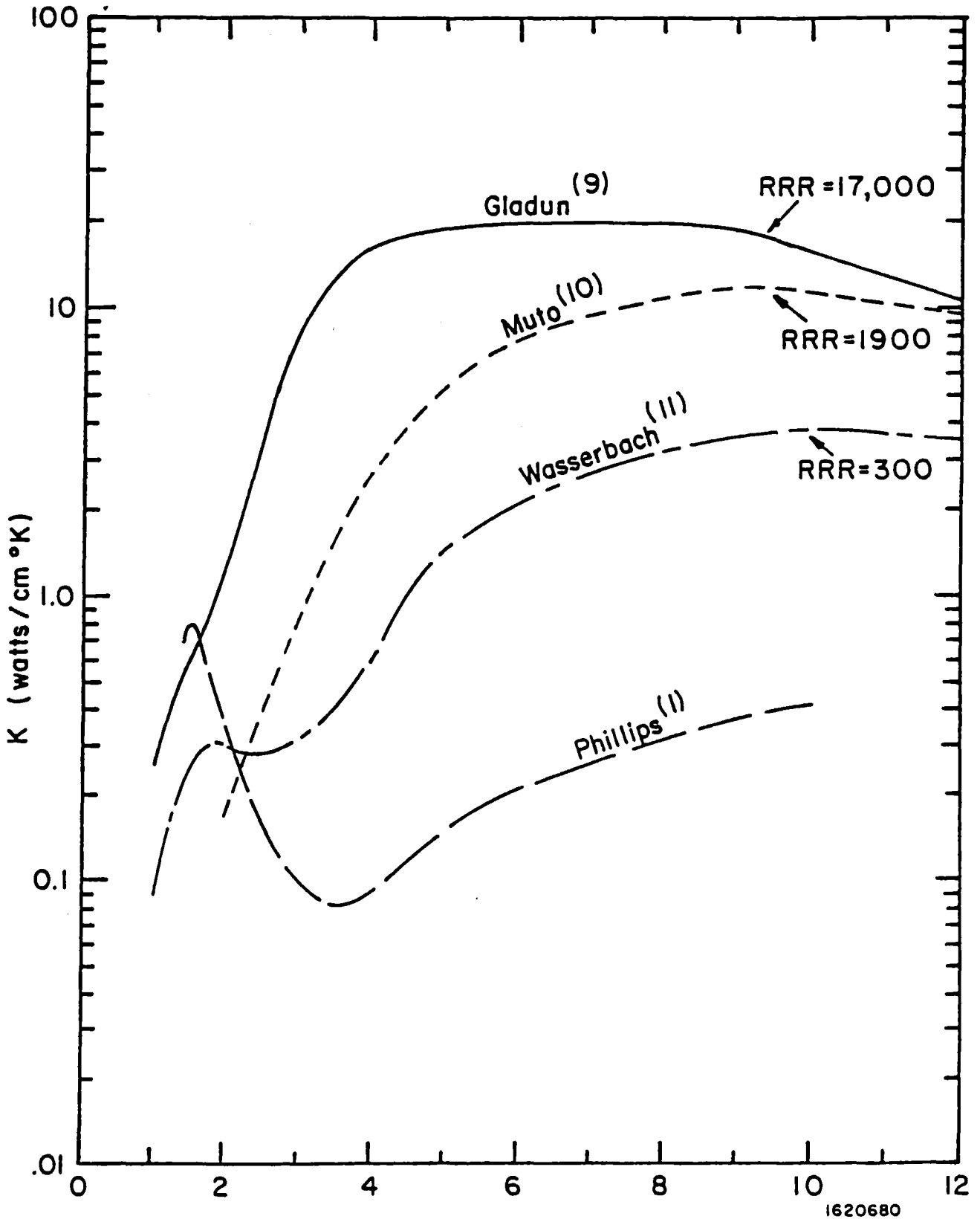


Fig. 5: Thermal conductivity of electrodeposited Nb after first anneal.

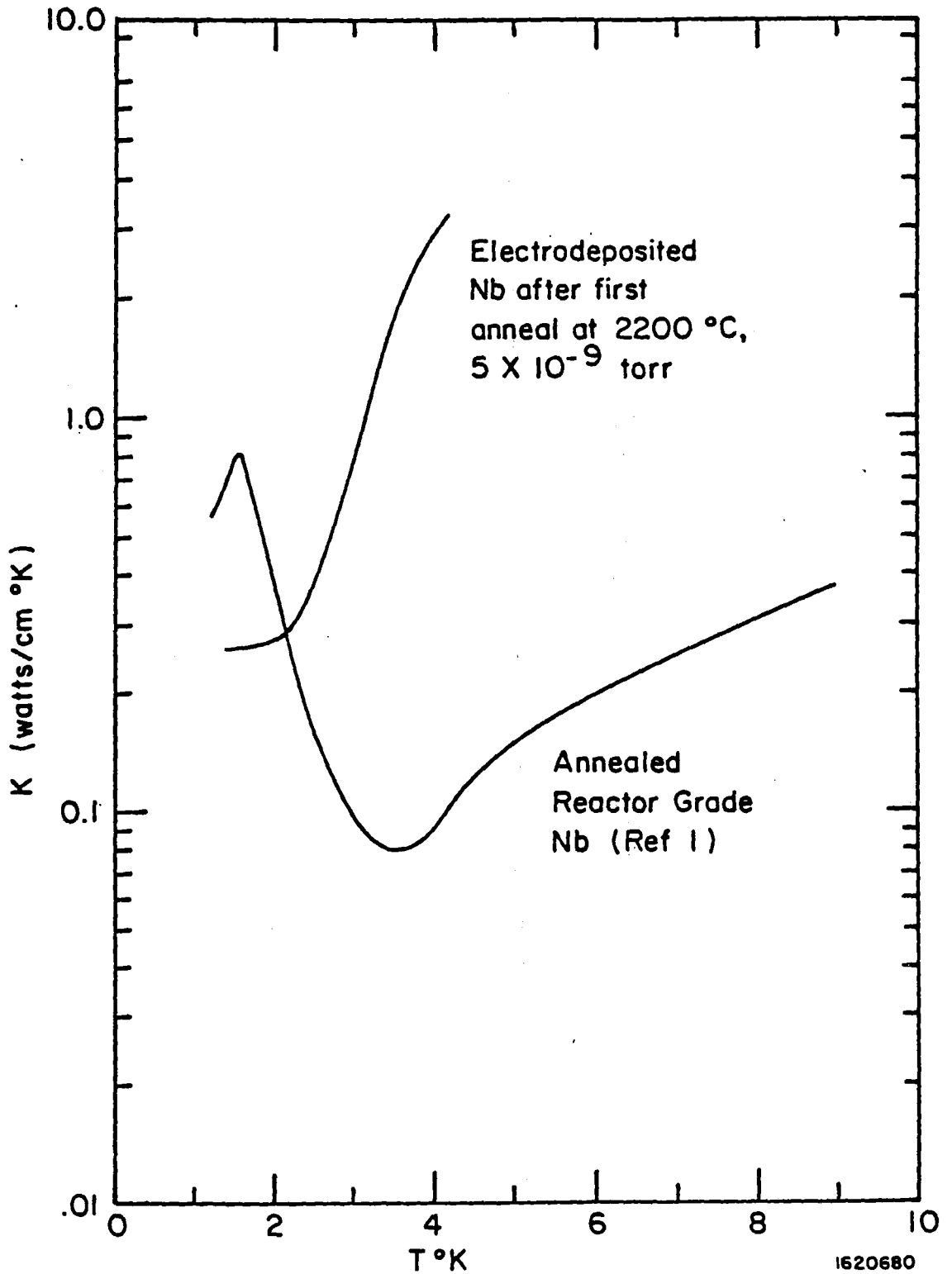


Fig. 6: Thermal conductivity of Nb₃Sn

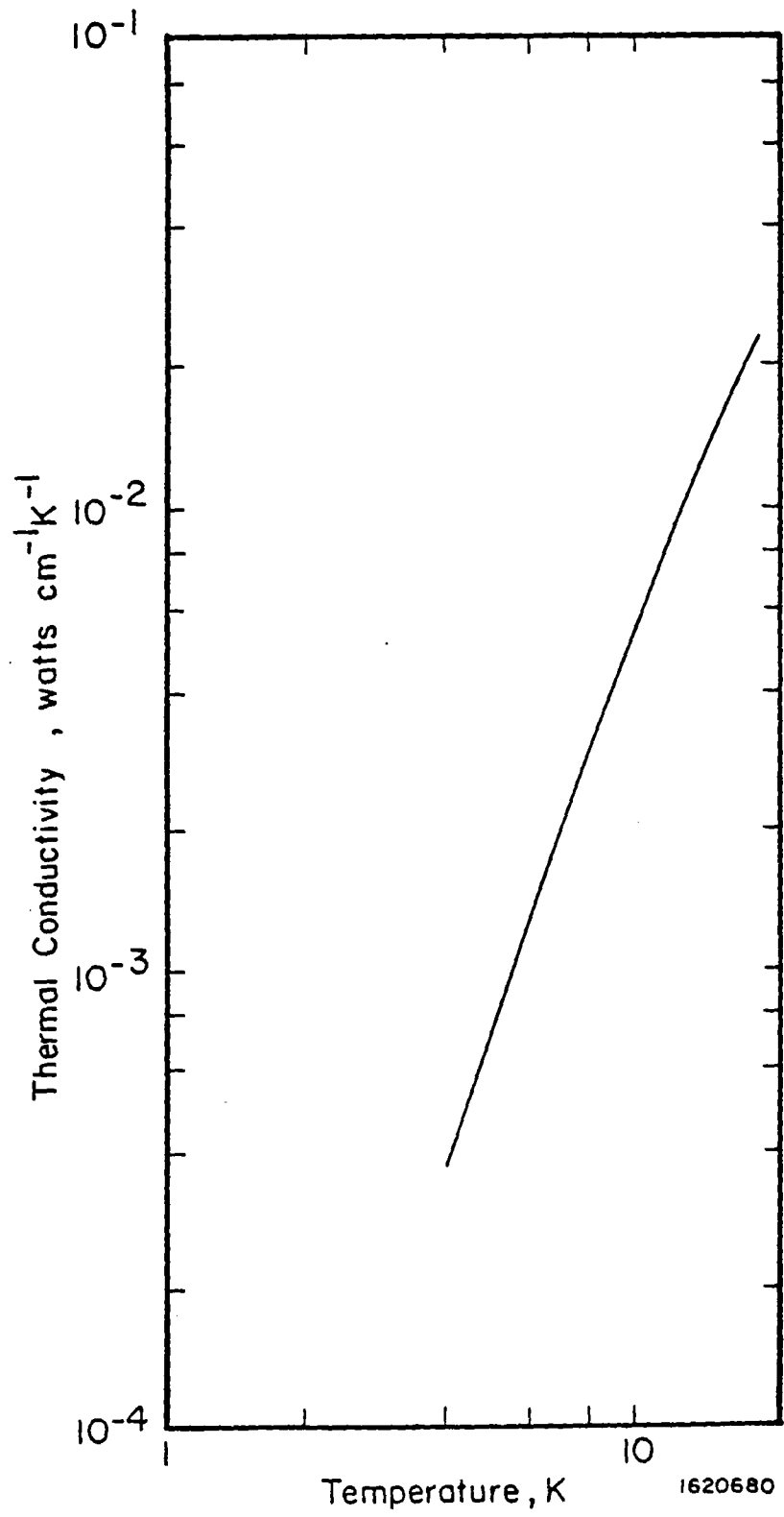


Fig. 7a: Kapitza conductance for copper and lead. Experimental data are from the Ref. 20 and from the compilation by Snyder¹⁾.

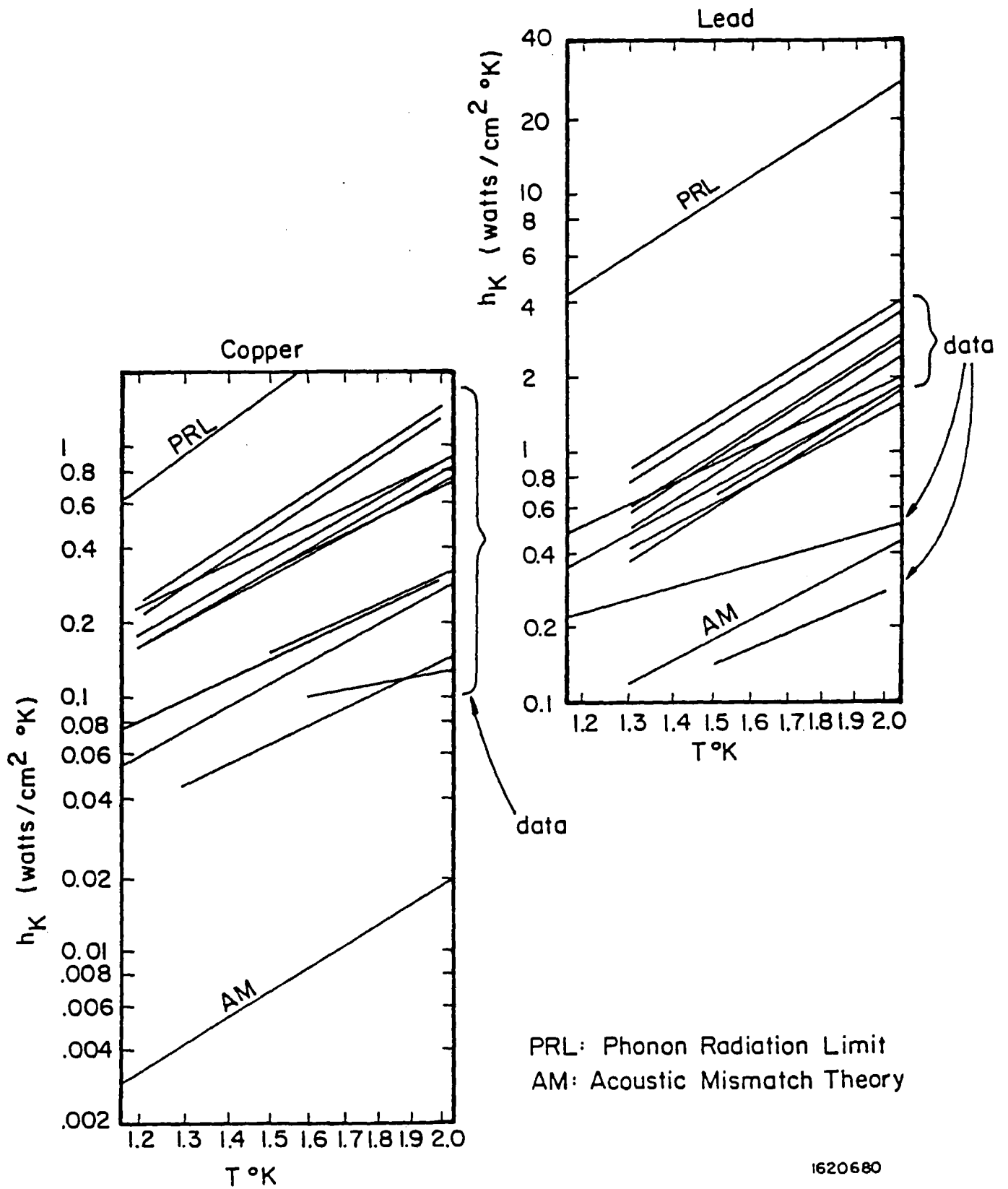


Fig. 7b: Kapitza conductance for Nb

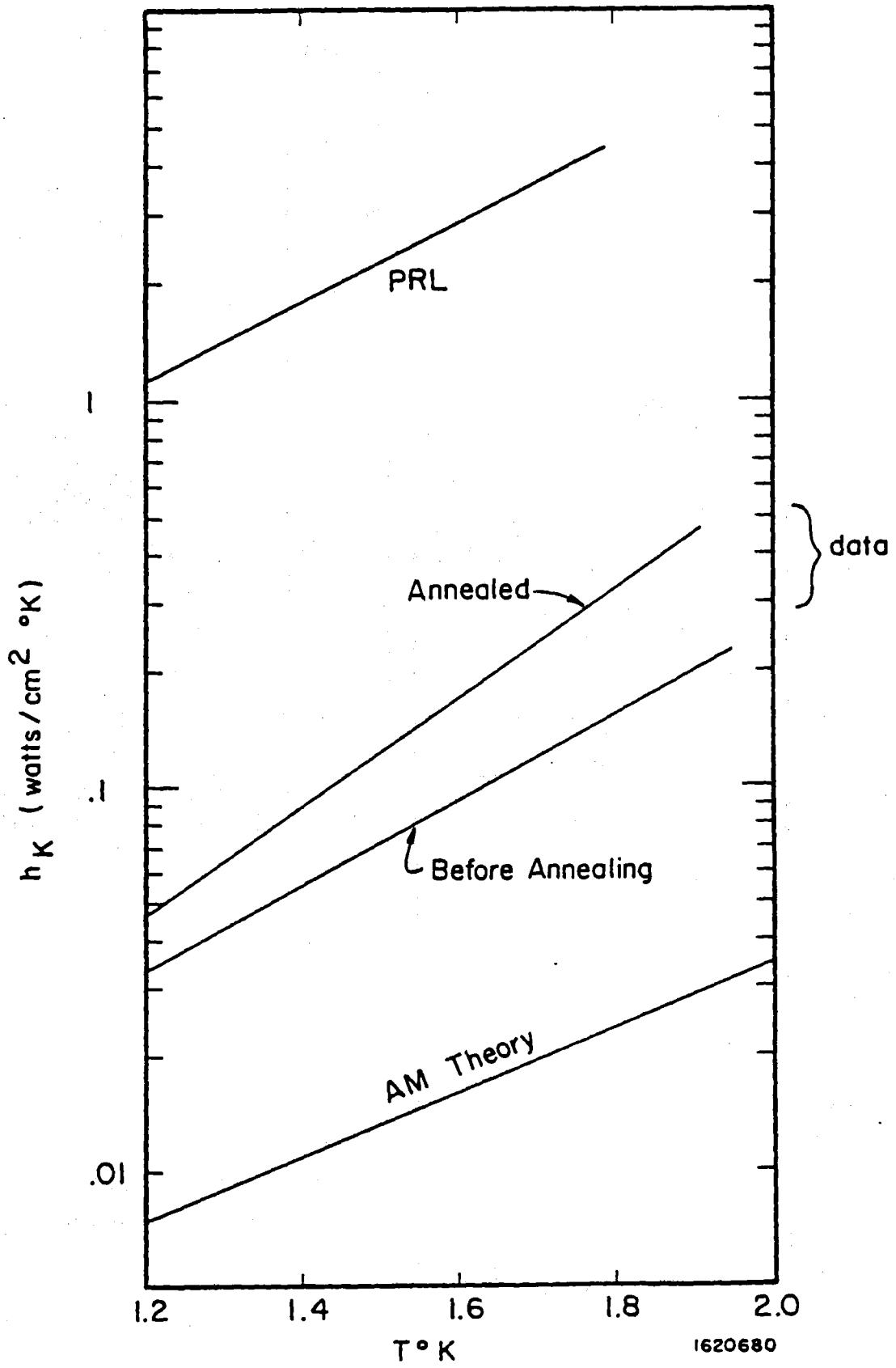


Fig. 8: Critical heat flux for He-II

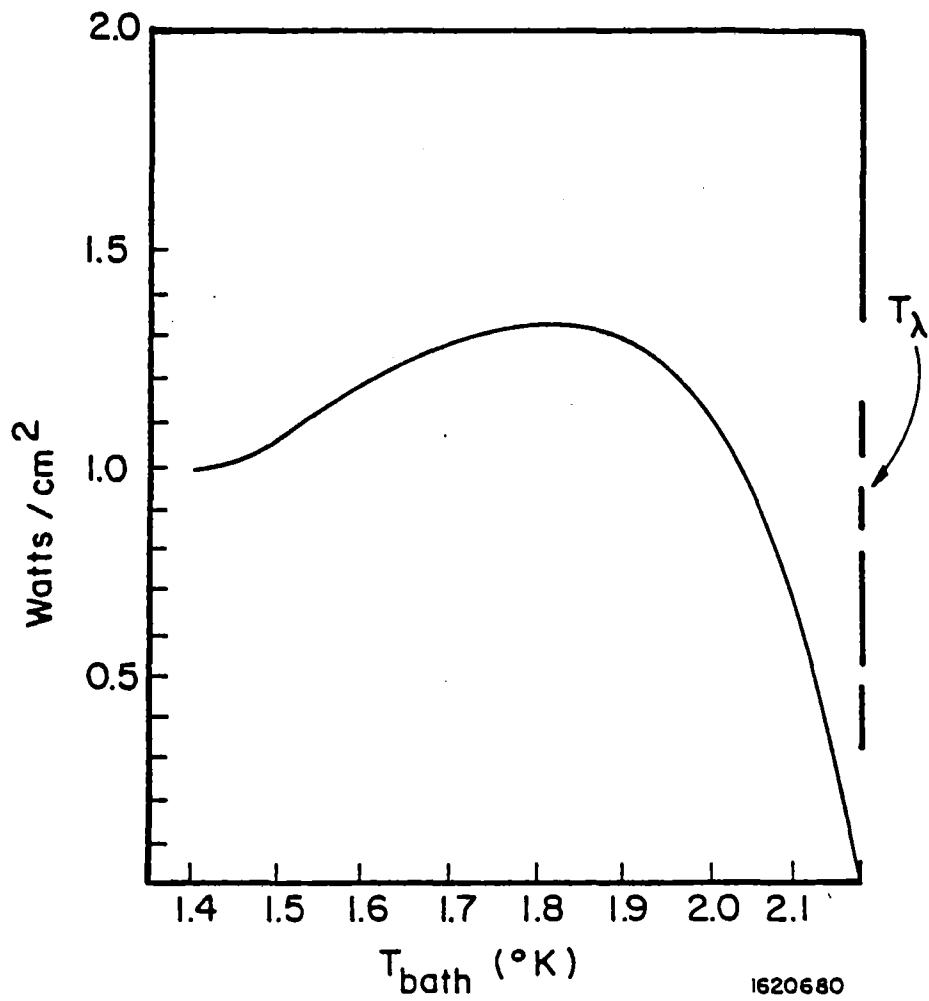
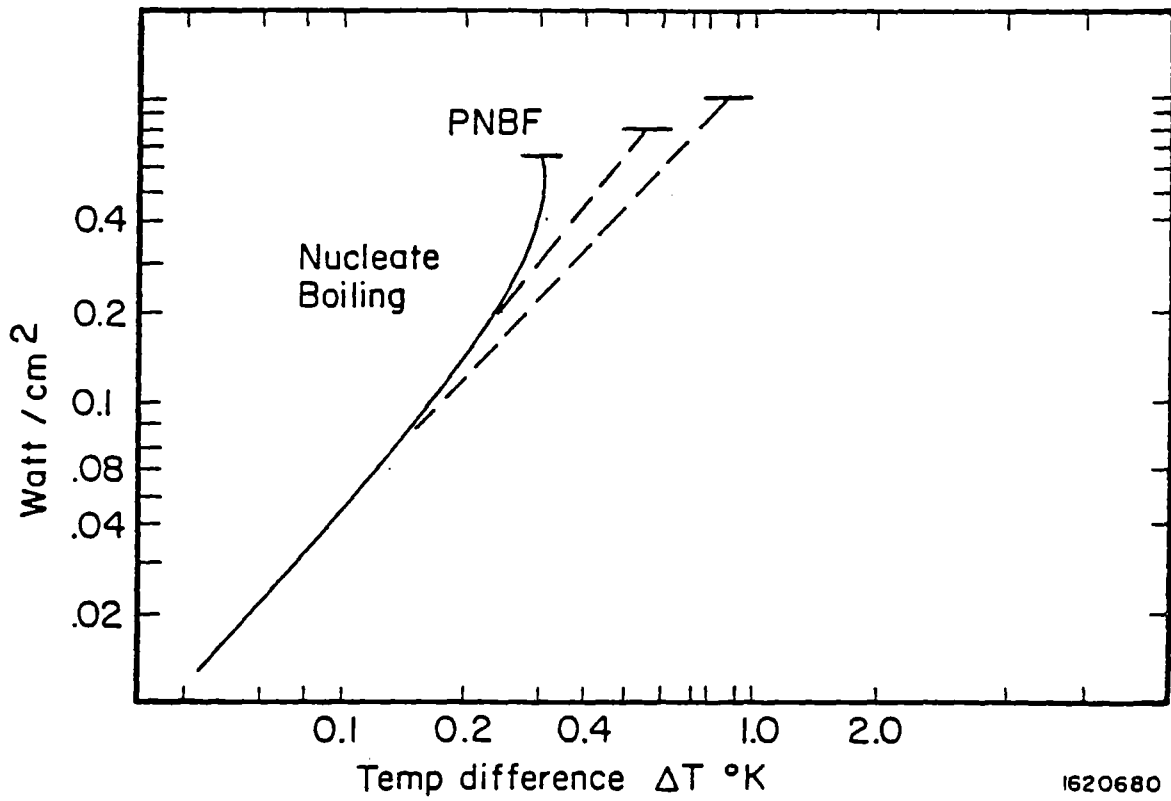


Fig. 9: Nucleate boiling curve and peak nucleate boiling flux (PNBF) for He-I



1620680

Fig. 10: Behavior of peak flux above and below the λ point

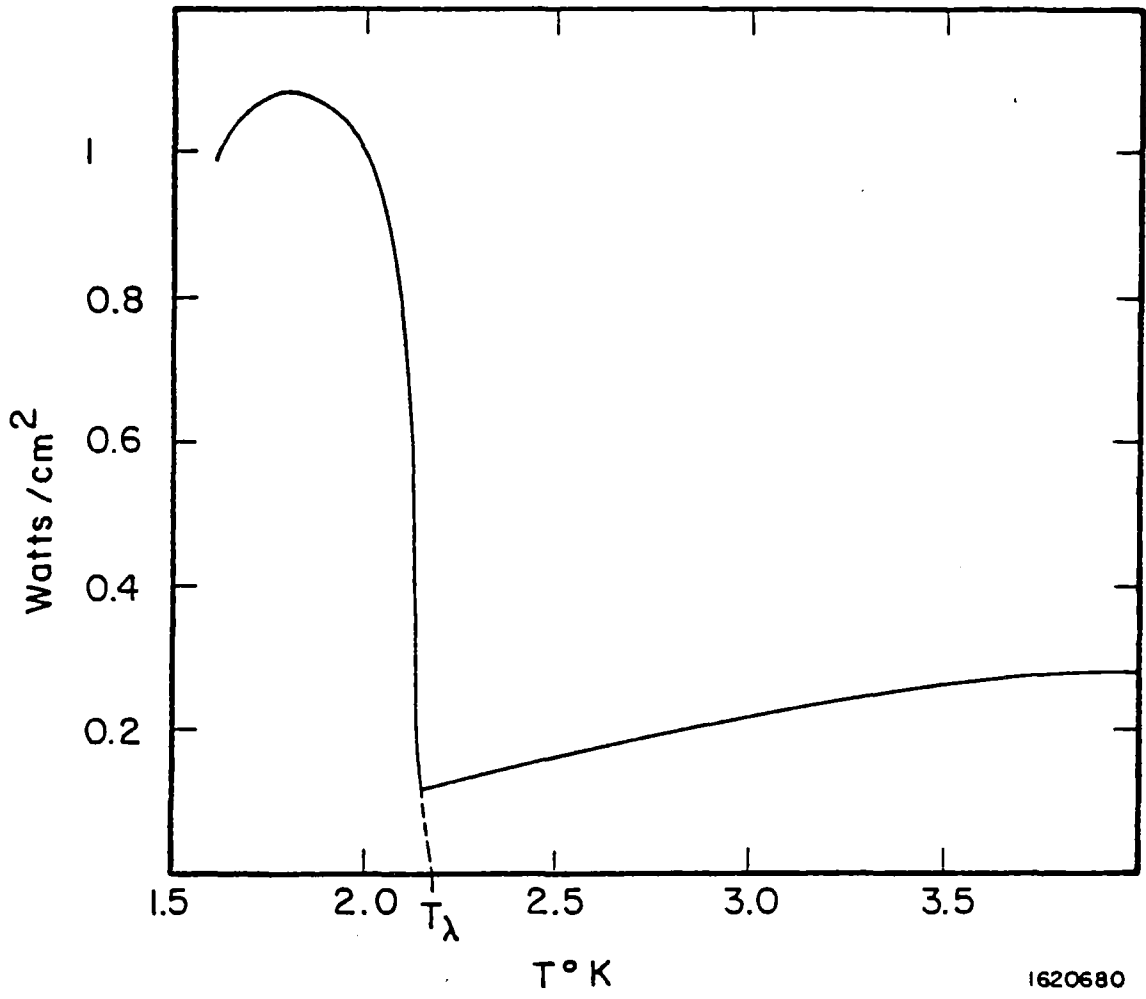


Fig. 11: Mode mixing experimental data to distinguish between thermal and magnetic breakdown.

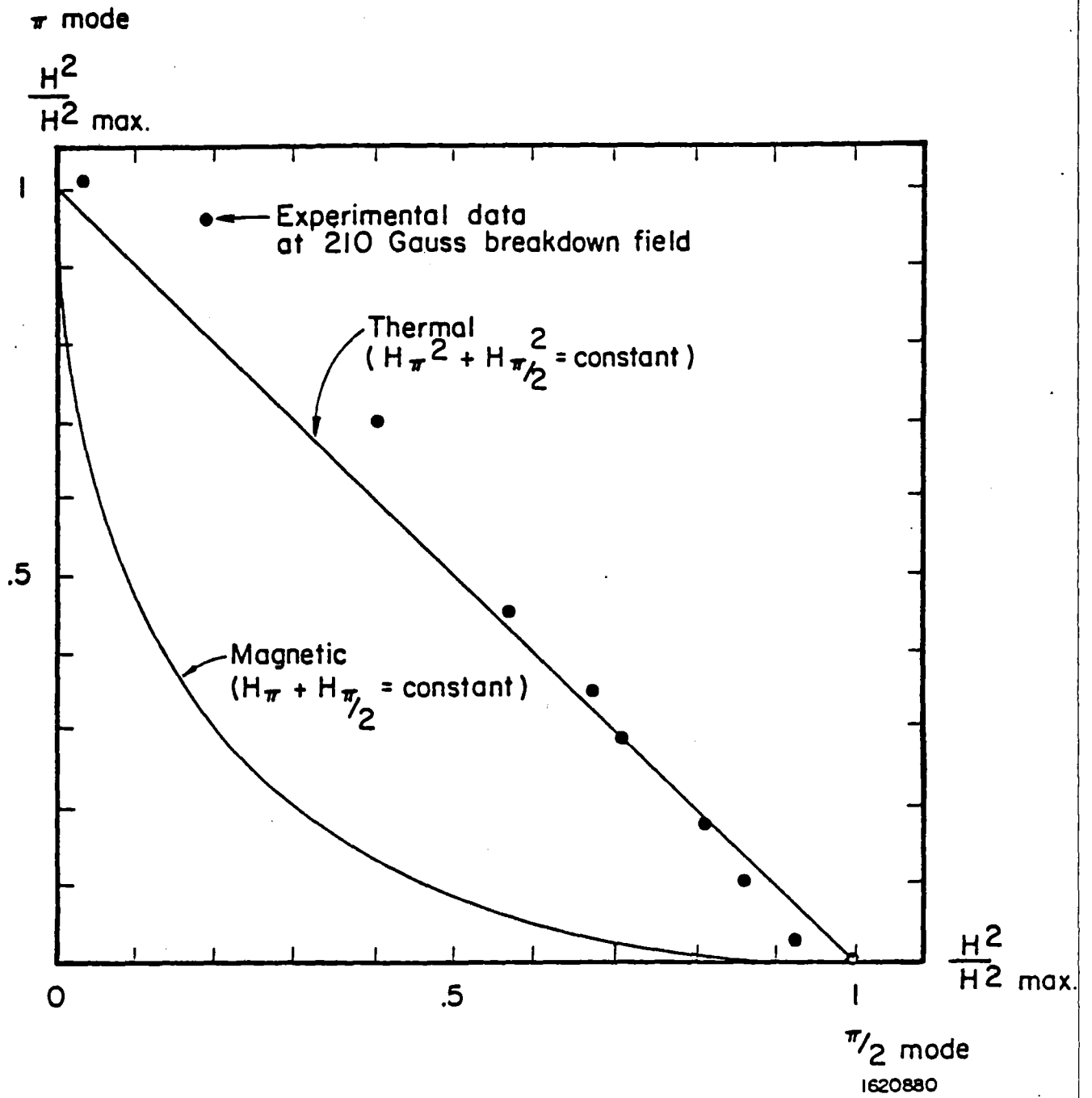


Fig. 12: Frequency dependence of H_{RF} as calculated from the thermal model for the defect free case.

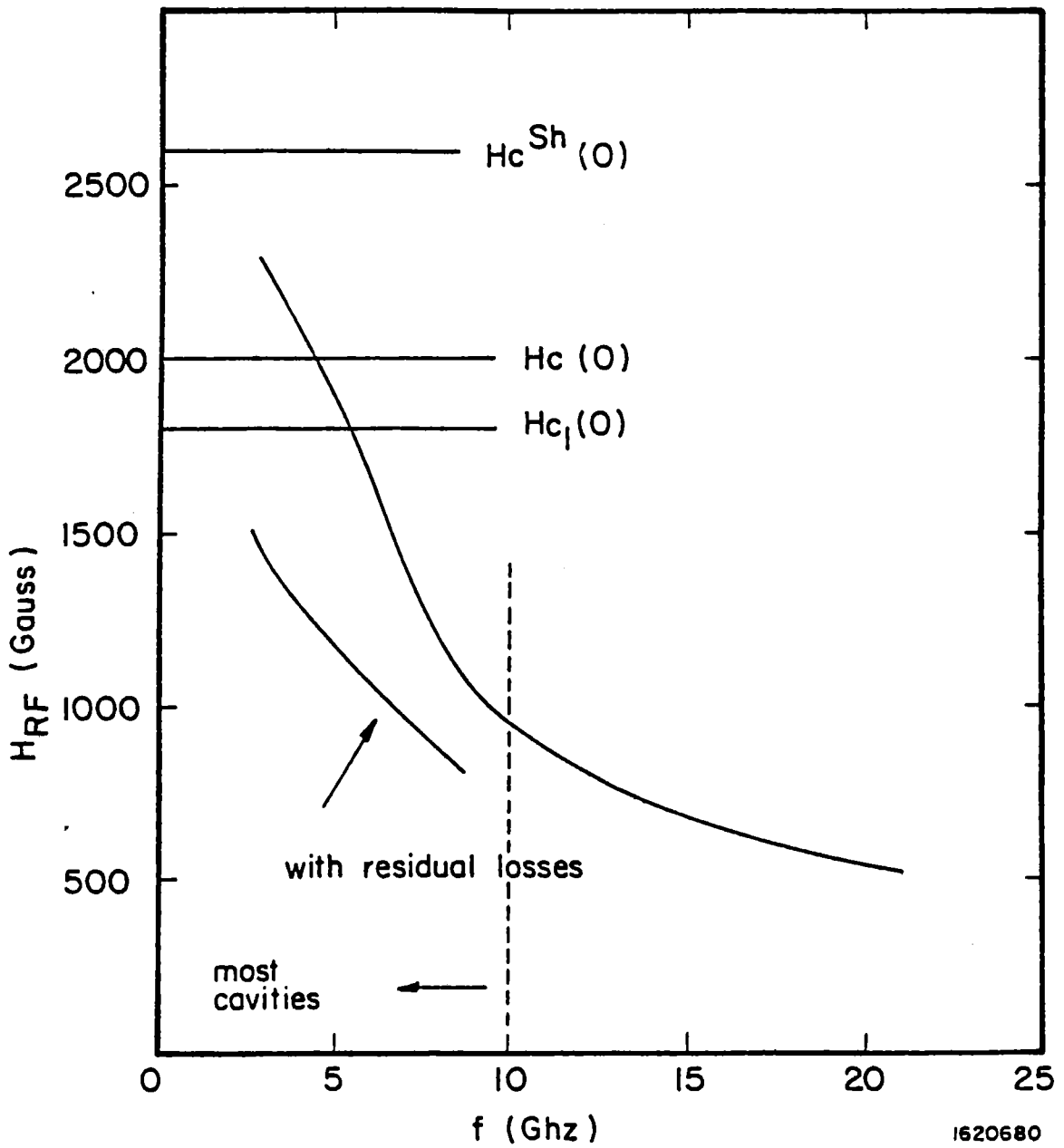


Fig. 13: Temperature dependence of H_{RF} at X-band for the defect free case as calculated from the thermal model and experimental data of Hillenbrand et al.⁽⁴⁰⁾

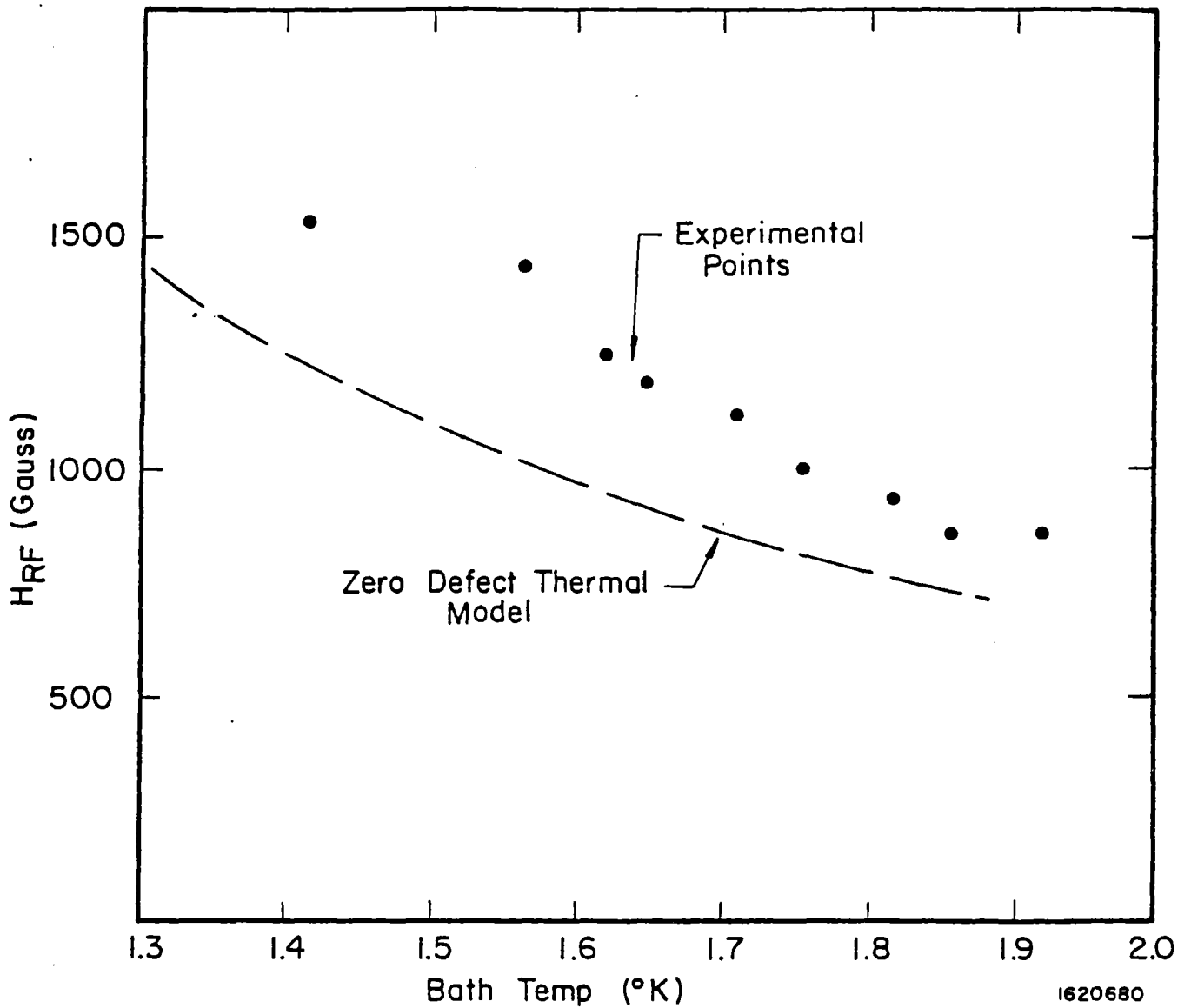


Fig. 14: Temperature profile (radial) at the rf surface near a defect for increasing magnetic fields.

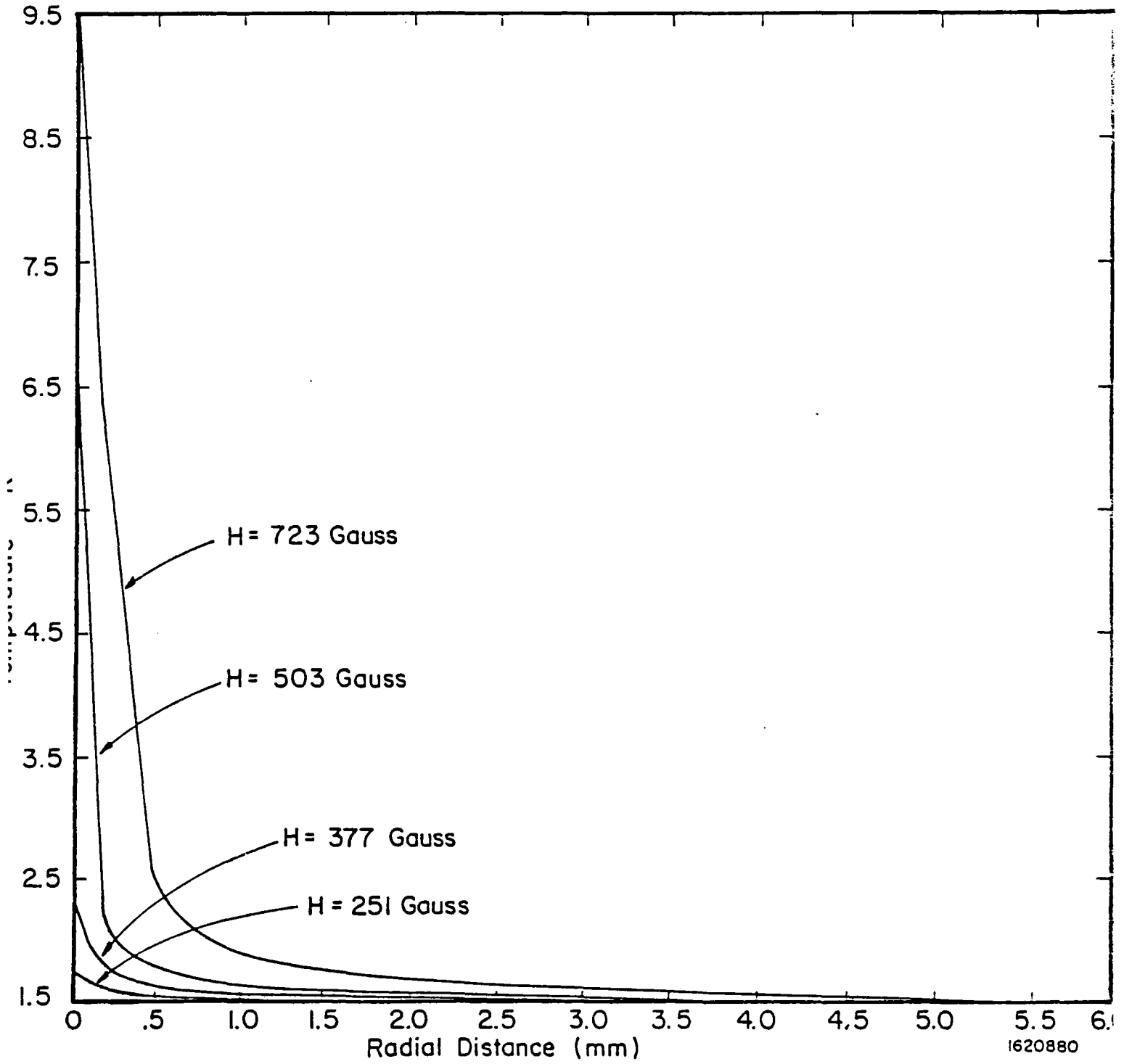


Fig. 15: Temperature profile (axial) from defect location to the helium bath.

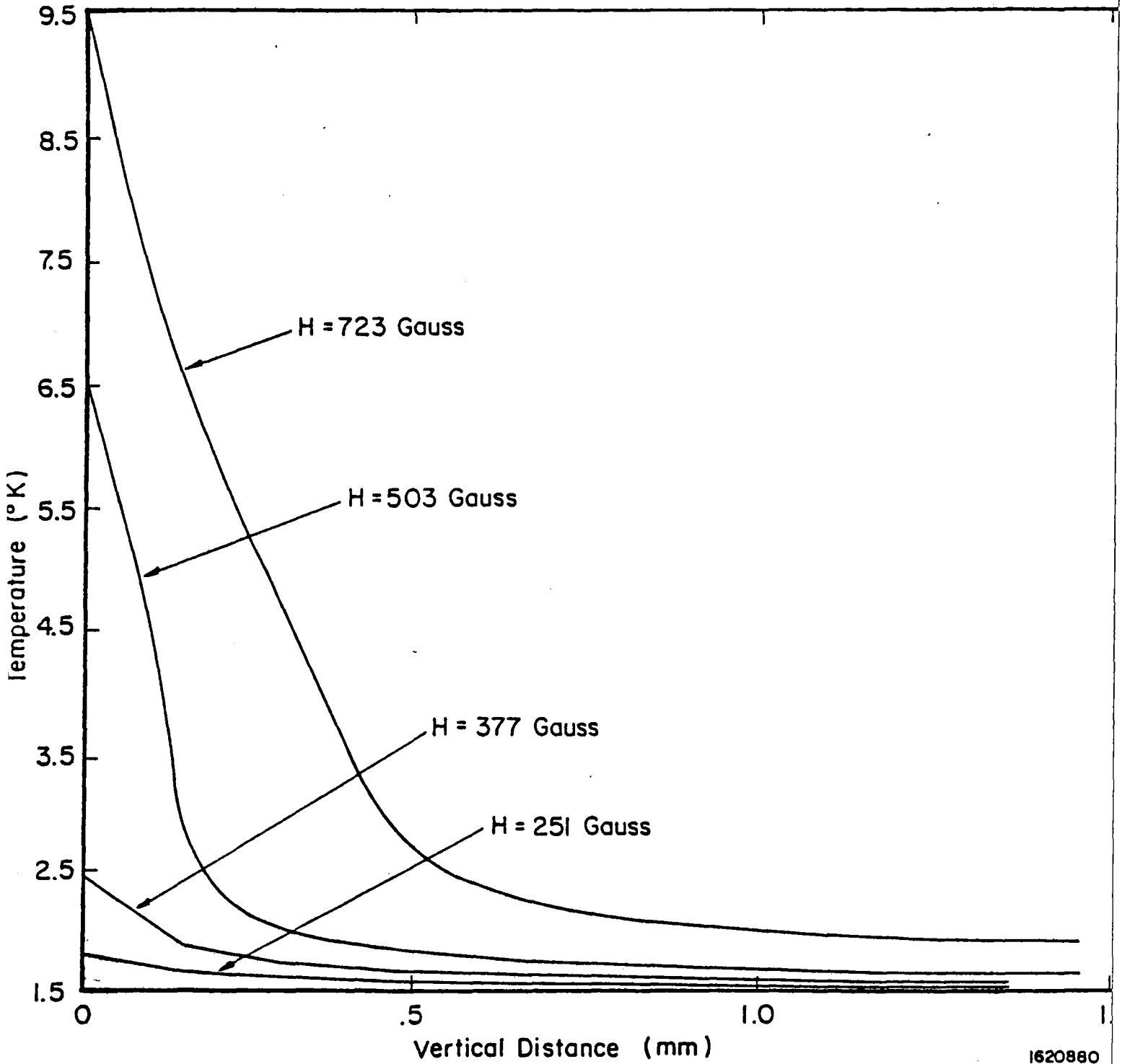


Fig. 16: Temperature of the Nb He-II interface (Nb side) near instability threshold.

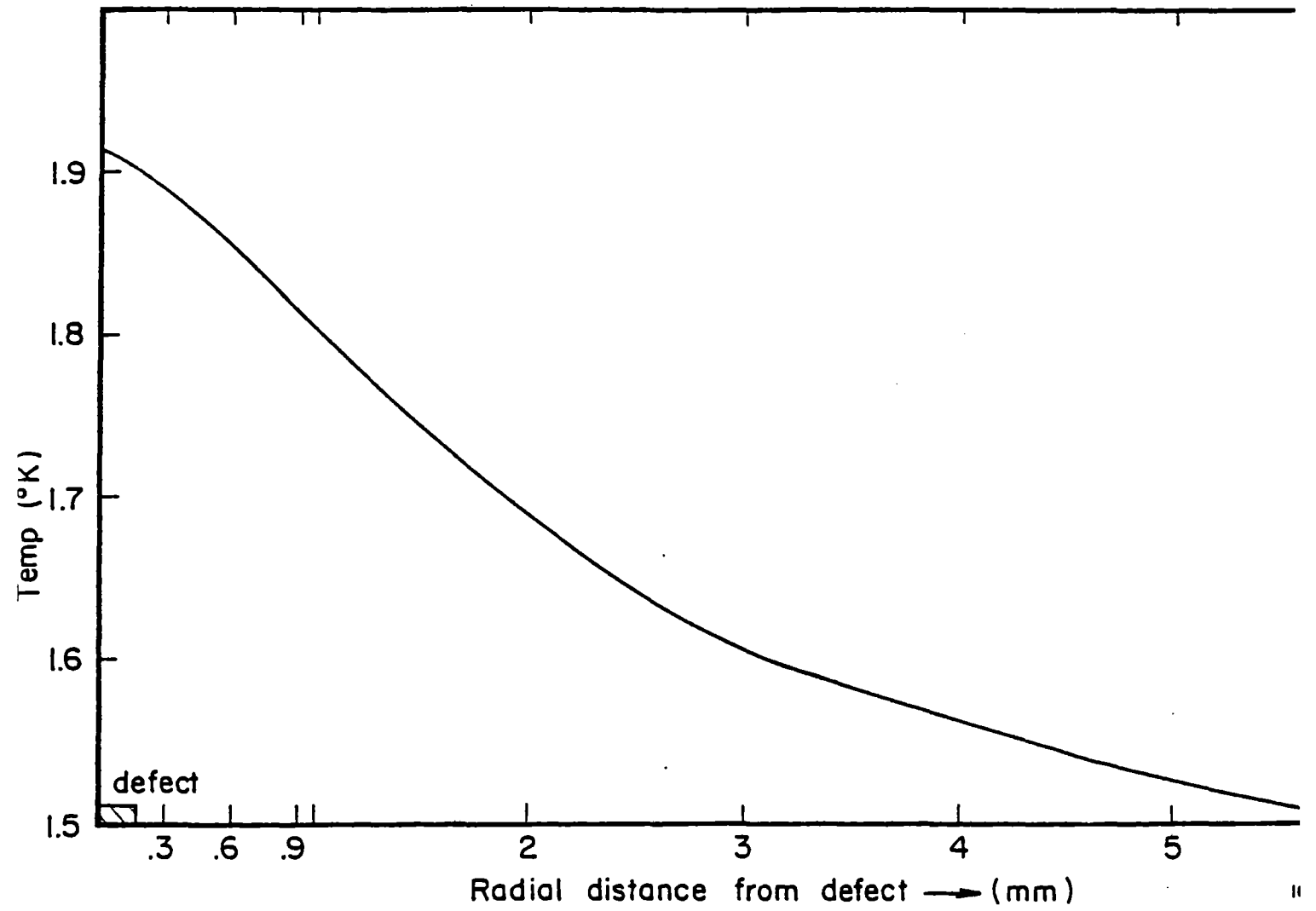


Fig. 17: Temperature dependence of H_{RF} for the defect case

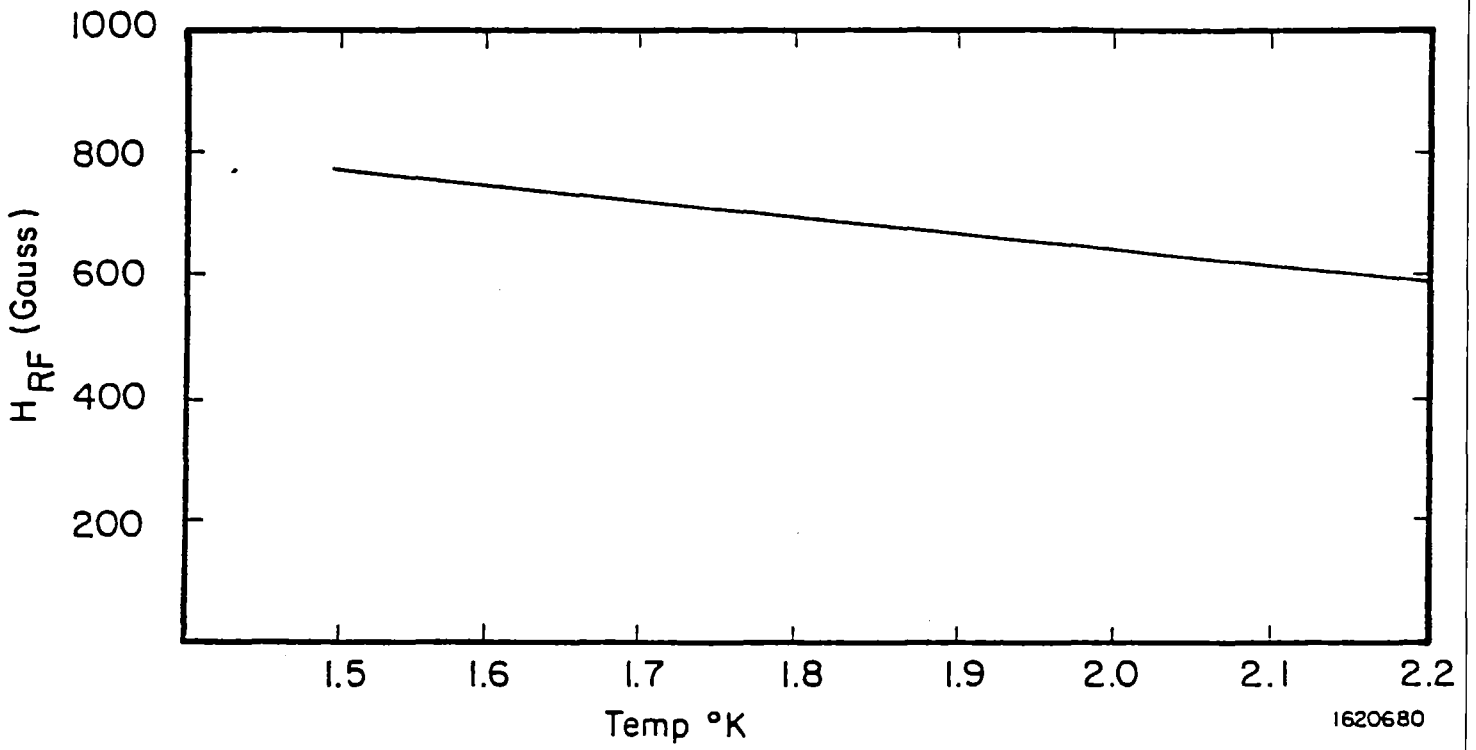
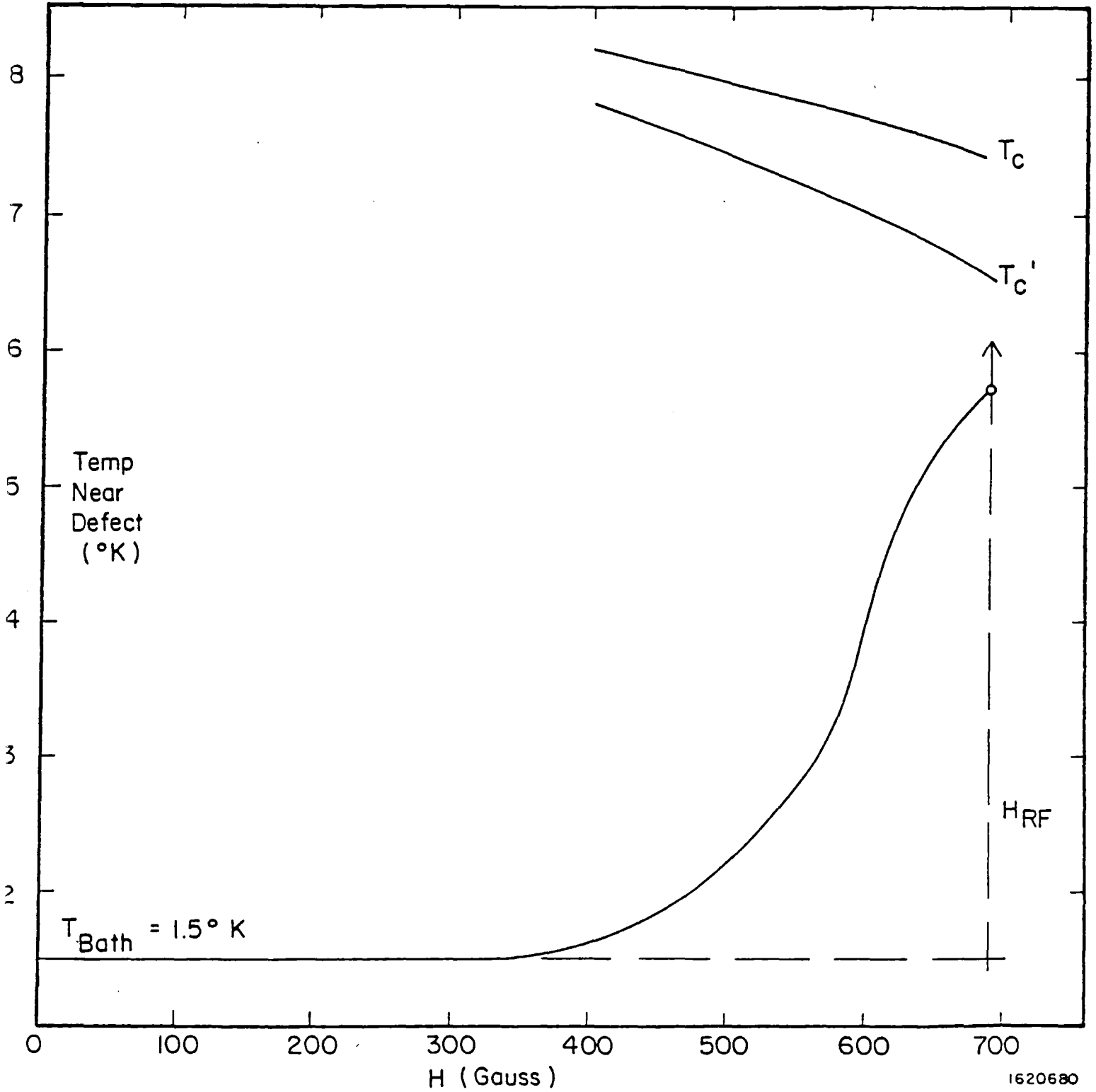


Fig. 18: Surface temperature of defect neighborhood for increasing rf fields.



THEORETICAL ASPECTS IN RF-SUPERCONDUCTIVITY

J. Halbritter

Kernforschungszentrum Karlsruhe

Institut für Kernphysik

P.B. 3640

7500 Karlsruhe

Federal Republic of Germany.

I. INTRODUCTION

As indicated in the title "theoretical aspects", there exists not a well defined theory on rf superconductivity, but several aspects which have been connected using the limited knowledge on: dirty surfaces, oxides, oxide - metal interfaces, inhomogeneities adjacent to such interfaces and superconducting interaction adjacent to such interfaces. All these aspects cannot be discussed in length in one paper. So we concentrate on Nb and on aspects, where new experimental and theoretical results exist.

Aspects mentioned shortly are:

Part. II : Stoichiometry of Nb-Nb₂O₅-sorption layers

Part III : BCS surface resistance $R_{BCS}(T,\omega)$

Part IV : Residual rf losses R_{resE} and R_{resH}

Part V : Deviations from thermal equilibrium

Part VI : Rf breakdown

In Part VII the electron emission out of excited states will be discussed, which is the basis of understanding of secondary- and rf field-emission of Nb cavities. With this knowledge in Part VIII multipactor - and field emission loading of superconducting Nb cavities will be analyzed.

II. STOICHIOMETRY OF Nb-Nb₂O₅-SORPTION LAYERS AND THEIR ELECTRONIC STATES

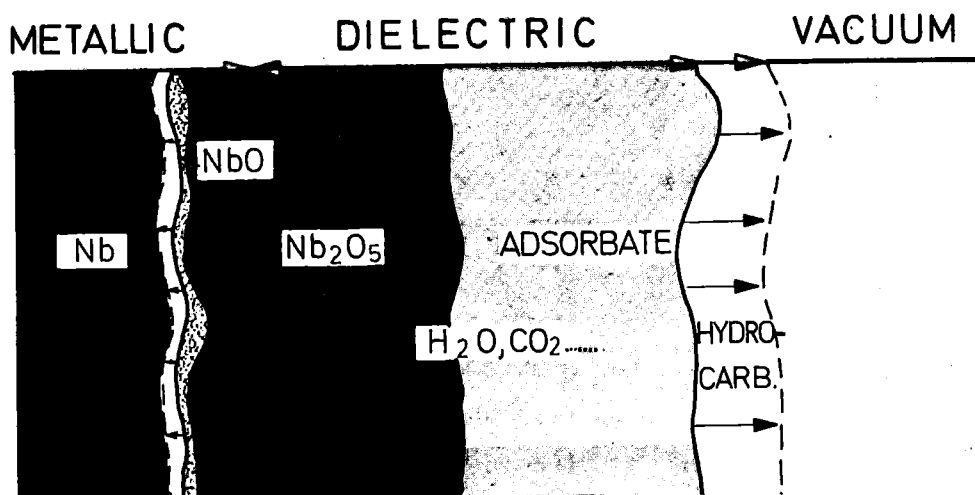


Fig. 1: Sketch of a niobium - niobium oxide - adsorbate surface region. Thicker ($\approx 1.5\text{nm}$) H₂O sorption layers may exist on not extensively pumped or heated Nb. On fresh Nb₂O₅, H₂O forms a chemisorption state which is positively charged by enhanced electron emission. By electron impact additional hydrocarbons get adsorbed (\rightarrow) and polymerized. These hydrocarbons get charged negatively by electron absorption.

Destruction free XPS measurements^{1,2} gave the picture of Nb surfaces shown in Fig. 1, where the following points have to be added: Beside dissolved H, O, C or Ta from the supplier or from the treatment, the Nb matrix adjacent to the surface shows Nb suboxide precipitates with $T_c^* \approx 7K$.³ These precipitates seem to be due to the oxidation of Nb, and their concentration grows with enforced oxidation, e.g. by anodizing or by electron impact.³ The volume concentration of these suboxide ($\approx NbO_{0.02}$) in the penetration region (~ 50 nm) is about 10% and has drastic effects on the surface impedance - see Part III - and rf breakdown - see Part VI.

The Nb-Nb₂O₅ interface is far from being ideal, e.g., at 4.2 K only 2% of the surface shows surface superconductivity,⁵ which in addition disappears above 7 K;³ and the conduction electrons hybridize with localized states in the oxide, which have been found by AES (Fig. 1) 2 nm deep inside the Nb₂O₅.¹ These deviations yielding states inside the energy gap shown in Fig. 2, are due to the above mentioned suboxides and due to the interface states acting pair weakening.⁶ Beside acting pair weakening on the superconducting state, these interface state cause also: - Diffuse surface scattering; - Rf residual losses as summarized in Part 4; - Smearing out the transition metal - dielectric oxide as simulated by a tipped potential barrier as transition from Nb to Nb₂O₅.⁷

About 2nm on top of the Nb, the dielectric behavior of Nb₂O₅ is given by $\epsilon_r = 36$.⁷ The conduction band starts about 0.2 eV⁷ above the Fermi energy, which is pinned by oxygen vacancies. The width of the conduction band is about 10 eV as shown² by the true secondary electron distribution reaching up to about 6 eV above the work function ϕ - see Fig. 3. The density of the oxygen vacancies, which are populated by 2 electrons, is below $10^{18}/cm^3$ eV, because otherwise an impurity band would exist.

On top of wet prepared Nb₂O₅, a Nb₂O₅ - H₂O chemisorption state exists.² This state has been identified by its secondary electron distribution curve (EDC), which peaks around ϕ and $\phi + 10$ eV.²

The sorption layer on top of Nb₂O₅ has a thickness between 1 and 3 nm and contains H₂O and hydrocarbons.² The amount of the latter grows with electron impact.² The hydrocarbons get "conditioned" by electron or x-ray impact showing up in an enhanced absorption (relaxation) of slow electrons.²

Large amounts (≈ 1.5 nm) of H₂O adsorbed on top of Nb₂O₅ may reduce the work function by 1 to 2 eV shown by assymmetric I-U-tunnel-characteristics.⁸ This thick H₂O layer is easily pumped away and so the XPS measurements^{1,2} show a thin H₂O layer (≈ 0.5 nm) only.

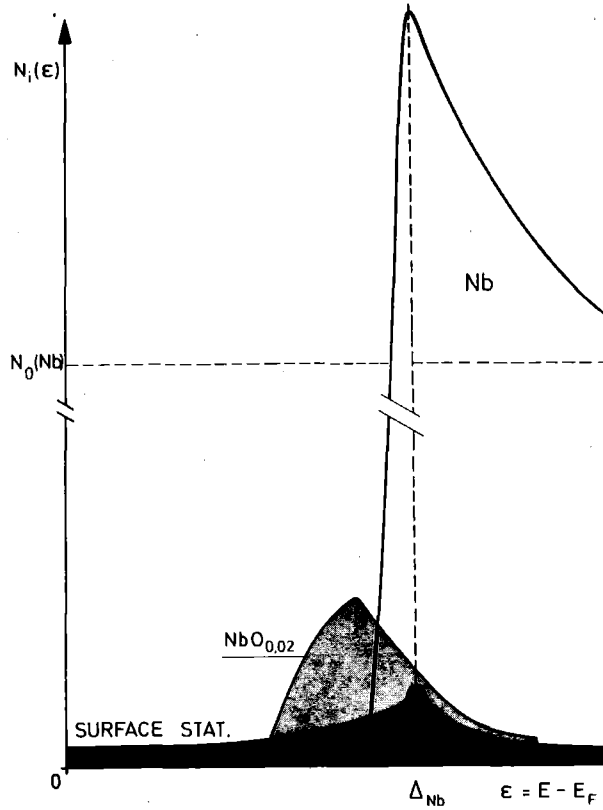


Fig. 2: Sketch of the density of bulk states $N(\epsilon)$ and of surface states at oxidized superconducting Nb surfaces. Due to small ($\ll 50$ nm) weak superconducting regions the BCS singularity is smeared out into the energy gap. If large (≈ 50 nm) suboxide ($\approx \text{NbO}_{0.02}$) regions exist states deeper inside the energy gap appear.

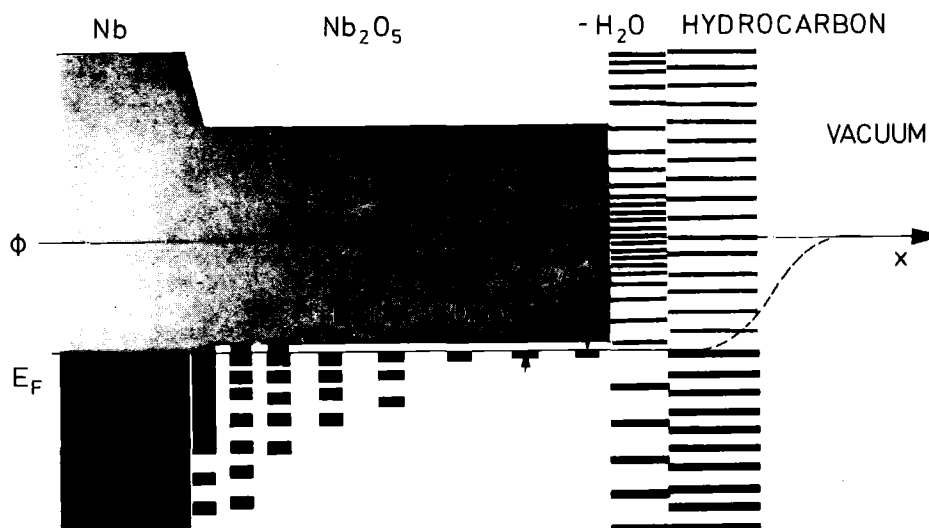


Fig. 3: Sketch of the electron states in Nb_2O_5 and its sorption layers. Due to the small ionization energy of oxygen vacancies of 0.2 eV, Nb_2O_5 is a semiconductor with appreciable conductivity at room temperature. The states in the sorption layers will not be arranged in bands because such layers are inhomogeneous.

The work function of Nb, Nb₂O₅ and sorption layers after prolonged pumping is not varying more than 0.5 eV for different treatments.

III. BCS SURFACE RESISTANCE $R_{BCS}(T, \omega)$

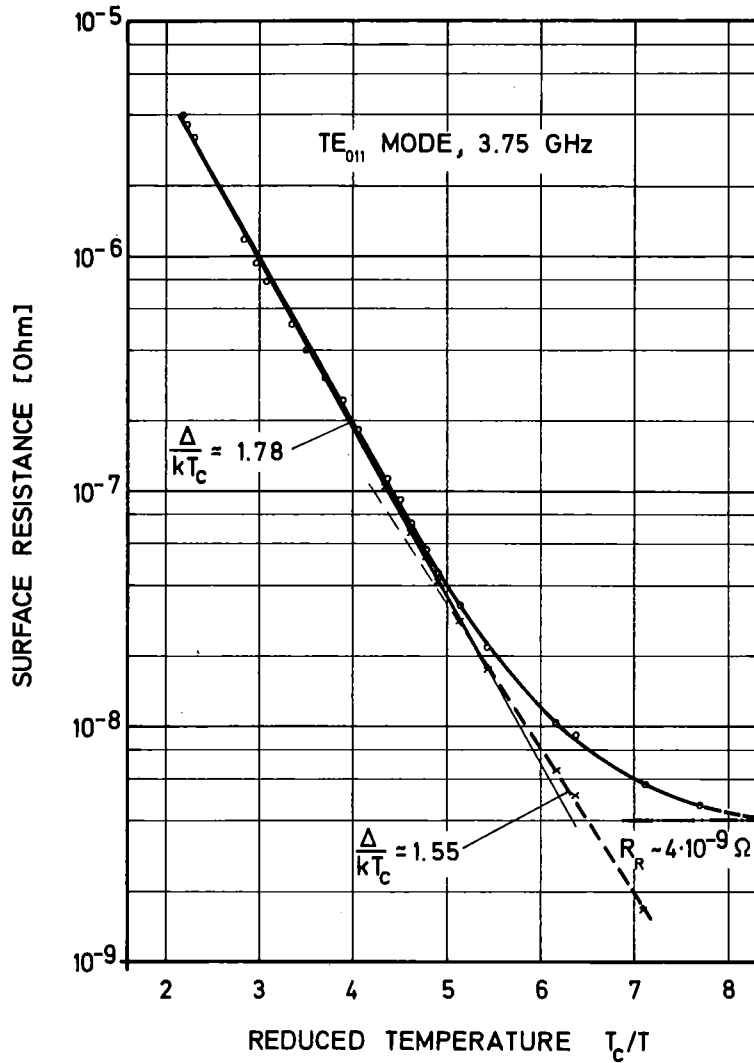


Fig. 4: Temperature dependence of the surface resistance of a slowly anodized cavity. After subtracting the residual losses $R_{resH} = 4 \cdot 10^{-9} \Omega$, the fit to the BCS temperature dependence $R_{BCS} \propto \exp(-\Delta/kT)/kT$ yields two different gaps. The upper gap represents Nb containing about 10% small ($\ll 50$ nm) suboxide regions, the lower gap hints to NbO_{0.02} lumps ($\gtrsim 50$ nm) with $T_c^* \approx 6.5$ K in a concentration of 2%.⁴

In Ref. 9 the surface resistance in the frame work of the BCS theory has been summarized assuming homogeneous and isotropic superconductors. As mentioned above Nb is not homogeneous and has states (Fig. 2) inside the energy gap of clean Nb, which has $\Delta(Nb) = 1.61$ meV corresponding to a $\Delta/kT_c = 2.02$.⁶ These states "inside $\Delta(Nb)$ " lower the Δ/kT_c -value deduced from the temperature dependence of

the surface resistance. For $T > 2K, \Delta/kT_c = 1.85$ is typical, which seems to rise with frequency. ⁴ In addition, this fitted Δ/kT_c can depend on temperature, as shown in Fig. 4, if some low lying excitations (Fig. 2) exist. Such low lying excitations occur for weak superconducting regions being larger than the coherence length $\xi_{GL} \approx 50$ nm. They can independently become superconducting - in our case for $\Delta^*/kT_c^* = 1.76, T_c^* = 6.5$ K was obtained. ⁴ This result agrees with the $T_c^* \approx 7K$ obtained by penetration depth measurements shown in Fig. 5 for heat treated Nb. For heat treated cavities, $R(T)$ did not show $\Delta/kT_c < 1.80$ indicating that the volume percentage of large regions with $T_c^* \approx 7$ K is below 1%.

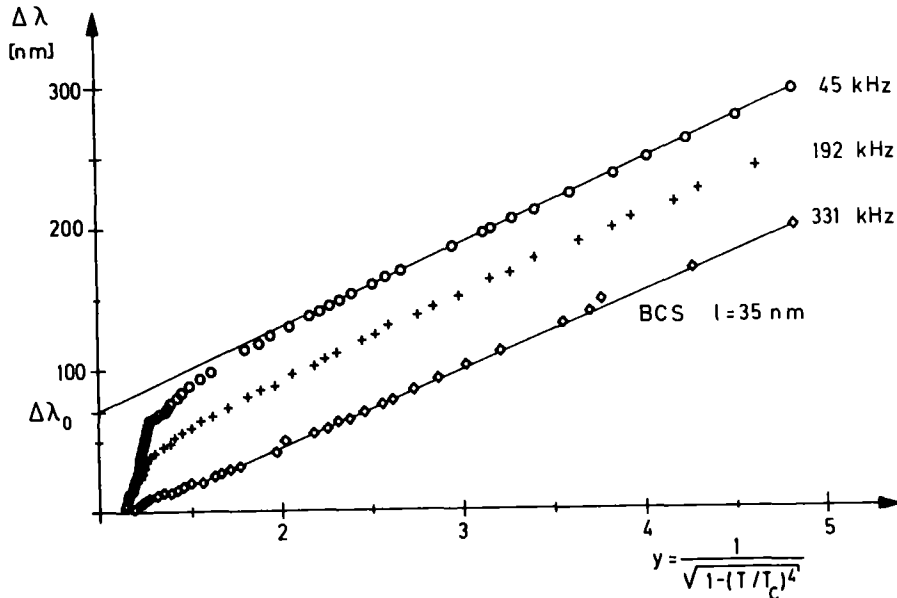


Fig. 5: Change of penetration depth versus $y = 1/\sqrt{1-(T/T_c)^4}$ for various frequencies at $B_{ac} = 60 \mu T$. The sample was fired at $1850^\circ C$ for 2 h in a vacuum better than 10^{-10} mbar and handled in air for about 1 day. Fits to the data above 8.5 K yield a mean free path $l^* \approx 35$ nm and $T_c = 9.24$ K. ³

Beside these effects of weak superconducting regions in Nb and of pair weakening at the Nb-Nb₂O₅-interface both depressing the $\Delta(Nb)$, the density of states gets smeared out ¹⁰ by these inhomogeneities as sketched in Fig. 2. This smearing reduces the surface resistance and yields $R_{BCS}(4.2K) \propto f^2$ below 5 GHz ($\hat{=} 0.016\Delta(Nb)$) as shown in Fig. 6. Between 12 and 18 GHz $R_{BCS}(4.2K) \propto f^{1.6}$ has been found (Fig. 6) which agrees with the BCS theory, indicating that the smearing of the BCS singularity is of the order of $\Delta(Nb)/50$.

If the weak superconducting regions have sizes $d \geq \xi_{GL} \approx 50$ nm, a magnetic field can drive them normal conducting at $T_c^* \approx 7K$ - see Fig. 5. ³ Such large regions seem to

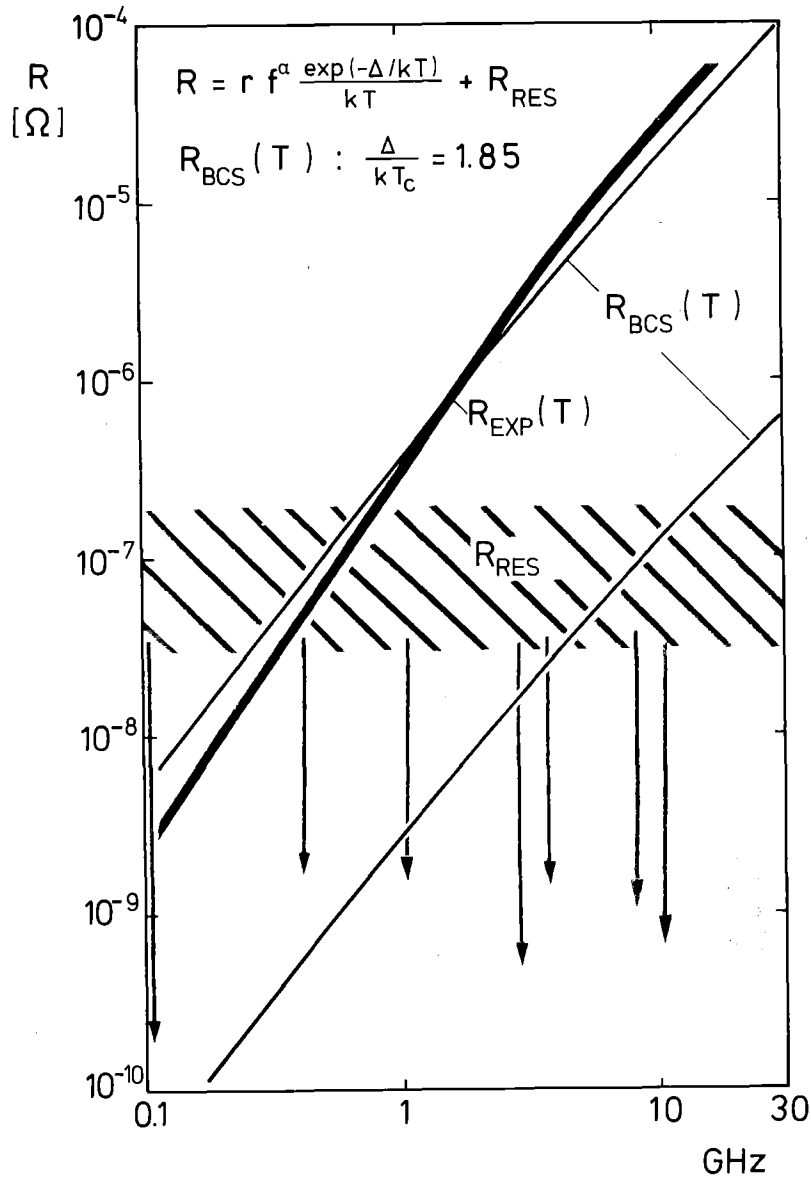


Fig. 6: Summary of experimental (■) and computed (-) surface resistances of Nb between 0.1 and 30 GHz. The $R(4.2 \text{ K}, f)$ -values show the cross over of experimental and computed values due to the smearing of the BCS singularity. The differences of the computed slopes at 4.2 K and 1.8 K are due to the growth of $\hbar\omega$. The residual losses show a large scatter depending on surface preparation. The arrows (↓) indicate best values.

occur in larger numbers and sizes ⁴ after anodizing or electron impact. ³ Such regions have a thermodynamic critical field $B_c^* \geq 100 \text{ mT}$, where at $T = 0$ the transition to the normal conducting state occurs. Below B_c , the BCS surface resistance depends on field only weakly. ^{11,12} So the field dependencies observed ^{13,14} are due to deviations from thermal equilibrium which will be discussed in Part. V. Because these deviations increase with increasing frequency, the above mentioned

frequency dependencies could be caused by deviations from thermal equilibrium also.

IV. RF RESIDUAL LOSSES

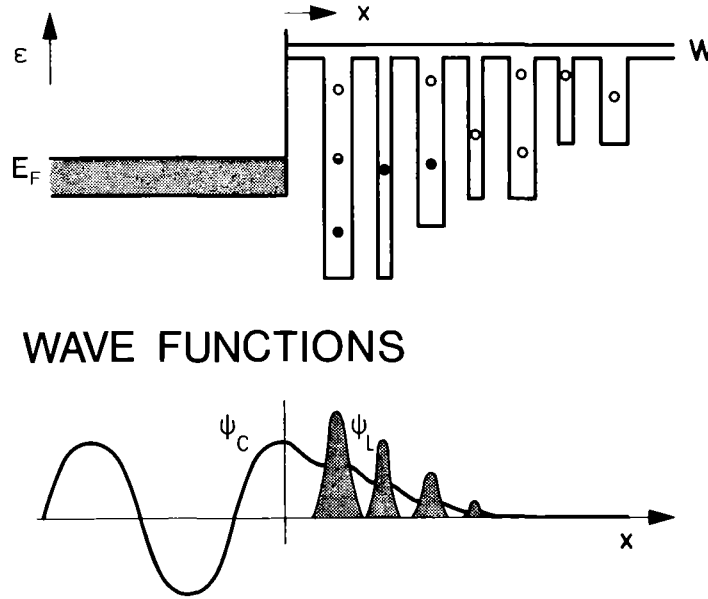


Fig. 7: Model metal-oxide interface showing the overlap of conduction electron (ϕ_C) and localized electron (ϕ_L) wave function, which corresponds to hybridization. The hybridization allows the transfer of perturbation from the system (ϕ_C) to (ϕ_L) or vice versa and enhances tunneling.

As shown in Fig. 4, with decreasing temperature the residual losses dominate, which are summarized in Fig. 6. As outlined in Refs. 15 and 16, these rf residual losses are due to interface states: As sketched in Fig. 7, conduction electron decay into the oxide like, $\exp(-\kappa x)$ and hybridize in the oxide with localized electron states n_L forming so new interface states, where properties of extended and localized states are mixed (Fig. 7). So momentum gained as extended state can be transferred to localized states exciting so phonons. The transfer is given by the beat frequency: ^{15,16}

$$v_E(x) = \frac{4}{h} \Gamma(x) = \frac{4}{h} \Gamma(0) \exp(-\kappa x) \quad \kappa = \sqrt{2m(E_C(x) - E_F)} \hbar^{-1} \quad (1)$$

with $\Gamma(0.3 \text{ nm}) \approx 1 \text{ eV}$, and $\kappa^{-1} \approx 0.5 \text{ nm}$

So the rf shielding currents, given by $H_{||}$, excite transverse phonons ¹⁵ proportional to $(\int v_E(x) n_L(x) dx)^2$: ¹⁵

$$P_H = \frac{R_{\text{resh}}}{2} H_{||}^2 ; \quad 10^{-7} > R_{\text{resh}} (\text{GHz}/f)^2 / \Omega > 10^{-12} \quad (2)$$

The longitudinal electric rf field $E_L(t)$ excites longitudinal phonons:

$$P_H = \frac{\epsilon_0}{2\mu_0} R_{res} E_L^2 \quad ; \quad R_{res} \lesssim 10^{-4} \Omega/\epsilon_r^2 \quad (3)$$

Both residual loss mechanisms sensitively depend on the hybridization and so on the conduction band in the oxide via κ (Eq.(1)) and on the density of localized states n_L near the Fermi energy. So, the residual losses are changed by surface treatments or rf processing. But it should be mentioned that chemical residues from cleaning or dust cause locally enhanced (electric) residual losses dominating at low frequencies - see Eq. (3) or Fig. 6.

V. DEVIATIONS FROM THERMAL EQUILIBRIUM

In the frame work of the BCS theory, the surface impedance increase only by 20%^{11,12} up to the critical superheating field $B_{sh} (\approx B_c(Nb))$, whereas experimentally much stronger field dependencies have been observed: At fields as low as $B_c/100$, R decreases with B_{rf} ¹³, as shown in Fig. 8, or R increases markedly with B_{rf} - see Fig. 9 - showing an rf breakdown around $B_c/10$. All these effects can be related to deviations from thermal equilibrium, which are not included in the BCS treatment.

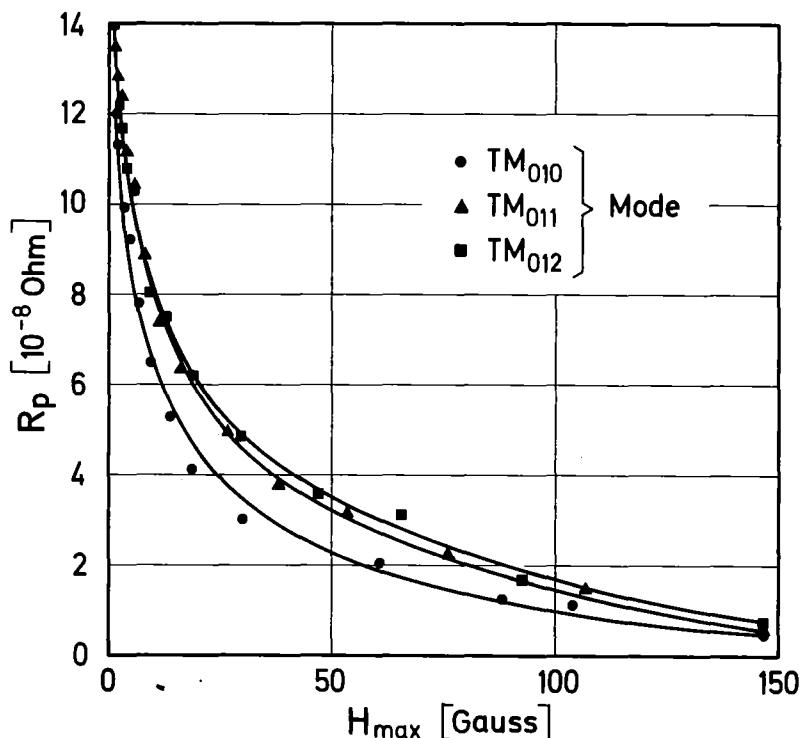


Fig. 8: Component of the surface resistance which depends strongly on rf field level¹³ for the mode family TM_{01n} ($n=0:2.17\text{GHz}$; $n=1:2.61\text{GHz}$; $n=2:3.62\text{GHz}$) at 1.2K. The analysis of the experimental curves results in $R_p \propto \omega^{\alpha(H)}$ with $0 < \alpha(H) \lesssim 0.6$.

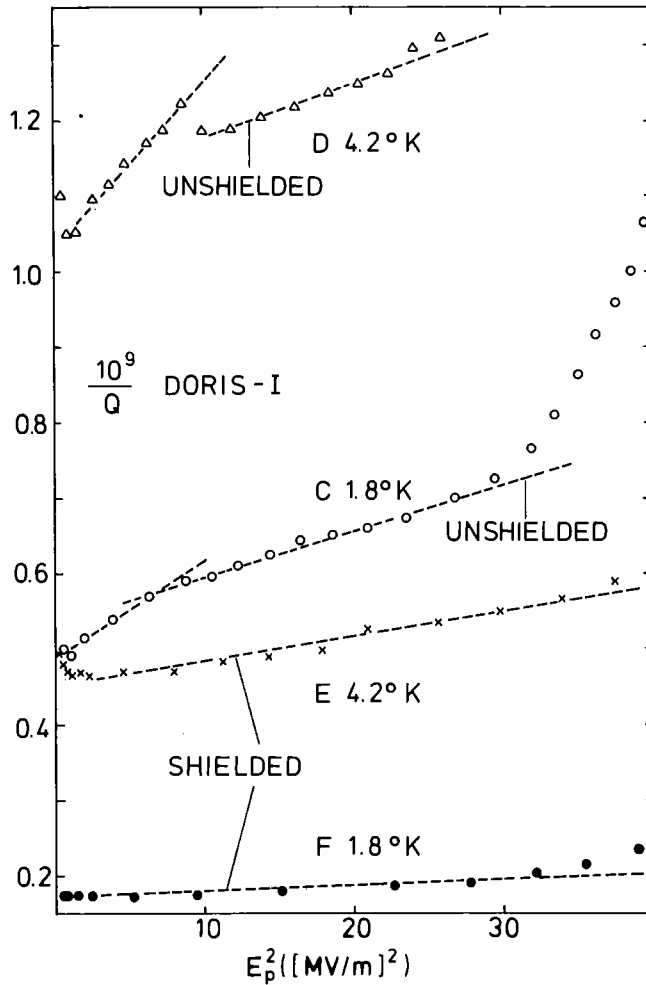


Fig. 9: $1/Q$ plotted versus E_p^2 . The straight lines above 3 MV/m, with slopes $\gamma \approx 50$, reflect the growth of normal conducting regions detected also by heat pulses.¹⁴ The kinks around 3 MV/m are likely due to a change in cooling. Because above 3 MV/m γ does not change with temperature and Q_0 , the cooling in He is the same at 1.8 and 4.2 K.

The first effect - Fig. 8 - is due to the long inelastic relaxation time of electrons with phonons τ_{in} :¹⁷

$$\tau_{in}(\text{Nb}) = 1.5 \cdot 10^{-10} (T_c/T)^3 \text{ sec}; \quad \ell_{in} = 10^{-2} (T_c/T)^3 \text{ cm} \quad (4)$$

i.e. the quasiparticle system is decoupled from the phonons the more the lower the temperature is. But also the phonons are not in thermal equilibrium as shown by their long relaxation time or mean free paths. E.g. at 4 K one can obtain¹⁷

$$\ell_{ph} \approx 2.6 \text{ cm} \quad (5)$$

So deviations from thermal equilibrium will play a major role in superconducting Nb cavities. In the following two types of deviations will be discussed: Deviation of the quasiparticles alone from thermal equilibrium and deviation of the quasiparticle and phonon temperature from the temperature of the He bath.

In the penetration region quasiparticles absorb rf photons in a rate $\sim \tau_{ab}^{-1}$ (1 mT) $\approx 10^{+9} \text{ sec}^{-1}$, which because of $\tau_{ab}^{-1} \propto H^2$, soon yields deviation from the thermal equilibrium because of $\tau_{ab} \ll \tau_{in}$. For homogeneous superconductors this bottleneck is no problem, because the quasiparticles excited in the penetration region can transfer their energy in the bulk to the phonons. In contrast, states localized in the penetration region cannot escape into the bulk and so the bottleneck will build up, finally yielding a constant distribution function for states below $\Delta(\text{Nb})$. So the rf absorption from regions with depressed Δ will diminish with H as found for weak superconducting regions - see Fig. 8 and Ref. 13 - and for normal conducting regions - see Ref. 3. Only in cases where the quasiparticles are strongly coupled to phonons as in "amorphous superconductors" ($\lambda < 5 \text{ nm}$) or in normal conducting regions extended far into the bulk, equilibrium R(T)-values can be used.

The quasiparticle and phonon temperature T^* can be enhanced over T_{He} of the He bath, but because of the large λ -values (Eqs. (4) and (5)), T^* cannot be evaluated by the usual heat conductivity equation: ¹⁸

$$\Delta T = T^* - T_{\text{He}} = \frac{R}{2} H^2 \sum_i \frac{d_i}{\kappa_i} \quad (6)$$

where d_i/κ_i are the different heat resistances. It should be mentioned that especially for normal spots ($R_{nc} H^2/2$) lateral heat flow in the Nb and the addition of heat flows ($R_{nc} + \alpha R_{sc}$) $H^2/2$ from different sources asks for a 3 dimensional treatment. The temperature increase ΔT increases the surface resistance R(T) which can be described by: ¹⁹

$$\frac{\Delta R}{R_0} = \frac{\Delta T}{R_0} \left. \frac{\partial R}{\partial T} \right|_{T^*} = \frac{R H^2}{2R_0} \sum_i \frac{d_i}{\kappa_i} \left. \frac{\partial R}{\partial T} \right|_{T^*} = \gamma \left(\frac{H}{H_c} \right)^2 \quad (7)$$

For cases where $R \approx R_0$ holds, γ will be independent of R_0 and nearly temperature independent below $0.8 T_c$ because the dominating electronic heat conductivity κ has the same temperature dependence as R. For $T^* \lesssim 5 \text{ K}$, $\gamma \lesssim 1$ can be evaluated and such small increases have not been observed, yet.

As shown in Fig. 9, γ 's $\gtrsim 50$ have been observed and such strong increases are due to the growth of normal conducting regions A_{nc} : ¹⁹

$$\frac{\Delta R}{R_o} = \frac{R_{nc} \Delta A_{nc}}{R_o A_{sc}} = \gamma \left(\frac{H}{H_c}\right)^2 ; \quad \Delta A_{nc} = \Delta T C_{nc} \quad (8)$$

Without numerical calculations the growth rate C_{nc} cannot be estimated. Experimental results ¹⁴ - Fig. 9 - show that also in this case γ is nearly independent of R_o changing with T or frozen in flux, indicating that the effective $\Delta A_{nc} \propto \Delta T \propto (R_{nc} + \alpha R_{sc})H^2$ is dominated by $\alpha R_{sc} > R_{nc}$. This indicates, that the growth is not given by the normal conducting regions but by superconducting regions with their losses, which are rapidly rising with temperature. This astonishing experimental result is well known from normal conducting regions in flux cores. ²⁰

VI. RF BREAKDOWN

As outlined in Ref. 21, the rf breakdown is due to a thermal explosion driven ¹⁸ by the more than 10^4 times larger rf losses in normal conducting regions as compared to the superconducting state. The beginning of this explosion at B_{crit} can be due to the occurrence of normal conducting spots at their local critical superheating field B_{sh} or due to an instability of the heat conductivity equation. ¹⁸ But small normal conducting regions embedded in superconductors have by more than 2 orders of magnitude reduced normal conducting losses ³ due to deviations from thermal equilibrium. ¹⁷ And, as shown also above, large normal conducting regions stationarily exist in superconductors as fluxoids ²⁰ or as larger regions, which grow like H^2 with field. For small normal conducting regions ($< 0.5 \text{ cm}^2$) the rf breakdown seems not to be caused by normal conducting losses but mainly by superconducting losses and by impinging electrons. ¹⁴

So, beside some qualitative theories ^{14,18,21} there exists no quantitative theory for the rf breakdown.

VII. ELECTRON EMISSION OUT OF EXCITED STATES

Electron loading in superconducting rf cavities is classified in multipactor (MP) and field emission (FEM) loading ²² as outlined in Part. VIII. Experimentally, both types of loading are very sensitive to the sorption layers and in both cases, electrons hit the emitting surface. ²² So, first the excitation, relaxation and emission of such states will be discussed. Secondly this will be applied to secondary emission of Nb-Nb₂O₅ ... surfaces. And thirdly the rf FEM of such surfaces will be discussed.

1. Excitation, relaxation and emission of electrons

Electrons impinging solids are slowed down by exciting electron hole pairs of energy around 30 eV. ^{2,23-25} These excited states of density $n_e(\vec{r}, E)$ relax by electron-electron (plasmon) interaction τ_{e-e}^{-1} , by phonon (LO) interaction τ_{LO}^{-1} , ²⁶ by escape into the vacuum τ_v^{-1} and by field emission τ_{FEM}^{-1} . τ_{e-e}^{-1} and τ_{LO}^{-1} are proportional to mean free paths ℓ_{e-e} and ℓ_{LO} . All these relaxation and emission rates depend on position \vec{r} and on excitation energy E , and so the (transport) equations for $n_e(\vec{r}, E)$ are very complicated. In Ref. 23, the transport equation using τ_{e-e} and τ_{LO} has been used to treat secondary electron emission. A simplified version of this approach reads as follows: ^{2,25} Neglecting band structure effects and electron diffusion, the electron-electron interaction soon ($\approx 10^{-14}$ sec) ²⁶ thermalizes the electrons to a distribution function:

$$\frac{dn_e}{dE} = \frac{n_e}{\bar{E}} e^{-\frac{E}{\bar{E}}} \quad (10)$$

with $\bar{E}(=k\bar{T})$ as mean energy (≈ 8 eV) ²⁵ and n_e the overall concentration of excited states being proportional to, e.g., the impinging electrons. This cloud of excited electrons relaxes ($\approx 10^{11}$ eV/sec) ²⁶ by phonon emission and is scattered by electrons and phonons ²⁶ in approaching the surface. Hitting the surface barrier, electrons with an energy E smaller than the electron affinity χ , will be reflected totally and for $E > \chi$ partially with a reflection coefficient $R(E)$:

$$R(E) \approx 1 - 4 \sqrt{\frac{E - (\chi + E_F)}{\chi + E_F}} \quad (E - \chi \gg \chi) \quad (11)$$

For semiconductors E_F has to be substituted by zero because E and χ are then relative to the conduction band edge. So with Eq. (10) as inner distribution of excited electrons, one gets as outer distribution:

$$n_t(E) = \frac{1}{2} n_o \left(1 - \frac{\chi}{E}\right) \exp\left(-\frac{E}{\bar{E}}\right) \cdot R(E) \quad (12)$$

which is well known as distribution of the true secondary electrons - see SE in Fig. 10. The factor $(1 - \chi/E)$ in Eq. (12) is due to the finite mean free path λ . ²⁵ The true secondary electrons escaping per incident electron are given by: ²⁵

$$\delta_t \propto \int_{\chi}^{\infty} dE \frac{\lambda_a n_t(E)}{2} \approx \lambda_a \exp\left(-\frac{\chi}{\bar{E}}\right) \quad (13)$$

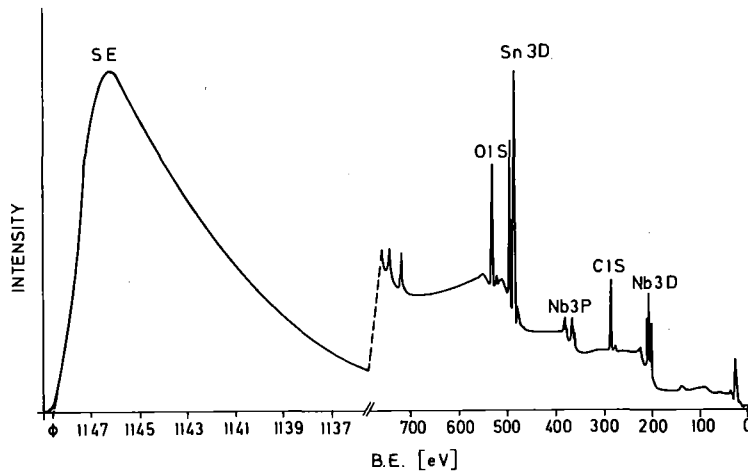


Fig. 10: XPS spectrum ^{1,2} of a Nb_3Sn surface coated by oxide and sorption layers. The labeled peaks are used for the studies of Nb, Nb and Sn oxides, O in oxides, adsorbed C and O and secondary electrons SE, where the latter contain about 80% of all photoelectrons. The secondary electron distribution curve (EDC) shown, is typical for the true secondaries δ_t , i.e. excited states distributed like $\exp(-E/\bar{E})$ emitted across a barrier of height $\chi \approx \phi$. This work function ϕ is defined by the intercept of the steepest slope with the axis. ²

In metals and semiconductors $\lambda_a = \ell_{e-e}$ is short and so the secondary yield is about $\delta_{tm} \approx 1.5$ at maximum. In insulators the electron-electron scattering is missing and hence $\lambda_a (> \ell_{LO})$ is large and $\delta_{tm} \approx 10$ has been found. ²⁴ Also the distribution $n_t(E)$ depends on the dominating type of relaxation: For emission out of a conduction band with dominating ℓ_{e-e} scattering, $n_t(E)$ has a maximum around $E - \chi \approx 2eV$, whereas for insulators the maximum is around 1 eV. ²⁴ For localized surface states the maximum can be even closer to χ because then also $R(E)$ is enhanced like in resonance tunneling.

For rf cavities also the time between impact and emission has to be discussed. The mean energy of secondary electrons is about $\overline{E - \chi} \approx 1eV$, which corresponds to a frequency ¹⁵ $\nu_E \approx 10^{15}$ Hz. So for GHz cavities the secondary electrons are emitted instantaneously.

If an electric field is applied to such a surface, the excited states will be emitted the stronger the higher their excitation energy is like in the case of F-T ²⁸ and photo field emission ²⁹. Because states having energies well above χ relax or are emitted fast in an rf field, states with $E \lesssim \chi$ will be emptied by an applied electric field E . As sketched in Fig. 11, the density of such states is

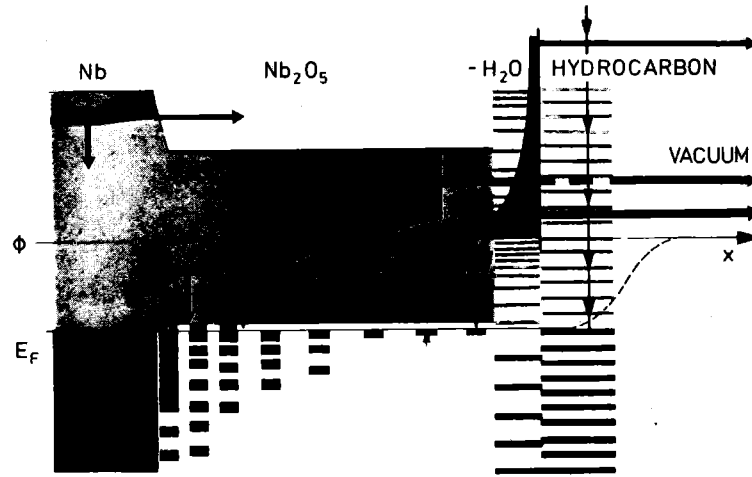


Fig. 11: Sketch of excited states in Nb-Nb₂O₅ sorption layers. The fast electron-electron interaction in Nb and Nb₂O₅ thermalizes the states to $n_e \propto \exp(-E/\bar{E})$ with $\bar{E} \approx 8\text{eV}$. The slow emission of longitudinal optical (LO) phonons (\downarrow) relaxes the excited states if no emission (\rightarrow) into the vacuum occurs. Localized states in the sorption layer approach equilibrium by emission into the vacuum and the slow LO emission. Conditioned - polymerized - hydrocarbons show enhanced absorption and relaxation of slow electrons.

very high and so the emission will be very strong - see Fig. 12 - and proportional to the impinging electrons. The emission time²² will be quite short in this case because of the low and narrow tunnel barrier.

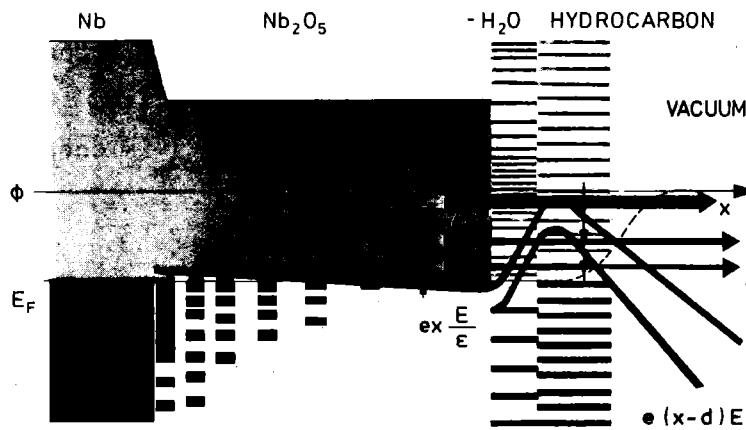


Fig. 12: Sketch of the field emission of a Nb-Nb₂O₅ .. surfaces with excited states. Because, according to Fig. 11, the density of such states at ϕ is very high their emission dominates the electron current. The barrier is very small for states in the sorption layer and so, e.g., Nb₂O₅-H₂O enhances the field emission very much by resonance tunneling. Polymerized hydrocarbons can absorb slow electrons and will so reduce the field emission current, especially because this absorption enhances the work function.

2. Secondary electron emission from Nb-Nb₂O₅ ... surfaces

To analyze the secondary yield of the Nb sketched in Fig. 1 we start with the yield of Nb and Nb₂O₅. The maximum in the true yield occurs at about 300 eV with $\delta_{tm} \approx 0.8$.² For clean Nb₂O₅ the true yield is about $\delta_{tm} \approx 1.1$ and not depending on temperature,³⁰ despite the fact that Nb₂O₅, as semiconductor with 0.2 eV activation energy (Figs. 11 and 12) becomes an insulator at He temperature. But according to electron current^{14,31} or yield measurements^{2,30} typical electron currents are above 10^{-9} A/cm². Because the secondaries are a small percentage of the excited states of a surface layer $\lambda_a \approx 5$ nm, the density of excited electrons is well above 10^{19} /cm³.

Then according to Ref. 26, the fast electron-electron scattering dominates yielding, e.g., $\lambda_a \approx 5$ nm.^{1,2} For such impinging electron currents (\gg nA/cm²) λ_a is short and temperature independent. The higher yield of Nb₂O₅ as compared to Nb could be due to the smaller electron affinity of Nb₂O₅ (0.2eV) - see Eq. (13), which also reduces the reflection coefficient R (Eq. (11)). The latter effect of enhancing the yield by reducing the reflection at $E \gtrsim \chi$ is fairly effective because the density n_e (Fig. 11) is very high at $E \gtrsim \chi$. The reflection coefficient is reduced further, by the Nb₂O₅-H₂O chemisorption state, because the peak in $n_t(E)$ occurs well below $E-\chi = 1$ eV - Fig. 13 - and

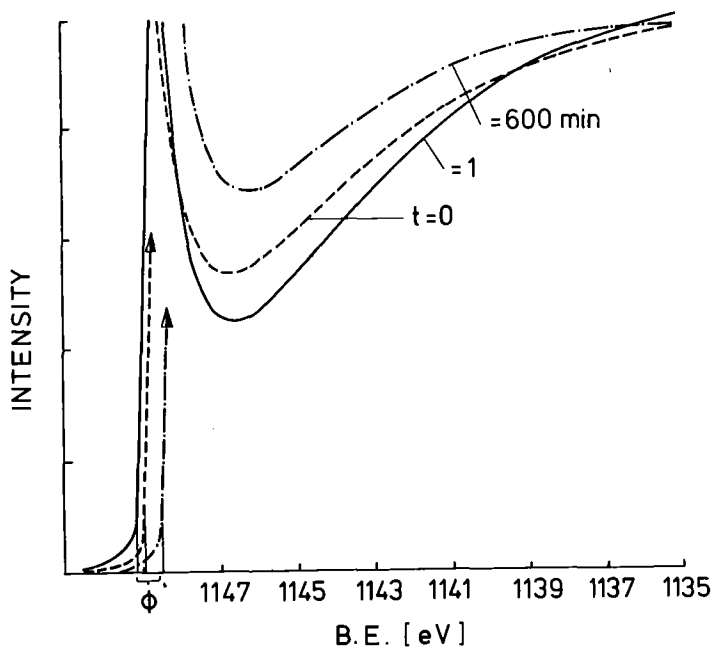


Fig. 13: EDC's of secondary electrons emitted by excited states of wet Nb₂O₅.¹
 The two peaks indicate the existence of electron emitting levels of the Nb₂O₅-H₂O chemisorption state below ϕ and around $\phi+10$ eV. The electrons being emitted out of the Nb₂O₅ conduction band (Fig. 11) seem to be resonantly scattered into the Nb₂O₅-H₂O states. With enforced polymerization of the hydrocarbons by electron impact, more - slow - secondary electrons get absorbed by the hydrocarbons lowering the yield δ_t (Fig. 14).

the yield δ_{tm} is enhanced up to 2. Because in this case the true peak of Nb_2O_5 at $\chi + 2eV$ cannot be seen, the $Nb_2O_5-H_2O$ seems to form a dense layer and the excited electrons of Nb_2O_5 are resonantly scattered into states around χ and $\chi+10eV$ from where they are easily emitted because of the small $R(E)$.

Another way sorption layers on Nb_2O_5 enhance the yield is by the reduction of the surface barrier $\phi \approx \chi$.² But according to Eq. (13) and Fig. 14, ϕ changes by less than 0.6 eV, which is insufficient to explain the about 50% yield reduction observed (Fig. 14).² As outlined in Ref. 2, the yield reduction is due to processes absorbing electrons in the insulating sorption layers by which negative charging occurs measured by C peak shifts or as ϕ increase.² I.e. charging in insulators indicates enhanced (or reduced) electron absorption. If thick enough H_2O sorption

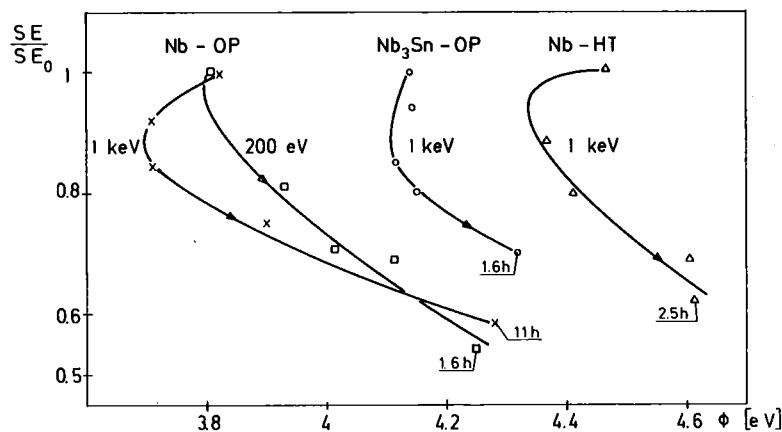


Fig. 14: Yield changes $\frac{SE}{SE_0} = \frac{\delta_t}{\delta_{to}}$ versus work function of 3 Nb samples (OP: oxipolished; HT = annealed in UHV at 1850°C for 2 h)¹ and one Nb_3Sn sample, subject to electron impact ($100 \mu A/cm^2$). The final duration of the electron impact of 1.1 - 11 h corresponds to electron doses between 0.4 and 4 Coulomb/cm².

layers (≤ 1.5 nm) exist, which lower ϕ by 1 to 2 eV as inferred from asymmetric tunnel characteristics,⁸ the yield can be drastically enhanced. This layer seems to be evaporated by prolonged pumping in UHV and so it was not found in the XPS and secondary yield measurements.^{2,30}

Above it was mentioned that the sorption layers are insulating and then the long λ_a (> 20 nm) should enhance the yield. But because the sorption layers - after prolonged pumping - see Ref. 2 - are only about 3 nm thick, this mechanism enhances the yield not more than 10%.

The most dramatic effect in the secondary emission of Nb is the reduction of the yields δ_t by about 40% by electron impact of 1 C/cm^2 - see Fig. 14. As discussed in Ref. 2, this yield decrease seems to be due to an electron impact induced polymerization involving hydrocarbons. This polymerization yields low lying ($\sim\phi$) electron states which resonantly absorb electrons and which relax fast. Details of this polymerization are not known, but the effect is dramatic, stable at He temperature but not stable at room temperature.

3. Rf field emission of Nb surfaces sketched in Fig. 1

Nb with its oxide and sorption layers has a work function above about 4 eV as summarized in Fig. 14. So the field emission current will be negligible²⁸ up to fields of $2 \cdot 10^9 \text{ V/m}$. Because electropolished Nb has nearly no roughness, a field enhancement factor $\beta_G \approx 100$ is an upper limit and so below $(2 \cdot 10^9 \text{ V/m})/100 = 2 \cdot 10^7 \text{ V/m}$ no field emission current should be observable. Thus, the observed FEM loading at^{14,31} 5 MV/m can only be due to FEM from excited states - see Fig. 12. Thermally excited states, e.g. due to heating proportional to E_p^2 , would yield an upward bending of the Fowler-Nordheim plot - see Fig. 4 in Ref. 28 - which has never been observed - see, e.g. Fig. 15. In contrast, in some cases a downward bending has been observed. So, one has to explain the Fowler-Nordheim dependence shown in Fig. 15 by other excited states. As discussed above - see Fig. 12 - electron impact excites states, which around ϕ are easily drawn by an electric field out of the dielectric sorption layers ($\leq \lambda_a$) where they in addition can gain the energy $\lambda_a eE/\epsilon_r$.

As indicated in Fig. 11 the density of excited states around ϕ is very high and their relaxation is fairly slow and given by $\exp(-t/\tau_0)$ with $\tau_0 \approx 10^{-10} \text{ sec}$.²⁶ Neglecting mirror charge effects the FEM out of excited states of energy E is given by ($E_c = E_F$):

$$j_{\text{FEM}} \approx e^{-\frac{4}{3}\kappa \frac{\phi-E}{E_p}} = e^{-\frac{c}{\beta E_p}}; \quad \kappa = \sqrt{2m(\phi-E)}/\hbar \quad (14)$$

Comparing this current with one assuming $\phi-E \approx \phi = 4 \text{ eV}$ one obtains as correction factor in the exponent

$$\frac{1}{\beta^*} = \sqrt{\frac{\phi-E}{\phi}} \frac{\phi-E}{\phi} \quad (15)$$

yielding for $\phi-E = 0.4 \text{ eV}$ $\beta^* = 31$. So β -values of 10^3 fitted to experimental data^{14,31-34} hint to emission out of states excited to about $\phi-0.4 \text{ eV}$. This type of FEM is proportional to the electron impact and varies slowly with ϕ like $\exp(-\phi/\bar{E})$

- see Eq. (13). So β changes observed hint to changes in $\overline{\phi-E}$, i.e. to changes in the states in the sorption layer. Chemisorption states and other states in front of Nb_2O_5 with its high $\epsilon_r \approx 36$, will enhance the FEM in the sense of resonance tunneling.^{27,34}

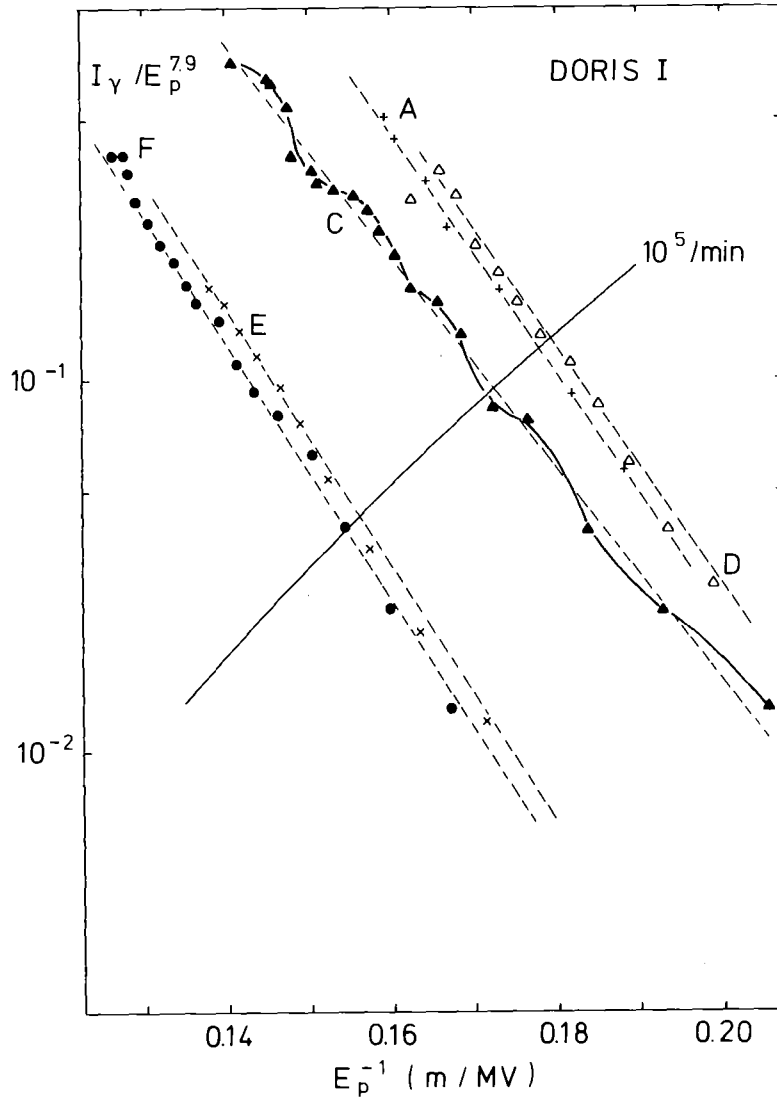


Fig. 15: Fowler Nordheim plot of the x-ray yield measured at the midplane of the cylinder of a 500 MHz TM_{010} mode cavity.¹⁴ With impinging FEM electrons (rf conditioning) the FEM is reduced. This reduction is mainly due to a reduction of the emitting area, whereas the β (≈ 700) only decreases by about 20%. The oscillations, which are most pronounced for run C, are an indication for emission out of excited states, which fits to the large β values.

Another hint to emission out of excited states is the oscillation on top of the Fowler-Nordheim dependence shown, e.g., run C in Fig. 15, which seems typical for tunneling through a thin barrier.²⁹ As already mentioned above, $\text{Nb}_2\text{O}_5\text{-H}_2\text{O}$

chemisorption states inside the FEM barrier most likely channel excited states into the vacuum and so the oscillation in $j_{\text{FEM}}(E_p)$ could be due to E_p -field induced level splitting.

For the secondary emission the changes due to Nb_2O_5 and sorption layers have been discussed above and in Ref. 2. For FEM these changes with sorption layers can be even stronger because states in the FEM barrier can enhance the FEM much stronger than the secondary emission, but less quantitative information is available in the case of FEM. The above summarized ideas offer some qualitative explanations for the FEM changes observed with surface treatment, rf processing or He-conditioning (Refs. 14, 22, 31-34):

- $\beta \approx 10^3$ hints to emission out of states with $\overline{\phi-E} \lesssim 0.4$ eV, which could be the states of $\text{Nb}_2\text{O}_5\text{-H}_2\text{O}$ found by the EDC (Fig.13) slightly below ϕ .
- β changes with He-conditioning³⁴ can be explained by an increase of $\overline{\phi-E}$ e.g., due to sputtering off the H_2O or by positive charging of the sorption layers.
- The reduction of j_{FEM} by rf conditioning seems to be due the enhanced absorption of slow electrons by polymerized hydrocarbons. So mainly the emitting area is reduced and not β - in agreement with some experiments - see, e.g., Fig. 15.¹⁴ But if this absorption charges the sorption layer negatively the enhanced ϕ should reduce β .¹⁴

The following points, which are important for the analysis of experimental results, should be mentioned:

As outlined in Ref. 22, FEM decreases with increasing frequency because of the finite beat frequency. This beat frequency increases exponentially with E_p reducing the fit parameter β up to a factor 1/3.²² Because in rf cavities FEM out of excited states will occur also at $E_p(t) = E_p \cos \omega t < E_p$, the fitted β is enhanced also by this effect. So, e.g., the downward bending of the Fowler Nordheim plot could also be due to shift of the FEM to earlier phases.

VIII. ELECTRON LOADING IN SUPERCONDUCTING Nb CAVITIES

In Part VII the mechanisms important for emitting electrons from Nb covered by Nb_2O_5 and sorption layers have been discussed. Whereas the secondary emission is now fairly well understood,² the mechanisms governing rf field emission are just becoming clear. But because both processes are intermingled in rf cavities, first the evolution of the electron emission will be discussed, and then the type of loading encountered.

1. Electron currents in an rf cavity

Assuming some impinging electrons, e.g., from noise, onto a surface with $E_{\perp} = E_p \cos \omega t$ present, the fast electrons escaping during the time $-\pi/2 < \omega t < \pi/2$ will be slowed down by E_{\perp} and so they lose energy and most are accelerated back to the surface. Only fast, i.e. backscattered, electrons can escape. Because true secondaries have energies below 5 eV and because their secondary yield is about 1, the secondaries emitted in $\{-\pi/2, \pi/2\}$ are collected at the surface. At $\omega t \geq \pi/2$ these electrons are accelerated away from the surface. Electrons impinging at $\pi/2 < \omega t < 3\pi/2$ produce instantaneous secondaries and excited states, E_p will draw electrons out of the excited states proportional to $\exp(-c/E_p(t))$ and this FEM will decay like $\exp(-t/\tau_0)$ with $\tau_0 \geq 10^{-10}$ sec - see Part. VII. The amount of electrons impinging at the different phases depends on the trajectories, which will be discussed in Part. VIII.3. Here it should be mentioned only, that electrons with impact energies between 100 and 2000 eV are most effective in producing secondaries and excited states.

2. Multipactor loading (MP)

As discussed, e.g. in Refs. 22 and 32, multipacting occurs at well defined field levels with starting phases $\omega t \geq \pi/2$. So secondaries produced during the wrong E_p direction ($< \pi/2$) are stored and will be accelerated into MP phase regions, i.e. they will enforce MP. Because electrons gain energy on MP trajectories, the "background loading" will be enforced in these field regions. For example, the second order one side MP shows up in a peak on the background FEM current as shown in Fig. 4 of Ref. 31.

Another example is two side MP: At such levels the electrons stored during $\omega t < \pi/2$, the secondary electrons and the field emitted electrons out of excited states will enhance the MP levels - see, e.g., Ref. 14 for orders $n \approx 20$ and Ref. 31 for $n = 1$ ($d_{\text{gap}} = 11$ cm). Due to the high E_p -field, FEM is the dominating enhancement mechanism in the latter example.

This discussion shows, that dc secondary yields can be enhanced very much in rf cavities due to the storage of slow electrons and due to FEM out of excited states which explains the occurrence of MP levels, where the dc yield is still smaller 1. Because the FEM out of excited states is changing more strongly than the secondary yield with variations of the sorption layers, this effect can explain the success of rf or He conditioning in overcoming MP levels. ¹⁴

3. RF field emission loading

The rf FEM loading seems the ultimate limitation in superconducting Nb cavities, yielding for narrow gap ($d_g < \lambda/2\pi$) cavities about $E_p \approx 20$ MV/m^{22,31,32} and for wide gaps ($d_g > c/\omega = \lambda/2\pi$) about $E_p \approx 16$ MV/m GHz.^{31,32} The appearance of the FEM loading is an electron current $j_{FEM} \propto \exp(-c/\beta E_p)$ (Eqs. (14) and (15)) with $100 \lesssim \beta \lesssim 2000$,^{22,32} which is shape and frequency dependent and which initiates rf breakdown by heating¹⁴ or limits the attainable fields simply by the absorbed rf power.³¹⁻³⁴

As already mentioned above, the high β -values together with the oscillations - see Fig. 15 - hint to FEM out of excited states-especially states in the FEM tunnel barrier - which explains its sensitivity to surface treatments like rf or He conditioning.

The question to be discussed in this part is then: where are the excitations coming from and why is this depending on shape and frequency?

The observations that FEM loading in narrow gap cavities ($d_g < \lambda/2\pi$) limits E_p to about 20 MV/m and that β -values are often smaller than in wide gap cavities, can be explained as follows: Electrons emitted around $\omega t \approx \pi$, where E_p is maximal, hit the opposing surface shortly afterwards. There, at this time E_p is still slowing down emitted electrons and so nearly all excited states will disappear like $\exp(-t/\tau_0)$. So the "temperature" of the excited states (around ϕ) in the sorption layer will be fairly low yielding $\beta \approx 200$.³¹

In contrast in wide gap cavities, electrons emitted around $\omega t = \pi$ will return roughly 2π later to the emission region with small impact energies. So electrons are excited at $\omega t \approx 3\pi$ where the large E_p -field enlarges the secondary emission by FEM out of excited states. In parallel plate geometry the maximum excursion distance d_{max} is given by:³⁵

$$d_{max} = \frac{\lambda}{2\pi} \operatorname{arctg} \frac{\lambda e E_p}{2\pi m_0 c^2} \quad (16)$$

That is for $\lambda e E_p / 2\pi < m_0 c^2$, $d_{max} \propto E_p$ grows with field amplitude, whereas for relativistic energies $\lambda e E_p / 2\pi > m_0 c^2$ the excursion no longer depends strongly on E_p , where

$$E_p = m_0 c^2 (2\pi/\lambda e) = 10 \text{ MV/m GHz} \quad (17)$$

holds.

In accelerator cavities E_p decreases due to beam holes and roundings with distance from the surface. So

an electron starting at $\omega t = \pi$ will return in $\{2\pi + \alpha\}$. For the nonrelativistic case, where d_{\max} increases with E_p , the trajectories see with increasing E_p more inhomogeneous fields, which lowers the return efficiency. For the relativistic case, d_{\max} (Eq. (16)) becomes independent of $E_p > 10 \cdot f$ MV/m GHz, i.e. independent of E_p some trajectories will return to the region where they have been emitted. At this spot, the electrons in the oxide and sorption layers get excited allowing so secondary and FEM emission with large β values. Because in this field region, the impact energy ϵ scales like $\epsilon \propto f^{-2}$, the number of excited states will diminish like f^{-2} . Thus β will decrease with increasing frequencies in agreement with experiments ^{22,32} if the large variations of β with sorption layers are taken into account. This is also an explanation why for $f > 2$ GHz higher E_p fields have been obtained than for narrow gap structures.

The frequency dependence of the maximal field in wide gap cavities is with $E_{p\max} \approx 16$ MV/m GHz in good agreement with Eq. (17) where this type of rf FEM loading should become dominant. According to the ideas outlined above, a strong decrease of E_p with distance from the surface for the high field region should weaken the loading, which would explain the differences between Refs. 31, 14 and 33 as due to larger beam holes and rounding. It is obvious that the above arguments can be made more quantitative only by trajectory calculations, ^{14,22,31,32} These have already shown that backscattered electrons will dominate the loading via their high β value. $(Nb) = 0.42$.

An elliptically shaped cavity should - besides theoretical and cleaning arguments - show reduced FEM loading ³⁶

R e f e r e n c e s

- 1 M. Grundner, J. Halbritter, J. Appl. Phys. 51, 397 (1980)
- 2 M. Grundner, J. Halbritter, J. Appl. Phys. 51, Oct. (1980)
- 3 W. Schwarz, J. Halbritter, J. Appl. Phys. 48, 4618 (1977)
- 4 A. Philipp, J. Halbritter, IEEE Trans. MAG-17, (1981)
- 5 A. Das Gupta, W. Gey, J. Halbritter, H. K pfer, J.A. Yasaitis, J. Appl. Phys. 47, 2146 (1976)
- 6 J. Halbritter, Solid State Comm. 34, 675 (1980)
- 7 W. Schwarz, J. Halbritter, Proc. 4. Int. Conference on Solid Surfaces, Cannes, Sept. 1980; W. Schwarz, KfK-report-2913 (Kernforschungszentr., KfK ,1980)
- 8 H. Ekrut, A. Hahn, Fr hjahrstagung der DPG, Freudenstadt, M rz 1980
- 9 J. Halbritter, Z. Phys. 266, 209 (1974)
- 10 J. Halbritter, KfK-Ext. 3/74-5 (Kernforschungszentrum Karlsruhe, 1974)
- 11 J. Halbritter, Proc. of Autumn School on Metal Physics, Piechowice (Poland) Nov. 1979
- 12 Tadashi Yogi, thesis (Cal Tech, Pasadena, 1977)
Guy Petterson, Hugo Parr, Phys. Rev. B 19, 3482 (1979)
- 13 P. Kneisel, O. Stoltz, J. Halbritter, Low Temperature Physics - LT 13 (Eds. E. Timmerhaus et al, Plenum Press, 19) Vol. 3, p. 202
- 14 Sh. Noguchi, Y. Kojima, J. Halbritter, submitted Nucl. Inst. Meth.
- 15 J. Halbritter, IEEE Trans MAG-11, 427 (1975) and
J. Halbritter, IEEE Trans. MAG-17, (1981)
- 16 J. Halbritter, Z. Phys. B 31, 19 (1978)
- 17 J. Halbritter, private communication
- 18 C.M. Lyneis, J.P. Turneure, IEEE Trans MAG-13, 339 (1977);
H. Padamsee, this workshop
- 19 J. Halbritter, J. Appl. Phys. 41, 4581 (1970) and KfK-Ext. 2/69-6 (Kernforschungszentrum Karlsruhe 1969)
- 20 B. Piosczyk, P. Kneisel, O. Stoltz, J. Halbritter, IEEE Trans. NS-20, 108 (1973)
- 21 J. Halbritter, Proc. 72 Appl. Superconductivity Conference, Anapolis (IEEE, New York, 1972), p. 662
- 22 J. Halbritter, KfK-report 3/78-1 (Kernforschungszentrum Karlsruhe, 1978)
- 23 e.g. H.J. Fitting, H. Glaefeke, W. Wild, phys. stat. solidi A43, 185 (1977)
- 24 B.L. Henke, J. Liesegang, St.D. Smith, Phys. Rev. B 19, 3004 (1979)
- 25 H.J. Fitting, H. Glaefeke, W. Wild, Surf. Sci. 75, 267 (1978)
- 26 D.H. Anston, S. McAfee, C.V. Shank, E.P. Ippen, O. Teschke, Solid-State Electronics 21, 147 (1978); D. von der Linde, J. K hl, H. Klingenberg, Phys. Rev. Lett. 44, 1505 (1980)
- 27 J.W. Gadzuk, Phys. Rev. B1, 2110 (1970)
- 28 W.W. Dolan, W.P. Dyke, Phys. Rev. 95, 327 (1954)
- 29 M.J.G. Lee, R. Reifenberger, Surface Science 70, 114 (1978)
R. Reifenberger, private communication
- 30 N. Hilleret, private communication

- 31 K. Yoshida, M. Yoshioka, J. Halbritter, IEEE Trans. NS-26, 4114 (1979)
- 32 C.M. Lyneis, this workshop
- 33 H. Piel, this workshop
- 34 H.A. Schwettman, J.P. Turneaure, R.F. Waites, J. Appl. Phys. 45, 914 (1974)
- 35 J. Halbritter, Part. Acc. 3, 163 (1972)
- 36 J. Halbritter, P. Kneisel, to be published

ROUND TABLE DISCUSSION "WHAT TO DO NEXT?"

Chairman: G. Loew SLAC

Participants: Citron (Karlsruhe), Halbritter (Karlsruhe), Hillenbrand (Siemens, Erlangen), Lyneis (HEPL), Loew (SLAC), Piel (Wuppertal), Padamsee (Cornell), Septier (Orsay), Tigner (Cornell)

Loew: Before we start this round table I would like to make a confession to the audience and this confession is that this round table gives me very mixed feelings. I have feelings of pessimism and I have feelings of optimism. The reasons I have pessimism are that the best round tables I have been to or I have seen are about subjects like politics or the social sciences. This round table will be about science. And I asked myself what it was, and the answer, I think, is very simple. The reasons that round tables are very good about politics and subjects of this kind are because everybody has an opinion, and with a lot of opinions you can make a very vital discussion. Conversely at science of course there are supposed to be facts and there is not much room for opinions. About facts you can not have a vital discussion. Now, my reason for optimism on the other hand is that in this field, I think, we all agree there is still room for opinions because a lot of facts are missing. In order to focus the discussion, since there is an endless number of topics and infinite numbers of subjects to discuss I have thought a little bit about it, and I would like to suggest that we start with the following thing. Let us try collectively to look first at the possible machines that people are talking about here. The reason for that is obvious because the machines themselves are only a base part of our work, they are in some way the driving forces. Infact, if you look at the past you will probably agree that at times the driving force has been a negative force in some way, because with all over and over, been driven and coming up with some machine, we are often been forced into doing things much too fast because there was some kind of expectation in the end. In the other hand, you might say that the different work for these expectations would not be here without anything. So you have to agree with the fact that these machines are here, people want to build them, people expecting things from us. So the question is what is it that they expect? More than half of you are in lab's where you are being requested to build some kind of machine. I thought it would be interesting to locate what are the demands on the horizon. Obviously they differ from there to there, and so we try to make a list. I do not think we should illuminate the low β machines, because they are not well represented within this group. So we

should concentrate on $\beta \approx 1$ or may be a little smaller than 1. That possibly will simplify the discussion and make it possible to fill out the table. I was trying to order the lab's. I thought may be we should have the future linacs or present linacs first, and then look at the people who are trying to build storage rings and then there are some cases in between and at the end there is SLAC.

Anyway, I also put down some of the parameters Prof. Citron used in his talk and if you look at these, well, the first one is frequency, the second one is temperature, the next one is the accelerating field. I allways put down two cathegories, those which had been obtained, and those that you feel that you can get them out. Des does not mean design, it means desire. As Prof. Citron just mentioned the desire is infinity, but let us not put infinity, let's put what we think we need for the machine that people are expecting us to build. At the end of the session it would be nice to have these numbers so that may be in two or three years from now when we look back we see this was the status of 1980 and now we have made progress or we have not made progress."

Each "knight of the round table" filled out the following table and explained his numbers.

TABLE 1: Possible machines

LAB	f (GHz)	T (K)	E _{acc} (MV/m) OBT DES	E _P (MV/m)	H _P (mT)	Q _o	Energy	L (m)	P _{rf} (MW)	P _{Ref} (W)	G \$
HEPL	1.3	1.9	1.75 2.1	5 6	9.0 11.5	10 ⁹	(MeV) 160(75%) 230(15%)	30	0.05	300	
WUPPERTAL	8 3	1.8 1.8	3.6 5.0	41.5 13	74 17.5	10 ⁹ 3×10 ⁹	1.7 130	0.5 10		2 100	3×10 ³
GENOA	4.5	1.3	8 5.0	20 13	45 30	0.5×10 ⁹	10	2		25	10 ⁻³
KfK DESY CERN	0.5	4.2	3 5.0	6 10	10 15	10 ⁹	(GeV) 2 × 130	600	90	5×10 ⁴	
CORNELL	1.5	1.8	3 3	9 9	18 18	10 ⁹	2 × 50	500	10	2500	0.15
CERN	0.352					2×10 ⁹					1
KEK	6.5	1.6	3 3	10 5	15 10	0.6×10 ⁹ 10 ⁹	2 × 40	400	25	10 ⁴	

After this first round the discussion was continued as follows:

Loew (SLAC): "I would like to go around the table again and now ask each representative to describe the most urgent problems for his machine. By urgent I mean the things that really have to be done in the period we are thinking about, the next year or two years or whatever the timetable is. It is obvious that we do not have infinite resources to look at it in a different way. What is most important for you in the next future?"

Lyneis (HEPL): "We know what we can get. What I would like to work on are the questions of field emission loading, non-resonant loading. The other question is to maintain a high Q_0 for a long period of time. In our machine it does not make any sense to talk about gradients of 6 MV/m, unless you get to much higher Q's. If you look at the questions of cost which is Q and field level, 6 MV/m does not make any sense, 3 MV/m perhaps, but you have to get Q's of 2 or 3×10^9 in our structures. Considering our manpower the main thing we are interested in and attacking it is a long range question, is trying to improve the gradient by looking at the field emission."

Piel (Wuppertal): "Under more fundamental questions we are interested in the same kind of problems as far as field emission phenomena are concerned, especially at higher frequencies we are interested in the spots which produce the thermal instabilities, about the nature and how we can exclude them. In terms of the actual accelerator design one very important thing is how do we fabricate our structures. Do we have in multicell spherical structures different field emission phenomena from single cell? We are very much interested to find a production process of the 1 m unit for the recyclotron which can be replaced at once and also which gives the provided tolerances. We want to investigate the refrigeration and the cryostat. The cryostat is a very big part of the cost of such an accelerator, so we are more involved in the practical cost consideration of this design."

Pagani (Genoa): "We plan to build spherical multicell cavities, but we have first to put our 3 cell cavity into the accelerator."

Citron (Karlsruhe): "Our immediate problem is to match the high power requirements for storage rings, that is a question of a test with something like 100 kW of rf power into a cavity which can only dissipate on the order of 5 W. We have a solution, but the solution has to be tested, and this is one of the aims for the test this fall at DESY. Related to that is the other question of coupling out the higher order modes."

In principle, we would like to see to which extent we can couple out the higher order modes and also get some information, how necessary it is to couple out the higher order modes. When we have solved these problems for the single cell cavity, the next move is to transfer this to the multicell structure, to the 3 to 5 cell structure. Of course, besides from that, we try to increase our understanding of the limitations and hopefully contribute to some improvements."

Loew (SLAC): "Prof. Septier, there is no immediate plan to have a machine in your own house?"

Septier (Orsay): "No".

Tigner (Cornell): "In our case we have a lot of engineering problems. In this project we have, as already mentioned, to couple high power in and out. There exist proposals which say we can do it, but we also have to do it for a certain cost."

Lengeler (CERN): "I can repeat for us is the aspect of simplicity absolutely prior. Simple surface treatments are necessary, we consider for a machine like LEP chemical treatment is not simple enough. Therefore, I think, there will be a big push at CERN to see if we can do things with ion-bombardment-cleaning or with rf processing at room temperature. The other thing is that we believe that we can hold the peak values in multicell cavities."

Loew (SLAC): "We do not have an immediate goal in terms of building a machine at SLAC. We are trying to do some of the R+D-work between the microwave effort and the surface physics effort."

CERN/EF 80-4
22 August 1980

DESIGN OF SUPERCONDUCTING ACCELERATOR CAVITIES

H. Lengeler
CERN, Geneva, Switzerland

Superconducting cavities already equip recirculating linacs for electrons [1,2], electron synchrotrons [3], proton [4] and heavy ion linacs [5-7], and particle separators [8]. Their use is considered for linear accelerators [9-12] and large e^{\pm} storage rings [13,14]. In the following a few aspects for the design of s.c. cavities are discussed by taking into account results of computations and laboratory tests on single and multicell cavities and the practical experience gained during the construction, testing and operation of existing devices. As additional requirements for low β structures will be treated in the next talk [15], I will concentrate mainly on electron accelerators.

In order to simplify the presentation two groups of electron machines are considered:

- Linear accelerators, recirculating linear accelerators and electron synchrotrons where frequencies between 1.5 - 3 GHz are used.
- Electron-positron storage rings for energies well above 20 GeV where a frequency range between 350 - 1500 MHz is presently under discussion.

For all machines, accelerating fields not exceeding 3-5 MV/m are assumed.

The specific problems of large storage rings, e.g. synchrotron radiation and higher mode excitation will be treated in more detail in a following talk [16]. Problems dealing with regenerative and cumulative beam break up in existing linear accelerators will only be considered marginally.

1. CHOICE OF FREQUENCY

Electron linac and synchrotron users favour at present high acceleration fields and are less concerned with low r.f. losses. As there has been established in the last years a clear increase of achievable breakdown field levels with frequency the highest possible frequencies should be aimed at. Explanations for this relation can only be given in rather vague terms but the fact is supported by such a wealth of experimental evidence [17] for single and multicell cavities of different geometries that, for the time being, there is no stronger argument for the frequency choice. For linear accelerators the upper frequency limit is set by machining tolerances and by the requirements of beam emittance and beam steering. Frequencies well above 5 GHz seem to be excluded for this reason. For electron synchrotrons special structures with an enlarged opening in the plane of synchrotron radiation (like e.g. the Cornell "muffin tin" structure [3]) are already necessary if the frequency should be raised to ~ 3 GHz. The requirement for high fields should not hide the fact that there are also arguments favouring low frequencies like e.g. smaller r.f. losses for a given operating temperature (cf. below) and smaller cell numbers in multicell cavities.

In large storage rings the question of frequency choice is still a subject of discussion. The requirements of beam dynamics and higher mode excitation favour low frequencies. Frequencies of 350 MHz [18] and 1500 MHz [14] have been considered. For more details we refer to [16].

2. TYPES OF CAVITIES

Numerous types of cavities have been proposed in the past for particle acceleration [19]. They are almost exclusively of the periodically loaded waveguide type. Many of these cavities have been proposed with the aim of achieving high shunt impedance, a goal which for superconducting cavities is not nearly as important as for normal conducting cavities. Among the cavities considered for electron acceleration we note:

- Disc loaded waveguides of cylindrical shape with flat discs, shaped discs (nose cones) and coupling slots.
- Disc loaded waveguides of spherical cell-shape.
- Side coupled structures.
- Disc and washer structures.
- "Muffin tin" rectangular structure.
- Cross bar structures of circular or rectangular shape.

As soon as superconducting versions of these cavities are considered, one can rule out a few of them, mainly because of their complexity. This is certainly the case for all kinds of side coupled cavities and to some lesser extent also for the disc and washer structures despite their high shunt-impedance and coupling factor (which could be an advantage for the handling of higher modes). Cross bar structures especially in their improved version of "ridged easitron" [20] show excellent cooling properties and good coupling factors but their high H_p/E_{acc} values and unknown multipactor behaviour are strong drawbacks. So we will consider in the following only two candidates for superconducting cavities: the disc loaded waveguide of different shapes and the "muffin tin" structure.

3. SHUNT IMPEDANCE

For normal conducting structures in large accelerators a high shunt impedance outweighs all other requirements because it determines to a large extent the operation costs of accelerators. In order to illustrate the difference between normal conducting and superconducting cavities with

respect to this parameter we write down the well-known formula for the cavity losses P_{diss}

$$P_{\text{diss}} = \frac{E_{\text{acc}}^2}{r} = \frac{E_{\text{acc}}^2}{(r/Q)Q_0}$$

- r : shunt impedance.
- E_{acc} : accelerating field.
- Q_0 : quality factor of the cavity.
- r/Q scales with ω and is a loss-independent quantity determined only by the cavity geometry; this quantity cannot be varied over a large range without affecting in an intolerable way other parameters like e.g. peak fields and coupling constants. For normal cavities Q_0 is given by the surface resistance of such good conductors as Cu or Al and is nearly independent of temperature and surface quality. Thus, a decrease of P_{diss} can only be obtained by an increase of r . For superconductors the situation is very different. Q_0 can be varied over orders of magnitude by an adequate choice of temperature and material; it depends in a very critical way on the surface preparations applied to a cavity. An adequate upper limit depends on the field level which should be achieved. With the present state of technology one can reach, even in long and complicated structures, Q_0 values which up to field levels of a few MV/m are sufficiently high for avoiding thermal breakdown and for keeping r.f. losses comparable to the losses of cryostats. One should nevertheless stress the importance of low Q_0 values for large accelerators where operating costs have to be kept as low as possible.

4. H_p/E_{acc} , E_p/E_{acc}

Two parameters obviously linked to the achievable field levels are the ratios H_p/E_{acc} and E_p/E_{acc} . For the disc loaded structures their behaviour is dominated by disk opening and thickness. An adequate shaping of the disc rounding can decrease one of these parameters [21], generally at the expense of the other. Coupling slots in multicell cavities as well as openings for coupling r.f. in or higher modes out can increase the

magnetic field at their border and their effect should be carefully studied. For the "muffin tin" structure E_p/E_{acc} and H_p/E_{acc} are mainly determined by the gap distance and the disk thickness [22]. Field limitations in cavities with an operating frequency of a few GHz are predominantly produced by magnetic field effects whereas in low frequency structures electron loading is a common field limitation. Therefore one should tend to decrease as much as possible H_p/E_{acc} in the former and E_p/E_{acc} in the latter case.

5. MULTIPACTOR

There has been in the last years a break-through in the understanding of one and two side electron multipactor. The computations of multipactor trajectories and electron multiplication were crucial for this achievement and allow by now a detailed cavity design with respect to multipactor. A few simple guiding rules for avoiding or decreasing multipactor have been established with the help of these programmes. For more details we refer to ref. [23]. Any cavity shape, where multipactor properties cannot be computed at least approximately, will need a very long and painstaking measurement programme for determining its multipactor behaviour. This is a considerable disadvantage compared to the disc loaded structures [24,25] (without coupling slots!) or the "muffin tin" structure [26] for which multipactor programmes have been developed. A new technique for avoiding multipactor which is structure independent uses grooves within the multipactor area [27]. This may turn out also very useful for inhibiting multipactor around openings for coupling r.f. in and out or near coupling slots. Finally we note that in single cell spherical cavities at 4.5 [28], 3 [29] and 0.5 GHz [30] multipactor has never been observed. This has been confirmed by computer calculations [31] and there exist first indications that this property is conserved also for multicell cavities operated in a π mode [10].

6. ELECTRON IMPACT REGIONS

Electron impact can cause local heating, increased field emission and irreversible surface damages. It is obvious that the combination of electron impact and high magnetic or electric fields should be avoided. However, there exists such a vast number of possible electron trajectories due to multipactor, field emission, backscattering, photo effect [25] and such a broad variation of trajectories depending on the location of emitting areas and field levels that it seems rather hopeless to avoid electron impact at regions of high fields. Moreover, the distribution of H and E fields cannot be changed a great deal if a useful range of cavity parameters is conserved. Figs 1-3 illustrate the situation for a spherical disk loaded structure. In fig. 1 the electric and magnetic field distributions for the CERN 500 MHz test cavity [32] are given. A strong nose coning of the iris hardly changes the magnetic field distribution. It increases the electric field at the disk tip and reduces only slightly the overlap of electric and magnetic fields in the disk region. In fig. 2 computed electron trajectories for field emitted electrons starting in the region of high electric field are shown [33]. Electron trajectories of this kind cause a temperature increase along one meridian of the cavity. In fig. 3 an example is shown. The measured temperature distribution can be fitted by the electron source and trajectory family given in fig. 2 [33]. As can be seen, the temperature increase affects nearly the whole cavity along the meridian where the electron source is situated.

7. MODES AND STRUCTURE LENGTH

For linear accelerators and electron synchrotrons the use of multicell cavities has never been a point of discussion. On the contrary for the low frequency structures to be used in large storage rings the choice between multicell and single cell cavities is still controversial. Linear accelerators and, to a lesser extent recirculating linacs should aim at a high geometrical "filling factor" which can only be realized by multicell cavities. The use of independent structure modules is obvious but compared to normal conducting structures the length of such modules will tend to be shorter a.o for reasons of handiness, easy surface treatments and r.f. input power. Therefore the π mode structure can be an interesting

solution. It has the additional advantage of providing the smallest E_p/E_{acc} and H_p/E_{acc} values and its multipactor behaviour approaches the one of single cells. The need for relatively short structures also makes high coupling factors

$$k = \frac{2 (f_{\pi} - f_0)}{f_{\pi} + f_0}$$

f_0 : frequency of 0 mode

f_{π} : frequency of π mode,

less important. The choice of k depends of course on the number of cells, the field flatness requirement and the machining tolerances one is willing to accept. In general high coupling factors correspond to low r/Q or high peak fields. An example is given in fig. 4.

For large storage rings the strongest argument for a high coupling factor comes possibly from the excitation of higher modes. A high group velocity may avoid the loading down of higher modes in every cell and will be essential if coupling out is considered at the middle cell or at the beam tubes. For more details we refer to ref. [16].

Multiperiodic structures which combine the high dimensional stability of the $\pi/2$ mode with the merits of the π mode have been chosen for the HEPL [1] and Urbana [2] recirculating linacs. They allow joining of subunits at field free cells with removable r.f. contacts. They have the inherent advantage of different cell lengths within one module inhibiting the propagation of higher modes, particularly of the TE type mode with their strong dependence of frequency on cell-length. This can decrease regenerative beam break up by a factor $(N_{sub}/N)^2$ (N_{sub} : number of cells of same kind in a subunit, N : number of cells in a module) [35]. However, the containment of higher modes within a subgroup can also be a draw back: if higher modes are excited loading down may be necessary for each type of subunit, thereby increasing the number of coupling out devices. Whether the advantages of multicell cavities can outweigh the drawback of an increased number of coupling out probes and the more complicated fabrication has to be judged for any particular case.

6. TECHNICAL ASPECTS

For the application of r.f. superconductivity to large accelerator systems economic aspects will be of the highest importance. This is already one reason for aiming at simple layouts of structures, cryostats and refrigerator systems. There are in addition some technical aspects asking for simple cavity layout. Cavity fabrication out of Nb sheet material by inexpensive methods as e.g. spinning and deep drawing has been applied successfully for a number of cavities of different shape and frequency [36] and cavity shapes should be designed accordingly.

The advantages of electron beam weldings from inside have been demonstrated [29]. A simple shape may turn out also crucial if sputtering or vapour deposition techniques will be applied for producing s.c. surfaces. Similar arguments are valid for all surface treatments. The temperature maps taken recently with the CERN 500 MHz test cavity [30,37] are very instructive to this respect. Despite the smooth, spherical shape inhomogenous temperature distributions were found with r.f. losses varying by orders of magnitude from one region to another. It has been demonstrated that these differences are caused by the chemical polishing applied and in particular by the relatively slow evacuation of the etching solution. The evaporation of rinsing liquids like methanol even under dust free conditions also may have an influence on the inhomogeneities. There is no doubt that e.g. nose cones or sharp corners would render these surface treatments more difficult. Temperature maps taken at CERN have not only shown the high degree of inhomogeneity of s.c. surfaces with respect to r.f. losses; these losses are produced by many pointlike defects with normal conductivity or at least with increased residual resistances ($\sim 10^{-3}$ Ohm). It has been found that the surrounding niobium (wall thickness: 2 mm) can stabilise defects of this kind up to magnetic field levels of at least 150 G if an efficient cooling from the outside is applied. The existence of such pointlike defects may rule out the possibility of cooling by LHe filled tubes which are welded to the cavity walls [38] and of thin irises which cannot be cooled up to their tip by the He bath.

Within the temperature range where s.c. cavities have been operated the surface resistance shows about two orders of magnitude variation; for

niobium a typical ratio for the BCS resistances is

$$R_s(4.2)/R_s(1.8) = 123.$$

This allows a wide range for matching the value of R_s to the requirements of a given accelerator. However, it turns out that in practice only two temperatures are applied for the operation of large system. One is the normal boiling temperature of He. If lower temperatures must be used one as well should go down to the domain of the HeII with its excellent cooling properties. The disadvantages of the HeII temperatures are well known. Cryogenic installations get more complicated and the thermodynamical efficiency is lower. The cost of the HeII installation doubles roughly as compared to a 4.2 K installation. Another disadvantage sometimes is overlooked: the tightness of the whole cold He circuit against atmosphere is essential; already leaks of the order of $1 \text{ mb} \cdot \ell/\text{s}$ can block the operation of heat exchangers after a few days of operation. We therefore feel that at least for very large systems on operation temperature of 4.2 K should be aimed at. The upper limit for surface resistances enabling safe operation at a given acceleration field is determined by two requirements: the r.f. power loss per unit length in the cavity walls which should be made comparable to cryostat losses and the thermal stabilization of bad spots at the cavity surface [39]. It turns out that for niobium both requirements set an upper limit to the frequency around 700 MHz. If higher operating frequencies should be necessary, the development of cavities coated with high T_c material like e.g. Nb_3Sn would be essential.

9. SUMMARY

A summary of the most important aspects of cavity design is given below. The order reflects somewhat my personal choice of priorities. However, it should be kept in mind that priorities depend not only on the type of accelerator which is considered but also on its size and costs:

- (a) Cavities should be as simple as possible for fabrication, surface treatments and cooling. Simple fabrication methods from sheet metal and inside weldings must be used. Complicated surface treatments, if any, should only be applied to cavity parts prior to assembly. After welding surface treatments affecting only the inner surfaces would be

preferable. Simple geometries for sputtering or vapour deposition should be used.

- (b) The highest possible frequency should be aimed at in order to reach high acceleration fields.
- (c) Cavity geometries allowing computation of multipactor properties, exact field configurations, electron trajectories and higher modes are essential.
- (d) Multicell cavities constructed in easily handable modules and using π mode or multiperiodic structures should be considered.
- (e) Operation at 4.2 K is desirable especially for very large machines. If frequencies above 700 MHz have to be used in large machines, high T_c materials should be developed.
- (f) For large storage rings the cavity design has to include right from the beginning higher mode studies.

Acknowledgements

I would like to thank H. Padamsee for information on the muffin-tin structure and H. Piel for many valuable discussions.

REFERENCES

- [1] C.M. Lyneis, M.S. McAshan, R.E. Rand, H.A. Schwettman, T.I. Smith, J.P. Turneaure and A.M. Vetter, Proc. Conf. on Future Possibilities for El. Acc., Charlottesville 1979.
- [2] P. Axel, L.S. Cardman, H.D. Graef, A.O. Hanson, R.A. Hoffswell, D. Jamnik, D.C. Sutton, R.H. Taylor and L.M. Young, IEEE Trans. NS-26 Nr. 3 (1979) 3143.
- [3] J. Kirchgessner, H. Padamsee, H.L. Phillips, D. Rice, R. Sundelin, M. Tigner and E. von Borstel, IEEE Trans. NS-22 Nr. 3 (1975) 1141.
- [4] A. Citron, M. Kuntze, A. Brandelik, W. Herz, R. Hietschold, A. Hornung, W. Kühn, D. Schulze, K.W. Zieher, IEEE Trans. NS-26, Nr. 3 (1979) 3571.
- [5] G. Hochschild, B. Piosczyk, J.E. Vetter, H. Ingwersen, E. Jaeschke, R. Repnow, H. Schwarz and Th. Walcher, IEEE Trans. NS-24, Nr. 3 (1977) 1150.
- [6] J. Aron, R. Benaroya, L.M. Bollinger, B.G. Clifft, W. Hennig, K.W. Johnson, J.M. Nixon, P. Markovich and K.W. Shepard, paper presented at the XI Int. Conf. High Energy Acc. Geneva, 1980.
- [7] J.R. Delayen, G.J. Dick, J.E. Mercereau, J.W. Noé, P. Paul and G.D. Sprouse, IEEE Trans. NS-26 (1989) 3664.
- [8] A. Citron, G. Dammertz, M. Grundner, L. Husson, R. Lehm and H. Lengeler, Nucl. Instr. & Meth. 164 (1979) 31.
- [9] G. Arnolds, H. Heinrichs, R. Mayer, N. Minatti, H. Piel and W. Weingarten, IEEE Trans. NS-26, Nr. 3 (1979) 3775.
- [10] V. Lagomarsino, G. Manuzio and R. Parodi, to be published in the Proceedings of the Int. Conf. Cryog. Engin., Genova (1980).
- [11] T. Furuya, K. Hosoyama, T. Kato, Y. Kojima and O. Konno, to be published in Proc. 1979 Lin. Acc. Conf., Montauk L.I.N.Y.
- [12] K.W. Zieher and A. Hornung, private communication
- [13] W. Bauer, Proceedings of the LEP Summer Study, Les Houches, CERN 79-01, vol. 2 (1979) 351.
- [14] D. Ritson and M. Tigner, Cornell University, CLNS-406 (July 1978).
- [15] M. Kuntze, this conference.
- [16] M. Tigner, this conference.
- [17] A. Citron, this conference.
- [18] CERN/ISR-LEP/79-33 (August 1979).

REFERENCES (Cont'd)

- [19] G. Loew and R.B. Neal, in *Linear Accelerators*, edit. by P. Lapostolle and A. Septier, North Holland Comp., 1970.
- [20] H. Padamsee, M. Banner and M. Tigner, *IEEE Trans. Mag.* 15, 1 (1979) 606.
- [21] e.g. W. Bauer, private communication
- [22] W. Weingarten and R. Blaschke, *Nucl. Instr. & Meth.* 156 (1978) 597.
- [23] See Cl. Lyneis, this conference.
- [24] C. Lyneis, H.A. Schwettman and J.P. Turneaure, *Appl. Phys. Lett.* 31, 8 (1977) 541.
- [25] J. Halbritter, *KfK Ext. Bericht* 3/78-1 (1978).
- [26] H. Padamsee and A. Joshi, *J. Appl. Phys.* 50, 2 (1979) 1112.
- [27] H. Padamsee, D. Proch, P. Kneisel and J. Mioduszewski, to be presented at 1980 *Appl. Superc. Conf.*, Santa Fe, New Mexico.
- [28] V. Lagomarsino, G. Manuzio, R. Parodi and R. Vaccarone, *IEEE Trans. Mag.* 15 (1979) 25.
- [29] U. Klein, D. Proch and H. Lengeler, *Gesamthochschule Wuppertal, Interner Bericht WU B80-16*, May 1980.
- [30] P. Bernard, G. Cavallari, E. Chiaveri, E. Haebel, H. Heinrichs, V. Picciarelli and H. Piel, paper to be presented at the XI *Int. Conf. High Energy Acc.*, Geneva 1980.
- [31] U. Klein and D. Proch, *Gesamthochschule Wuppertal, Int. Bericht, WU13-78-31* (1978).
- [32] P. Bernard, H. Heinrichs, H. Lengeler, E. Picasso and H. Piel, *CERN LEP Note* 209 (1980).
- [33] H. Heinrichs, private communication.
- [34] E. Chiaveri, E. Haebel and H. Heinrichs, private communication note (1980).
- [35] A.M. Vetter, C.M. Lyneis and M.A. Schwettman: *Proc. Conf. on Future Possibilities for Electron Accelerators*, University of Virginia, Charlottesville (1979).
- [36] W. Bauer, this conference.
- [37] H. Piel and R. Romijn, private communication
- [38] L. Szecsi and R. Vincon, private communication
- [39] H. Padamsee, this conference.

FIGURE CAPTIONS

- Fig. 1 Electric and magnetic field distribution along the cavity wall of the CERN 500 MHz test cavity.
- Fig. 2 Computed electron trajectories corresponding to the field distribution given in fig. 1. The location of the electron source is indicated. Parameters: emission phase with respect to the r.f. field $E_{acc} \sin\phi$ and impact energy E_i .
- Fig. 3 Measured temperature increase and X-ray intensity along one meridian for the cavity shown in fig. 1. The resistors are distributed along one meridian of the cavity body. R1 corresponds to position (1) R20 to position (4) and R40 to the position symmetric to (1).
- Fig. 4 R/Q and E_p/E_{acc} as a function of coupling constant for a disk loaded spherically shaped cavity [34]. Th: disk thickness.

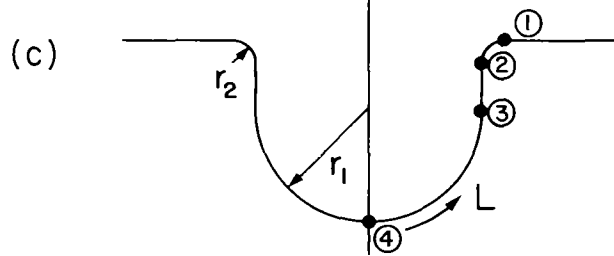
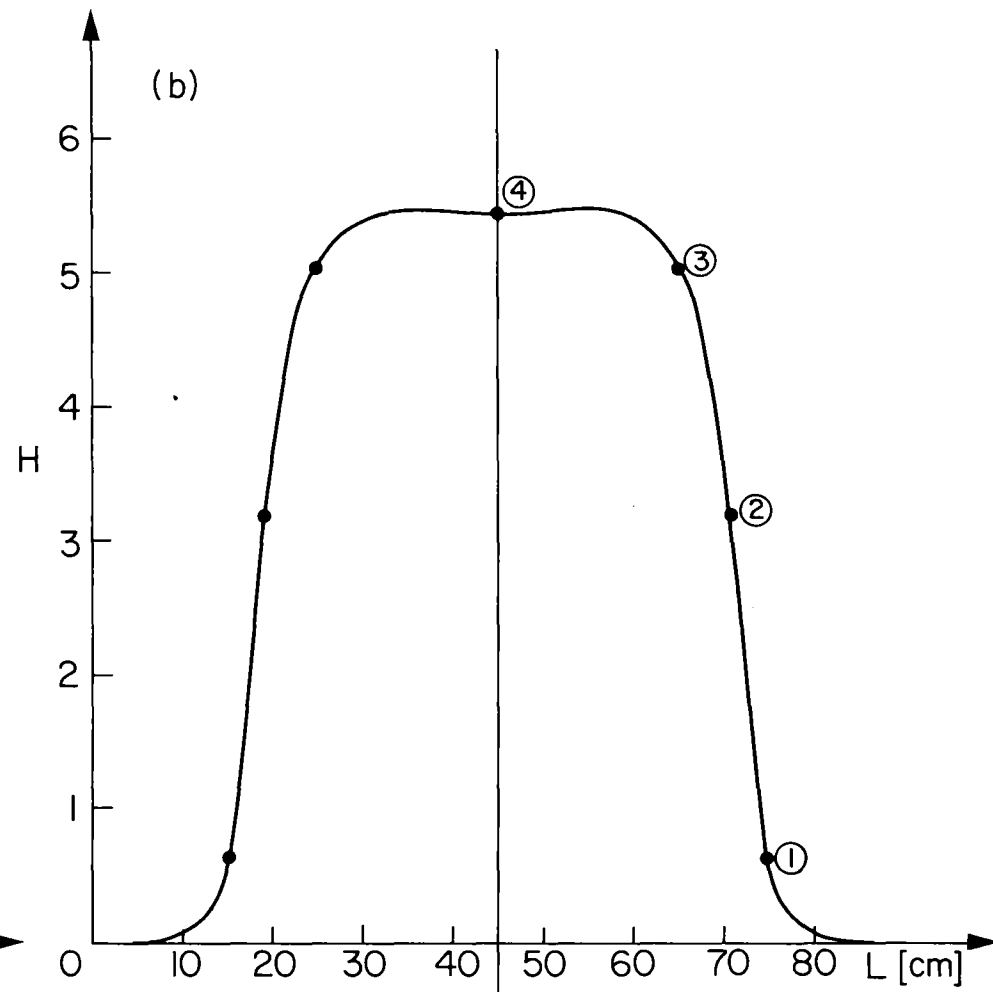
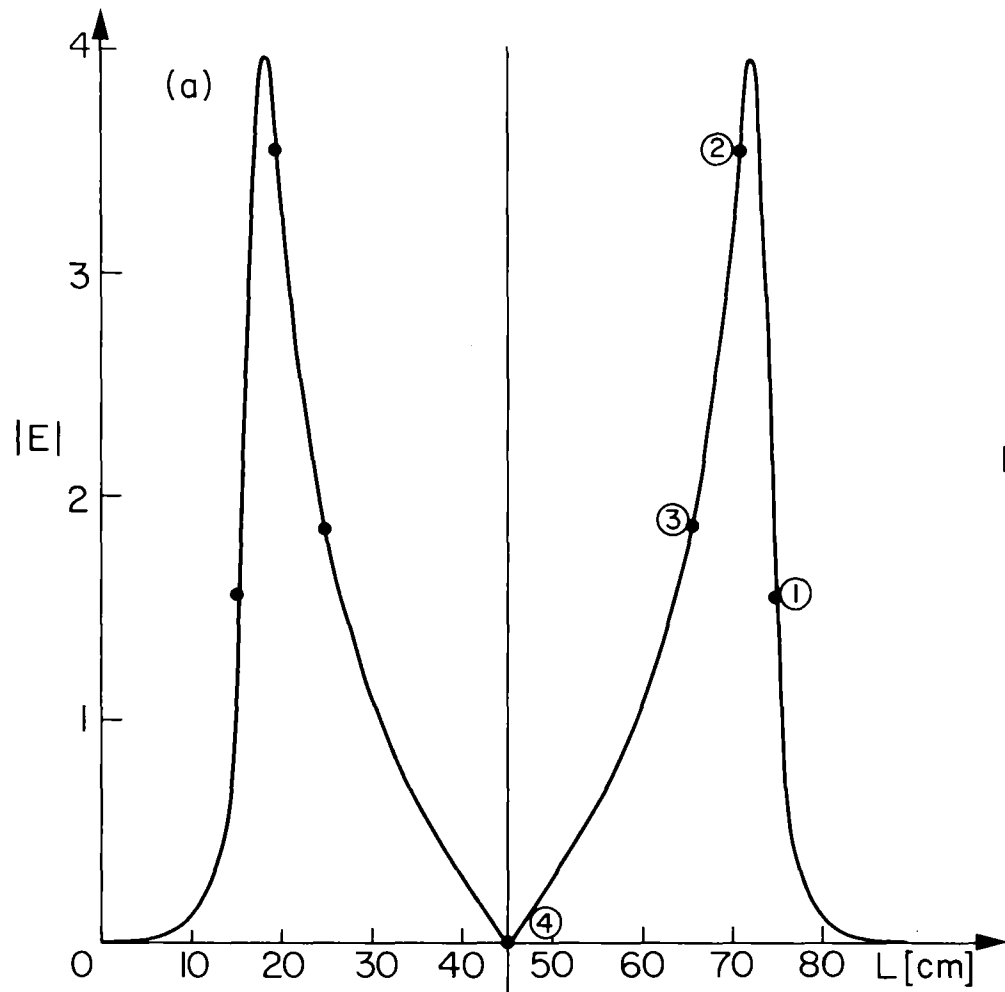


Fig.1

PHI HIT ID=EC+KST+PHI

325079

DATE 15/04/80

LO = 1

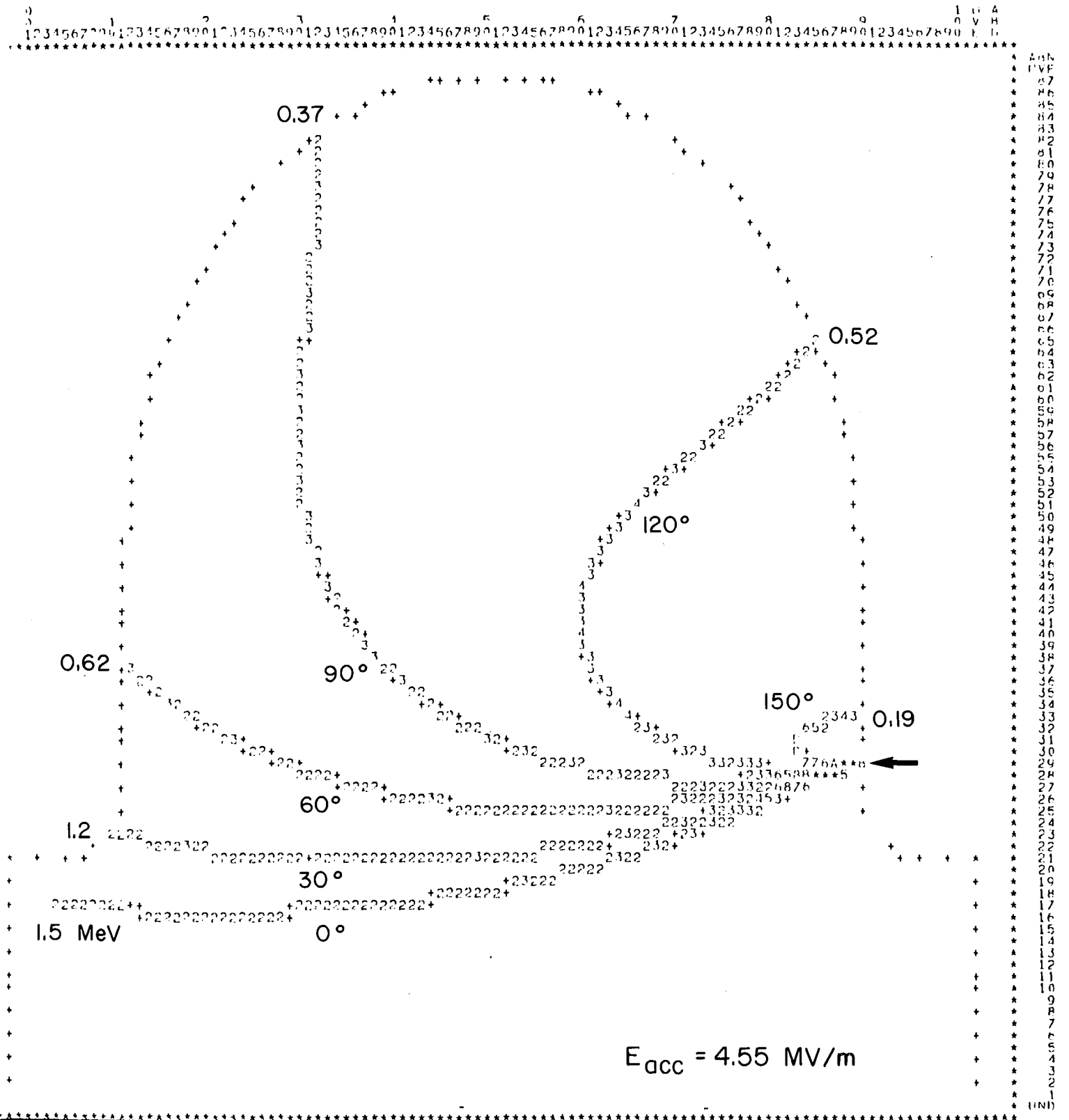


Fig.2

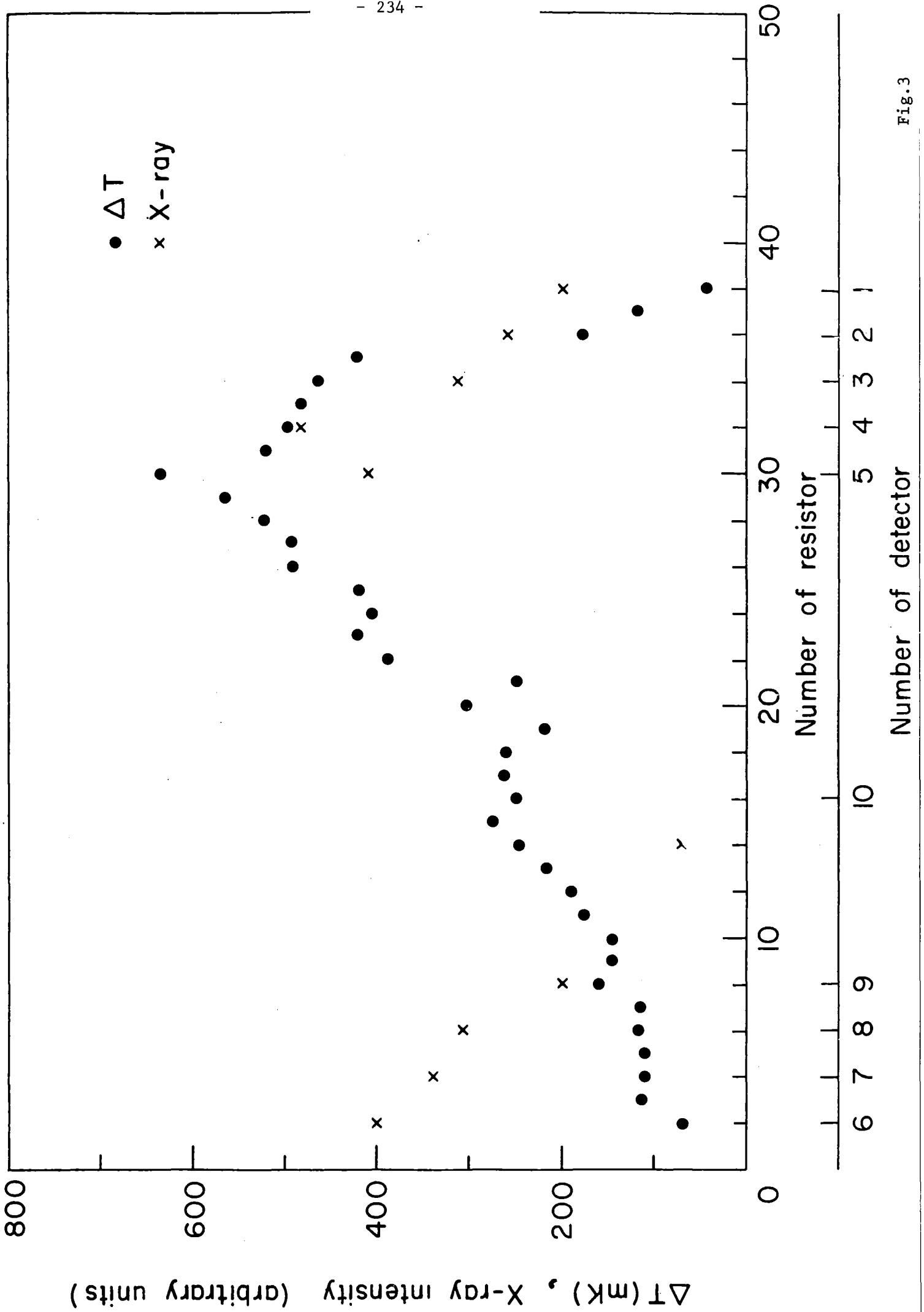


Fig.3

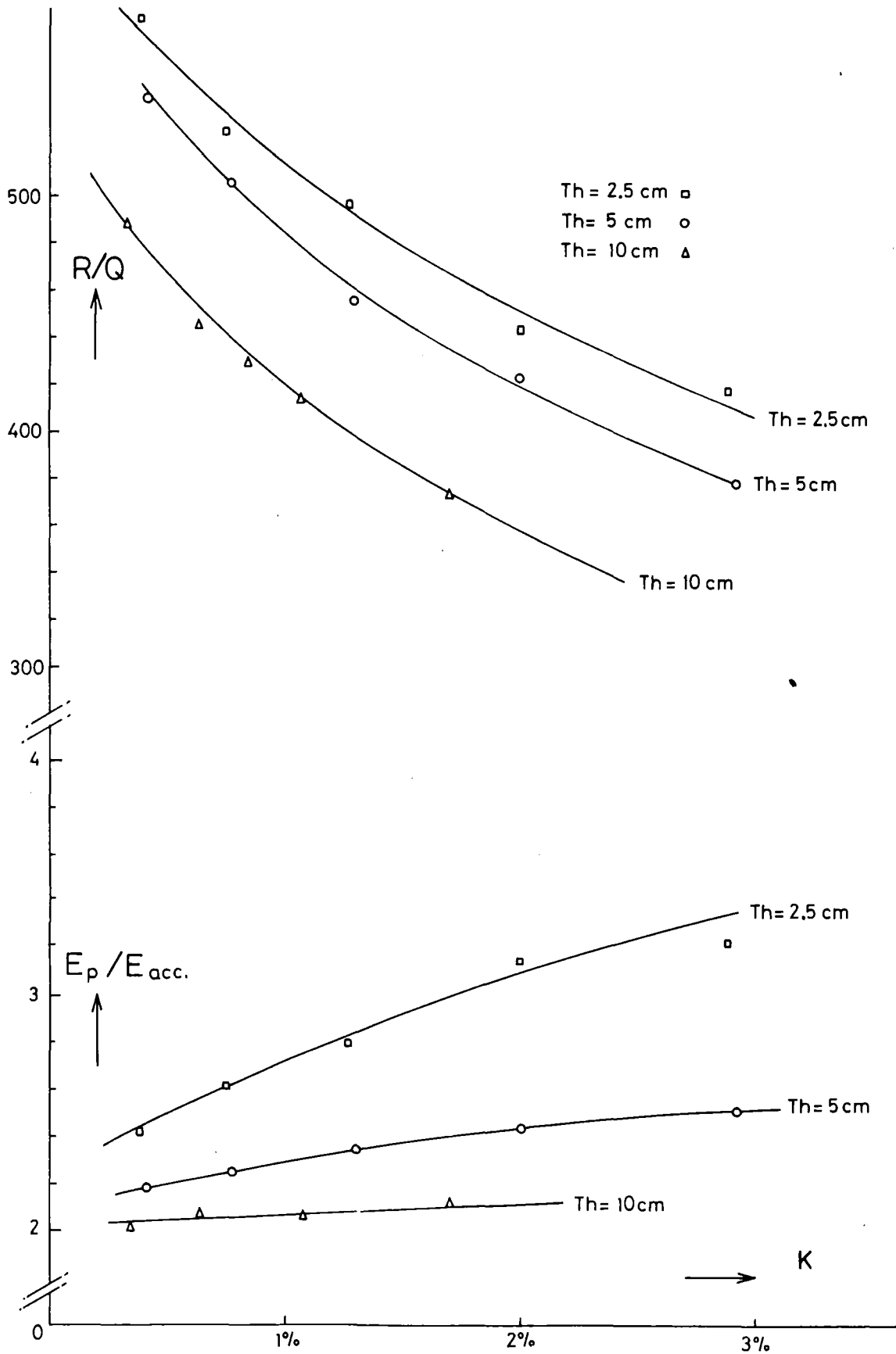
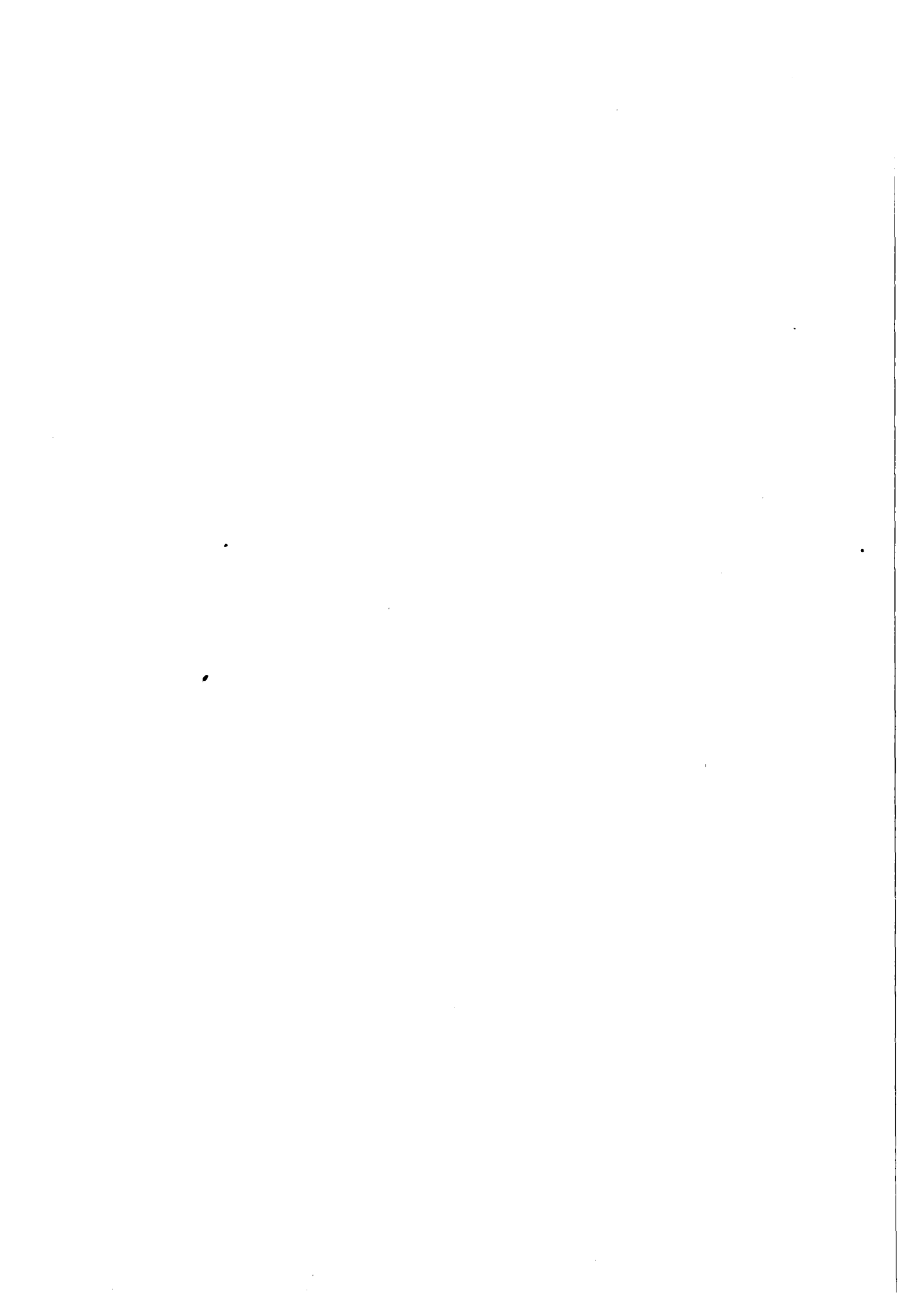


Fig. 4



ADDITIONAL DESIGN CRITERIA FOR LOW β STRUCTURES

M. Kuntze

Kernforschungszentrum Karlsruhe, Institut für Kernphysik
P.B. 3640, 7500 Karlsruhe, Federal Republic of Germany

Low β structures are used in proton and ion accelerators. This paper is restricted to additional design criteria for the superconducting accelerator projects. The room-temperature booster at Heidelberg, ¹ and the design of room-temperature proton and heavy ion linacs will not be included. Essential elements stimulating the increasing activity are the development of new accelerating structures uniquely suited to the acceleration of very low velocity heavy ions. The helix resonator ²⁻⁵, the split-ring resonator ^{6,7} and the re-entrant cavity ⁸ have been developed as superconducting accelerator structures for low-velocity applications. Fig. 1 shows the Karlsruhe helix resonator, fig. 2 shows the Argonne split ring-resonator and fig. 3 the Cal Tech /Stony Brook split loop. All of the new structures consist of a large number of independently phased resonators which may be adjusted to accelerate ions over a wide velocity range without changing the frequency. The velocity profile is established by phasing rather than by increasing lengths of successive accelerating units. Since the velocity need not to be matched to the resonator length, the projectile phase may change greatly while it traverses the structure. Nevertheless, phase focussing is present in the same way as in a multiple cell structure with a well-established velocity profile. Such a linac is exceedingly flexible with regard to the mode of operation and hence is tolerant of sub-standard performance of resonators. A failure of resonators to provide the design accelerating field will reduce the maximum beam energy, but the linac still can be used efficiently. On the other hand, if needed energy variability is easily achieved by varying the phase of individual resonators.

Thus, for a given particle velocity range an average β -value is chosen and identical resonators for a fixed frequency can be designed. The frequency, in turn is a compromise between the desire to have as low a frequency as possible (to

minimize the bunching problem and to maximize the accelerating length of an individual unit) and the desire to limit the radial dimensions and the stored energy. Higher frequency means lower stored energy which simplifies phase and amplitude control. But more essential is the mechanical rigidity of the resonator. Vibration induced frequency modulations have to be compensated by rf control.⁹⁾ If the structure is mechanically stiff, the rf frequency is insensitive to mechanical vibrations and in turn makes feasible phase and amplitude stabilization by direct rf feedback. If the vibration-induced frequency modulations exceed a certain limit a fast tuning unit must be used. Fast tuners based on a voltage-controlled reactance, PIN diodes, have been developed, which can switch up to 10 kilowatts of rf reactive power^{9,10}. But of course the problem of the fast tuning unit is magnified with low mechanical rigidity and with increased stored energy. As a measure for the rigidity the vibration-induced frequency modulation Δf (Hz peak to peak) is used and the radiation pressure frequency shift Δf_{Stat} at a given field level.

Another key design decision for a superconducting low β structure is whether to mount the fast tuning element directly to the resonator or use a high-power rf coupling line for the fast tuner. Both possibilities have been realized successfully, but have different disadvantages. The pin diodes are inaccessible in case of failure⁶ (Argonne), the high-power rf coupling lines show multipactoring and gas discharge problems at the cold rf window³ (Karlsruhe).

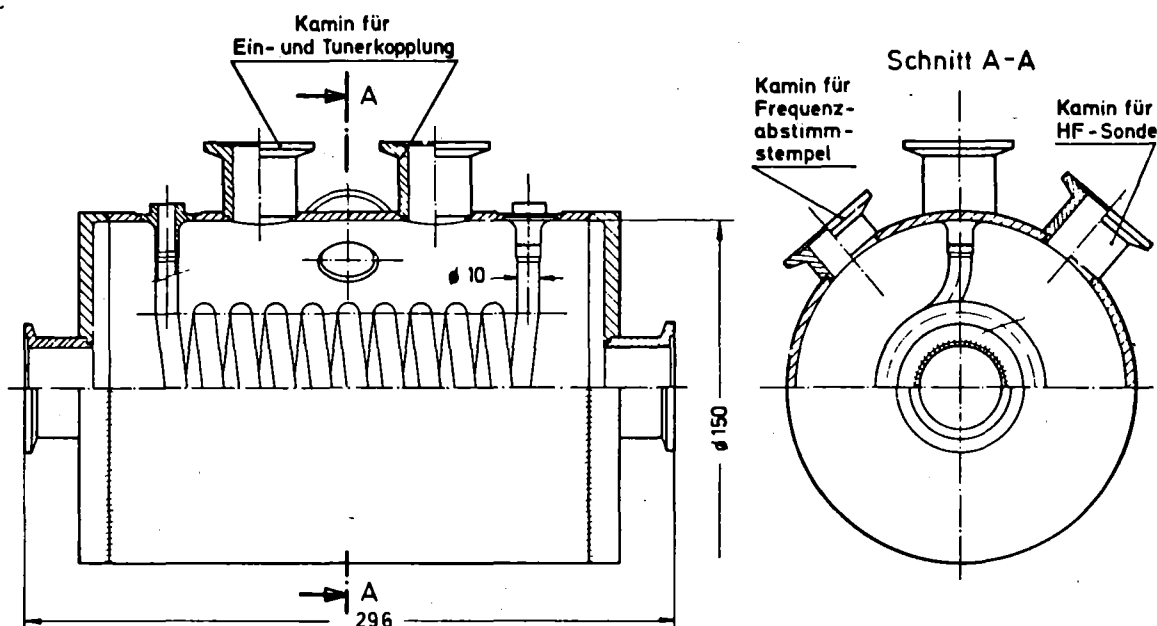


Fig. 1: Single $\lambda/2$ -helix-resonator, operating frequency 108 MHz

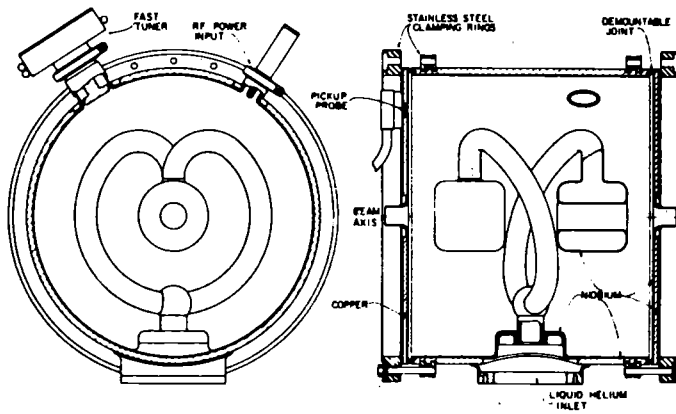


Fig. 2: 97-MHz, 14-in. length, high-beta split-ring resonator. The inner loading structure is made of Nb and is hollow to permit cooling by forced-flow of liquid helium. The outer housing is formed of an explosively-bonded Nb-Cu composite and is cooled by conduction.

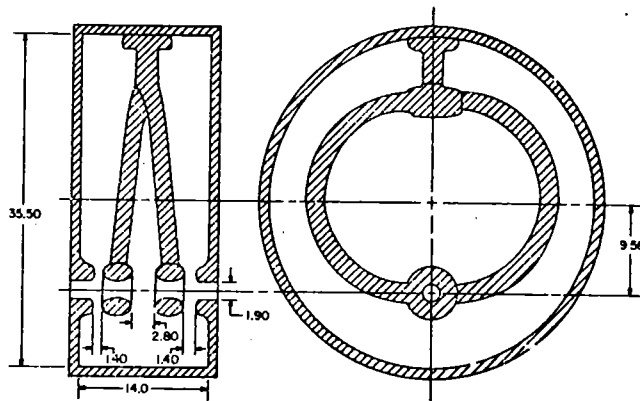


Fig. 3: The $\beta = 0.055$ 150 MHz prototype split loop cavity of Cal Tech/Stony Brook. Dimensions are in cm.

In addition, low surface fields and good cooling are required for the new structures. In comparison to $\beta = 1$ structures the ratio of peak to average surface field is exceedingly higher for low β -structures. The split-ring resonator has been designed for $E_p/E_{acc} = 6.3$, whereas the $\lambda/2$ -helix resonator with $E_p/E_{acc} = 12.0$ is less favorable from this point of view. Recently a new type of helix resonator has been developed at Karlsruhe⁵, the tapered helix resonator, to reduce E_p/E_{acc} .

flow of liquid helium within the resonators. Each arm of the split-ring assembly has a high point which will accumulate helium gas generated by the rf power loss in the resonator. Some resonators seem properly cooled and will operate at gradients greater than 3.5 MV/m, while the average obtainable cw field is limited to 3 MV/m.

The Cal. Tech/Stony Brook split-ring resonator is fabricated from OFH copper pieces joined by electron beam welds and plated with a ~ 15 micron thick layer of lead. The cooling properties are somewhat better by conduction cooling of the solid copper drift tubes. The accelerating gradients are limited due to field emission and the relatively low Q-value of the lead plated resonator.

In comparison the obtainable gradients with the Karlsruhe helix resonators are limited due to field emission only. The cooling by forced flow of helium is superior compared to the split-ring.

Also included in table 1 is the re-entrant cavity, which has been developed at Stanford on the technology for the Stanford superconducting electron linac¹¹. The good features of the design are axial symmetry which eliminates beam steering effects, wide velocity acceptance of a single gap structure and good mechanical rigidity. These advantages are obtained at the cost of an exceptionally strong sensitivity to multipacting, a low average field gradient and an uncomfortably high rf frequency (430 MHz)

Completely different low β structures for the acceleration of protons are the 5 cell Alvarez-resonator¹² (fig. 5) and the 2 cell slotted Iris resonator which

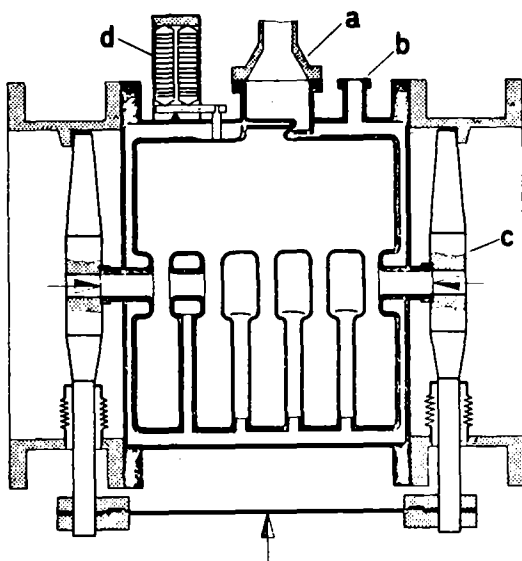


Fig. 5: 720 MHz Alvarez for 5.8 MeV protons to be used in prototype accelerator, showing also rf input (a), helium input (b), mechanical tuner (c), piezo-tuner (d)

have been developed at Karlsruhe for a frequency of 720 MHz. The structure diameter is about 30 cm, the geometry was optimized with the help of the LALA-program. The slotted Iris has four circular slots per disc with 4.6 cm diameter, giving a passband of 17 MHz.

R e f e r e n c e s

- 1 E. Jaeschke, H. Ingwersen, R. Repnow, T. Walcher, B. Huck, and B. Kolb, IEEE Trans. NS-26, No. 3 (1979), 3667
- 2 A. Brandelik, A. Citron, P. Flécher, J.L. Fricke, R. Hietschold, G. Hochschild, G. Hornung, H. Klein, G. Krafft, W. Kühn, M. Kuntze, B. Piosczyk, E. Sauter, A. Schempp, D. Schulze, L. Szecsi, J.E. Vetter and K.W. Zieher Part. Acc. 4 (1972) III
- 3 A. Citron, M. Kuntze, A. Brandelik, W. Herz, R. Hietschold, A. Hornung, W. Kühn, D. Schulze, and K.W. Zieher IEEE Trans NS-26, No. 3 (1979), 3751
- 4 G. Hochschild, B. Piosczyk, J.E. Vetter, H. Ingwersen, E. Jaeschke, R. Repnow, H. Schwarz, Th. Walcher, IEEE Trans. NS-24, No. 3 (1977), 1150
- 5 K.W. Zieher, A. Hornung, private communication
- 6 K.W. Shepard, IEEE Trans. NS-26, No. 3 (1979), 3659
- 7 R. Benaroya et al, IEEE Trans. Mag. MAG-13, 516 (1977)
- 8 P.H. Ceperley, I. BenZvi, H.F. Glavish, S.S. Hanna, IEEE Trans NS-22, No. 3 (1975), 1153
- 9 D. Schulze, A. Hornung, P. Schlick, IEEE Trans. NS-26, No. 3 (1979), 3748
- 10 G. Hochschild, D. Schulze, F. Spielböck, IEEE Trans. NS-20, No. 3 (1973), 116
- 11 C.M. Lyneis, J. Sayag, H.A. Schwettman, J.P. Turneaure, IEEE Trans. NS-26, No. 3 (1979), 3755
- 12 K. Mittag, IEEE Trans. NS-24, No. 3 (1977), 1156

Joints, Couplers, and Tuners

Ronald M. Sundelin
Cornell University
Ithaca, New York 14853 USA

I. Joints

Only demountable joints will be discussed here, as welded joints are discussed as part of Cavity Fabrication.

Demountable joints are used for several purposes. They are used to connect short structure sections. The use of short sections facilitates fabrication, chemical processing, and firing; it also permits defective sections to be rejected without rejecting the entire structure. Demountable joints are also useful for attaching couplers, tuners, and beam pipes when it may be desirable to remove and alter these objects at a later time, or when the location of these joints makes them accessible for bolting but not welding.

Considerations in the design of demountable joints include avoiding RF losses (by placing the joint at a low field region or by making low loss contact), using a superconducting joint material, avoiding damage to the structure sections, maintaining leak tightness during temperature cycling, avoiding an unpredictable shift in the structure frequency, avoiding contamination of the structure vacuum, and permitting a low temperature bakeout of the system.

The HEPL recyclotron accelerating structures (Fig. 1) are assembled using indium seals.¹ Each structure has $\lambda/2$ cells in the center and $\lambda/3$ cells at the ends, leading to a null in the magnetic field at the joint location. This joint has proven to be satisfactory.

The muffin-tin accelerating structure tested in the Cornell synchrotron² (Fig. 2) used the principle of waveguide-beyond-cutoff to produce a low field region for the use of indium seals (Fig. 3). Simultaneous niobium-to-niobium

contact outside the seal prevented unpredictable frequency disturbances upon assembly. Some spring was provided to one of the niobium members in contact with the indium to prevent the development of leaks upon temperature cycling. Long tantalum bolts, which provide good strength, an expansion coefficient similar to that of niobium, and springiness by virtue of their length, were used together with conical beryllium copper washers (for additional springiness) and aluminum alloy nuts (to avoid galling) for joint assembly. An exponential taper in the crack leading to the joint was necessary to eliminate resonant stripline modes from this region, which modes otherwise are excited by slight asymmetries in the structure. The indium wire was chemically cleaned to remove the kerosene used in its extrusion. This joint has been satisfactory.

A choke joint (Fig. 4) has been used by Wuppertal³ to join accelerator sections in an X-band test accelerator. The joint is placed at a nominal null in the magnetic field, and the use of a choke joint provides added insurance against joint losses. Indium is the sealing material. A separate test cavity in which the choke joint could be exposed to high or low magnetic fields demonstrated that its contribution to losses was minimal. Except for one incident in which apparent chemical residues degraded the joint's performance, this joint has been satisfactory. A 65 cell structure employing this joint recently reached an E_{peak} of 41.6 MV/m, B_{peak} of 78.7 mT and Q of 1×10^9 .

A joint with high conductivity is the crocodile joint (Fig. 5) used in the Karlsruhe-CERN separator⁴ and in the Karlsruhe-DORIS cavity⁵ (Fig. 6). This joint uses a niobium ring with two inwardly protruding niobium rims. These rims deform slightly when the joint is assembled, and provide enough transverse motion to abrade through the oxide layer and provide excellent electrical contact. Vacuum sealing is provided by indium seals outside the RF joint. Long bolts are used to

provide springiness. This joint has been found to reliably support fields in excess of 7 to 20 mT. This property is important in the separator not only because cell tuning imperfections cause fields in nominally empty cells, but also because it has been found useful to operate the separators in different modes to accommodate different velocity beams. The crocodile sealing rings are prepared by rough machining, annealing at 1200°C for 2-3 hours, fine machining with trichloroethane, and etching in cold polish for 30 seconds.⁶ It has been found advisable to slightly change the diameter of the contact location on successive assemblies because the structure surface is dented by the sealing ring. The crocodile joints provide satisfactory performance; their principal disadvantages are that they are difficult to machine, can be used only once, that the structure sealing surface must be remachined after no undented sealing regions remain, and that the cell frequency disturbance caused by the joint is somewhat unpredictable.

Another style of high conductivity joint developed at Karlsruhe⁵ has proven to be unsatisfactory. This joint consisted of a niobium ring with an H-shaped cross-section placed in a hexagonal groove. The primary problem with this joint was that the ring was not self-aligning, and did not provide uniform azimuthal contact. It was also in poor contact with the liquid helium⁶.

An H-shaped gasket (Fig. 7) is used to seal the end plates to the Argonne split-ring accelerator structures⁷. The gasket and structure are made of niobium, and the joint will support a field in excess of 2 mT, which is quite adequate for use in the split ring resonator. Conical spring washers are used in assembly.

Several materials other than indium have been used as vacuum sealing materials.

The Cal Tech-Stony Brook split-ring lead plated accelerator⁸ uses indium to seal the resonator end plates, but uses a Sn-In alloy to seal the split ring to its housing.

The Karlsruhe-CERN separator⁹ uses Kapton windows to separate the structure and insulating vacua, and to separate the insulating and beam pipe vacua.

The CERN LEP cavity¹⁰ uses lead joints at the end of cut-off tubes to permit baking at 200°C, but this seal has not yet been subjected to a large number of temperature cycles.

In summary, a number of demountable joints have been devised which do not appreciably degrade the performance of the structures in which they are used. It is clear that an even higher conductance joint would simplify cavity construction, but the absence of such a joint is not limiting progress in superconducting RF.

II. Couplers

Couplers used on superconducting cavities are used to couple either fundamental frequency power or higher mode power. First consider fundamental frequency couplers designed to handle moderate to high levels of RF power.

Primary considerations in the design of high power input couplers include simultaneous minimizing of thermal conduction losses and RF heating losses in the portions of the feedline connecting the LHe temperature structure to the LN₂ temperature structure, and the LN₂ temperature structure to the room temperature structure, minimizing refrigerator loading caused by window dissipation, minimizing magnetic and electric field enhancements in the cavity, avoiding multipacting engendered by perturbing the cavity fields, avoiding interferences with the cryostat assembly associated with the feed line penetration, avoiding resonances associated with unwanted transmission modes within the line, avoiding multipacting at the ceramic windows, providing variable coupling if required, and providing damping of other modes if required.

The HEPL recyclotron¹¹ has a hybrid coaxial and waveguide coupling system capable of coupling several kilowatts into the beam in each structure. This system works well, except that some of the feed-throughs have been found to have miniscule helium leaks which shift the frequency of the structure¹².

The Cornell 11-cell S-band muffin-tin structure tested in the synchrotron² at 4 GeV used a coaxial electric probe (Fig. 2) which provided variable coupling. The center conductor of this probe entered the cut-off region from the side and was in line with the iris between two cells. The center conductor was maintained at LN₂ temperature, with a transition to room temperature. The outer conductor used a stainless steel bellows for the transition from

LHe to LN₂ temperatures. This probe was capable of handling 1 kW, and provided satisfactory performance.

The Karlsruhe-DORIS cavity¹³, incorporates a coaxial magnetic probe (Fig. 8) in which the LHe to LN₂ and LN₂ to room temperature transitions use inner and outer choke joints. One window is at LN₂ temperature and a second at room temperature. A field transformer is used in conjunction with the coaxial loop. Care has been taken to keep the VSWR of each probe section below 1.02. This probe is being prepared for high power testing.

Wuppertal has developed a hybrid waveguide and coaxial coupler¹⁴. (Fig. 9.) The center conductor of the coaxial line is hollow and is coaxial with the beam line, providing a passage for the beam. This type of coupler has the advantages that it minimally disturbs the fields within a cell, and does not destroy the axial symmetry in the neighborhood of the cells. It can be made to have variable or fixed coupling. The problem of providing a thermal break in the center conductor between LHe and LN₂ temperatures is eliminated because the entire center conductor is at LHe temperature. One disadvantage of this type of coupler is that, if the coaxial line diameter is large, modes other than the TEM can propagate, and the line length must be made non-resonant for these other modes.

A coupling system for a muffin-tin cavity (Fig. 10) is being developed at Cornell¹⁵ to handle 60 kW at 1500 MHz. The cavity consists essentially of eleven cells, with the bottom of one of the cups replaced with a waveguide which acts as a continuation of the cup. A ceramic waveguide window at LN₂ temperature will be used. Copper plated stainless steel waveguide will be used for the two heat breaks.

Higher mode damping requirements vary greatly depending on the nature of the accelerator. For some accelerators, no damping other than that

provided by the main power coupler and the finite accelerator Q is required. Linacs require relatively little coupling, as transverse instabilities are caused primarily by the propagation of higher mode power from the beam output end of the structure toward the beam input end. The required damping is relatively small, and is proportional to the square of the length of the accelerating structures. Recyclotrons and microtrons require more extensive damping because the beam, deflected on its first pass, tends to amplify its generation of higher mode power on each successive pass. Operation with integer or half-integer optics helps to suppress this effect. Storage rings require even more extensive damping because integer and half-integer optics are not stable, the currents tend to be much higher, and longitudinal instabilities require damping because synchrotron oscillations are present. Operation with a long time between bunch passages reduces the damping requirements.

General considerations in the design of higher mode damping probes include determining the required damping for each mode, selecting accessible locations in the structure where the modes requiring the most damping have the highest fields, determining whether or not the higher mode propagation between cells is sufficient (transmission stop-bands can occur at certain frequencies), and minimizing the number of probes required to achieve the necessary damping. The probes can be electric, magnetic, or hybrid electric and magnetic, or some combination of these types. The hybrid can sometimes be used to advantage to increase the coupling to modes requiring damping while decreasing the coupling to the fundamental mode. Notch filters, sometimes incorporated directly into the coupling mechanism, are used to avoid damping the fundamental mode; it is important that the filter location be such that no part of the coupling structure is resonant at the fundamental frequency. Electric

and magnetic field enhancement near the coupling probe should be minimized, and probe-engendered multipactoring needs to be avoided. Transverse modes have two orthogonal polarizations, and care must be taken that a probe does not alter the polarization axes in such a way that one polarization is not coupled by the probe.

Regenerative beam break-up has been encountered in the HEPL linac and recyclotron¹¹. A combination of 16 H_z , H_θ , and E_r probes (Fig. 1) were adequate to damp the break-up modes in a 23 cell structure and permit the one-pass acceleration of a 100 μ A CW electron beam. The required Q_{ext} values were typically 10^8 . The H-probes are equipped with half-wave stub notch filters to reject the fundamental mode; the E_r probes, by virtue of their location, have intrinsic rejection. The probe and filter are niobium to avoid excessive refrigerator loading; the coaxial niobium center conductor is conduction cooled. The probe tips are 3 to 4 mm outside the cavity. A total of 52 modes in the TM_{01} , TE_{11} , and TM_{11} bands were considered to be potentially dangerous, and were measured and provided with adequate damping.

Upon recirculation, additional modes were found troublesome in the Illinois-HEPL microtron¹⁶. A hybrid E and H probe is being used to damp these modes. The break-up threshold in the HEPL recyclotron¹¹ has also been found to decrease as the number of turns increases.

The Karlsruhe-DORIS cavity¹³ is equipped with two Szecsi couplers (Fig. 11). These couplers damp all modes with frequency less than four times the fundamental to a Q_{ext} of less than 10^4 . The couplers use field transformers and coaxial loops, followed by an exponentially tapered coaxial line. The geometry of these components is such that the fundamental is rejected with better than 50 dB rejection, and higher modes are well

matched to an external load. Work on these couplers is continuing.

As previously mentioned, the Wuppertal¹⁴ fundamental coupler damps higher modes, a process which is helped by the large beam holes between cells.

One probe (Fig. 12) is presently used per cell on each of the normal conducting Cornell CESR cavities¹⁷, together with a separate polarizing stub elsewhere in the cell. Damping requirements in this case are particularly stringent, since the bunch spacing during injection is 42 nsec with anticipated currents up to 94 mA. Q_{ext} values below 10^2 are achieved for some modes, and all modes are adequately damped. The coupling loop is an E and H hybrid. A concentric copper coaxial notch filter provides a fundamental rejection of 56 dB. The two-stage design of this filter avoids additional notches below 4 times the fundamental frequency. This probe, which has been operated in a structure with $E_{\text{acc}} = 1.62$ MeV/m, CW, could be readily adapted for superconducting use, although its implications for multipacting enhancement are not known in the superconducting case.

A niobium loop coupler has been tested in an S-band muffin-tin structure at Cornell. This structure exhibited a low Q value which further decreased as the power was increased. This problem is attributed to difficulties in making, bending, and welding the small tube which forms the center conductor. However, further investigations of this problem have not yet been made.

A slot coupler, designed to couple to H_z (Fig. 10), has been tested in an S-band muffin-tin cavity at Cornell.¹⁵ This slot penetrates the cup bottom and also enters the end of a waveguide which propagates the higher modes, but not the fundamental. This structure yielded an E_{acc} of 5 MV/m and a Q_0 of greater than 2×10^9 . Three subsequent tests with an H_x coupler yielded, at best, an E_{acc} of 2 MV/m and a Q_0 of 1.5×10^9 . This coupler causes

a 60% local field enhancement. The breakdown was magnetic, and is under investigation. Both of these tests used cups with grooved bottoms to suppress multipacting. Room temperature measurements on both of these couplers has shown that one of each type in a 5-cell 1500 MHz structure would be nearly sufficient to prevent transverse and longitudinal instabilities if used in CESR at 5.5 GeV with a 60 mA beam having a 2.5 μ sec passage interval.

Higher mode couplers have become an extremely complex problem as the required damping has increased with the application of superconducting RF to high current e^+e^- storage rings. The only relief in sight comes from the increased damping time permitted by low rates of bunch passage.

III. Tuners

Permanent tuning methods, slow dynamic tuners, and fast dynamic tuners will be discussed. Requirements depend on the number of cells, intercell coupling, operating mode, structure rigidity, vibration sources, reactive beam loading, and loaded bandwidth.

Permanent fine tuning on the HEPL recyclotron¹¹ structures has been performed by selectively cold polishing various cells of the structure. Bead pulls taken between polishing cycles are processed using a computer to indicate the degree of etching required in each cell.

A similar process has been used in the Cornell 11 cell muffin-tin structure¹⁸ using differential and integral electropolishing. Differential electropolishing was accomplished by using a tight Teflon barrier between cells. A field flatness of $\pm 0.4\%$ was achieved.

More recent Cornell muffin-tin structures made out of stamped sheet niobium¹⁹ have been tuned by deforming the cup bottoms. This is a simple process because the cup bottoms are flat.

Slow dynamic tuners in use consist of plungers or elastic squeeze tuners. Care must be used to avoid coupling vibrations into the structure and to avoid a large, partially isolated thermal mass.

Plungers (Fig. 13) have been used in the Karlsruhe-CERN separator⁹. One coarse and one fine tuner is used per section. One problem encountered is that a change in tuner position induces multipacting, which subsequently processes away. Tuning during beam operation has been found to be unnecessary.

Wuppertal has used motor-driven squeeze tuners to deform thin-walled regions in their 8 GHz structure¹⁴, and plans to use axial squeezing to tune a bellows-shaped S-band structure by ± 200 KHz²⁰ (Fig. 14).

Cornell used a motor driven squeeze tuner to tune its 11-cell S-band muffin-tin structure.² The structure was designed so that the cup region was rigid, but could be moved elastically relative to the opposite cup region. The motor drive was linked through an elastic member so that small motor motions would not represent a large frequency change. Dynamic tuning under beam conditions was done, but was not found to be necessary. A small amplitude frequency modulation with a 33 Hz period was observed, but its origin was never determined.

Karlsruhe uses motor driven squeeze tuners on its helix accelerator²¹. End plate deformation is employed.

The Cal Tech-Stony Brook lead plated split ring cavities⁸ also use end plate squeeze tuners.

The Karlsruhe-DORIS cavity¹³ uses an end plate squeeze tuner linked through a flexible band.

Fast dynamic tuners are used when frequency shifts caused by vibrations, radiation pressure, ponderomotive forces, or beam loading can cause a frequency shift which is a significant fraction of a cavity's loaded bandwidth.

The Karlsruhe helical accelerator²² uses feedback on amplitude and on a voltage controlled reactance to stabilize the structure against ponderomotive oscillations which would otherwise occur. This same feedback also reduces the effects of external vibrations. The reactances are switched in and out by a set of PIN diodes.

The Argonne split ring accelerator²³ also uses a voltage controlled reactance, switches by pin diodes.

Wuppertal¹⁴ has used piezoelectric tuners on thin-walled portions of cavities and is planning to use them on an S-band structure (Fig. 14) to obtain a range of ± 4 KHz²⁰.

In conclusion, tuners have been devised which satisfactorily meet the requirements of all intended applications.

Acknowledgments:

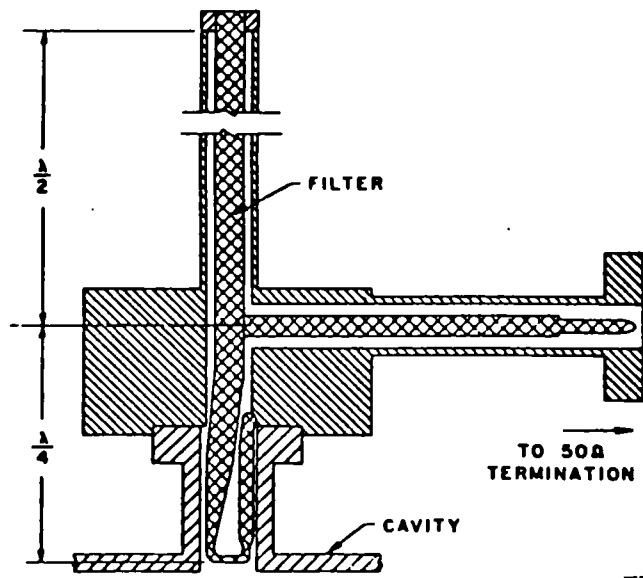
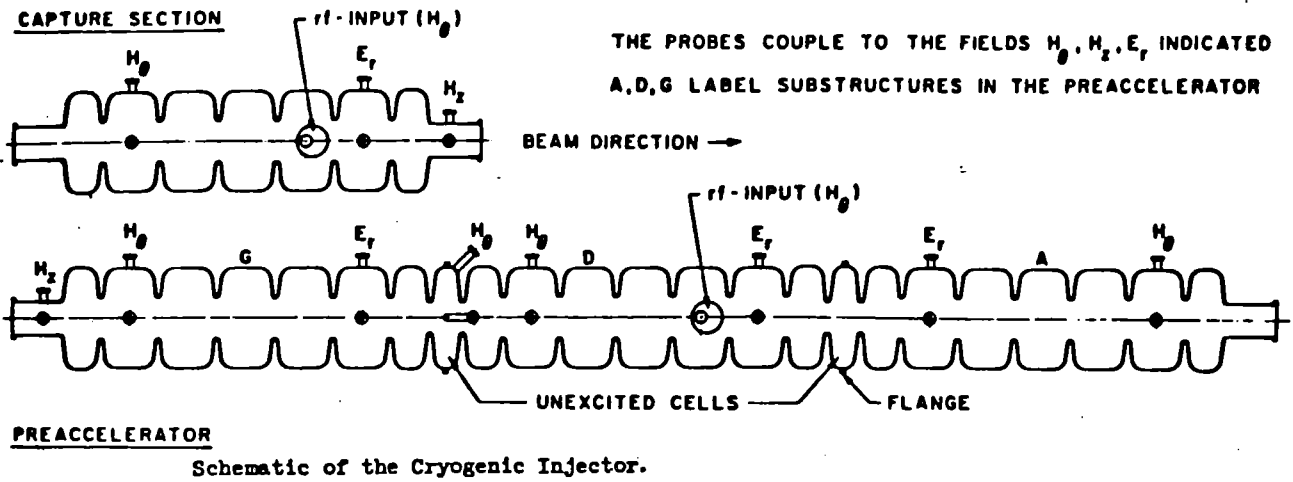
The author wishes to thank P. Kneisel, W. Bauer, H. Lengeler, W. Weingarten, C. Lyneis, and K. Shepard for supplying information for this paper.

REFERENCES

- 1) K. Mittag, H. A. Schwettman, and H. D. Schwarz, "Beam Break-up in a Superconducting Electron Accelerator," HEPL-685 (1972), High Energy Physics Laboratory, Stanford University, and Proceedings of the 1972 Proton Linear Accelerator Conference, Los Alamos, New Mexico.
- 2) J. Kirchgessner, H. Padamsee, H. L. Phillips, D. Rice, R. Sundelin, M. Tigner, and E. von Borstel, "Superconducting Cavities for Synchrotron Use," IEEE Transactions on Nuclear Science, Vol. NS-22, No. 3, June 1975, p. 1141.
- 3) H. Heinrichs and W. Weingarten, "An RF Contact for Superconducting Cavities", Nuclear Instruments and Methods 171 (1980), p. 185.
- 4) M. Grundner, H. Lengeler, and E. Rathgeber, "RF Contact for Superconducting Cavities," Nuclear Instruments and Methods 141 (1977), p. 57.
- 5) W. Bauer, private communication.
- 6) P. Kneisel, private communication.
- 7) K. Shepard, private communication.
- 8) J. R. Delayen, G. J. Dick, J. E. Mercereau, J. W. Noe, P. Paul and G. D. Sprouse, "Status of the Stony Brook Superconducting Heavy-Ion Linac", IEEE Transactions on Nuclear Science, Vol. NS-26, no. 3, June 1979, p. 3664.
- 9) A. Citron, G. Dammertz, M. Grundner, L. Husson, R. Lehm, and H. Lengeler, "The Karlsruhe-CERN Superconducting RF Separator", Nuclear Instruments and Methods 164 (1979), p. 31.

- 10) H. Lengeler, private communication.
- 11) C. M. Lyneis, M. S. McAshan, R. E. Rand, H. A. Schwettman, T. I. Smith, and J. P. Turneaure, "The Stanford Superconducting Recyclotron," IEEE Transactions on Nuclear Science, Vol. NS-26, no. 3, June 1979, p. 3246.
- 12) C. M. Lyneis, J. Sayag, H. A. Schwettman, and J. P. Turneaure, "Performance of a Superconducting Accelerating Structure with a Modified Geometry," IEEE Transactions on Nuclear Science, Vol. NS-26, no. 3, June 1979, p. 3755.
- 13) W. Bauer, A. Brandelik, A. Citron, W. Lehmann, L. Szecsi, and M. Yoshioka, "Superconducting Accelerating Cavities for High Energy e^+e^- Storage Rings," IEEE Transactions on Nuclear Science, Vol. NS-26, no. 3, June 1979, p. 3252.
- 14) G. Arnolds, H. Heinrichs, R. Mayer, N. Minatti, H. Piel, and W. Weingarten, "Design and Status of an Experimental Superconducting Linear Accelerator for Electrons." IEEE Transactions on Nuclear Science, Vol. NS-26, no. 3, June 1979, p. 3775.
- 15) J. Kirchgessner, P. Kneisel, H. Padamsee, J. Peters, D. Proch, R. Sundelin, and M. Tigner, "Design Studies for a 1500 MHz Superconducting Accelerator Cavity for use in an e^+e^- Storage Ring," to be presented at the XIth International Conference on High Energy Accelerators, CERN, Geneva, 1980.
- 16) P. Axel, L. S. Cardman, H. D. Graef, A. O. Hanson, R. A. Hoffswell, D. Jamnik, D. C. Sutton, R. H. Taylor, and L. M. Young, "Operating Experience with MUSL-2," IEEE Transactions on Nuclear Science, Vol. NS-26, no. 3, June 1979, p. 3143.

- 17) R. M. Sundelin, J. L. Kirchgessner, and M. Tigner, "Parallel Coupled Cavity Structure," IEEE Transactions on Nuclear Science, Vol. NS-24, no. 3, June 1977, p. 1686.
- 18) R. M. Sundelin, J. Kirchgessner, H. Padamsee, H. L. Phillips, D. Rice, M. Tigner, and E. von Borstel, "Application of Superconducting RF Accelerating Sections to an Electron Synchrotron-A Progress Report," Proceedings of the IXth International Conference on High Energy Accelerators, Stanford Linear Accelerator Center, Stanford, CA (1974), p. 128.
- 19) H. Padamsee et al., IEEE Trans., MAG-13 (1977), p. 346.
- 20) W. Weingarten, private communication.
- 21) A. Citron, M. Kuntze, A. Brandelik, W. Herz, R. Hietschold, A. Hornung, W. Kuhn, D. Schulze, and K. W. Zieher, "Performance of the Karlsruhe Superconducting Proton Linear Testaccelerator," IEEE Transactions on Nuclear Science, Vol. NS-26, no. 3, June 1979, p. 3751.
- 22) D. Schulze, A. Hornung, and P. Schlick, "Progress in Electronic Frequency Control of Superconducting Helix Resonators," IEEE Transactions on Nuclear Science, Vol. NS-26, no. 3, June 1979, p. 3748.
- 23) K. W. Shepard, "Initial Operation of the Argonne Superconducting Heavy-Ion Linac," IEEE Transactions on Nuclear Science, Vol. NS-26, no. 3, June 1979, p. 3659.



Schematic of Band-stop Filter.

Fig. 1

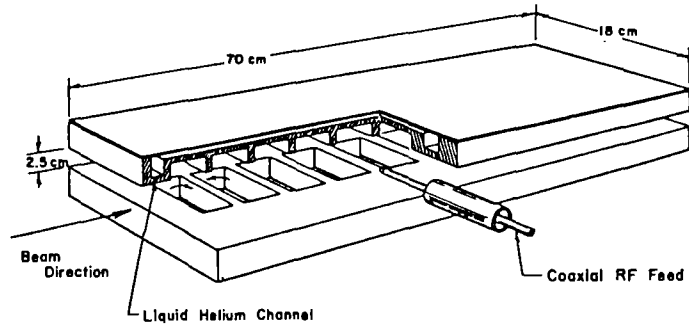


Fig. 2

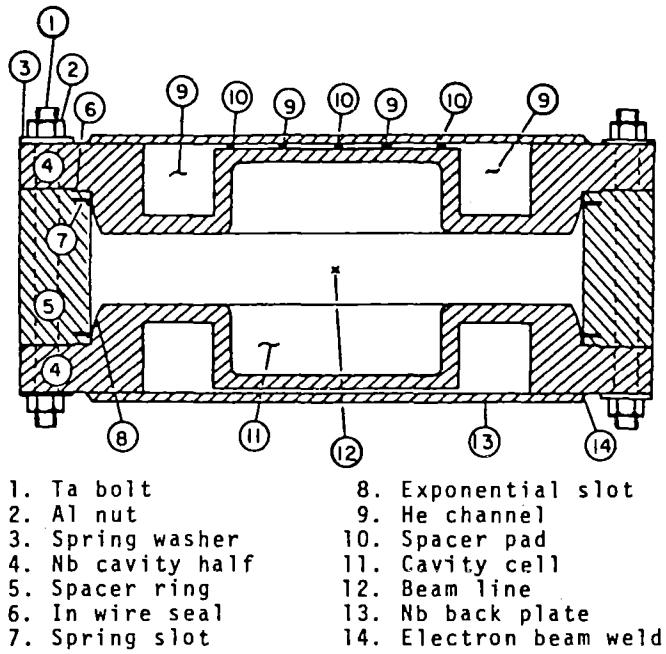
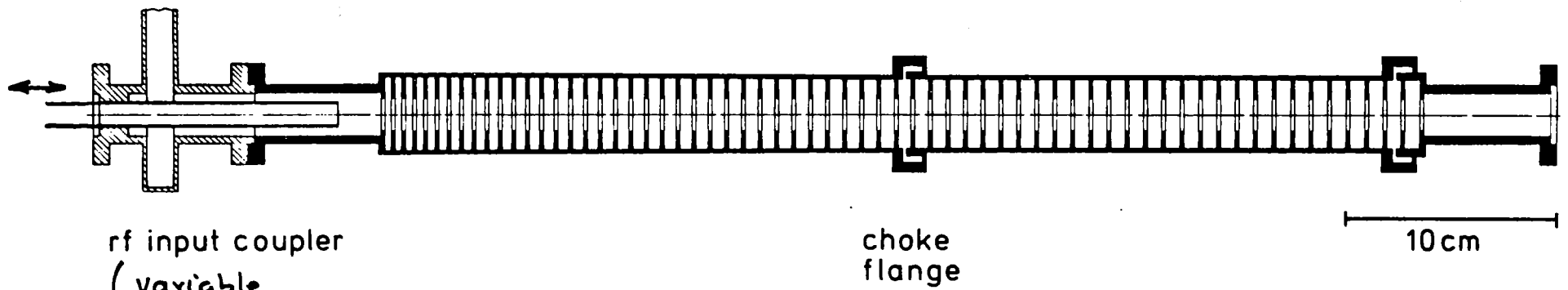


Fig. 3



rf input coupler
 (variable
 length of the
 inner conductor)

choke
 flange

10 cm

Capture section with increasing phase velocity

8 GHz

Fig. 4

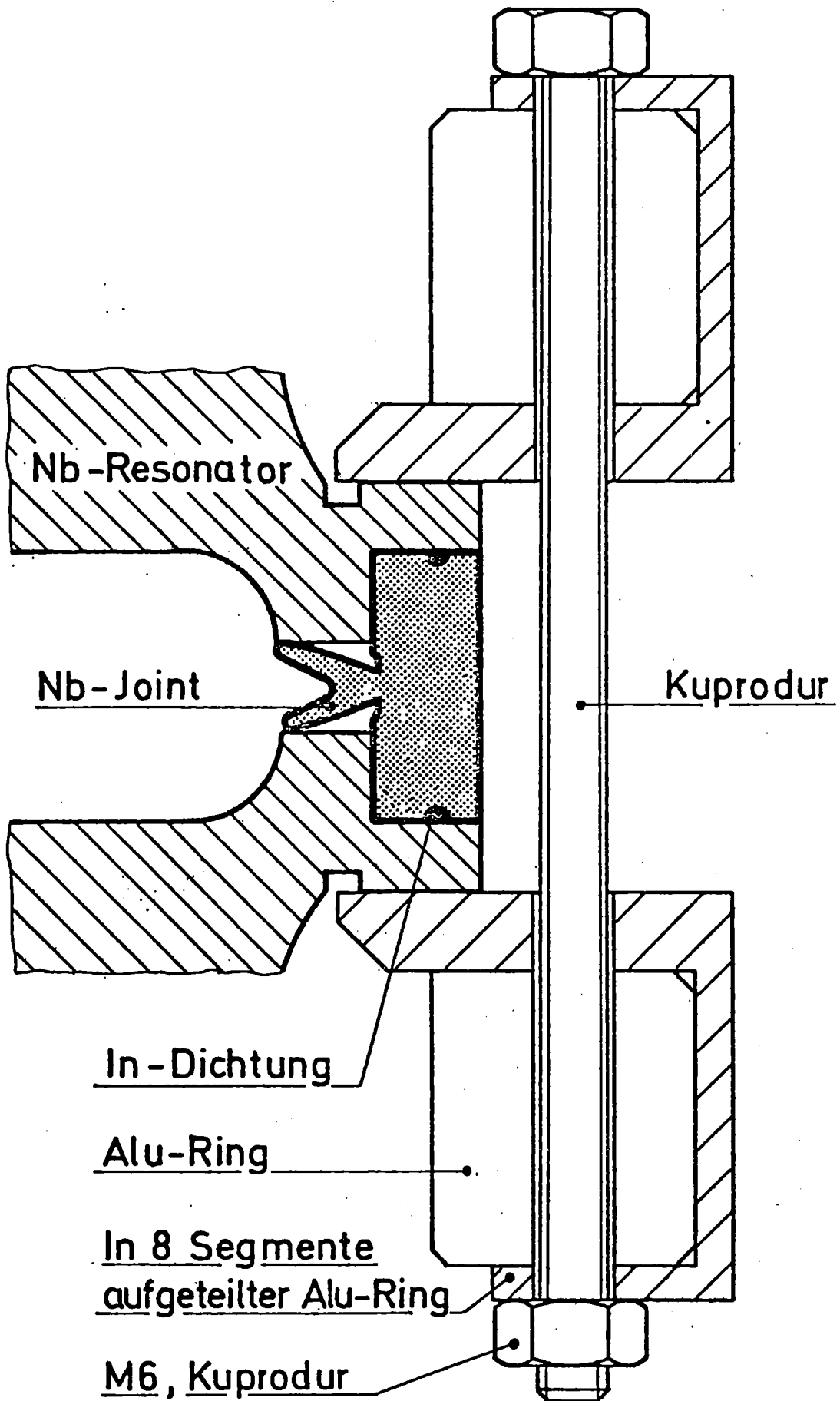


Fig. 5

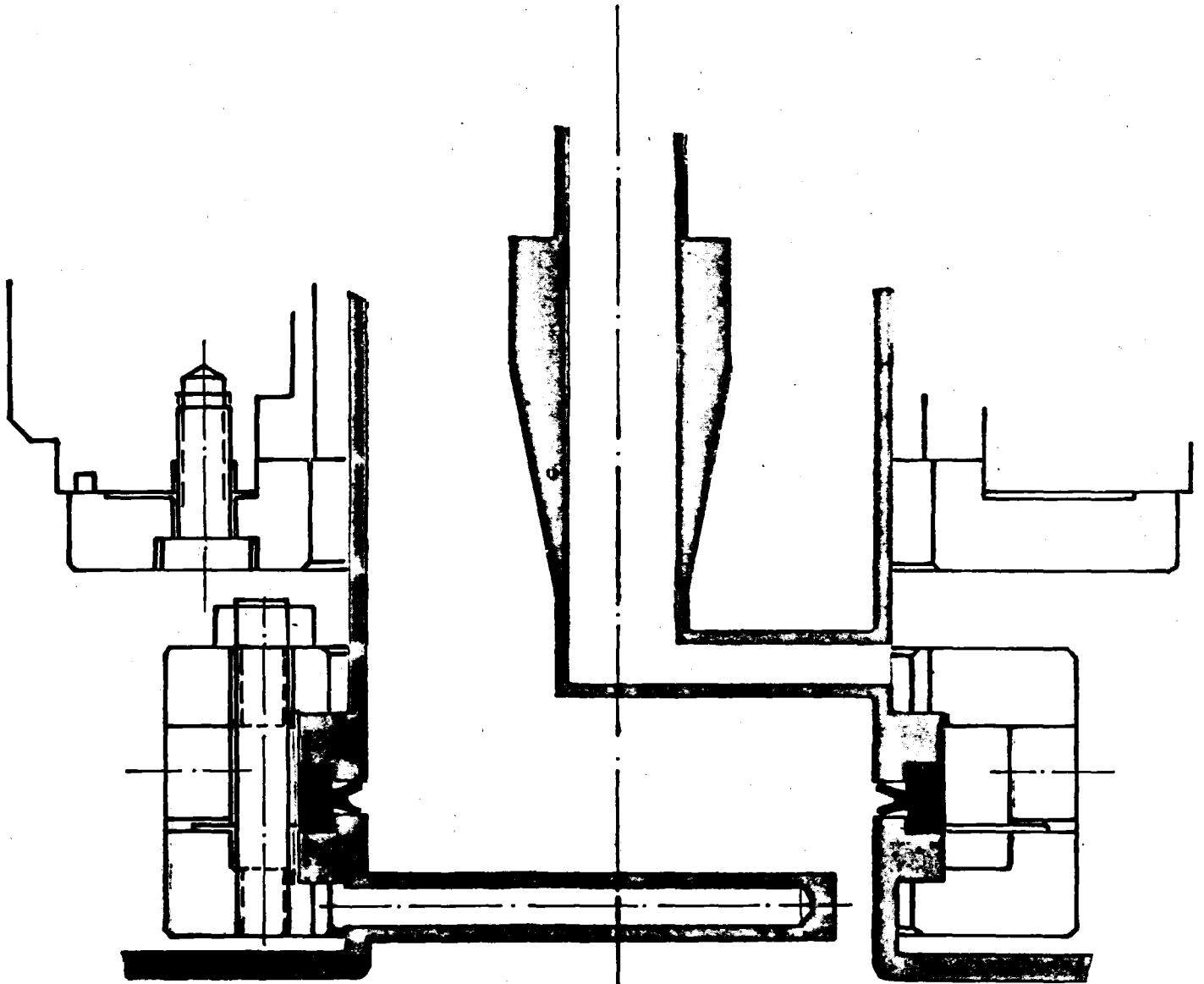
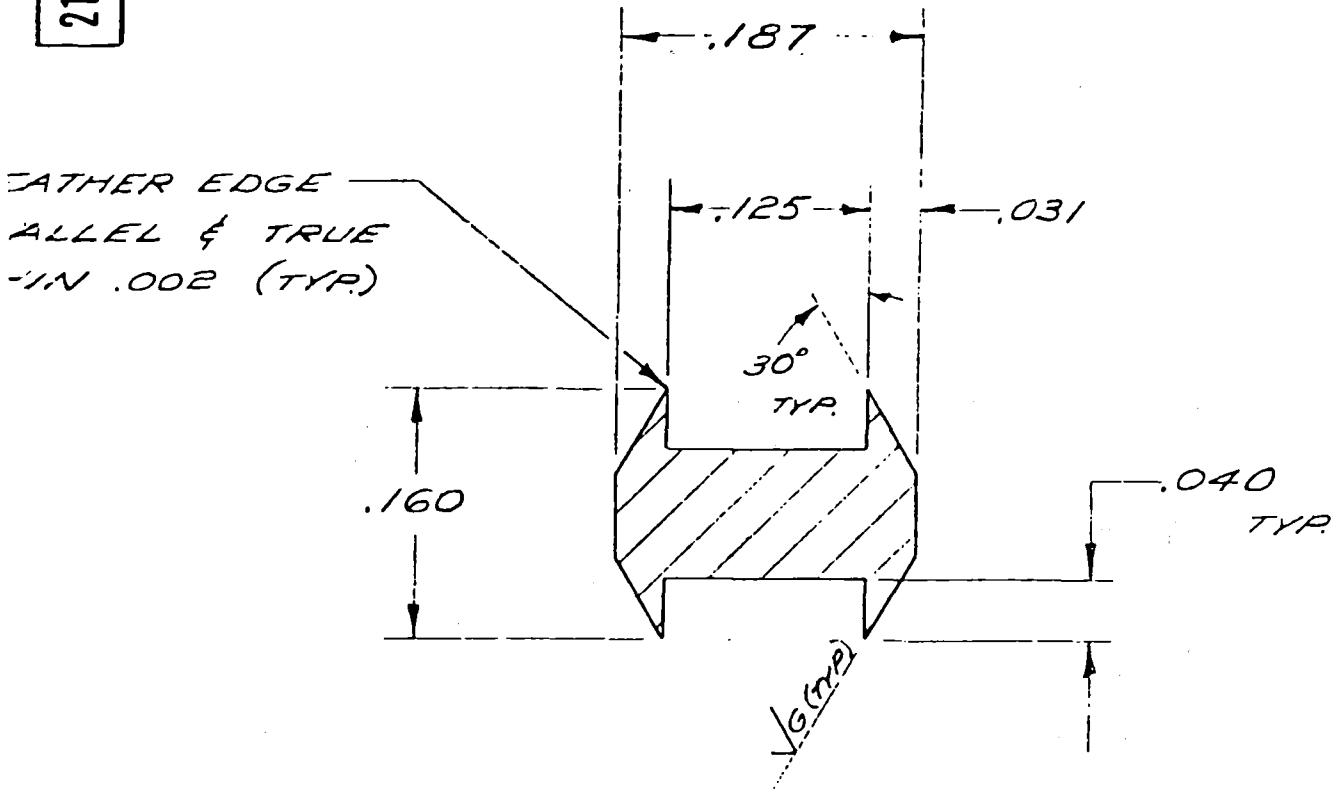


Fig. 6

211-HA-9154-B



SECTION A-A

(SCALE: 8/1)

Fig. 7

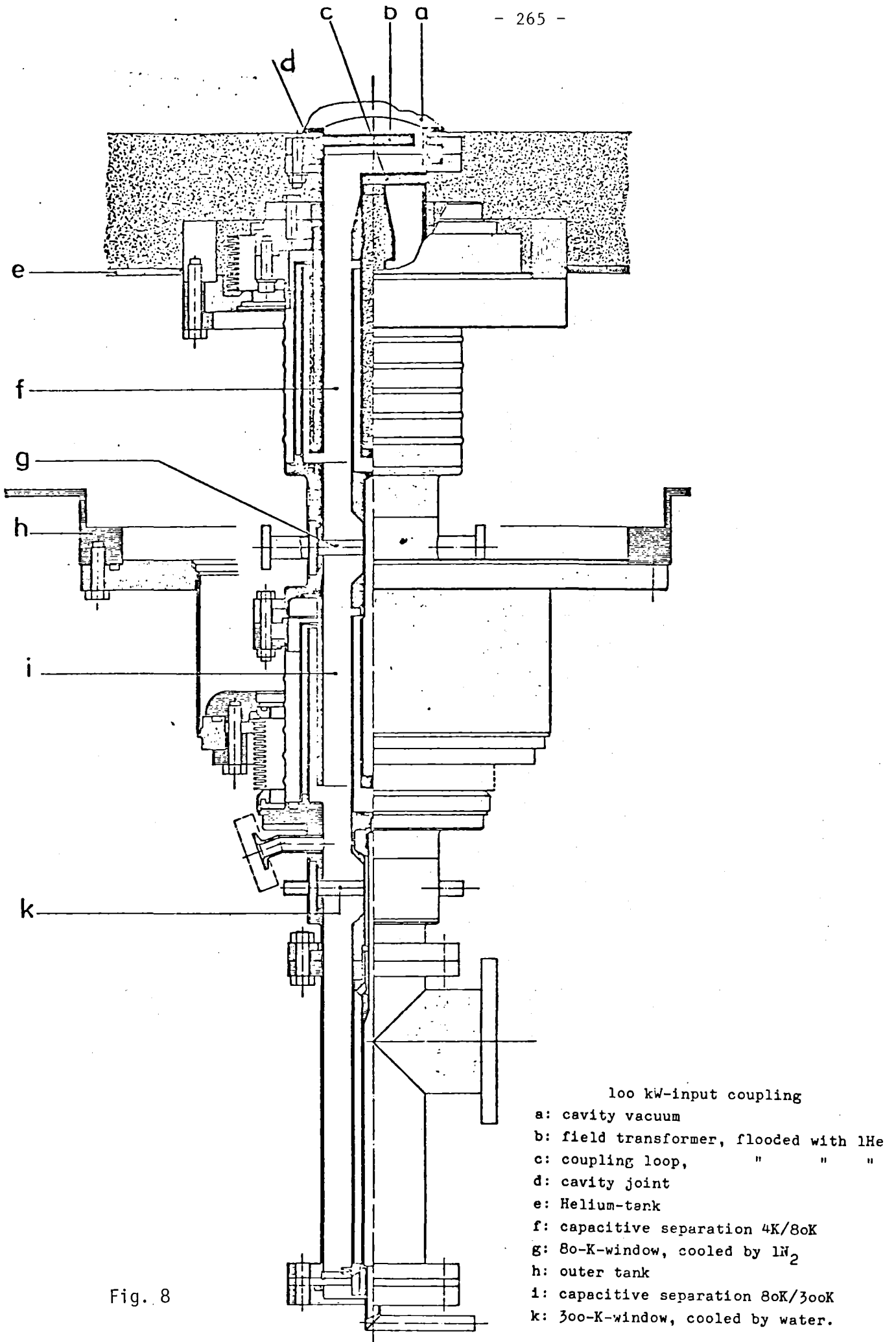


Fig. 8

- 100 kW-input coupling
- a: cavity vacuum
 - b: field transformer, flooded with lHe
 - c: coupling loop, " " "
 - d: cavity joint
 - e: Helium-tank
 - f: capacitive separation 4K/80K
 - g: 80-K-window, cooled by lN₂
 - h: outer tank
 - i: capacitive separation 80K/300K
 - k: 300-K-window, cooled by water.

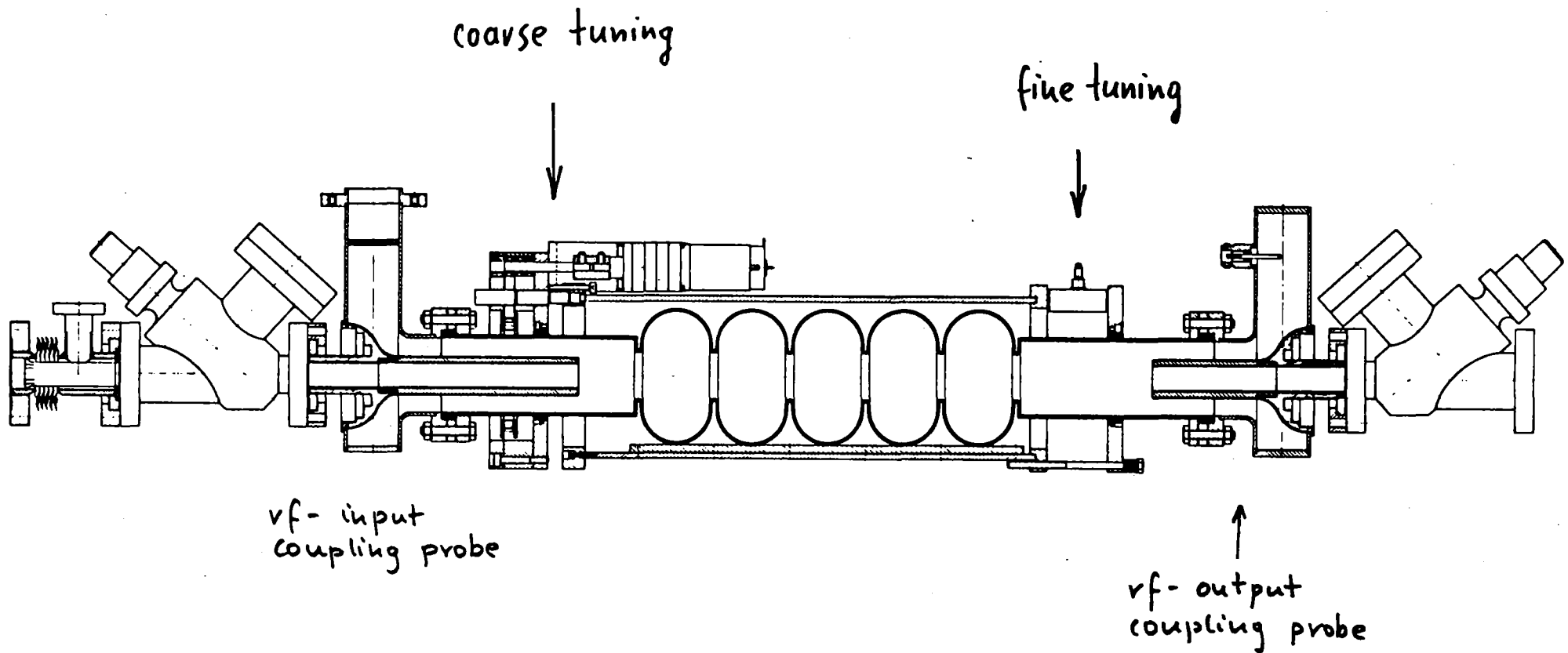


Fig. 9 Die fünfzellige Struktur
mit Frequenzabstimmung und
Ein- und Auskopplung

This 3GHz-structure
is now being built at
Interatom-company, Bergisch-
Gladbach 2, W. Germany

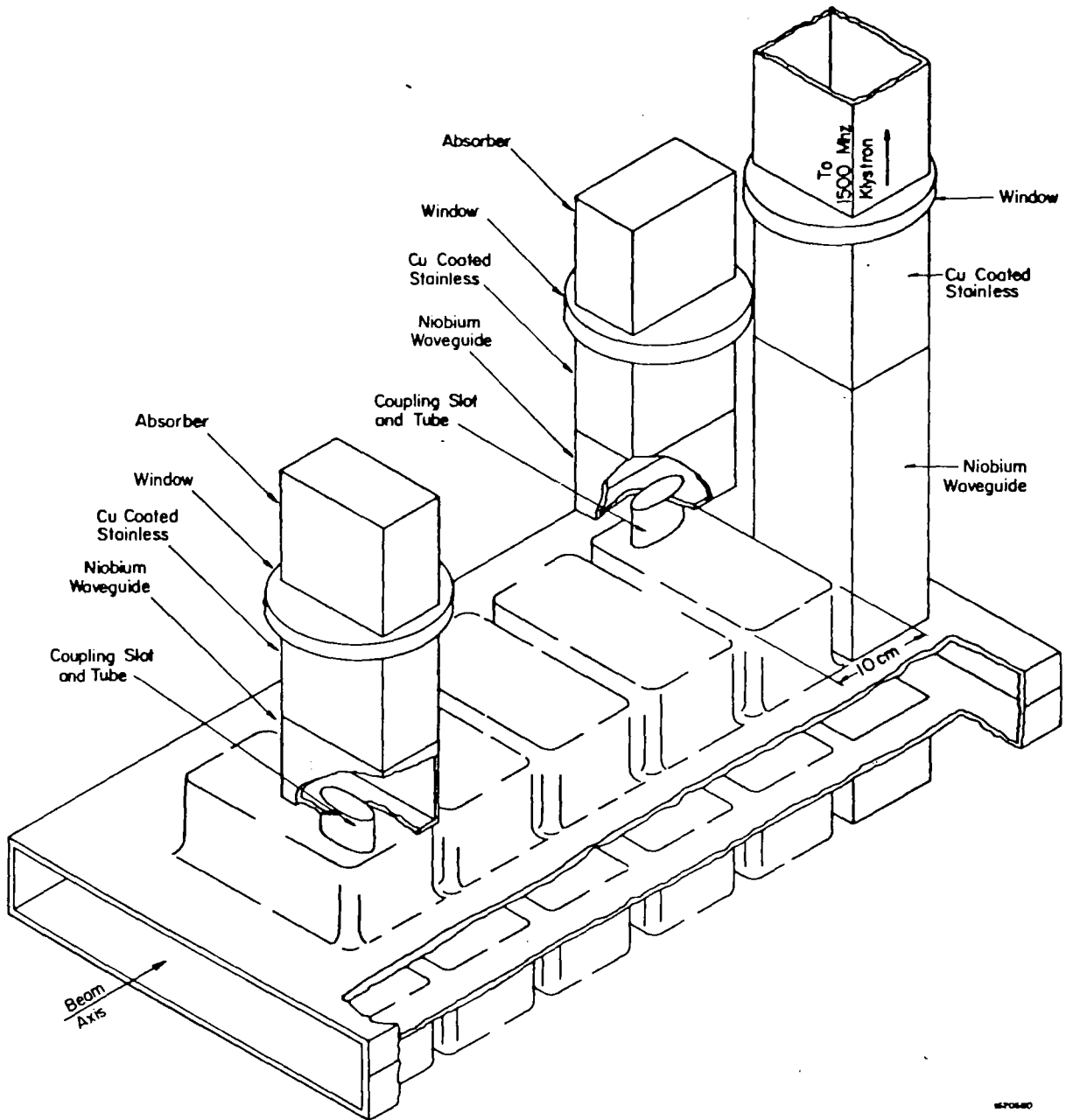
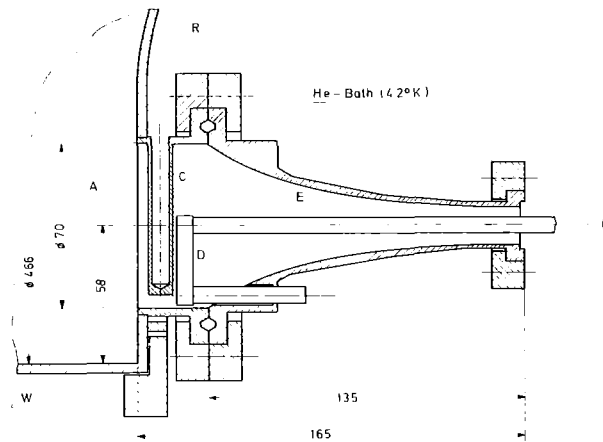
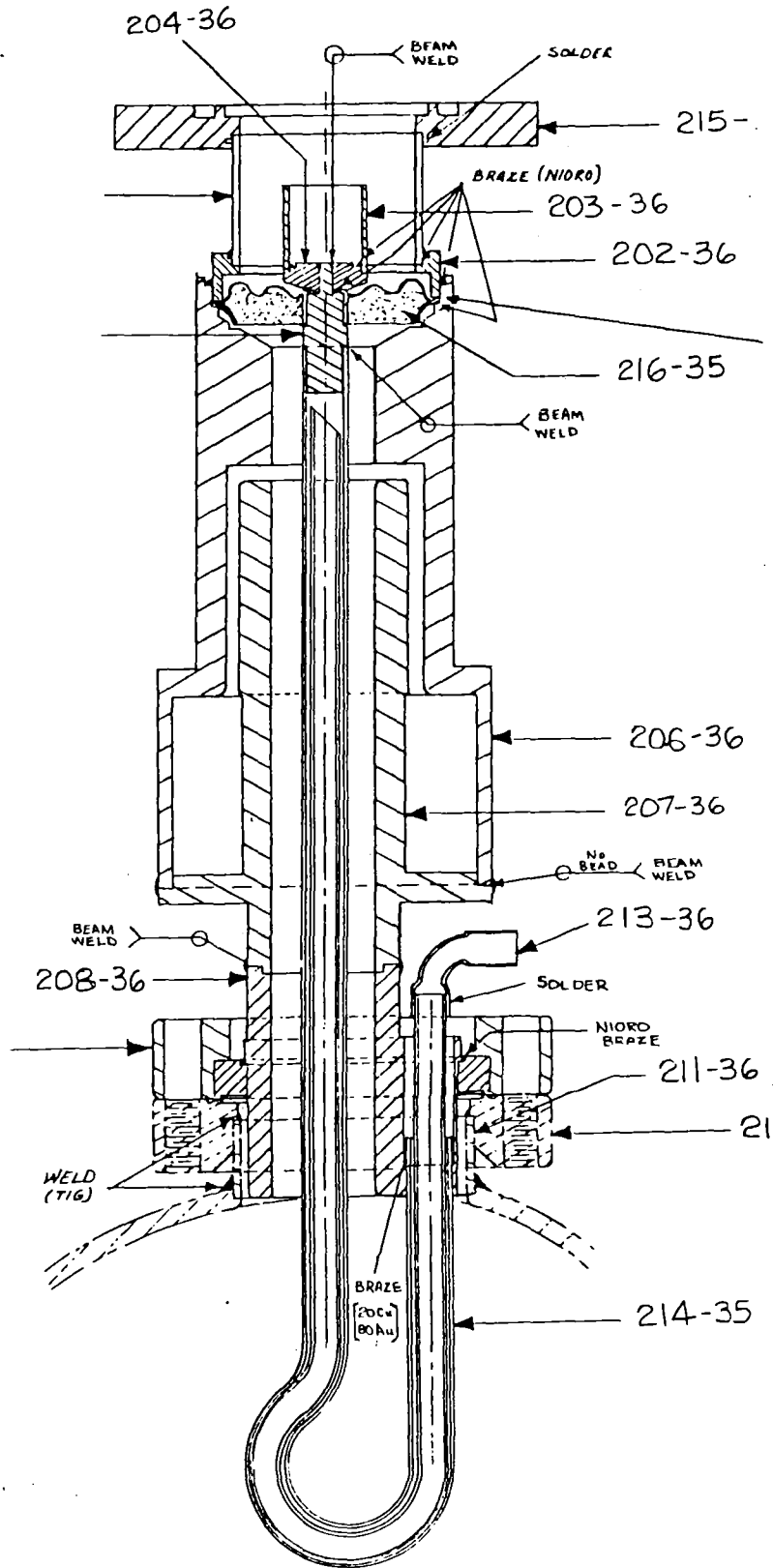


Fig. 10

Fig. 11: Higher mode output coupler developed by Szecsi

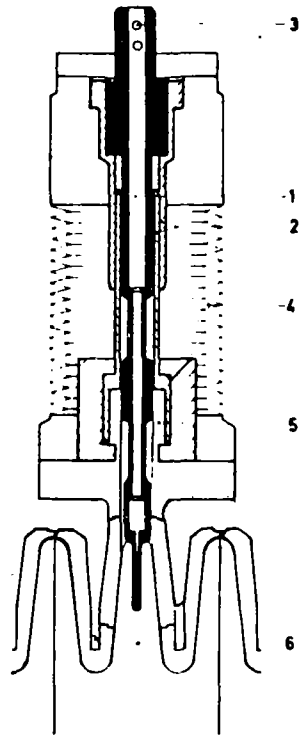
- A: cavity interior,
- B: coaxial line
- C: field transformer
- D: coupling loop
- E: exponential outer conductor of coaxial line
- R: cavity endplate
- W: cavity cylinder wall





200 HIGHER MODE PROBE SUB-ASSEMBLY (14 REQ'D.)

Fig. 12



Mechanical layout of a frequency tuner (fine tuner) (1) Nb-plunger with a cooling channel, (2) Cu-guiding cylinders, (3) hole for He-II entry, (4) bellows, (5) Nb-cylinder of deflector and (6) tuner cell.

Fig. 13

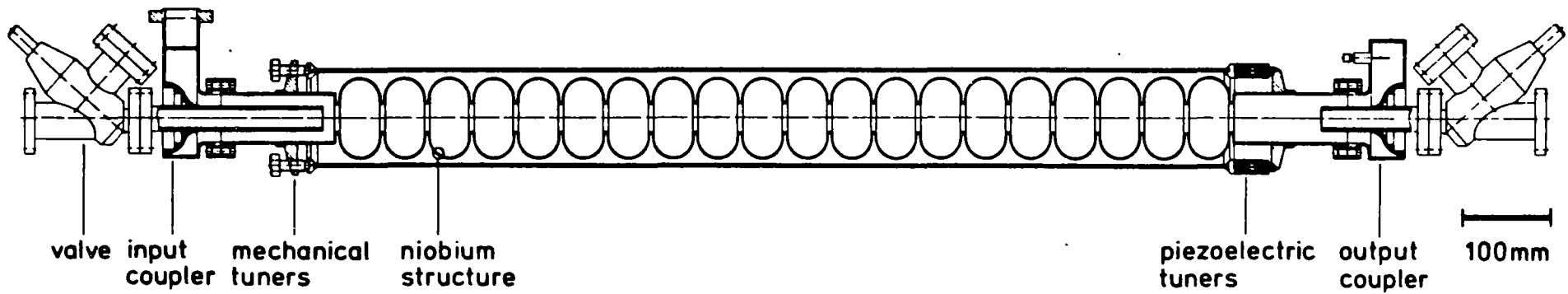


Fig. 14

Die 1m- Struktur mit
Frequenzabstimmung und
Ein- und Auskopplung

This 3 GHz - structure
is ordered now.

FABRICATION OF NIOBIUM CAVITIES

W. Bauer

Kernforschungszentrum Karlsruhe, Institut für Kernphysik
P.B. 3640, 7500 Karlsruhe, Federal Republic of Germany

I. Introduction

For the application of RF-superconductivity in accelerators, storage rings and RF-separators ¹ Niobium is most widely used as superconducting material. A few cases, where lead or Nb₃Sn were tried, will not be considered here. With one exception ², all cavities were made of pure Niobium - either from solid material or sheet. The specifications for the Niobium used - often referred to as "Stanford - specifications" are shown in Table I.

TABLE I: Ordering Specifications for Niobium

Niobium "Reactor grade", purity 99,8%
Tantalum content less than 1000 ppm
Electron beam melted
cold forged
Sheets cross-rolled
Fully recrystallized

The Tantalum content used to be 300 ppm, but since last year the suppliers report difficulties about achieving this purity. The now quoted Ta content of 1000 ppm may have consequences for the heat transfer ⁴ because it reduces the thermal conductivity. A typical chemical analysis is shown in Table II. ³ It should be pointed out to the niobium supplier, that scratches on the sheet surfaces should possibly be avoided; covering the sheet by a protective paper layer before delivery would be very helpful to maintain smooth surfaces. The following report collects the methods for fabrication of cavities out of this material.

II. Mechanical Properties of Niobium

We start with a collection of mechanical properties of Niobium, the knowledge of which is necessary for designing and fabricating cavities. It is clear, that they depend very much on the state of the material, e.g. on the purity and on previous heat treatments (where the temperature, the time and the vacuum are important). Experience shows, that the behaviour of the material may differ without any noticeable change in specifications or chemical analysis, from one charge of material to the other. Very little is known about mechanical properties of Niobium at low temperatures.

Table II: Typical Analysis of "Reactor grade Niobium" ³

<u>CHEMICAL ANALYSIS IN PPM</u>		
	<u>Top</u>	<u>Bottom</u>
Al	<20	<20
B	<1	<1
C	40R,40R	60R,70R
Ca	<20	<20
Cd	<5	<5
Co	<10	<10
Cr	<20	<20
Cu	<40	<40
Fe	<50	<50
Hf	<50	<50
Mg	<20	<20
Mn	<20	<20
Mo	<20	<20
Ni	<20	<20
Pb	<20	<20
Si	<50	<50
Sn	<10	<10
Ta	415	480
Ti	<40	<40
V	<20	<20
W	56	53
Zr	<100	<100
O	<50	100
N	14	27
H	<5	<5
<u>INGOT HARDNESS, BHN</u>		
Average		55
Low		44.9
High		85.7
500 kg load		
<u>METALLOGRAPHY TEST RESULTS</u>		
Micro no:	AM-310	
Material is 100% recrystallized.		
ASTM Grain Size Ave. no. (LONG.) 3.5		
<u>PRODUCT HARDNESS</u>		
50HV10		

Table III can be used as a guide-line for the design of Niobium cavities. The data are collected from many sources ^{3,5-10}. For comparison, the values for pure oxygen free copper are also given, which show that in many respects Niobium can be handled like soft copper. Fig. 1 shows the strong influence of the oxygen content on the hardness. An important feature of Niobium is the fact, that it getters oxygen, but also hydrogen, carbondioxide, hydrocarbons and others at temperatures above 200°C. The brittleness caused by dissolved gases can be removed by a heat treatment in vacuum. Hydrogen can be outgassed at $\geq 800^{\circ}\text{C}$, for

removing oxygen temperatures above 1500°C are needed. In addition, Niobium is always covered with an oxide layer.

Table III: Mechanical properties of Nb and Cu

Nb: purity 99.8%, electron beam melted, cold forged, recrystallized

Cu: Oxygen free, annealed, 99.95% purity

		Nb	Cu
density	g/cm ³	8.57	8.96
modulus of elasticity	N/mm ² · 10 ⁵	1.05	1.2
tensile strength	N/mm ²	207-274	196-245
bending strength	N/mm ²	138	-
yield point	N/mm ²	20*-196	117
elongation	%	25-25	30-50
vickers hardness	N/mm ²	800**	400-500
melting point	°C	2468-2497	1080
heat of fusion	J/g	298.5	188.4
specific heat (300 K)	J/g/°K	.267	.375
recrystall. temp.	°C	830-1230	500
thermal expansion (L _{4.2} -L ₂₇₃)/L _{4.2}		1.43 x 10 ⁻³	3.3 x 10 ⁻³

* annealed several hours at 1800°C and 10⁻⁸ torr; ** see Fig. 1

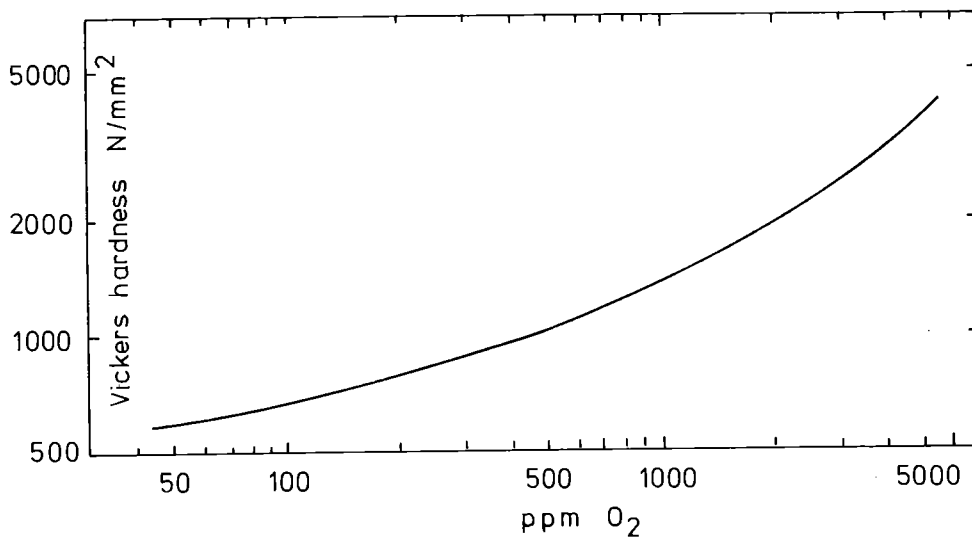


Fig. 1: Vickers hardness of Niobium versus Oxygen content ³

Another property of pure Niobium is its ductility: It can be cold worked up to 99% without intermediate annealing. In practice, however, annealing in vacuum at $\sim 1000^{\circ}\text{C}$ was found to be advantageous.

The conclusions from these properties for fabricating Niobium cavities can be summarized as follows:

- Shaping by machining, deep-drawing, spinning is possible, similar as for soft copper
- Welding needs a high temperature and much heat input because of the high heat of fusion and has to be done in completely oxygen-free environment, i.e. in vacuum or in a very clean inert gas atmosphere.

III. Machining

Machining tests have been carried through at all places, where Niobium cavities have been built. Machining Niobium needs much experience, especially in shaping the tool for free removal of the chips. Machining speed and cooling has to be adjusted to avoid heating up the material. Sometimes one charge of material is more difficult to machine than others. In some cases a previous heat treatment resulting in large grain sizes was reported advantageous, in others better results were obtained without heat treatment.

The tolerances achieved are of the order $\leq .01$ mm, i.e. as good as for other materials. In general deformations caused by heat treatment and welding have much more influence on the final tolerances than the initial machining.

Table IV. shows some parameters for machining which are recommended by Niobium suppliers and have been proven useful at many laboratories. They must be considered as a starting point, since every worker collects his own experience in shaping the tools and operating the lathe or mill.

As is shown in the table many lubricants or coolants have been tried, some of which underlying certain safety regulations like Trichlorethylene, which can only be used, if the lathe is equipped with an gas exhaust system. Although all other coolants give satisfactory results it is still generally agreed that Tri should be used for very delicate surfaces and small parts.

The surface roughness achieved by careful machining can be as small as $\leq 5\mu$. In one case ¹¹ a surface roughness of 0.2μ has been reported.

Table IV: Parameters for Machining Niobium

Cutting tool:	High speed steel, sometimes also used: tungsten carbide (Widia) (only for fast light cuts, danger of breaking the tool).
Approach angle:	15° - 20°
Side rake:	20° - 25°
Side and end clearance:	5°
Plan relief angle:	10° - 20°
Nose radius:	0.5 - 0.75 mm
Cutting speed:	20 - 25 m/min HSS 75 - 90 m/min Widia
Feed, roughing:	0.2 - 0.3 mm/rev
Feed, finishing:	0.01 - 0.1 mm/rev
Depth of cut, roughing:	0.75 - 3 mm
Depth of cut, finishing:	0.03 - 0.1 mm
Lubricants:	Trichlorethylene, Tetrachlorcarbon, Chlorotene (safety regulations!) water, freon, air, oil
Achieved surface roughness:	≤ 5 μ

IV Sheetmetal Forming Techniques

Considering the fabrication of many cavities especially for low frequencies machining from solid is not possible for economical reasons. Several sheet metal forming techniques have been applied:

- Spinning: The sheet is fixed against a die on a lathe and rotated; then the material is pressed against the die by a handle. This method is used for single piece production, since the tools are relatively inexpensive.
- Deep-drawing: The sheet is formed in a hydraulic press between a die and a punch. This requires expensive tools and is the appropriate method for mass production.
- Hydroforming: The sheet is pressed into the die by hydraulic pressure of oil.
- Coining: The material fills after pressing the entire space between two tightly fitting dies.

1. Spinning

Experience in spinning Niobium exists at CERN¹², KEK¹³, University of Wuppertal¹⁴, and at the companies W.C. Heraeus⁵, and Siemens¹⁵. The die is made of hard wood

brass, bronze, steel, which is sometimes polished and hardened or aluminum anodized with a thick oxide layer.

At CERN¹² the first spinning step is done using an aluminum die with the exact cavity dimensions. Then an annealing at 1000°C in a vacuum of 10⁻⁵ torr has been considered advantageous. After that the spinning is continued using a hard wood die with a slightly smaller diameter. Finally the piece is pressed into the aluminum die again and the spinning is completed.

Preferably the die should be on the inner cavity surface to achieve the best surface quality.

The handle can be brass or steel; sometimes it is equipped with a steel roll.

Peripheral speeds of 150 - 1000 m/min are reported; the high speed is considered advantageous to reduce the need of intermediate annealing.

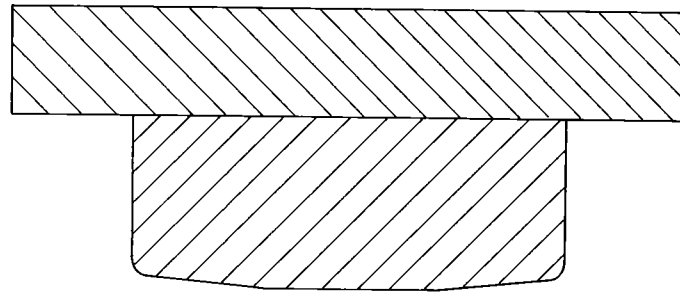
The tolerances achieved by this method are about 0.2 - 0.3 mm on a ~ 600 mm diameter.

2. Deep drawing

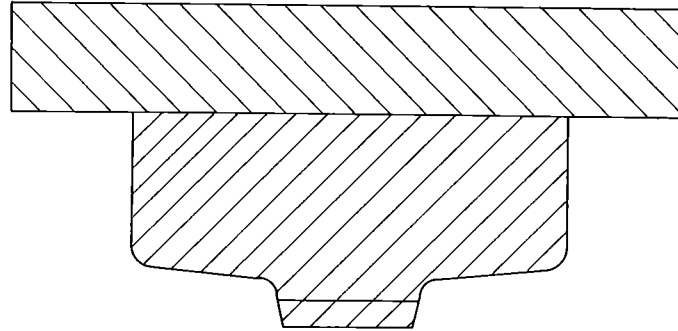
Deep drawing is used at Cornell¹⁶, Genua¹⁷, Interatom¹⁸, Siemens¹⁹ and others. Fig. 2a - 2c show examples for dies and punches used by Siemens for deep-drawing of separator-half-cells. If one aims at tight tolerances and good reproducibility one has to deal with the following difficulties:

- thickness tolerances of the material
- elastic properties of Niobium may change from one charge to the other
- removing the parts from the die is sometimes difficult and may result in dimensional changes. Experiments on suited die surfaces and lubricants might be necessary.
- in some cases machining of the inner surface after deep-drawing was considered necessary in order to achieve the tolerances and the surface finish required.

Table V shows a typical procedure, which was worked out at Siemens¹⁹ for fabricating the CERN-Karlsruhe RF-particle separator. Later on this scheme was abandoned in favour of machining the whole cavity from solid. More recently Interatom¹⁸ has built S-Band cavities for the University of Wuppertal¹⁴ using a deep-draw technique without intermediate heat treatment or final machining.

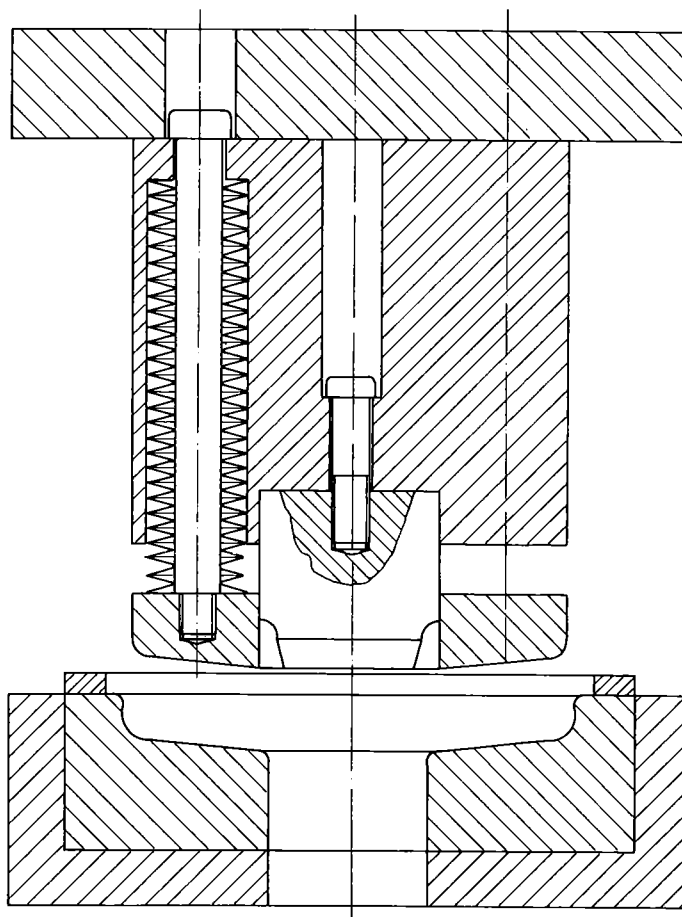


2a)



2c)

Fig. 2. Deep-drawing tools used by Siemens¹⁹⁾ (Table V)



2b)

10 mm

Table V: Typical deep-drawing procedure ¹⁹

1. Material 3 mm, cross rolled
2. cut circular plates 141 \emptyset
3. cut central hole 35 \emptyset
4. anneal at 900°C, 1 h, 10^{-5} torr
5. make mechanically plane
6. machine flat on both sides 2.65 mm thickness!
7. deep-draw 1. tool (outer edge)
8. increase central hole, make central to outer radius
9. deep-draw 2. tool
10. anneal 1200°C, 1 h, 10^{-5} torr
11. deep draw 3. tool
12. machine seam for electron beam welding

3. Other forming techniques

The cylindrical part of the KfK-DORIS-Cavities is simply rolled and longitudinally welded. The diameter tolerance achieved is 0.3 - 0.5 mm.

At HEPL ²⁰ the cavities are shaped by hydroforming and are machined afterwards. SLAC ²¹ has investigated a special technique called coining. There the exact amount of material is brought between two dies and is squeezed until it fills the entire volume. Removal of the parts requires a heavily oxidized niobium surface.

V. Welding

Niobium can only be heated or melted in vacuum or in a clean inert gas atmosphere to avoid brittleness. Two welding techniques are widely used: Electron beam welding and Tig (tungsten-inert-gas, argon-arc) - welding. Both methods need much experience and many tests for each new geometry, often for each new material are required. In any case welding from inside is to be preferred, if possible. It is difficult to decide which method is superior, the choice is usually made by the availability of the installations existing at the individual place. In table VI a comparison is tried. Fig. 3a-d show some examples of seam shapes used for electron beam welding, the voltage and current values given can only be used as starting points for detailed welding tests. Fig. 4a-c continue this for TIG welded parts. Some parameters for TIG-welding are collected in Table VII.

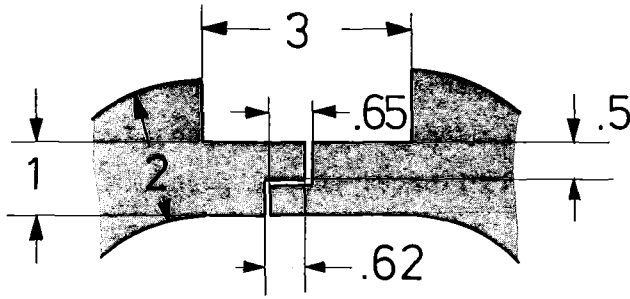
Table VI: Comparison between EBW - and TIG

Electron beam welding	TIG-welding
Requires tight tolerances of the parts to be welded, which are difficult to achieve with large parts formed from sheet. (But: see Fig.3c!)	Tolerance requirements are not so stringent, since the torch is guided manually. This makes also more complicated shapes possible. On the other hand, some tooling is required for fixing the parts during welding.
Complicated shapes of the weld have to be avoided, as all movements in the box must be mechanically and remote controlled.	Although the welds are macroscopically uneven and much broader than with EBW the RF-results are not distinguishable. No spatter has been observed.
Welding from outside often gives rise to uneven inner surfaces. Spattered little Niobium balls often have to be removed mechanically or chemically.	Pumping of the box is also necessary before fitting it with Argon or He. After some welding (~ about 1 m of weld) the outgassed contaminants have decreased the purity of the argon so much, that an exchange of the argon becomes necessary. Very clean Argon (or He) is absolutely essential.
Rather long waiting times are needed for pumping and cooling.	
The great advantage is the fact, that little heat is brought in and only little deformation by stress relieve can occur. Also delicate parts in the vicinity of the weld remain cooler. (e.g. ceramic windows).	
EBW is considered more expensive, but conclusive numbers are not available.	

Table VII: Parameters for TIG-welding

Thickness (mm)	Current (A)	Welding speed (cm/min)
.3	40	~ 50
.5	60	~ 50
.75	80	~ 50
2	110	~ 50

Fig. 3: Examples for Electron Beam Welds



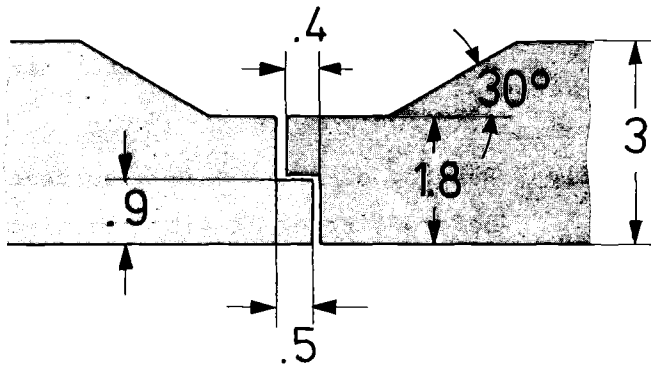
3a:

Interatom-Wuppertal

110 - 130 kV

3.8 - 4.4 mA

shrinkage 0.15 mm



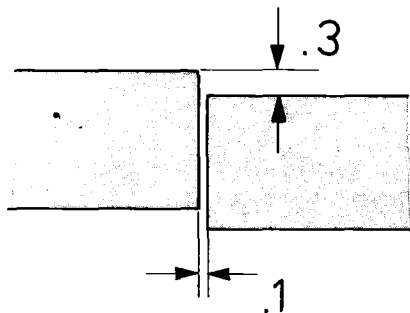
3b:

Siemens (RF-Separator)

110 kV

4.5 - 4.8 mA

shrinkage 0.2 mm



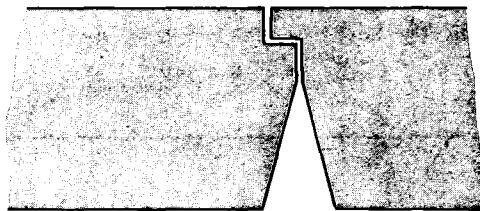
3c:

CERN (500 MHz-cavity)

55 kV

42 mA

shrinkage 0.15 mm



3d:

I. Ben-Zvi

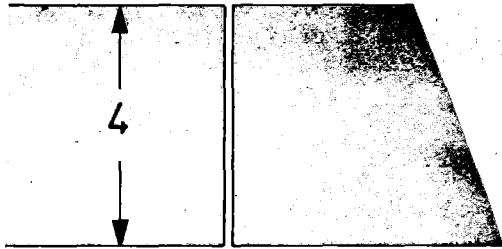
100 kV

20 mA

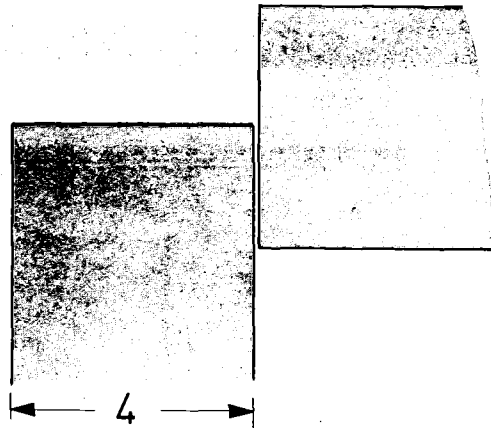
shrinkage negligible

electron monitor inside!

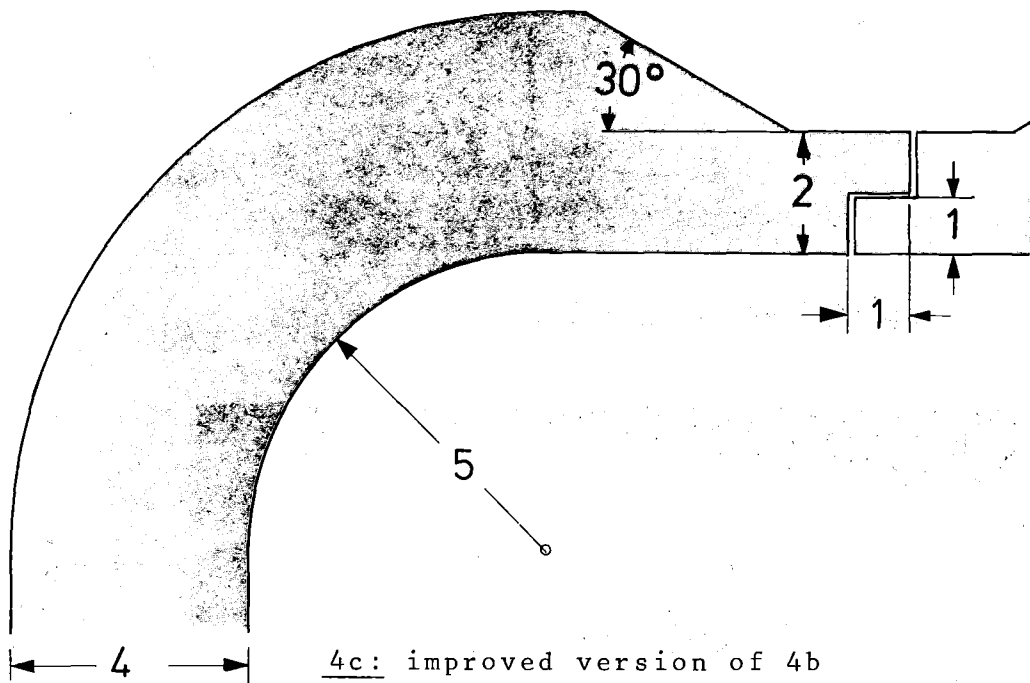
Fig. 4: Examples for Argon-Arc-welds



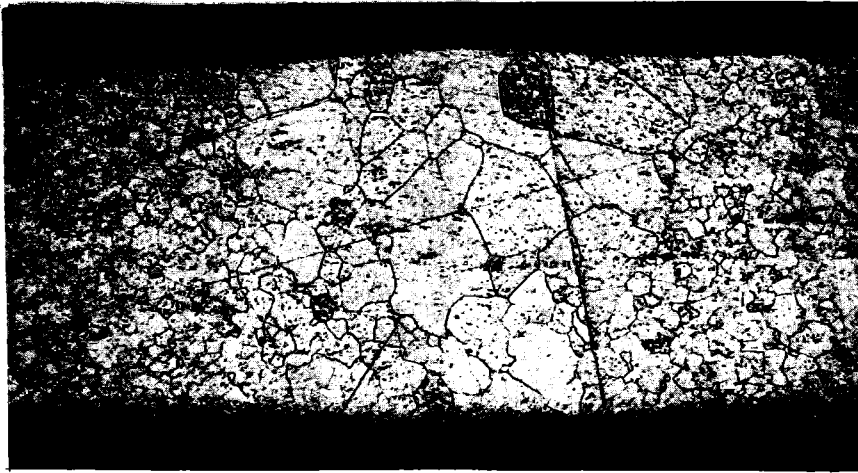
4a: DORIS-cavity cylinder wall



4b: DORIS-cavity endplate - cylinder wall



4c: improved version of 4b

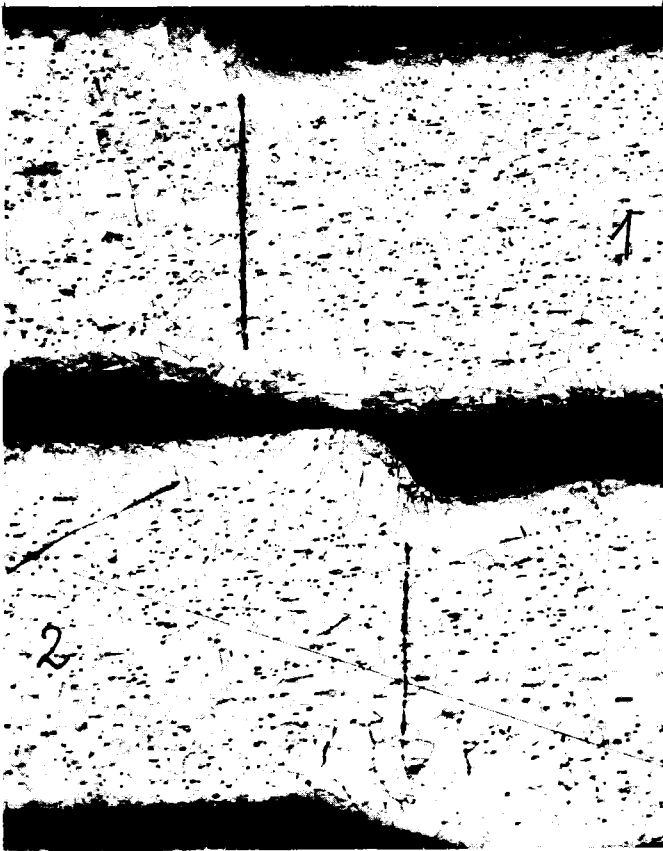


5 a

Fig. 5:

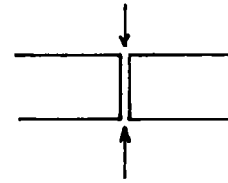
EBW-tests Interatom

1 single piece, 1 mm
beam from both sides
grain size!

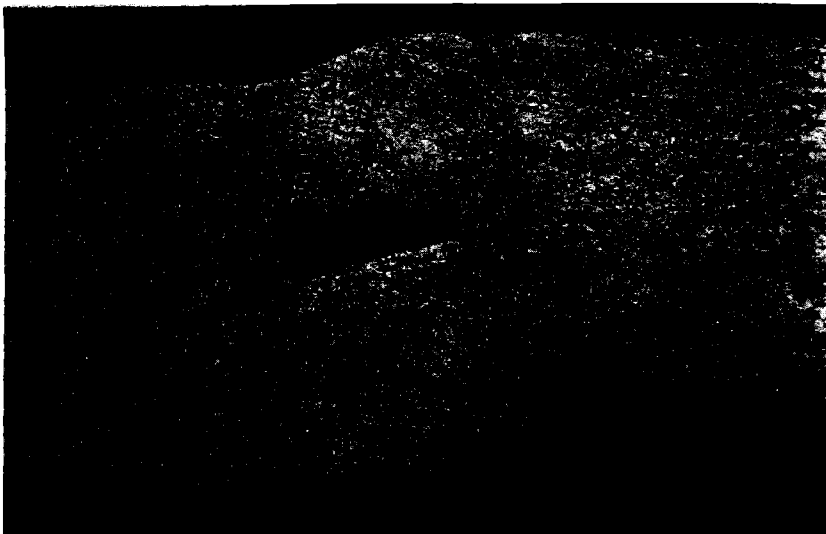


5 b

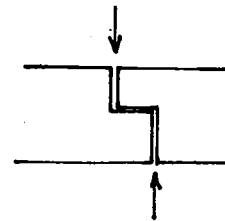
2 pieces 1mm



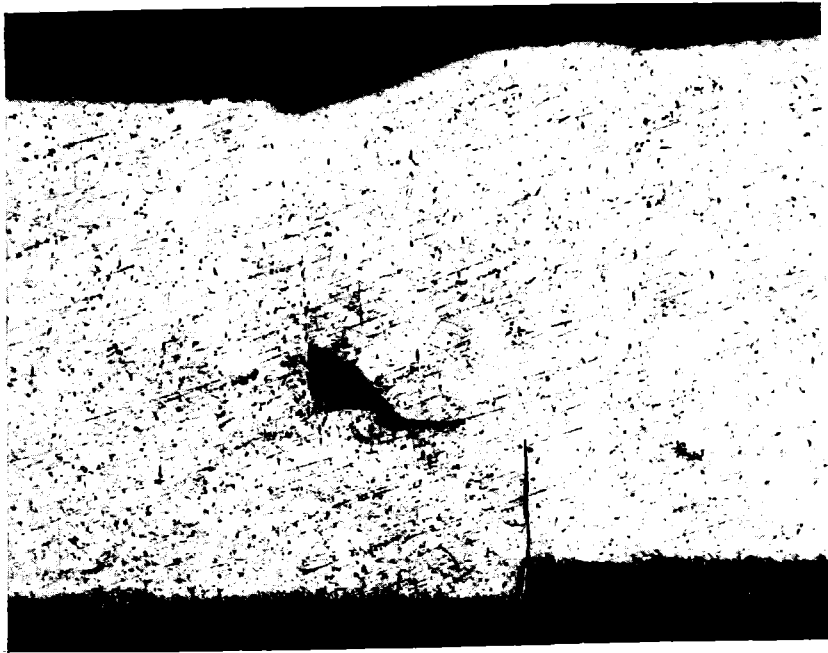
remaining slot,
shift!



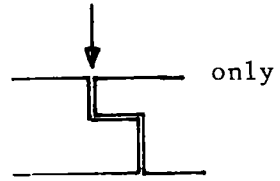
5 c



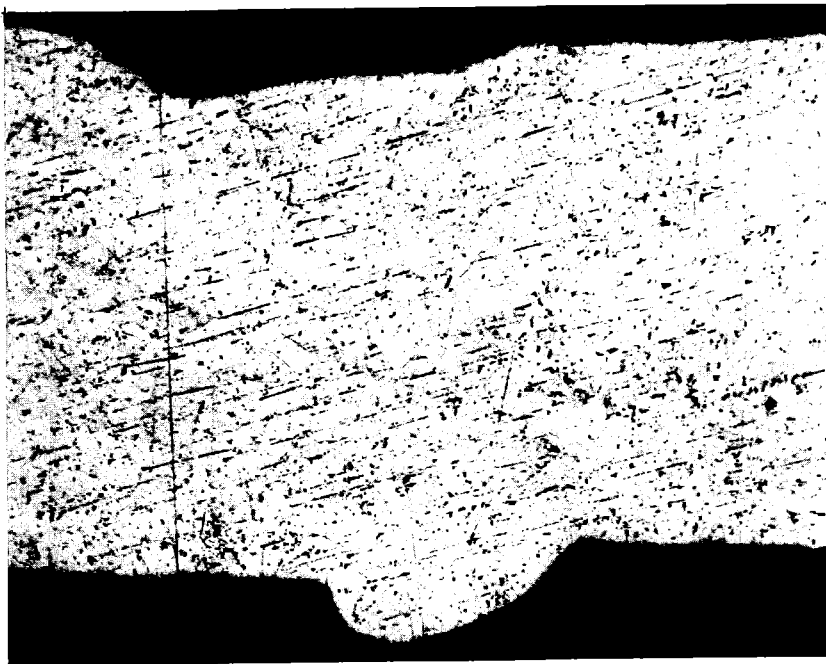
remaining hole
shift!



5 d

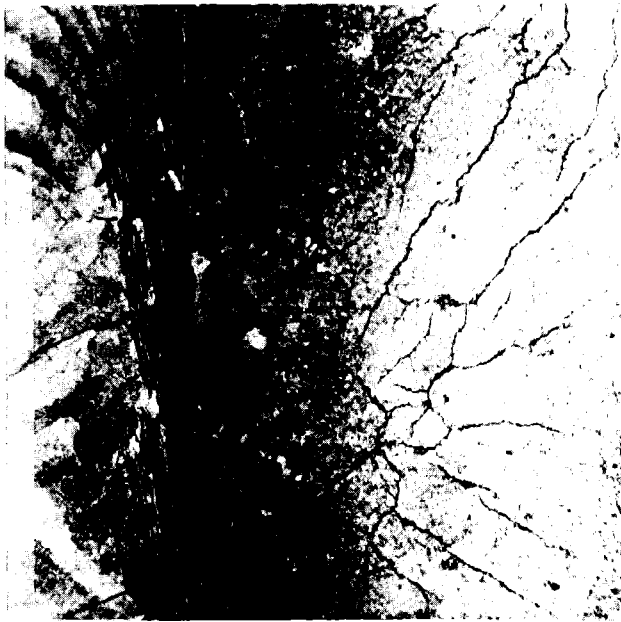


remaining hole and slit,
shift



5 e

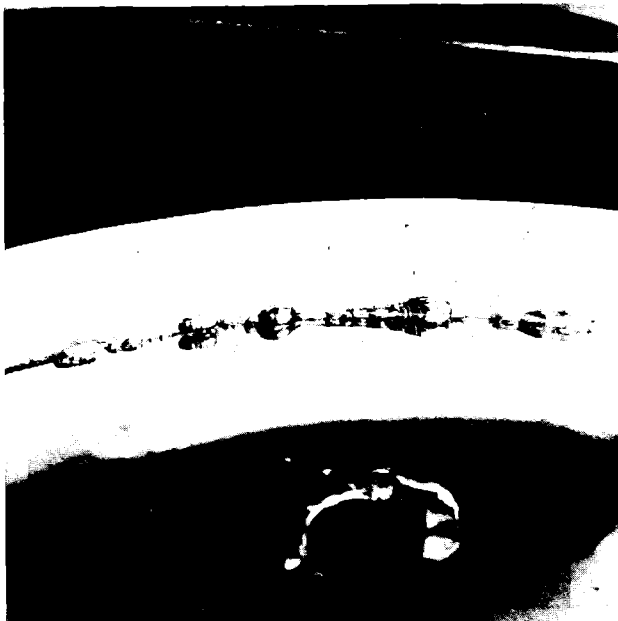
same as above,
more current



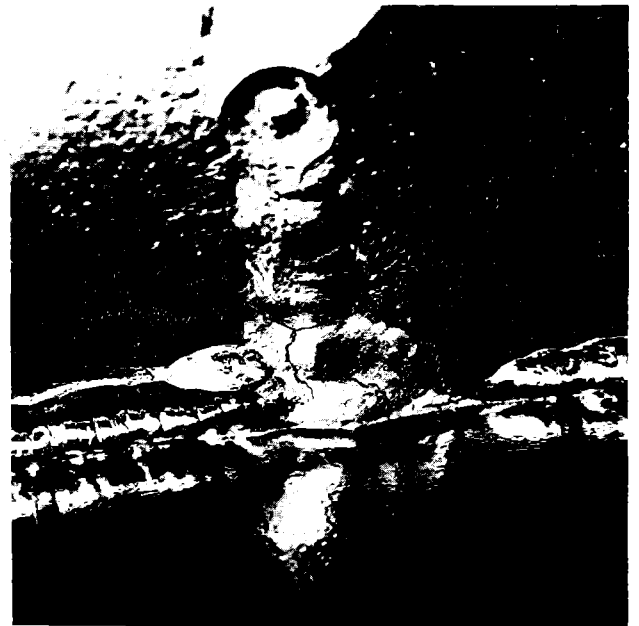
a



b



c



d

Fig. 6: TIG-welding the DORIS-cavities

a: fissures in cylinder wall

b: endplate - cylinder wall

c: Detail of b

d: crossing of welds in cylinder wall and corner

Fig. 5a-e show a few examples of electron beam welding tests made by Interatom. ²²

The photographs Fig. 6a-d taken during the fabrication of the DORIS-cavities show that argon-arc welding sometimes gives rise to difficulties: Fissures in the longitudinal weld of the cylinder wall originating in the weld and extending into the material next to the weld could be explained by a not completely clean box (Siemens). Similar cracks together with a mat surface of the weld were observed at Heraeus, which were explained by some mysterious behaviour of the material that did not show up by any chemical or metallurgical analysis. This problem could be overcome by heating the material to 1800°C in a vacuum of 10^{-8} torr. All welds done after this heat treatment appeared shiny and vacuum tight. The weld in the corner between endplate and cylinder wall of DORIS I shown in Fig. 6c-d was very uneven, especially at the crossing between the longitudinal weld in the cylinder wall and the corner weld. It was rewelded from inside at KfK. The two DORIS-cavities made by TIG-welding were 1-3 mm out of tolerances. Apparently more effort is needed to fix the parts in the box during welding, although not all tolerance problems can be attributed only to the welding.

CERN²³ reported about TIG-welding without a box, where a stream of argon is guided along the weld in such a way, that no air contaminates hot parts.

Another welding method has been described by Isagawa²⁴, and was also used at KfK for welding niobium tubes on sheet²⁵: Clean, smooth niobium surfaces are mounted in an ultrahigh vacuum furnace and pressed by niobium weights. By diffusion at 1800°C the parts are tightly welded. This method certainly avoids contamination better than any other and combines a heat treatment which is considered desirable for other reasons with the welding. For large cavities made of sheet, however, it might be difficult to apply the necessary weight.

VI Costs

It is impossible at the moment to answer the question about large scale fabrication costs precisely. Experience exists only for some single cavities and very preliminary quotations have been obtained for the production of ~ 1600 m of cavities in the frequency range 350-700 MHz. More conclusive numbers can only be obtained after a real design has been made, which certainly has to take into account minimizing the fabrication costs. Since the material costs have been increased considerably during the last year, it seems advisable, to reconsider niobium-saving fabrication methods like sputtering or electroplating thin layers of Nb or explosion-bond² thin Nb-sheet on copper. This, of course has to take into account the questions of heat transfer⁴ and the pro's and con's of the heat treatment at high temperatures. By

electroplating one may increase the Nb purity with positive consequences for heat transfer.

In addition to the fabrication and material costs one has to take into account the costs for surface treatments which generally are dominated by manpower and installation costs. (One surface treatment of the DORIS cavity requires DM 200,-- for chemical solutions + 2 man-days + an existing installation that has costed about DM 100.000,-- + 4 days treatment in a furnace that has costed 1 Million DM!)

Table VIII collects some figures of the amounts involved which should show the direction, where to go to arrive at reasonable fabrication costs.

Table VIII: Costs

1. Single cavities	fabrication KDM	material KDM	total KDM
DORIS I/II (TIG, 4mm wall)	20	18	38
DORIS III (offer: EBW)	30 (+ 10 tools)	18	48 (58)
CERN 500 MHz (EBW, 2 mm)	16	7.2	23.2
2. Mass production	fabrication KDM/m	material KDM/m	total KDM/m
Interatom 3 GHz	27	~ 3.5	30.5
Cornell ²⁶ 1,5 GHz			30*
SLAC ²⁶ 1.5 GHz			54*
Inquiries 1600 m:	KDM/m	KDM/m	KDM/m
Single cells 350 MHz	12-30	30	42-60
Single cells 500 MHz	14-31	25	39-56
7-cell-Iris 700 MHz	7- 9	17	24-26
* including couplers, tuners ...			

VII. Conclusions

The fabrication methods for niobium cavities have been reviewed. Machining, sheet metal forming and welding techniques have been described. Handling of niobium presents no particular difficulties, but it requires much experience. The transfer of the know-how gained in the laboratories to the industrial scale is possible, but needs some training. It cannot be repeated often enough that niobium is a very soft material, and that therefore all inner surfaces and es-

pecially all flanges have to be protected against accidental scratches. To reduce material costs methods of producing thin Niobium layers on a copper substrat should be investigated again.

Acknowledgements

I would like to thank all laboratories and companies, who have contributed to the informations collected in this review, especially CERN, Cornell, HEPL, SLAC, the University of Wuppertal and the companies Interatom, Kawecki, Siemens, and Wah Chang. The state of the art reported is the outcome of more than 10 years of competent work of many technicians in all laboratories and companies where niobium cavities have been built. Their effort should be greatly acknowledged.

R e f e r e n c e s

- 1 A. Citron, this workshop
- 2 L. M. Bollinger, private communication
- 3 Teledyne Wah Chang, Albany, Oregon, 97321 P.O.Box 460
"Columbium, Properties, Processes and Products"
- 4 H. Padamsee, this workshop
- 5 W.C. Heraeus, Postfach 1553, D-6450 Hanau 1
- 6 Gmelins Handbuch der Anorganischen Chemie
System-Nr. 49: Niob (1969)
Verlag Chemie, Weinheim, Bergstraße
- 7 R. Küffer, H. Braun
"Vanadin, Niob, Tantal"
Springer Verlag (Berlin, Göttingen, Heidelberg), 1963
- 8 G.L. Miller
"Tantalum and Niobium"
Butterworth's Scientific Publication (London), 1959
- 9 F.T. Sisco, E. Epremian
"Columbium and Tantalum"
John Wiley and Sons Inc., (New York, London) 1963
- 10 "Niob, ein seltenes Metall mit Zukunft", Ingenieur-Digest 11, Heft 8,
1972, p. 55-58
- 11 J. Aggus, W. Bauer, S. Giordano, H. Hahn, H.J. Halama,
private communication

- 12 Ph. Bernard, G. Cavallari, E. Chiaveri, E. Haebel, H. Heinrichs, H. Lengeler, E. Picasso, V. Picciarelli, H. Piel
"First Results on a Superconducting RF-Test Cavity for LEP"
Proceedings XI. Int. Conf. High Energy Acc., CERN (Geneva), 1980
(to be published)
- 13 Y. Kimura, "Tristan"
in ref. 12
- 14 U. Klein, D. Proch, H. Lengeler
private communication
- 15 H. Diepers, Fa. Siemens AG, Zentrale Forschungslaboratorien, Postfach 3240, 8520 Erlangen 2
- 16 H. Padamsee, J. Kirchgessner, M. Tigner, R. Sundelin, M. Banner, J. Stimmwell, H.L. Phillips
private communication
- 17 V. Lagomarzino, G. Manuzio, R. Parodi
"Measurements on Niobium Multicell Superconducting C-Band Structures for Linear Accelerator Application"
Proceedings IPC-Conf. (Genova), 1980, to be published
- 18 A. Palussek, Interatom, Friedrich-Ebert-Straße, D-5060 Bergisch Gladbach 1
- 19 H. Diepers
private communication
- 20 J.P. Turneaure, H.A. Schwettman, H.D. Schwarz, M.S. McAshan,
"Performance of 6-m 1300 MHz superconducting Niobium Accelerator Structures", Appl. Phys. Lett. 25, 1974, p. 247-249
- 21 R.R. Cochran
private communication
- 22 A. Palussek, Interatom, private communication
- 23 H. Lengeler, CERN, private communication
- 24 S. Isagawa, "Fabrication of superconducting niobium cavity by the diffusion bonding method", J. Appl. Phys. 49, (1978), p. 881-885
- 25 L. Szecsi, R. Vincon, private communication
L. Szecsi, "Einrichtung zum Kühlen eines supraleitenden Resonators und Verfahren zum Herstellen desselben", Patent DE-AS 28 09 913 (1979)
- 26 D. Ritson, M. Tigner, private communication

SUPERCONDUCTING CAVITIES FOR ELECTRON STORAGE RINGS
A REVIEW

M. Tigner
Cornell University
Ithaca, New York 14853 USA

Since no one has as yet had the temerity to build a storage ring with superconducting cavities, the thinking on this subject is still in its infancy. Thus any remarks with regard to such use must needs be of a general nature and will likely be in error to some extent.

The subject matter I want to cover can be broken into several parts. First a few remarks about the basic reason for interest in rf superconductivity for storage ring service. Then we'll discuss the choice of frequency followed by some considerations about the engineering problems peculiar to the use of superconducting cavities in storage rings.

In all that follows, I shall tacitly assume that we are speaking of storage rings for beam energies of tens of GeV so that we'll be dealing with a situation in which the resonant and non-resonant impedance of the vacuum system components is dominated by the rf system consisting of several hundreds or thousands of individual cells.

Why Contemplate the Use of Superconducting Cavities
for Storage Rings

As we all know, the basic reason for pursuit of this technology is economic. The storage rings of which we speak will require rf voltages of the order of 10^9 volts. Normal conducting rf systems to produce such accelerations will cost hundreds of millions in any western monetary unit. Since a large portion of these costs is simply for rf power that is dissipated in the cavity walls and since rf superconductivity offers shunt resistance improvements of 10^5 or more, it is clear that one stands to gain large factors in cost by use of rf superconductivity. This is, of course, only true provided

that the cost of the superconducting cavities is not enormously greater than for the normal cavities and that the refrigerator is not more costly than the rf power tubes and power supplies it replaces. One must, however, look deeper than this simple observation. Let us take but one example for illustration. The estimated cost for the LEP stage 1 normal rf system is 250 MSF, about one-fifth of the total cost. You might note that even if this cost were reduced to zero, while it would save a Kings' ransom, it would not change the overall cost by a very large fraction. That observation would be correct but it ignores a very important fact: Were that LEP stage 1 designed ab initio with superconducting cavities in mind, the lower unit cost for producing rf voltage would be reflected in lower costs for all of the storage ring systems and thereby have a profound affect on the overall cost. To see how this comes about one can write the cost of a storage ring¹ as

$$C - C_0 = g_\rho \cdot \rho + (g_{cav} + L_0 \cdot g_{Lum}) \frac{E^4}{\rho} \dots \quad (1)$$

$$C_0 \approx \text{fixed costs} \sim \text{independent of } E \text{ \& } \rho; \frac{C_0}{C} \ll 1$$

g_i = unit costs; ρ = bending radius

E = beam energy, L_0 = scaled luminosity

The first term represents the standard accelerator components such as magnets, vacuum, control and housing, the total costs for which are proportional to the radius of the machine. The second term represents the cost of the rf system and is proportional to the voltage which the rf system must produce. The first part of the second term represents the cost of the cavities and refrigerator and involves the operating gradient and equipment unit costs while the second part represents the cost of making the luminosity, and involves the cost of rf power, the dependence of luminosity on beam current, and the maximum charge density allowed by the beam-beam effect. Naturally, the costs for the cavity and refrigerator involve a further optimization process in which one chooses the optimum combination of cavity length and refrigerator power. A typical

Table I

Beam Energy (GeV)	Peak Luminosity ($10^{32} \text{cm}^{-2} \text{sec}^{-1}$)	Cavity Type	C-C ₀ Capital (M\$)	C-C ₀ Capital + 5 yr. Oper (M\$)	Δ Capital (M\$)	Δ Capital + 5 yr. oper. (M\$)
50	.3	sc	93.5	128.7	0	0
50	.3	nc	192.7	248.8	99.2	120.1
50	1	sc	135.9	208.5	42.4	79.8
86	.3	sc	248.8	320.9	153.3	192.2
86	.3	nc	557.3	707.1	463.8	578.4
86	1	sc	336.1	495.9	242.6	367.2
86	1	nc	613.9	832.4	520.4	703.7

Δ Compares costs in rows 2-7 with corresponding costs in row 1.

prescription for achieving this is given in reference 2.

For a given energy one can find the radius that minimizes the overall cost of the storage ring. Using eqa. 1 we find in general that

$$\rho_{opt} = \sqrt{\frac{g_{cav} + L_o \cdot g_{lum}}{g_p}} \cdot E^2 \dots \dots \quad (2)$$

Thus, the lower g_{cav} is, the smaller the radius and the smaller the radius the less tunnel, magnet, vacuum system, etc. are needed thereby decreasing the cost of the complete machine. For a reasonable range of parameters the cost of the machine for fixed energy and luminosity can be halved by use of superconducting cavities. Table 1 shows some numerical examples taken from reference 3.

In summary, having chosen an energy and luminosity, the use of superconducting cavities can halve the cost of the accelerator itself. It goes without saying that the savings in operating power gained by use of superconductivity are also well worth while as indicated in Table 1.

Choice of Frequency

The choice of frequency is governed, unfortunately, by conflicting demands and is a complex systems problem. On the economy side one would like as high a frequency as possible giving high R/Q, small sizes and consequent low material and manufacturing and handling costs as well as smaller rf distribution systems, windows, etc. This simple picture is made somewhat more complex by the ω^2 dependence of the BCS surface resistance which tempts one to use lower frequencies so that the Q at 4.2K is good enough to obviate the need for operation at below atmospheric pressure on the helium coolant. One might think that the improved Carnot efficiency and savings on the massive vacuum pumps would offset the extra expense for the larger cavities and liquid helium pumps. Unless the storage ring itself demands the lower frequencies I believe that the 4.2K system when

taken in toto will be at least as expensive and complex as a superfluid system at higher frequency. A definitive answer can probably be had only after large systems with both designs have been built and operated extensively. Another economic factor that is sometimes cited in favor of lower frequencies is the higher reputed efficiency of klystrons at lower frequencies. While there may be an effect here it is not large in the range of practical interest. Klystrons with efficiencies in excess of 60% have been built for the low UHF region but klystrons with similar efficiencies are now under development at 1000 MHz. I adopt the view, based somewhat on judgment and experience with systems with a range of frequencies, that the highest frequency allowed by the storage ring design will be the least costly. Unfortunately the science of storage ring design is not far enough advanced to allow a definitive answer to the question; given the desired energy, luminosity, and free space needed at the interaction region, what is the highest rf frequency allowed.

Today one can give only a partial answer and to do even that would require an extensive treatise on accelerator physics. Here I can give only an indication of the important considerations and outline the areas in which further work is required.

The most obvious consideration is one of aperture. Given the basic parameters I listed above, one can compute the required aperture by rather well established principles of storage ring design.^{4,5,6} For the class of storage rings we're considering, the results of the calculation range from 3 to 5 cm depending upon exact details. Clearly the wavelength of the rf should be greater than the aperture. From this consideration alone one might reason that a wavelength of 20 cm might be as small as one would want. The greater the wavelength, the more comfortable the situation.

Another important consideration has to do with stored energy. As the beam bunches pass through the cavity they extract energy from the fields therein. If the fraction of the energy extracted is too high, the matching of the generator to the cavity beam system becomes poor and overall energy efficiency suffers and moreover the cavity gradient seen by different parts of the beam can be different. This latter effect, if severe enough, can be deleterious to the dynamic stability of the beam. If the fraction is small enough, say 10 percent, then these effects are not very pronounced. As the rf frequency becomes higher, for a fixed accelerating field, the stored energy per cell decreases. For superconducting cavities the fields can economically be higher than in copper cavities so that from this point of view superconducting cavities could be used at higher frequencies than normal cavities. For the machines under consideration, the aperture requirement is slightly more restrictive on the wavelength than is the stored energy requirement, if superconducting cavities are used, so we will not delve into this consideration in any more detail.

Two other, interlinked, considerations of prime importance need to be taken into account in choosing the frequency. These are the frequency of energy oscillations and the bunch length. The frequency of the energy or synchrotron oscillations has in past designs usually been a very small fraction of the revolution frequency, .001 to .05 or so. (In the Cornell 12 GeV-synchrotron with an S-band superconducting acceleration section installed, successful operation at 0.5 was achieved but it is generally considered that storage ring operation puts on more stringent requirements than does synchrotron service.) In the extreme case in which the synchrotron oscillation frequency approaches the revolution frequency a dynamic instability, independent of beam current, can occur if the rf is not uniformly distributed around the ring.⁷

Since this will not be a case encountered in practice we need not consider it further. More generally, as the synchrotron oscillation frequency arises, the inherent coupling between the longitudinal energy or phase oscillations and the transverse betatron oscillations increases. The effect of this coupling is to add a new network of resonance lines, the so called synchrobetatron lines, to the structure and imperfection resonances with which the storage ring design has to deal. The practical results of such lines are a reduction in luminosity both through limitations in beam current or constriction of the "working space" for the beam and thereby a reduction in allowed charge density. Any mechanism which links the phase or energy of a particle with a transverse kick can in principle effect this unwanted coupling. Both coherent and incoherent coupling mechanisms are known. The mere existence of the accelerating system coupled with dispersion at the cavities - there always is some no matter how small - can do the job,⁸ as can the beam-beam interaction itself if the beams cross at a small angle or if there is dispersion at the crossing point.⁹ In addition parasitic modes in the accelerating cavities¹⁰ or other vacuum components can also provide strong coupling.¹¹ At the present time it is not within the power of accelerator theory to write a general prescription for the avoidance of deleterious effects of these couplings. Mute witness to the truth of this statement is born by the fact that all of the most recently built electron storage rings are hampered in one way or another by these synchrobetatron resonances. Expert judgment at this time holds that a synchrotron oscillation frequency in excess of 0.1 of the rotation frequency is already dangerously high. Both LEP¹² stage 1 and the Cornell 50 x 50 designs¹³ have a factor of approximately 0.15. The subject is under intense scrutiny and we may hope for significant theoretical advances in the next few years. This phase oscillation frequency depends on the rf frequency as $f_{rf}^{1/2}$ as well as on the energy and focussing strength of the ring. In LEP Stage 1 a Q_s of .15 corresponds to an

f_{rf} or 350 MHz whereas in the Cornell design $Q_s \sim .15$ at 1500 MHz. Thus the maximum allowed rf frequency is machine dependent. In general, as the size of the machine goes up, the rf frequency must come down such that the harmonic number does not exceed some maximum value. One may expect that the ultimate prescription which will give the maximum allowed harmonic number will also involve the bunch length, a quantity that also depends upon the rf frequency. The reason for the involvement of the bunch length has to do with the beam-environment interaction. This subject also is not yet well enough understood that rigorous design prescriptions can be written. At small current and fixed energy and focussing strength $\sigma_z = K\lambda^{1/2}$ the higher the frequency, the shorter the bunch length. This length depends upon the dynamic equilibrium between the synchrotron radiation damping and the excitation of the phase oscillations by quantum fluctuations in that radiation. Generally the shorter the bunch length - or alternatively the higher the peak currents - the larger are the beam induced fields in the irregular vacuum chamber components and cavities and the higher are the frequencies associated with these beam induced voltages. These beam induced electric and magnetic fields have three major effects: the bunches lose energy into parasitic cavity modes of the vacuum chamber, longitudinal and transverse instabilities of the beams can be excited and the synchrotron resonances can be aggravated.

The energy loss problems is fairly well understood and quantitative design calculations can be made. References 14, 15, 16, 17 will give access to the extensive literature on the subject. In cases of current interest with bunch lengths in the few centimeter region, the energy loss on a single pass through an rf accelerating cavity, $\sigma_z \ll \text{gap}$, is proportional to σ^{-1+3} . The dependence of loss on σ can be much more rapid for cases where $\sigma_z \sim \text{gap}$. At any rate one can now compute or measure losses on the bench. At a minimum, one arranges the design so that parasitic mode losses are small compared to the

synchrotron radiation losses, typically 10 percent or less in designs recently built or now under study in which rf frequencies from 350 to 1500 MHz are contemplated.

Instability criteria are likely to place more stringent requirements on the useable frequencies. There is an enormous literature on this subject. References, 18, 19, 20, 21, 22 give access to a large part of it. Instabilities, both longitudinal and transverse, can arise from both resonant and non-resonant interaction between the beam and the impedances presented to it by irregular vacuum chamber components and cavities in both fundamental accelerating modes, higher accelerating modes and deflection type modes. While there seems to be a basic understanding of the physical causes for the various instabilities, hardware design prescriptions for avoiding them are not well in hand.

Aggravation of the synchrotron resonances comes about when there is severe distortion of the accelerating potential versus tune due to heavy loading and higher mode excitation in the cavities, a problem that gets worse as the bunches (rf wavelengths) gets shorter. Access to the literature on potential well distortion and its effects on bunch shape can be had in references 23, 24. The basic mechanisms are two. Distortion of the restoring force for phase oscillations can generate rather high harmonics of the basic phase oscillation frequency and thereby reduce the potential operating space for the beams. Due to the natural energy spread in the beam, this potential distortion also spreads the phase oscillation frequencies so that parts of the beam may always be overlapping one of the dangerous resonances. At best this tends to dilute the beam phase space density, at worst the beam life can be shortened.

Again, in the areas of longitudinal and transverse instabilities and in the excitation of synchrotron resonances great progress is being made and one can be hopeful that the next generation of storage rings will be built on a more solid foundation than the last. One may expect that there will be downward pressure on the maximum allowed operating frequencies.

To summarize, the firmest criteria that we now have for choosing a suitable rf frequency are those of the aperture and highest synchrotron oscillation frequency allowed. In the future, criteria based on instability theory may well prove more stringent. At present, frequencies in the UHF through low L-band are favored for manufacturing reasons and because of the ready availability of rf power sources in these bands.

One final remark about choice of frequency: If one had any idea how to build lumped element, low frequency, accelerating structures, for $\beta = 1$ particles, that had anything like the shunt impedance and field capability of true microwave structures, there is no doubt that they would be vastly preferable to the systems now being contemplated. Bunch lengths could be many centimeters and storage ring design would be much simpler. Failing that we must strive to achieve a detailed understanding of the complex physics of bunches short compared to vacuum chamber dimensions.

Engineering Considerations for Superconducting Microwave Structures

My remarks will be based on the idea that useful superconducting structures for storage rings can be built at the present state of the art: accelerating fields of 3 to 5 MV/m and Q_0 of more than 10^9 . Exploitation of the theoretical potential of rf superconductivity is for the future and has been the subject of our earlier discussions.

Engineering of these structures must take into account the peculiar sensitivities of superconducting cavities, namely their poor ability to support high local heat loads and the very high inherent Q_0 's of all of the resonant modes. In the hostile environment of an accelerator combined with challenging cryogenic problems, compactness and economy and simplicity of engineering style will be of paramount importance.

Synchrotron Radiation Masking

In an accelerator where megawatts of synchrotron radiation power are sprayed onto the walls of the vacuum chamber, the cavity walls which can only sustain energy depositions of less than 1 watt/cm² must be unusually well masked from the bending magnets. In the very large radius machines with very long straight sections this should be achievable with careful engineering. Fig. 1 shows schematically how this might be done. The magnetic field should be tapered to the smallest feasible value at the ends of the acceleration straights to suppress the local bend radiation to the highest possible degree. A filter-absorber straight of a few meters will then be required to suppress the diffusion of radiation scattered out from the upstream magnets. Complete absorption will depend upon careful attention to the forward Bragg scattering and to the excitation of fluorescence in the material of the chamber wall. The filter section may well need to be a composite structure with graded Z beginning back in the last bend to minimize the amount of diffuse radiation propagating down the beam pipe. It may even be desirable to grade the Z longitudinally as well as radially to minimize the length of filter section needed.

One must also be aware that significant radiation can also emerge from the quadrupole magnets due to the slight bending of the beam particles therein. This radiation can be stronger than normal if there are orbit errors. The power radiated from the quadrupoles, one beam only, is given approximately by the formula

$$P_Q = 1.3 \times 10^3 i \times l E^2 \times g^2 \times \sigma^2 \quad (\text{watts})$$

i = beam current (amps)

l = magnetic length of quad. (meter)

E = beam energy (GeV)

g = quad. gradient (T/m)

σ = rms beam size (meter)

In the case that the beam is not centered in the quadrupole the extra power radiated can be estimated by substituting the orbit displacement for sigma in the formula. In typical designs the radiated power will be a few tens of watts. The radiation is emitted at very small angles to the axis if the beam is well aligned

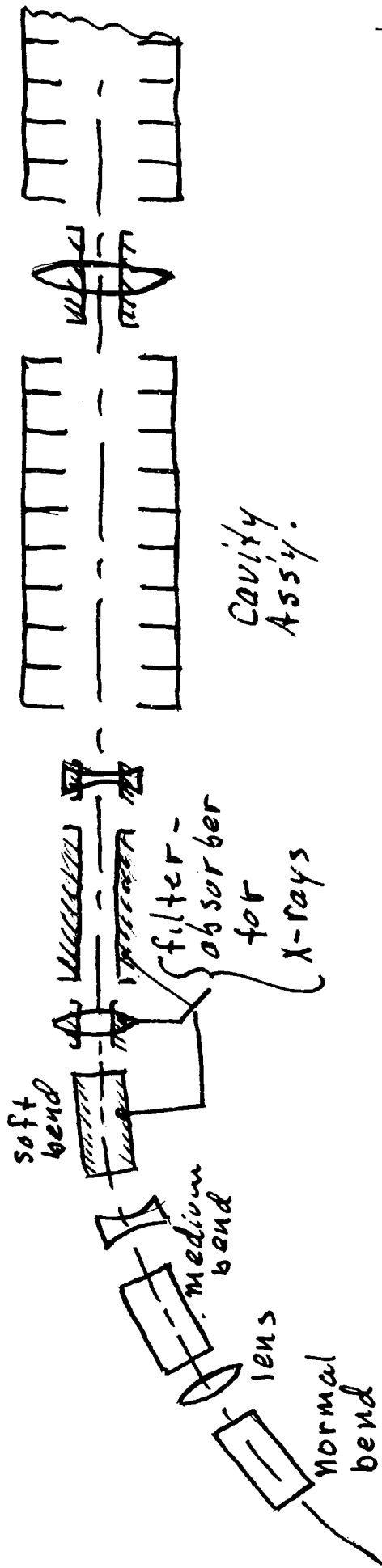


FIG 1.

and will travel several hundreds of meters before striking the vacuum chamber wall. Typical orbit errors may cause emission at angles of 10^{-4} radian, allowing the radiation to strike a few hundred meters away from the source if apertures are a few centimeters.

Perhaps more important than the steady synchrotron radiation is the possibility of a beam dump into the cavity. Stored energies in the beams will be in the range 10 to 100 kJ, more than enough to do permanent damage to the cavities. Heavy metal showering masks combined with a beam abort system that triggers on magnet failures will probably be necessary for guaranteed cavity protection. In any event it will be wise to make the cavity aperture somewhat larger than the apertures of the quadrupoles in the acceleration straights with the quadrupole chambers designed to suppress scattered X radiation and to shower high energy particles effectively. To give examples, this criterion would demand that the LEP cavities have an aperture of 8 cm with 3 cm being required for the Cornell 50 x 50 design. All in all it appears that careful engineering will solve the radiation masking problem for designs now under consideration.

Higher Mode Coupling

The primary *raison d'être* for the superconducting cavities is their high Q_0 at some fundamental frequency f_{rf} , which is arranged to be a harmonic of the beam revolution frequency, f_0 . This mode is driven by the transmitter which supplies energy to the beam. As is only too well known, any structure that can support a useful accelerating mode inevitably supports many tens of other modes which can in principle interact with the beam and, moreover, which have Q_0 's comparable with that of the fundamental. One might imagine two approaches to coping with these other modes. First one might hope to tune the resonant frequencies of all of the modes which can interact with the beam such that they did not coincide with any possible resonant frequency

of the beam. Second, one might provide heavy damping for the modes so that resonant build-up would be impossible. Both approaches would be difficult, the first may, in some cases, be impossible or, at best result in severe restriction of the possible operating points for the accelerator tunes. If one adopts the first, or detuning approach, there are at least three known classes of frequencies to avoid: 1. $f_m = h f_0$; 2. $f_m = h f_0 + k f_s$; 3. $f_m = (h + Q_{H,V}) f_0$ where f_m is the frequency of any mode which can interact with the beam, f_0 is the revolution frequency of the beam, f_s is the synchrotron oscillation frequency and $Q_{H,V}$ are the betatron tunes of the accelerator, having non-integral parts that can vary from 0 to 1. f_s may vary, in practical cases, over the range .04 to perhaps 0.2. h and k are integers. These families form a rather dense comb within the band of important cavity frequencies. In cases under consideration that band will be 1 to 4 GHz wide while the spacings of the family $h f_0$, for example, will be 10 kHz to 50 kHz.

Coincidence between one or more of the cavity modes and one of the families 1, 2 or 3 can have two results. The first and most obvious is that beam kinetic energy is converted to energy in the cavity field which must be dissipated by the refrigerator. If the mode(s) in question are without any coupling to the outside, then the beam excited field will unavoidably lead to breakdown of the cavity by multipactoring or a thermal effect. The second and more complex class of effects are the beam-cavity instabilities. If one or more of certain of the CHOM (cavity higher order modes), those having a transverse gradient in their longitudinal electric fields, are close to a member of family (1), ($h f_0$), than incoherent synchrotron oscillations¹⁰ of the beam are excited. These oscillations dilute the beam phase space at best and shorten the beam life at worst. If one or more of the CHOM is close to a member of family (2), ($h f_0 + k f_s$),

then a rich family of longitudinal beam instabilities can be driven,²⁵ also leading to beam loss. If one or more of the CHQM is close to a member of family (3), $(h = Q_{H,V}) \cdot f_0$, another popular class of transverse beam instabilities can be driven.²²

The members of family 1 have, at least, the virtue of being known in advance and of remaining fixed throughout the life of the accelerator. Families 2 and 3, per experience at the most successful e^+e^- storage rings built to date, will be changed in frequency during operation to accommodate special injection problems, various energies and the vagaries of the beam-beam interaction. Thus, no fixed tuning of the CHQM can allow use of the full tune space for synchrotron and betatron operating points.

For a crude quantitative understanding of the seriousness of these modes one might note that in CESR, with only 14 cavity cells at least 7 modes were measured which if coincident with one of the 3 families of frequencies mentioned above would result in severe beam blow up or beam loss unless strong damping is applied. For example, the shunt impedances of these modes, undampened, are up to 30 times higher than necessary to destroy a few milliampere beam. The widths of these resonances, undamped, are tens of kilohertz. Clearly the situation in which there are hundreds or thousands of cells, with revolution harmonics separated by a few tens of kilohertz will be made more difficult.

Figure 2 summarizes what I have been saying. The details are quite complex and will depend upon individual ring designs, energies and beam currents. Nevertheless, there will always be several frequencies in between each revolution harmonic which must be avoided. These dangerous spectral lines can move over the full spacing between the revolution harmonics as the betatron and synchrotron tunes change.

f_0 = Beam Revolution Frequency
 h = integer

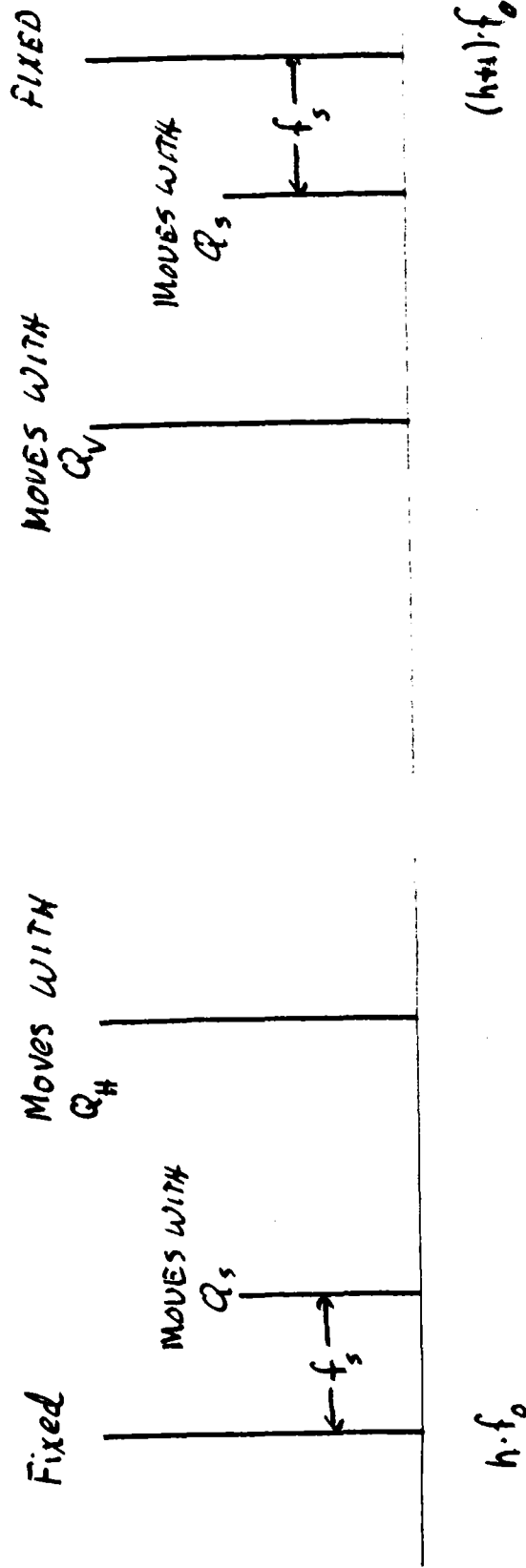


FIG. 2

Some of the frequencies to be avoided by detuning of the cavity higher mode spectrum.

One final remark in this regard. Even if one chooses to fix the storage ring operating point and to avoid unwanted coincidences between cavity higher mode resonances and beam resonances by individual cavity tuning, the task may be overwhelming. Perturbation tuning of these cavity frequencies is not an orthogonal process as any perturbation of the cavity shape will change the frequencies of many modes simultaneously. Even if this extreme multidimensional problem has a solution, which in some cases it may not, the concomitant distortions of the surface fields may engender unwanted one point multipactoring.

Adopting for the moment the view that complete flexibility in the machine optics is important, we must conclude that the only practical approach to the higher mode problem is heavy damping. While this is far from easy, preliminary measurements indicate that with hard work sufficient damping for a sufficient number of modes can be accomplished.

Having made the decision to damp the higher modes one must do a good job of it. It turns out that the coupling strength criterion for removal of higher mode power from the helium temperature environment is probably less stringent than that for the suppression of beam-cavity instabilities. In designs presently under study, the higher mode power deposition is of the order of kilowatts per meter of structure. If room temperature equivalent coupling factors of $\beta \approx 1$ for all of the important modes that are shock excited by the beam, then, with an improvement factor of about 10^5 due to the superconductivity, we would sustain losses into the helium of tens of milliwatts per meter only.

Coupling factors of 0.1 of that would still be quite acceptable.

The couplings required for the suppression of instabilities can be computed only from detailed measurements on the rf structure combined with details of the accelerator and beam properties. An upper limit can, however, be readily estimated. If the coupling to the important modes is such that the field decay time is of the order of the time between bunch transits of the cavity, then no resonant buildup of the harmful fields can occur. For optimally placed cavities the time between transits would be one half the bunch spacing in a single beam. For example, in the machine being studied at Cornell, the time available for damping is 4.5 microsec.; in LEP it would be about 12 microsec.. Since the unwanted modes begin at frequencies close to that of the fundamental, we can get a lower limit on the required loaded Q from the relation

$$Q_L \sim \frac{\omega_{rf} \cdot \tau_{spacing}}{2}$$

For the Cornell case then $Q_L \sim \frac{2\pi \times 1.5 \times 10^9 \times 4.5 \times 10^{-6}}{2} \sim 2.1 \times 10^4$

Since the room temperature equivalent Q_0 is about 15000 in the Cornell case, a room temperature equivalent $\beta \sim 1$ would give a Q_L of 7×10^3 , affording almost 3 damping times between bunch passages. Thus $\beta \sim 1/3$ would suffice to suppress any resonant field buildup. An identical argument could be applied to LEP with similar conclusions. Detailed studies show that one does not need this coupling in many cases.²⁷ Detailed measurements of a 5 cell model of a possible structure for the Cornell 50 x 50 machine show it is possible to have room temperature equivalent coupling factors in excess of 1 for almost all of the 30 higher modes so far studied. One transverse slot and one longitudinal slot coupler of modest size for each 5 cell group plus the fundamental coupler for each group of 10 cells were employed. Details of the results are given in refs. 3 and 27. Fig. 3 is an artists view of the coupling scheme. We have not made these measurements for a cylindrical structure but a similar scheme might work there provided that the beam line coupling for the important higher modes is good. For modes with

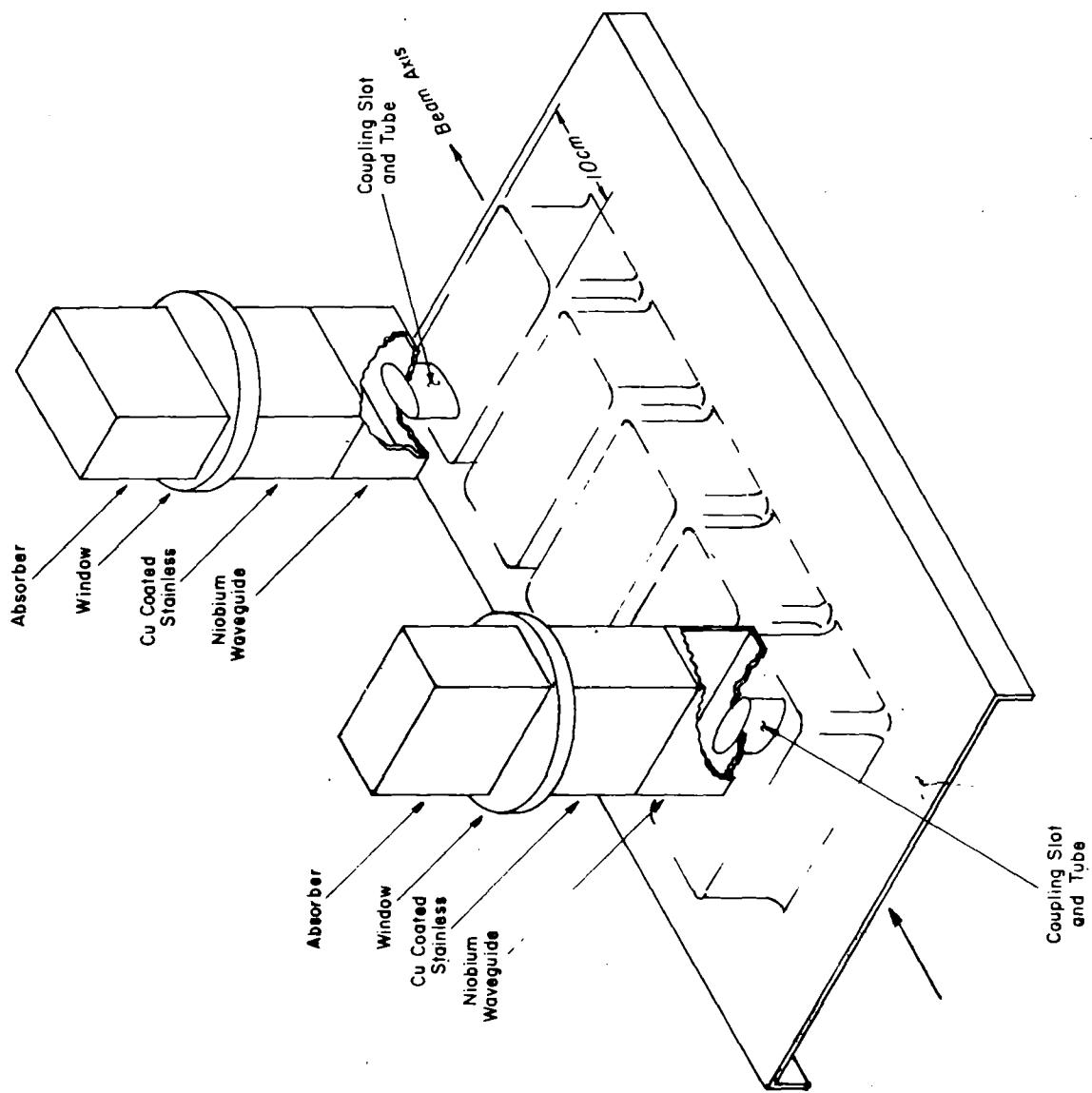
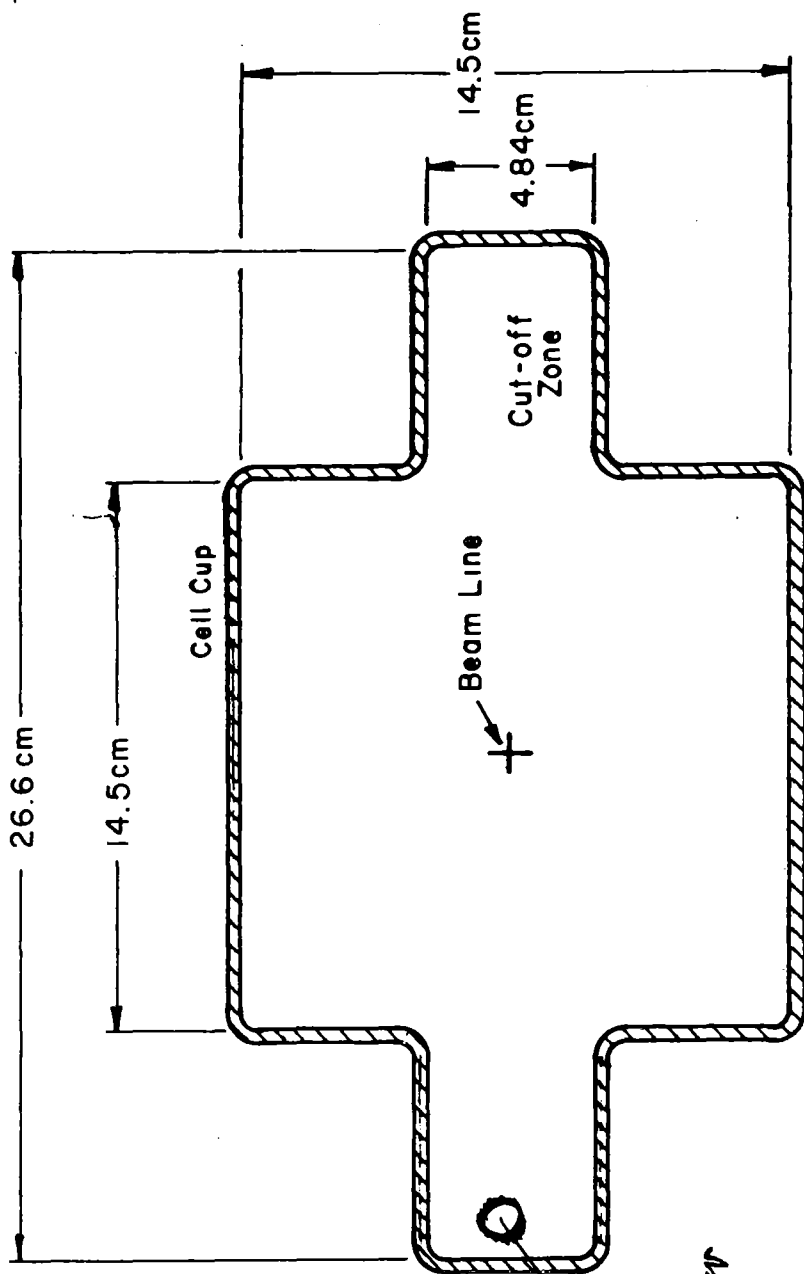


Figure 3



absorber for
 $f_m > 2f_{fund}$

Figure 4

frequencies much in excess of twice the fundamental frequency, no evaluation has yet been made experimentally. The couplers already present will still be effective to some degree. If necessary we plan to put nitrogen cooled absorbers into the cut off zone to the side of the main cavity chambers as indicated in Fig. 4.

Materials and Appropriate Cavity Forms

I shall assume that for the present materials other than niobium are out of the question so that operation at greater than 4.4 K is not under consideration.

A most important question for the designer of superconducting storage cavities has to do with the basic geometry. Should the cavities be cylindrically symmetric or could it be advantageous to make them with a rectangular geometry? Should the accelerator be an array of individual cavities isolated from one another along the beam line or should they be multicell structures coupled on the beam line. At this time I do not believe it possible to give a definitive answer to even these most basic of questions. Each form of cavity has its advantages and disadvantages the relative values of which are hard to quantify properly. Perhaps we should start by describing what we want. We need the simplest possible structure with minimum number of current carrying welds, which can support average accelerating fields of between 3 and 5 MV/m without significant multipactoring, maintain and average $Q_0 > 10^9$ while allowing removal of higher mode energy to a high temperature sink with minimum number of room temperature penetrations. Table 2 is a matrix which displays eight basic design decisions that have to be made. Figs. 5 and 6 are sketches showing extreme cases. If it can be made to work a multicell structure with off line higher mode coupling is the most economical since the fewest coupling devices are necessary. It appears that multicell rectangular cavity assemblies can be protected against multipactoring with grooves. Experiments with S-band models give hope that the offline higher mode coupling will work without deleterious effect on the Q_0 and multipactoring performance. The primary mechanical disadvantage of the rectangular structure is the large number

Table 2

	single cell	multi-cell	off-line higher mode coupling	on-line higher mode coupling
cylindrical geometry				
rectangular geometry				

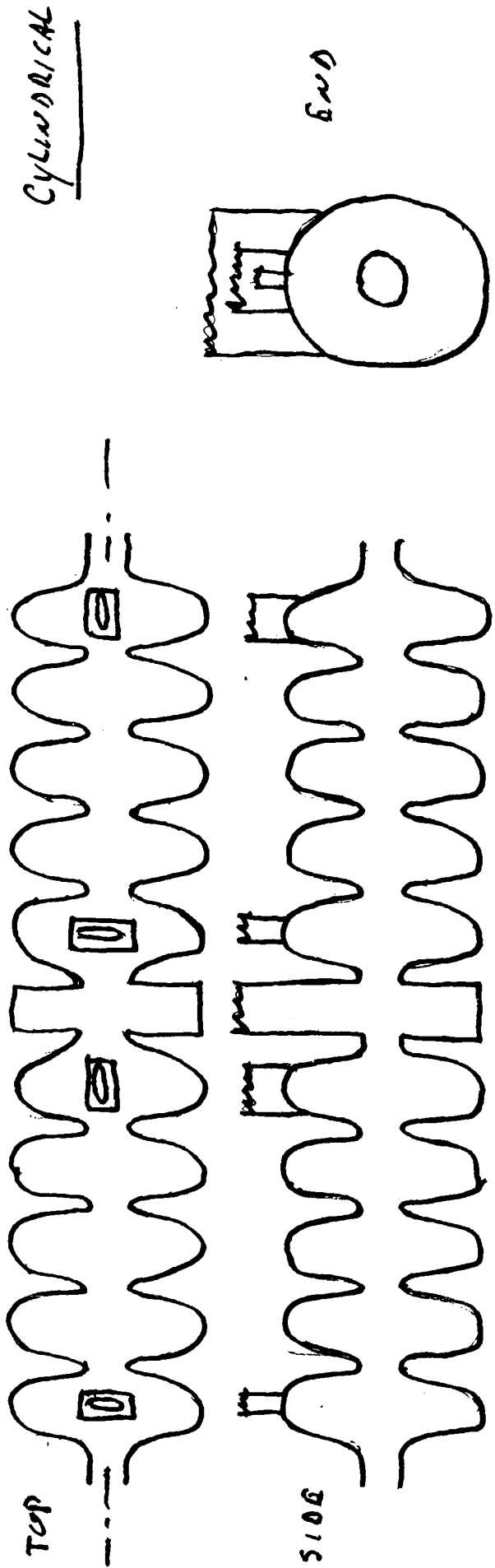
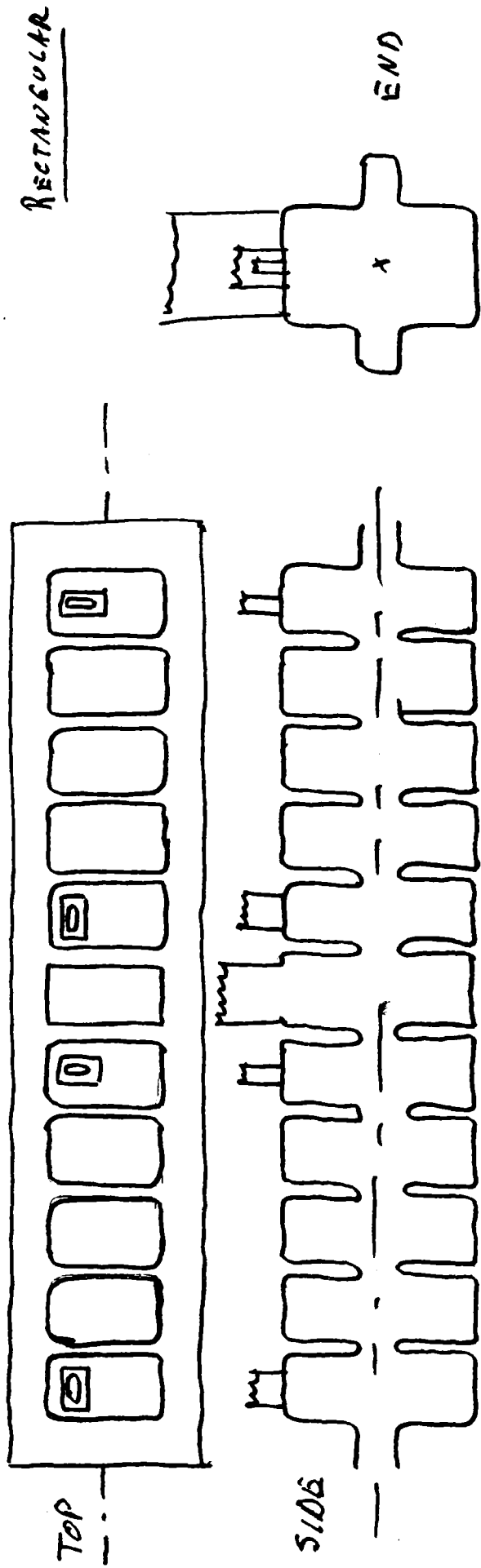


FIG 5

SINGLE CELL
ARRAY WITH
ON-LINE HIGHER
MODE ABSORPTION
FOR $f_m > 2f_0$
300MHz f_0

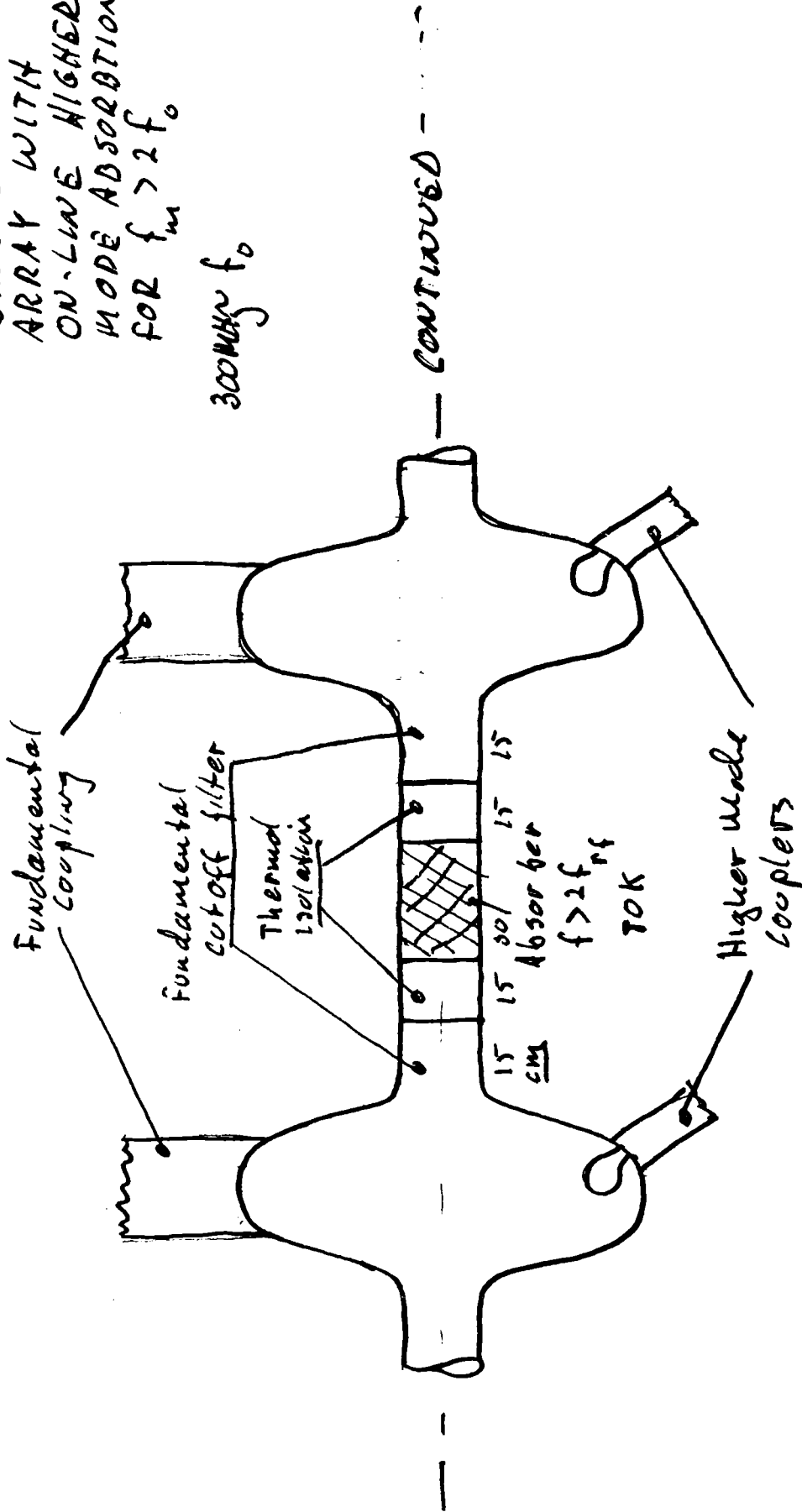


FIG. 6

of welds required by present technique and the rather broad, flat expanses which require bracing against pressure change deflection. On the plus side, all of the current carrying welds are made on the side carrying the current so that all surfaces can be protected from weld splatter and all welds can be inspected and polished before losing access to them when the cavity is sealed by a non-current carrying joint. Perhaps multiple cups can be drawn from the same piece of metal making the construction at least partially seamless. That will be very difficult, however. Figure 7 is an artists view of what a complete accelerator module based on the rectangular geometry might look like. In closing the discussion of the rectangular geometry I should point out a remaining doubt about its ultimate utility. Hand in hand with a straight line rectangular geometry goes a transverse gradient in the accelerating field which could have a deleterious affect on beam life through strong excitation of synchrotron lines. We are now examining this question with care. If the effects turn out to be serious we may be able to retrieve the situation by introducing a slight curvature into the surfaces perpendicular to the beam line.

The only really long multicell structures at the lower frequencies that we have extensive experience with are the Karlsruhe separators and the HEPL L-band accelerator structures. Being an accelerator structure, the HEPL construction is probably closest to being a prototype for a cylindrical storage ring cavity assembly. As that design is plagued with multipactoring it cannot be taken over as is. Perhaps application of the spherical shape²⁸ or grooving will ameliorate this problem. The higher mode couplers also would need beefing up to take care of the higher power involved in the storage ring case. Perhaps the most attractive thing about cylindrical geometry for multicells of spherical shape is the very real possibility of producing them by true mass production methods similar to the making of bellows from seamless tubing thus ridding us from current carrying welds in grand style.

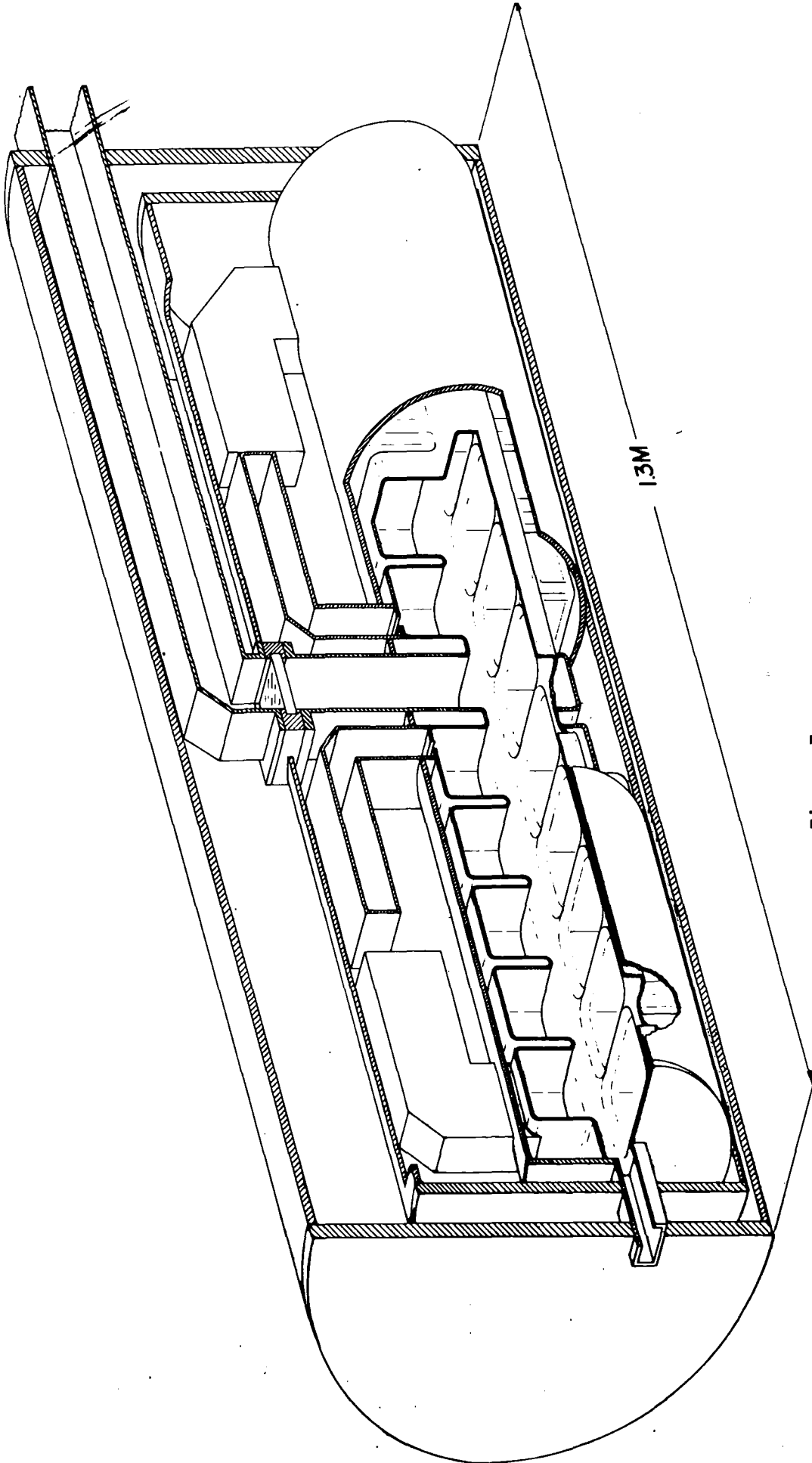


Figure 7

In the case of either rectangular or cylindrical geometry for multicell structures, past experience makes it clear that they need to be built in easily rf tested modules which can be scrapped cheaply if they do not perform properly.

The ultimate in small modules is the assemblage of more or less independent single cells. They have the advantage of easy testability and relatively easy handling. It should be possible to build the main body without current carrying welds by a cold forming technique. One also believes that one now knows how to make low frequency cavities free of multipactoring by using the spherical shape although this must be demonstrated in the presence of offline couplers. Obviously this approach multiplies the number of couplers in the extreme. In a single cell case one is tempted to think of on line absorption of higher mode power for frequencies above twice the fundamental. This would allow one to use the cut off beam pipe itself as the rejection filter for the fundamental. At first blush, however, this appears to be inordinately costly in space along the beam line as indicated in Fig. 6. All in all, I should say that we would have to have been rather badly defeated on the multicell front before retreating to a single cell solution because of the immense cost of that approach.

It is clear that we are just learning to take our first baby steps in the engineering of large assemblies of superconducting cavities for storage ring service. The most basic questions about the cavity design haven't been answered in a hard way yet. The next level of questions having to do with the coupling of megawatts into the helium temperature environment, of the cryostat and coolant flow problems and of tuning and control have barely been scratched. In the end we will only be successful if we can achieve an elegantly simple design, thereby assuring high manufacturing yield and operating reliability far beyond that achieved to date.

Acknowledgements

It is a pleasure to acknowledge that most of what I've learned of this subject has been taught to me by colleagues with whom I've worked over the past few years: Joe Kirchgessner, Peter Kneisel, Hasan Padamsee, Larry Phillips, Dieter Proch, Dave Ritson, Bob Siemann and particularly, Ron Sundelin. Errors herein are all my own.

References

1. D. Ritson, M. Tigner, CLNS-406 Cornell Univ. (1975)
2. M. Tigner, IEEE Trans, Mag 15, 15 (1979)
3. Design Study Proposal for High Energy Electron Positron Collider CLNS 80/456 Cornell University (1980)
4. M. Sands, The Physics of Electron Storage Rings, SLAC-121 Stanford Linear Accelerator Center, (1970)
5. E. Keil, Perspectives in Colliding Beams, IXth International Conference on High Energy Accelerators, Stanford (1974)
6. B. Richter, NIM 136, 47 (1976)
7. See for example A. Piwinski, NIM 72, 79-81 (1969)
8. See for example A. Piwinski and A. Wrulich, DESY 76/07 DESY (1976)
9. See for example A. Piwinski, DESY 77/18 DESY (1977)
10. See for example R. Sundelin IEEE Transactions NS-26, 3 (1979)
11. SPEAR Group, IEEE Trans. NS-22, 3 1366 (1975)
12. LEP Design Study, CERN/ISR-LEP/79-37
13. Op. Cit. 3
14. Op. Cit. 12, p. 63
15. T. Weiland, CERN/ISR-TH/80-07 (1980)
16. M. Sands, J. Rees, PEP-95, Stanford (1974)
17. M. Billing et al. IEEE Trans. NS-26, 3 (1979)
18. C. Pellegrini and M. Sands, Phenomenological Analysis of Current Limits in Storage Rings, to be published in Nuclear Instruments and Methods,
19. E. Messerschmidt and M. Month, NIM, 136, 1, 1976
20. C. Pellegrini, Nuovo Cimento 64A, 447, 1969
21. R. D. Kohaupt, DESY H1-74/2 and DESY H1-73/1
22. F. Sacherer, IEEE, NS-20, 3 25, 1973
23. E. Keil, PEP-126, Stanford, 1975
24. Op. Cit. 12, p. 62

25. Theoretical Aspects of the Behavior of Beams, etc. CERN 77-13 (1977)
p. 139 ff
26. A. Hutton LEP Note 208
27. J. Kirchgessner et al, to be published in the proceedings of the 1980
International Accelerator Conference
28. See for example Chiaveri et al private communication

ROUND TABLE DISCUSSION: CONCLUSION

Citron (Karlsruhe) as chairman of the final round table discussion asked all speakers of the workshop to give a short statement.

Tigner (Cornell) explained the following foils:

S u m m a r y

1. If we can get 3 MV/m, $Q_o > 10^9$
can cut e^+e^- -storage ring cost $\div 2$
2. Desire $f < 100$ MHz
 - dont know how to do
 - keep f as low as possible.Max. f allowed depends in details on structure design parameters.
Complex physics problems can they be solved in 2 years ??
3. HOM coupling out crucial if present understanding of accelerator physics correct.
4. Multicell (< 10 cell/unit) seems most desirable from cost view seems possible at moment.
5. Many unanswered accelerator physics problems (bunch-length \leftrightarrow instabilities, max. number of cavities allowed).
Engineering problems remain:
(cavity shape, surface treatment, couplers).
Outlook ?
Fantastic !!

Piel (Wuppertal) agreed with these statements and in addition pointed out that multipacting problems also occurred with the long Wuppertal structures. Lyneis (HEPL) emphasized more the problems of electron loading. Septier (Orsay) explained the following foils:

SURFACE STUDIES Summary by Septier

I. S U R F A C E P R O P E R T I E S

- 1. - Ion processing:
 - mechanisms $\begin{cases} \rightarrow \text{desorbed species} \\ \rightarrow \text{surface modifications} \end{cases}$
 - influence on $R_s, E_p, H_p \dots$
 - influence on emissions

 - 2. - Structure and composition of surface layer
 - various oxides
 - adsorbates
 - hydrocarbons
 - (lees, iets,

 - 3. - Conduction through surface layer
 - localized states
 - (tunneling exo-electrons ..)
 - influence of adsorbates
 - work function, charging
 - photo- and thermo currents

 - 4. - Identification of "bad spots"
- Need for fundamental research !

II. E M I S S I O N

- 1. - Field emission from real surfaces:
 - theory $(\beta^*, \phi^* \dots)$
 - resonant tunneling
 - influence of adsorbates (*)
 - practical means fo lowering f.e.
 - ↓
 - influence on $R_s \dots E_p$

- 2. - Secondary emission
 - same parameters (*)
 - se + Malter effects
 - (charged layer)
 - lowering of δ :
 - practical methods
 - ↓
 - R_s, E_p
 - (thinfilms - ion processing)

- 3. - Identification of "bad spots"
 - (induced defects)

The discussion concentrated then on field emission. There are indications that field emitting sources are just created during rf operation of a superconducting cavity at high fields, even if one starts with a very clean surface (Piel). The field emitted electrons then can cause surface damage which in turn leads to a hot spot, which causes breakdown even at a lower field level. Padamsee (Cornell) summarized the breakdown phenomena as follow:

1) There is strong evidence that Thermal instabilities is the major driving force for breakdown below 500 Gauss, at defects. Two types of evidence support this

A Heating is observed below breakdown when looked for

B Mode mixing experiments show

$$H_1^2 + H_2^2 = \text{constant and } \underline{\text{not}}$$

$$H_1 + H_2 = \text{constant.}$$

We intend to continue both A + B types of measurements.

2) If 1 is true then all heat transfer parameters are important K, λ_x , film boiling limits.

3) Very little is known about defects.

4) An alternative approach to elimination of defects that cannot be gotten rid of by chemistry etc. is to try to stabilize the defect by increasing $K(T)$. This may also allow us to tolerate more heating due to electron loading.

LIST OF PARTICIPANTS

1.	G. Arnolds	GHS	Wuppertal
2.	B. Aune	CEN	Saclay
3.	W. Bauer	KfK	Karlsruhe
4.	F. Baumann	Uni	Karlsruhe
5.	M. Baye	IEF	Orsay
6.	R. Blaschke	GHS	Wuppertal
7.	A. Brandelik	KfK	Karlsruhe
8.	P. Breitfeld	KfK	Karlsruhe
9.	W. Buckel	Uni	Karlsruhe
10.	R. Calder	CERN	ISR
11.	G. Cavallari	CERN	EF
12.	J. Chelius	Kawecki	Lakewood
13.	E. Chiaveri	CERN	EF
14.	A. Citron	KfK	Karlsruhe
15.	M. Dwersteg	DESY	Hamburg
16.	D. Farkas	SLAC	Stanford
17.	O. Fischer	Uni	Genf
18.	J. Fouan	CEN	Saclay
19.	H. Gerke	DESY	Hamburg
20.	G. Geschonke	CERN	
21.	W. Giebeler	Interatom	Bergisch Gladbach
22.	H.D. Graef	GSI	Pfungstadt
23.	J. Griffin	Fermi-Lab.	Batavia
24.	Th. Grundey	GHS	Wuppertal
25.	E. Haebel	CERN	EF
26.	H. Hahn	BNL	Brookhaven
27.	J. Halbritter	KfK	Karlsruhe
28.	J. Hasse	Uni	Karlsruhe
29.	H. Heinrichs	CERN/Wuppertal	
30.	W. Herz	KfK	Karlsruhe
31.	B Hillenbrand	FL Siemens,	Erlangen
32.	N. Hilleret	CERN	ISR
33.	H. Hogg	SLAC	Stanford
34.	H. Hübner	KfK	Karlsruhe
35.	S. Isagawa	CERN	
36.	U. Klein	GHS	Wuppertal

37.	P. Kneisel	KfK	Karlsruhe
38.	Y. Kojima	KEK	Japan
39.	W. Krause	FL Siemens	Erlangen
40.	M. Kuntze	KfK	Karlsruhe
41.	R.M. Laszewski	Univ.	Illinois
42.	R. Lehm	KfK	Karlsruhe
43.	W. Lehmann	KfK	Karlsruhe
44.	H. Lengeler	CERN	EF
45.	G. Loew	SLAC	Stanford
46.	Cl. Lyneis	HEPL	Stanford
47.	A. Mathewson	CERN	ISR
48.	R. Meyer	GHS	Wuppertal
49.	G. Müller	GHS	Wuppertal
50.	R. Delesclefs	Uni	Genf
51.	V. Nguyen Tuong	IEF	Orsay
52.	Sh. Nogushi	Uni INS	Tokyo
53.	H. Padamsee	Univ.	Cornell
54.	C. Pagani	Univ.	Milano
55.	A. Palussek	Interatom	Bergisch Gladbach
56.	R. Parodi	INFN	Genoa
57.	C. Passow	KfK	Karlsruhe
58.	J. Peters	DESY	Hamburg
59.	M. Pham Tu	IEF	Orsay
60.	A. Philipp	KfK	Karlsruhe
61.	H. Piel	GHS	Wuppertal
62.	J. Sayag	IEF	Orsay
63.	F. Schürerer	KfK	Karlsruhe
64.	A. Septier	IEK	Orsay
65.	R. Sundelin	Univ.	Cornell
66.	L. Szecsi	KfK	Karlsruhe
67.	M. Tigner	Univ.	Cornell
68.	J. Vetter	KfK	Karlsruhe
69.	R. Vincon	KfK	Karlsruhe
70.	L. Wartskj	IEF	Orsay
71.	W. Weingarten	GHS	Wuppertal

SUMMARY OF THE WORKSHOP ON RF-SUPERCONDUCTIVITY AT KARLSRUHE, JULY 2-4, 1980

A. Citron

Kernforschungszentrum Karlsruhe, Institut für Kernphysik, P.B. 3640, 7500 Karlsruhe,
Federal Republic of Germany.

ABSTRACT

A workshop on rf superconductivity was held in Karlsruhe on July 2-4, 1980. A summary of the rapporteur talks, the round tables and the discussion is given.

INTRODUCTION

I would like to report on the workshop that was held last week at the Kernforschungszentrum Karlsruhe.

Table 1 shows the programm. There were rapporteur talks and round tables only, no contributed papers.

Table 1

The Organizing Committee:	Kernforschungszentrum
A. Citron (Karlsruhe)	Karlsruhe
H. Lengeler (CERN)	
H. Piel (Wuppertal)	
A. Septier (Orsay)	

WORKSHOP ON RF SUPERCONDUCTIVITY
July 2-4, 1980

1. Compilation of experimental results and operating devices	Citron (Karlsruhe)
2. Surface preparation Nb	Kneisel (Karlsruhe)
3. Surface preparation Nb ₃ Sn	Hillenbrand (Siemens)
4. Surface studies	Septier (Orsay)
5. Diagnostic methods and identification of phenomena	Piel (Wuppertal)
6. Electron loading (description and cures)	Lyneis (HEPL)
7. Theory	Halbritter (Karlsruhe)
8. Heat transfer	Padamsee (Cornell)

9. Round table discussion: "What to do next?"	Loew (SLAC)
10. Discussion on Nb and on surface physics	Septier (Orsay)
11. Design of superconducting structures	Lengeler (CERN)
12. Additional requirements for low β -structures	Kuntze (Karlsruhe)
13. Joints, couplers, tuners	Sundelin (Cornell)
14. Fabrication of Nb cavities	Bauer (Karlsruhe)
15. Special problems for storage rings (higher order modes, multicells etc.)	Tigner (Cornell)
16. Round table discussion: conclusion	Citron (Karlsruhe)

Table 2 shows the institutions that were represented.

Table 2

Institutions represented:

1. BNL, USA	12. Cornell University, USA
2. CERN, Geneva	13. University of Geneva
3. CEN, Saclay	14. University of Genoa
4. DESY, Hamburg	15. University of Illinois, Urbana, USA
5. FNAL, USA	16. University of Karlsruhe
6. GSI, Darmstadt	17. University of Milano
7. HEPL, Stanford, USA	18. University of Paris, Orsay
8. KEK, Japan	19. University of Wuppertal
9. KfK, Karlsruhe	20. Interatom (manufacturer of structures)
10. SIEMENS Fl., Erlangen	21. Kawecki (suppliers of niobium)
11. SLAC, Stanford, USA	

At the end of the workshop, all rapporteurs gave a summary of their talk, which was then discussed. I shall not, however, just give you the sum of these summaries, but shall attempt to stress those points of interest to a wider audience. I shall restrict myself to that part of the contributions devoted to high β -structures in line with the scope of the present conference.

The workshop started by a survey of the state of the art. Table 3 lists the laborato-

ries that were included in this survey.

Table 3

LABORATORIES REPORTED UPON
AND OPERATING DEVICES

	OBJECT
<u>U.S.A.</u>	
HEPL	X,S,L-BAND RESONATORS, RECYCLOTRON URBANA MICROTRON
SLAC	X-BAND RESONATOR
CORNELL	MUFFIN-TIN STRUCTURE IN X,S AND L-BAND, SYNCHROTRON
ANL	SPLIT-RING STRUCTURE
CAL TECH./ STONY BROOK	SPLIT-RING STRUCTURE IN Pb
BNL	X-BAND DEFLECTOR, S-BAND-RESONATOR
<u>JAPAN</u> KEK	C-BAND RESONATOR (SPHERICAL AND CYLINDRICAL)
<u>ISRAEL</u> W.I.	400 MHZ REENRANT RES. (FROM HEPL)
<u>EUROPE</u>	
SIEMENS GENOA	X-BAND RESONATORS C-BAND SPHERICAL
CERN	S-BAND CYL. AND SPHERICAL, 500 MHZ SPH. RES.
WUPPERTAL	X-BAND ACCELERATOR
KFK	S-BAND RESONATORS S-BAND SEPARATOR (CERN) 90-MHZ ACCELERATOR 100-MHZ HELIX RESONATORS (CEA) 700-MHZ RESONATOR 500-MHZ RESONATOR

At the same time the table presents those devices that have operated for an extended period, some for several years. It is important to know that superconducting devices can be operated without loss of performance for a long time. This alleviates the fears often expressed that superconducting devices might need frequent reprocessing.

Superconducting cavities are characterized by two quantities: the Q-value and the limiting field.

The Q-values are generally in the range about 10^9 . The custom to transform the Q-value into a surface resistance - generally between 100 and 200 nΩ - is not too meaningful, because the geometry factors take into account only losses connected with the magnetic, not with the electric field, and because the source of loss is, like the source of field limitation, often concentrated rather than distributed.

RF losses are not considered today to be the main concern. They enforce, however, the costly operation at 1.8 K for all devices operated above 1 GHz. Below this frequency, the

residual resistance that is temperature independent dominates. If Nb₃Sn with its higher critical temperature could be used, then also the high frequency devices could be operated at 4.2 K. Unfortunately, Nb₃Sn cavities are not yet competitive with niobium ones, although several laboratories work on them.

The use of lead is restricted today to one low β-application and was not discussed at the workshop.

For the discussion of limiting fields, the field distribution in the cavity is important. In the high-β-range, only three types of cavities were considered, namely: cylindrical, spherical and muffin-tin. Their field distributions are characterized by the figures given in table 4 and are seen not to scatter very widely. Fig. 1 shows the peak magnetic field as a function of frequency. Three types of structures are included, namely: labora-

tory resonators (TM modes only), accelerating and deflecting structures. Most accelerating and deflecting structures have single and multiple cell versions. It is seen that the peak field usually decreases with increasing cell number. In this connection, it is good to remember, however, that peak fields are not measured directly, but calculated on the basis of a theoretical field distribution. A reason for the decrease in peak field can lie in the fact that for long structures the fields are not ideal, but show unflatness due to fabrication tolerances. This hypothesis is confirmed in the case of a Wuppertal structure, where after careful chemical tuning, the 65 cell-structure reached the performance of the 3-cell-structure. Thus there is hope to raise some of the lower field values for the longer structures.

Table 4

HIGH β-STRUCTURES

FREQUENCY RANGE 0.5 ÷ 10 GHz

PARAMETERS OF FIELD DISTRIBUTION:

$$E_p/E_{ACC} = 2 \div 4,5$$

$$B_p c/E_{ACC} = 1 \div 2$$

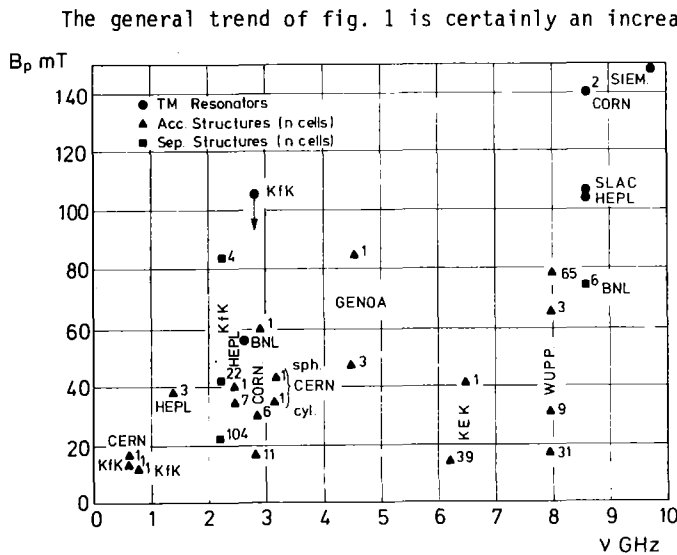
OR:

$$B_p/E_{ACC} = 3 \div 6 \text{ mT}\cdot\text{m/MV}$$

$$B_p c/E_p = 0.45 \div 0.77$$

OR:

$$B_p/E_p = 1.5 \div 2.6 \text{ mT}\cdot\text{m/MV}$$



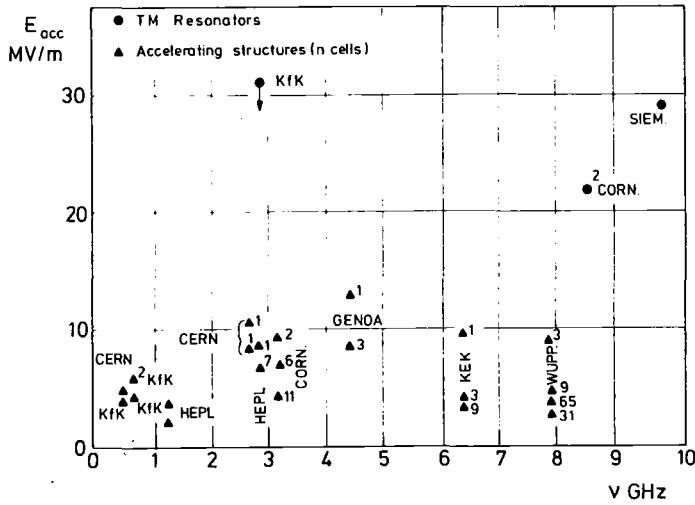
The general trend of fig. 1 is certainly an increase of B_p with frequency. In terms of magnetic field, this

Fig.1: Peak magnetic surface field reached versus frequency. In S-band, points are spread and some (e.g. ORSAY) omitted.

can only be understood by an increase of probability to find a defect with increasing structure dimensions, thus with decreasing frequency. All B_p lie

considerably below the critical field $B_c \sim 200$ mT.

The peak electric field versus frequency shows the same trend. The accelerating field is shown in fig. 2. Here at very high frequencies we find lower field values, because due to



tolerance and aperture problems the ratio of

Fig. 2: Peak accelerating field reached versus frequency.

accelerating field to peak fields decreases ($\pi/2$ mode operation). Generally fields around 3 MV/m can be reached at all frequencies. At present, C-band seems favoured for higher fields.

On the nature of the limitation it can be said that

at lower frequencies, the limitations are usually connected with electron loading, whereas at high frequencies so-called magnetic breakdown, usually blamed on "bad spots", occurs. Such "bad spots", if not related to electron loading, are usually described as defects with a locally lowered B_c . Padamsee emphasized a different aspect. Small normal conducting region can exist. Depending on their size, such regions could at zero-field be superconducting by proximity effect, but would soon turn normal as field is applied. They can still be thermally stabilized up to a critical heat flux, where they "explode". In favour of this model of thermal instability, three observations can be quoted, namely:

1. Heat peaks, observed before breakdown. This is best demonstrated by the technique of temperature mapping, developed at CERN (fig. 3). Fig. 4 (lower part) which is taken below breakdown, clearly shows heat-peaks in some locations of the cavity.
2. In mode mixing experiments carried out at Cornell, it was shown that if the field of two modes were superimposed with varying ratio of the two fields, the breakdown occurred for a fixed ΣB^2 and not for a fixed $\Sigma \vec{B}$ (fig. 5).
3. Plotting the effective loss resistance, derived from the Q-depression in a DORIS-cavity at Karlsruhe, against the square of the field, Halbritter finds straight portions that extrapolate to a finite resistance at zero field. This resistance is lower for magnetically shielded cavities and the slope at the curves depend on cooling conditions and resistance of the "bad spots" (fig. 6).

Fig.3: 500 MHz-Resonator at CERN showing movable arms equipped with resistance thermometers - R1 - R 39 and solid state x-ray detectors - D1 - D10.

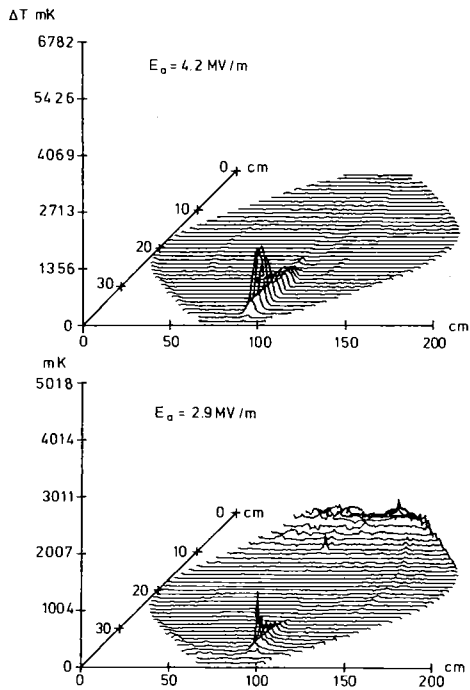
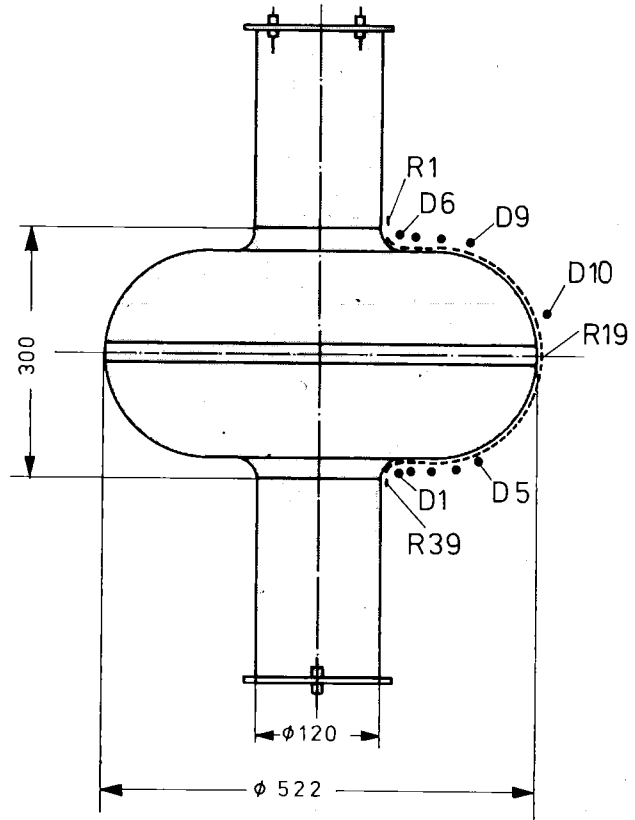


Fig. 4: Temperature map obtained with the equipment of fig. 3.

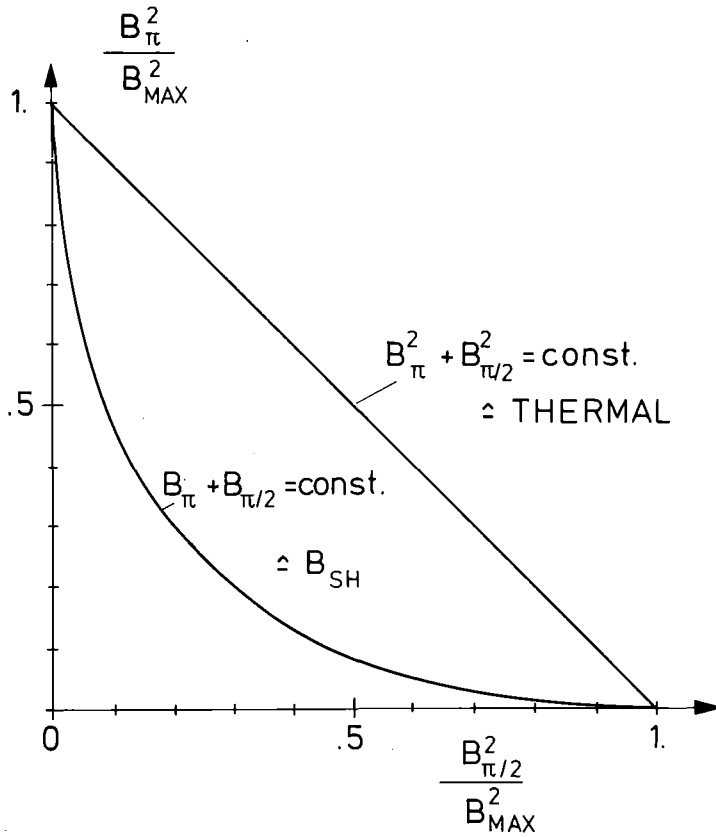


Fig. 5: Results of mode mixing experiment at Cornell

On the two axes, the fraction of field in each of the two modes is plotted. The curves show the locus of ΣB^2 and of ΣB at a critical spot in the cavity. Measured points fall on the ΣB^2 curve.

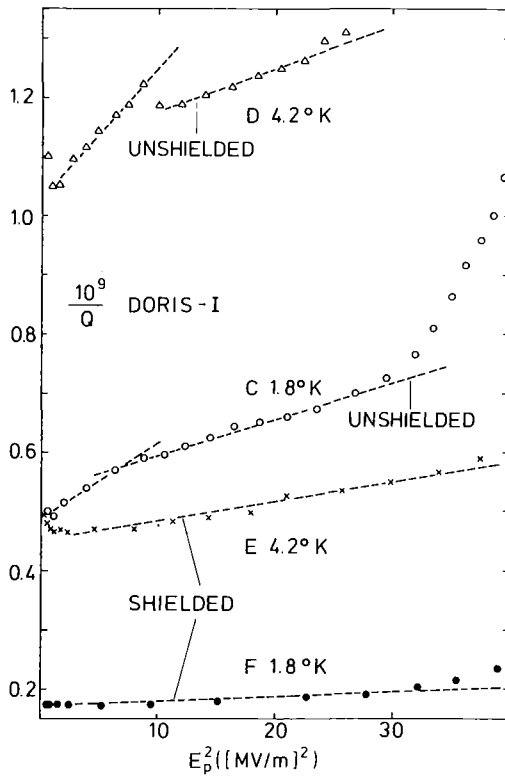


Fig. 6: Effective loss resistance derived from Q-depression as a function of E_p^2 for the DORIS-cavity (Halbritter).

The nature of "bad spots". There are several possible causes for a "bad spot". It can be due to external factor, such as radiation damage or a B-field enhancement for geometric reasons. Other causes can be:

- a trapped magnetic flux
- chemical inclusions (Fe, C ?)
- clustering of impurities
- clustering of suboxydes
- or just dirt on the surface.

Electron loading phenomena can be split into resonant and non resonant phenomena. Resonant electron loading, better known as multipacting, occurs in two varieties, namely: two- and one-side multipacting. The latter is at present the limitation in the HEPL-accelerator. Multipacting can be computed in not too complicated structures. There are a number of ways to avoid multipacting.

One way is to chose the shape of the cavity in such a way as to disturb one of the conditions necessary for multipacting. In a cylindrical cavity, this can be done by giving it sharp corners at the junction of the outer wall to the endplate (Stanford). In this way, the radial component of the electric field that drives multipacting at the cylinder walls is reduced. In a spherical cavity, the radial component of E is large, but also has a large gradient in axial direction so that the multipacting trajectory "walk away" fast (Genoa). Finally, one can cut grooves into the cylinder wall, which also disturbs the multipacting conditions (Cornell, Karlsruhe).

Multipacting depends on secondary emission of electrons upon electron impact. If the secondary emission coefficient could be made smaller than one over the whole range of energies, there would be no multipacting. This can sometimes be achieved by rf processing known from normal conducting cavities. It is also worthwhile to look for surface preparations that reduce this secondary emission coefficient.

In summary, it can be said that multipacting is not at present considered to be a final limitation for the fields that can be reached.

Non resonant electron loading, on the other hand, is today a limitation at lower frequencies. Here, the electron current shows an exponential increase with voltage, which is typical for field emission. From the so-called 'Fowler-Nordheim Plot' and using a work function at 4 eV, a field enhancement factor β can be derived that is the effective electric field responsible for pulling out the electrons from the metal divided by the macroscopic electric fields on the metal surface. β -values up to 2000 can be observed in electron loaded cavities that cannot be understood by geometric factors, such as surface roughness.

Electron loading can be studied via electron pick-ups, via X-rays, from the Q-degradation and from the heat deposited by the electrons on the walls. Fig. 7 shows an X-ray profile obtained at CERN by mounting silicon-detectors instead of the thermometers on the ro-

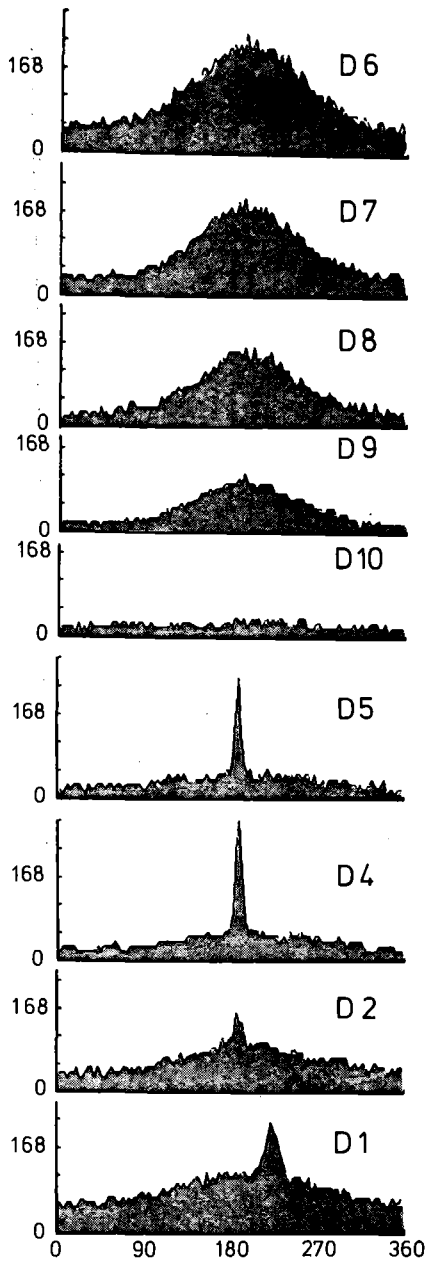


Fig. 7: X-ray distribution obtained at CERN by mounting silicon-detectors on the device shown in Fig. 3.

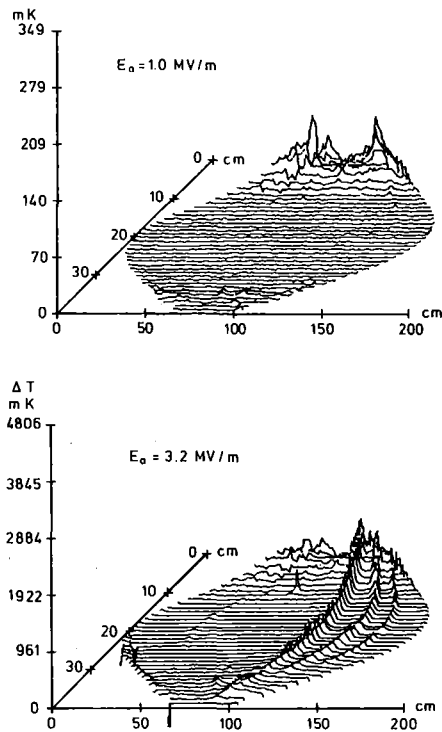


Fig. 8: Traces of heat peaks from a single electron source observed at CERN.

tating arm. Fig. 8 shows the trace of heat signals left on the cavity wall by electrons emitted from one spot in the cavity.

Sources of electrons can be dust particles brought into the cavity by air or by chemical solutions. Electrons can be created by electron impact through radiation damage or as secondary electrons. Not all mechanisms of electron emission are understood.

Like in the case of multipacting, rf processing can reduce the field emission. Glow discharge can sometimes reduce the electron emission and can in particular eliminate radiation damage. It can, however, also sensitize electron emitting areas.

This leads to the complex question of understanding the phenomena occurring at a niobium surface. Considerable time at the workshop was devoted to this subject. Fig. 9

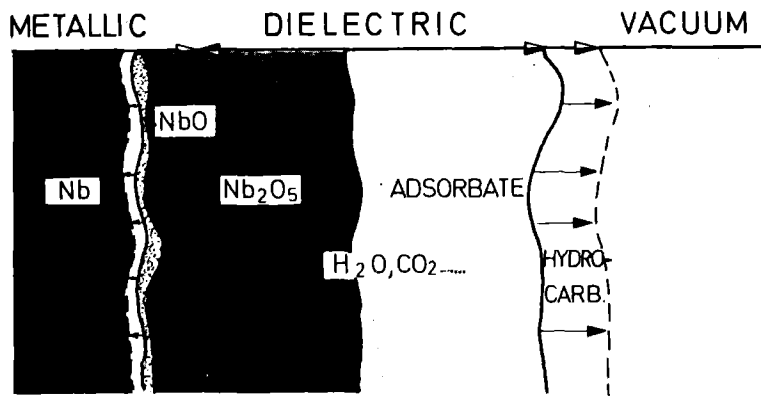


Fig. 9: Composition of a Nb-surface according to Halbritter.

shows Halbritter's view of the various layers that play a role here. Not only is an oxide layer unavoidable, but there are also suboxides between this oxide layer and the metal and an adsorption layer on the surface of this oxide. Different surface preparation methods yield different relative thicknesses of the layers. Fig. 10 shows an energy level diagram.

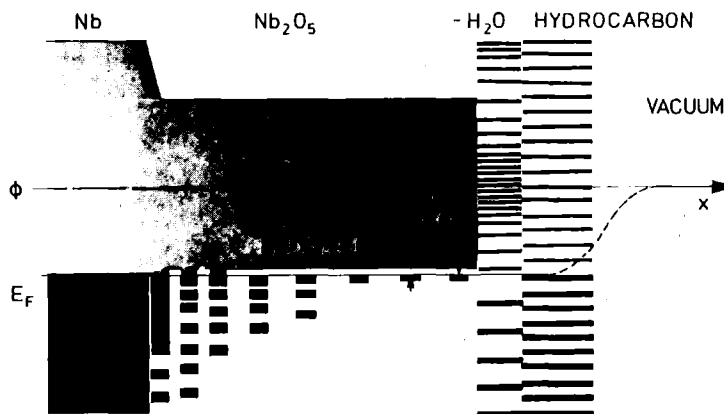
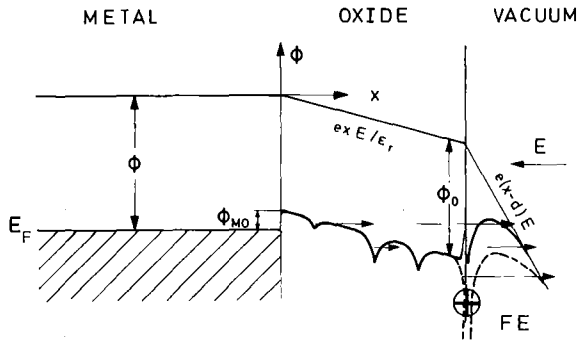


Fig. 10: Level scheme of Nb-surface according to Halbritter.

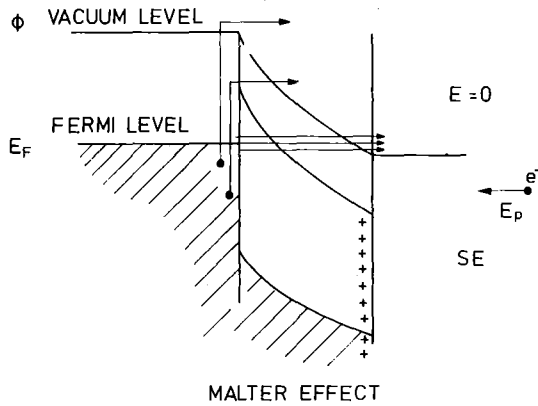
In the metal electrons move freely in the conduction band. In the oxide electron motion is

possible via localized electron states. Evidence for the suboxydes that become superconducting at 7 K, is obtained from penetration depth measurements, that show a discontinuity at this temperature. Evidence for the localized states is derived from tunnel measurements on Nb-Nb₂O₅-Pb junctions. Impacting electrons can change the surface conditions by excitation of electron states, but also simply by charging the oxide electrically. Fig. 11 shows how



field emission and secondary emission can be enhanced by such charging (Malter-effect).

Fig. 11: Enhancement of field emission and of secondary emission by charging of the oxide (Septier and Halbritter).



Although our understanding of chemical and physical properties of real niobium surfaces has made great progress, much effort will have to be devoted to increase our knowledge. From such studies, one hopes to finally derive recipes for surface preparation that are more than purely empirical. Septier drew up a table of possible studies

by a variety of methods used in surface physics (table 5). At present, the following laboratories work on this program: CERN, Karlsruhe, Orsay and SLAC. There was general agreement that these studies should be continued and intensified, but that they needed several years and should be free from the pressure of producing applicable recipes by certain dates. From such studies an increase of attainable accelerating fields may result.

An alternative approach to the question of field limitations, in particular to the 'bad spots' was introduced by Padamsee on the basis of an analysis of the heat transport from the heat source to the He-bath. Thermal instability depends not only on the heat generation, but also critically on the cooling condition. Better cooling can reduce the limiting effect of heat sources. Cooling is governed by:

1. heat conduction in the niobium parallel and at right angles to the surface. Unfortunately, reactor grade niobium shows a minimum of heat conduction

Table 5

SURFACE STUDIES

Summary by Septier

I. SURFACE PROPERTIES

1. - ION PROCESSING:	MECHANISMS INFLUENCE ON $R_s, E_p, H_p \dots$ " ON EMISSIONS	DESORBED SPECIES SURFACE MODIFICATIONS
2. - STRUCTURE AND COMPOSITION OF SURFACE LAYER	VARIOUS OXIDES ADSORBATES HYDROCARBONS (LEES, IETS,	
3. - CONDUCTION THROUGH SURFACE LAYER	LOCALIZED STATES (TUNNELING EXO-ELECTRONS .. INFLUENCE OF ADSORBATES WORK FUNCTION, CHARGING PHOTO- AND THERMO CURRENTS	
4. - IDENTIFICATION OF "BAD SPOTS"		
NEED FOR FUNDAMENTAL RESEARCH !		

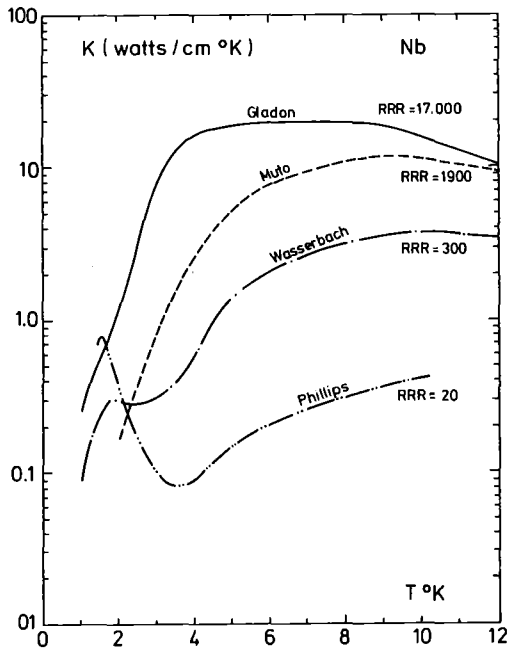
II. EMISSIONS

1. - FIELD EMISSION FROM REAL SURFACES:	-THEORY -INFLUENCE OF ADSORBATES (*) -PRACTICAL MEANS OF LOWERING F.E. INFLUENCE ON $R_s \dots E_p$	($\beta^*, \phi^* \dots$) RESONANT TUNNELING
2. - SECONDARY EMISSION	-SAME PARAMETERS (*) -SE + MALTER EFFECTS (charged layer) -LOWERING OF δ : PRACTICAL METHODS R_s, E_p (Thinfilms - ion processing)	
3. - IDENTIFICATION OF "BAD SPOTS"	(INDUCED DEFECTS)	

near 4 K, due to the reduction of the contribution of electrons to the heat conducting by Cooper-pair-condensation.

2. The Kapitza resistance to the fluid.
3. The heat transport processes in the fluid, namely conduction, convection and nucleate boiling, which are of course very different in He I and He II.

Padamsee suggested that for 4 K operation significant improvement in heat conductivity could be achieved by using purer niobium (fig. 12). Whereas the H-, O- and N-content can



be reduced by UHV-firing, there is little hope of getting lower tantalum content niobium from the manufacturers. If an electron deposition process for niobium

Fig. 12: Heat conductivity of Nb as a function of temperature for various degrees of purity (Padamsee).

could be developed it would automatically lead to lower Ta-content.

I shall be brief on the more technical parts of the workshop although they were a very important feature. Their results are, however, of more interest to the superconducting community than to a general audience.

Components to be used with superconducting resonators were discussed. Tuners do not appear to be problematic. They act by either squeezing the structure or by moving plungers in and out of the cavity.

Joints are more tricky. A number of demountable joints exist. Many of them cannot sustain high currents. High conductivity joints have been developed at Karlsruhe and ANL. They involve a niobium-ring, which has to be exchanged for each use in order to make contact with the fresh portion of the flange.

For storage ring applications, two more components are needed, namely couplers to feed in high power and couplers to remove higher order modes.

Power couplers up to 10 kW have been tested at Cornell and a power coupler up to 100 kW is in preparation at Karlsruhe. Higher order mode couplers have been developed at HEPL, Cornell and Karlsruhe. The Karlsruhe version, due to Szecsi, is shown in fig. 13. It is a wide band device that retains the fundamental mode and damps all higher modes strongly. Two such couplers will be used on the DORIS-cavity that will be tested in Hamburg shortly.

The design of the cavity has to be simple and has to avoid field enhancements and geometries favourable for multipacting. The number of cells will have to be a compromise

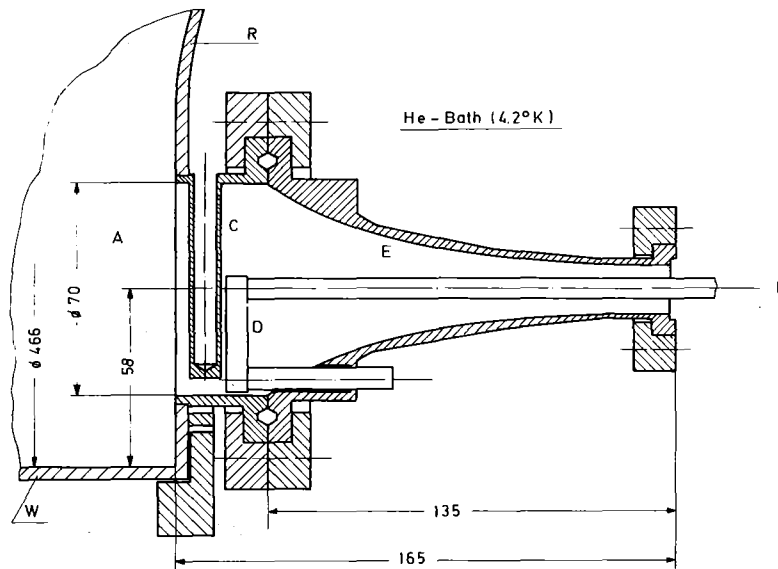


Fig. 13: Coupling for higher order modes developed at Karlsruhe by Szecsi.

between the desire to have a small number of units and the complications in handling long structures and in controlling the field in them.

The fabrication of cavities will have to start from Nb-sheet. It offers no special difficulties. Both electron beam and argon-arc-welding have been used successfully. It is not quite clear at the moment, which will be the most economic. A low oxygen contamination during welding is essential. The surface preparation always has to start with the removal of a damage layer up to .1 mm thick. A number of successful recipes exists. There was no unanimity on the question whether a heat treatment is essential. Attempts to replace traditional surface treatments by in situ treatments (glow discharge) are interesting but encouraging results are not yet available.

Finally, the application of superconducting cavities to storage rings was discussed by Tigner. He summarized this situation as follows:

1. A storage ring designed for superconducting cavities from the start can be cheaper by up to a factor 2 compared to a normal conducting one provided the structure cost per unit length is not too high.
2. The frequency should be chosen as low as possible. In the present (unsatisfactory) state of storage ring theory, 350 MHz for LEP and 1500 MHz for a

proposed 50 x 50 GeV-machine at Cornell were mentioned as upper limits.

3. Coupling-out of the higher modes is essential since they can become resonant not only with the revolution frequency and its harmonics, but also with betatron and synchro-betatron frequencies and their harmonics with moreover shift during operation.

Provided these (and all other problems discussed at the workshop) can be solved. Tigner termed the outlook as "fantastic".

Let me terminate with a parochial note by showing you a slide of the DORIS-cavity (fig. 14) that was inspected by most workshop participants and that is hoped to provide soon some answers to the problems just mentioned.

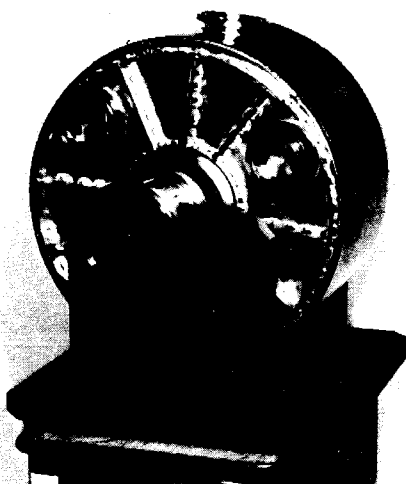


Fig. 14: The 500 MHz-cavity which will be tested in the electron-positron storage ring DORIS. In the endplate the two higher order-mode couplers can be seen.

REFERENCES

All references will be contained in the proceedings of the workshop that are going to appear as KfK-report 3019 and will be available from the Kernforschungszentrum Karlsruhe,

P.B. 3640, 7500 Karlsruhe, Literaturabteilung